INFORMATION TO USERS

This manuscript has been reproduced from the microfilm master. UMI films the text directly from the original or copy submitted. Thus, some thesis and dissertation copies are in typewriter face, while others may be from any type of computer printer.

The quality of this reproduction is dependent upon the quality of the copy submitted. Broken or indistinct print, colored or poor quality illustrations and photographs, print bleedthrough, substandard margins, and improper alignment can adversely affect reproduction.

In the unlikely event that the author did not send UMI a complete manuscript and there are missing pages, these will be noted. Also, if unauthorized copyright material had to be removed, a note will indicate the deletion.

Oversize materials (e.g., maps, drawings, charts) are reproduced by sectioning the original, beginning at the upper left-hand corner and continuing from left to right in equal sections with small overlaps. Each original is also photographed in one exposure and is included in reduced form at the back of the book.

Photographs included in the original manuscript have been reproduced xerographically in this copy. Higher quality 6" x 9" black and white photographic prints are available for any photographs or illustrations appearing in this copy for an additional charge. Contact UMI directly to order.

UMI

A Bell & Howell Information Company
300 North Zeeb Road, Ann Arbor MI 48106-1346 USA
313/761-4700 800/521-0600

A SOLID-STATE NMR INVESTIGATION OF STRUCTURE AND DYNAMICS IN NUCLEOSIDES AND METHYLATED DNA OLIGONUCLEOTIDES

by

Karen Brigitte Geahigan

A dissertation submitted in partial fulfillment of
the requirements for the degree of

Doctor of Philosophy

University of Washington

1998

Approved by _____
Chairperson of Supervisory Committee

Program Authorized
to Offer Degree CHEMISTRY

Date 3/17/98

Doctoral Dissertation

In presenting this dissertation in partial fulfillment of the requirements for the Doctoral degree at the University of Washington, I agree that the Library shall make its copies freely available for inspection. I further agree that extensive copying of this dissertation is allowable only for scholarly purposes, consistent with "fair use" as prescribed in the U.S. Copyright Law. Requests for copying or reproduction of this dissertation may be referred to University Microfilms, 1490 Eisenhower Place, P.O. Box 975, Ann Arbor, MI 48106, to whom the author has granted "the right to reproduce and sell (a) copies of the manuscript in microform and/or (b) printed copies of the manuscript made from microform."

Signature Karen B Gallagher

Date 3/17/98

University of Washington

Abstract

A SOLID-STATE NMR INVESTIGATION OF STRUCTURE AND DYNAMICS IN NUCLEOSIDES AND METHYLATED DNA OLIGONUCLEOTIDES

by Karen Brigitte Geahigan

Chairperson of the Supervisory Committee: Professor Gary P. Drobny
Department of Chemistry

This dissertation contains various experimental solid-state NMR techniques for probing structure and dynamics in nucleosides and DNA oligonucleotides. One- and two-dimensional solid-state NMR experiments were applied to four different nuclei in these investigations: ^{13}C, ^{15}N, ^{19}F, and ^{2}H. One-dimensional homonuclear dipolar recoupling experiments (i.e. Radio Frequency Driven Dipolar Recoupling (RFDR) and Dipolar Recoupling with a Windowless Sequence (DRAWS)) were used to measure internuclear ^{13}C-^{13}C and ^{19}F-^{19}F distances in [2,1'-$^{13}C_2$]- and [2,2'-$^{13}C_2$]-cytidine and the DNA dodecamer sequence, [d(CGCGAATT^{5Me}CGCG)]$_2$, which contained either [2-^{13}C]-thymidine or [5-^{19}F]-2'-deoxyuridine at the T_8 and [2-^{13}C]-5-methyl- or [5-^{19}F]-2'-deoxycytidine at the C_9 positions. These measurements indicate that methylation produces minimal distortion of the local geometry at the T_8-C_9 dinucleotide junction. Two-dimensional DRAWS and RFDR experiments were used for the chemical shift assignment of complicated multiply ^{13}C,^{15}N labeled nucleosides. Double-quantum (DQ) DRAWS was also applied to various selectively and uniformly ^{13}C enriched nucleoside monomers in order to obtain orientational

information for pairs of dipolar coupled nuclei. Our findings demonstrate that solid-state dipolar recoupling methods can provide valuable structural information about nucleosides and nucleic acids in polycrystalline and heterogeneous environments.

Solid-state deuterium NMR experiments were also implemented to probe the internal motions of the sugar ring, backbone, and base moieties of 5-methyl-2'-deoxycytidine incorporated at the C_9 position in the DNA dodecamer, $[d(CGCGAATT^{5Me}\underline{C}GCG)]_2$, as a function of hydration level. Replacement of the C_9 residue with its methylated analogue radically perturbs the large-amplitude dynamics of the exocyclic methylene group but only marginally alters the mobility of the furanose ring that was noted in a previous study by Hatcher and coworkers [70]. Base mobility in methylated and unmethylated derivatives was found to be similar. Reduced flexibility of the $^{5Me}C_9$ site may be directly correlated with inhibition of hydrolysis by the EcoRI restriction enzyme. The solid-state ^2H NMR findings indicate that there may be a dynamic component in the sequence-specific protein-DNA recognition mechanism that is hindered by methylation of the C_9 residue.

TABLE OF CONTENTS

LIST OF FIGURES

LIST OF TABLES

ACKNOWLEDGMENTS

I would especially like to thank my research advisor, Professor Gary Drobny for all his enthusiasm, patience, and support. A special thanks goes out to Julie Miller and Dr. Michael Kennedy for patiently introducing me to biochemistry and NMR during my first year of graduate school. Additionally, I would like to acknowledge my very good friends Dr. Mary Hatcher, Dr. Matt Merritt, and (soon to be) Dr. John Stringer for sharing with me all their expertise in synthesis and NMR spectroscopy and for keeping graduate school entertaining. Finally, I would like to thank my family and my husband, David, for all their love and encouragement throughout the many years of my education.

Chapter 1
Introduction

1.1 Nucleic Acids

Nucleic acids (DNA and RNA) are of paramount importance in all living organisms because they store and transmit information specifying the structures of their proteins. In order to carry out all of their biological functions, nucleic acids must be able to adopt a variety of conformations. Some of the more dramatic structural alterations include bending, kinking, hairpin and cruciform formation, base flipping, and supercoiling. Other subtle sequence-specific conformational changes may also be relevant for nucleic acid function. Clearly, DNA and RNA cannot be described purely in terms of static structure. Understanding the flexibility and structure of nucleic acids (and ultimately the relationship of structure, dynamics, and biological function) involves answering two fundamental questions: 1) what conformation does the molecule adopt at any particular instance, and 2) how does the molecule go from one conformation to another? Structural approaches can begin to address the first question. Some of these strategies are introduced in the following sections and will be further developed in subsequent chapters. The second question involves understanding the complex local and global motions that are achieved by the oligonucleotide polymer as the molecule samples conformational space.

The basic repeat unit in DNA and RNA is the nucleotide, composed of a five-membered furanoside-type sugar moiety (β-D-ribose in RNA or β-D-2'-deoxyribose in DNA), substituted at the C5' position with a phosphate group and at the C1' position (β-glycosyl linkage) with one of four planar nitrogen-containing heterocycles: thymine (or uracil in RNA), cytosine, adenine, or guanine [1]. Adenine and guanine

are purines which contain fused five and six membered aromatic rings. Cytosine, thymine, and uracil are pyrimidines which contain a single six membered aromatic ring. Nucleotides are linked by 3', 5'-phosphodiester bonds to form a polynucleotide chain (Figure 1.1). Double-helical DNA consists of two polynucleotide strands (Figure 1.2). The orientation of the two strands is antiparallel (i.e. their 5' $\rightarrow$ 3' directions are opposite), and the bases of one strand hydrogen bond to the complementary bases on the opposing strand. The double helix possesses two grooves: a wider major groove and a narrower minor groove, indicated in Figure 1.2. Because of the geometry of the double helix, a purine must always pair with a pyrimidine. Adenine forms two hydrogen bonds with thymine, and guanine forms three hydrogen bonds with cytosine. The stability of the double helix arises from the numerous hydrogen bonds and hydrophobic interactions between the strands.

The diversity in macromolecular properties and biological behavior of nucleic acids (DNA and RNA) is closely associated with the conformational variability of the fundamental nucleotide constituents. The overall structure of a nucleoside (i.e. a nucleotide without a 5' phosphate group) results from a complex interplay of five endocyclic (ν_1, ν_1, ν_2, ν_3, and ν_4) and two exocyclic (χ and γ) torsion angles which determine the conformation of a cyclic furanose ring, its orientation relative to the purine or pyrimidine heterocycle, and the orientation of the C5' methylene group about the C4'-C5' bond. Figure 1.3 depicts the atomic numbering scheme and definition of torsion angles for a polyribonucleotide chain. In nucleosides, these torsion angles are all correlated (except for γ), meaning that structural changes follow a concerted motion [1]. Additional angles are also defined for polynucleotides which describe the orientation of the phosphodiester backbone (α, β, δ, ε, and ζ). The endocyclic ν_3 and exocyclic δ describe the same torsion angle. In oligonucleotides, all sugar-phosphate backbone torsion angles (including γ) are interrelated.

The rotational position of the essentially planar base relative to the sugar ring is sterically restricted and exists in either of two conformational states (syn or anti)

[2]. In the anti conformation there is little steric hindrance between sugar and base, but in the syn conformation the bulky part of the base is located over the sugar, giving rise to close interatomic contacts. The difference between syn and anti conformations is illustrated in Figure 1.4. In order to alleviate torsional strain, the unsymmetrically substituted furanose ring is preferentially puckered with the C2' or C3' carbon atom farthest out from the C4'-O1'-C1' plane [3]. The correlation among the endocyclic torsion angles of the furanoside moiety can be most conveniently described in terms of pseudorotation phase angles and puckering amplitudes [4, 5]. Two regions of preferred puckering modes exist, C3'-endo (North) and C2'-endo (or equivalently C3'-exo) (South). Interconversion between these two puckering modes corresponds to an interchange of sugar ring substituents between axial and equatorial orientations (Figure 1.4 and Figure 1.5). Atoms lying on the same side of the C4'-O1'-C1' plane as C5' are designated endo and those opposite as exo. The North (N) and South (S) conformers are thought to exist in dynamic equilibrium in the solution-state. Rotation about the exocyclic C4'-C5' bond (γ) determines the position of the 5'-methylene group relative to the sugar ring [1]. Three staggered conformers are possible (Figure 1.4), +sc (gauche, gauche), -sc (trans, gauche), and ap (gauche, trans) [5]. The three ranges are not uniformly populated and depend on the base and sugar pucker.

Two hydrogen bonded polynucleotide strands can in principle form either right-handed or left-handed double helices [6]. The right-handed form predominates under physiological conditions. There are several polymorphs of the right-handed form of DNA and RNA. A-type and B-type families of DNA are of particular relevance in this dissertation. The essential distinction between A-form and B-form families lies in the sugar puckering modes. A-form adopts a C3'-endo conformation and B-form adopts a C2'-endo conformation. In both A- and B-DNA, the glycosyl bond is in the anti orientation. The different puckering modes result in changes in the distance between adjacent phosphates of the same polynucleotide chain in DNA, ranging from 5.9Å for C3'-endo to 7.0Å for C2'-endo (Figure 1.5) [1]. Due to these

changes in phosphate-phosphate distances, the two families of DNA can adopt very different macroscopic forms (Figure 1.6). In the canonical B-form, the stacked bases are regularly spaced 3.4Å apart along the helix axis, so there are 10 base pairs per helix turn. The base pairs are centered on the helix axis, and major and minor grooves are relatively equal in size. For A-type DNA, one helical turn requires 11 nucleotides, but the axial rise per nucleotide is 2.56Å. The base pairs are tilted by 20° relative to the helix axis, and the base pairs are dislocated from the helix axis resulting in a deep major groove and a shallow minor groove. The A-DNA helix appears broader and more compressed relative to the B-DNA helix.

1.2 The Role of Water

DNA structure is sensitive to cation type and hydration level [1]. The repulsive phosphate-phosphate electrostatic interaction is diminished by the high dielectric constant of water and hydrated counterions. Different cations have a profound effect on DNA secondary structure. Only sodium salts of DNA will be addressed in this dissertation. The uptake of water is defined by the parameter W (moles of water per moles of nucleotide). The primary hydration shell of DNA consists of 11 to 12 water molecules per nucleotide. Hydration occurs for the three constituents of the nucleotide subunit differently. At a relative humidity (RH) of 65%, (W=5-6), the phosphate oxygens are hydrated. Hydration of the amino, imino, and keto groups of the nitrogenous bases occurs above 65% RH (W=13-15). At 80% RH primary hydration of the DNA is complete with about 20 waters per nucleotide. Further hydration is accompanied by swelling of the sample and the formation of a second hydration shell. DNA adopts the B-form under high relative humidity. Generally, dehydrated states or increased ionic strength favor formation of the A-form. It is known from fiber diffraction studies that the transition from A- to B-form occurs between 75% and 92% RH [7].

1.3 Nucleoside Structure

Clearly, the structure of a highly conformational entity, such as a nucleoside, will be profoundly affected by changes in its physical environment. Most of the discussions about the molecular geometry of nucleosides are focused on results obtained from single-crystal diffraction studies or spectroscopic measurements. These methods have shown that ribo- and deoxyribonucleosides exhibit a remarkable amount of conformational flexibility. The next two sections describe the X-ray crystallographic and spectroscopic findings for nucleosides in the solid- and liquid-state.

1.3.1 X-Ray Crystallography

Analyses of numerous X-ray crystal structures indicate that C3'-endo and C2'-endo are equally populated by ribonucleosides and their derivatives, whereas, the C2'-endo conformation is preferred for deoxyribonucleosides [8]. Purine ribonucleosides with C2'-endo conformation adopt both syn and anti forms equally, but C3'-endo rings prefer an anti orientation. For pyrimidine ribonucleosides, the less sterically hindered anti conformation dominates and is tightly correlated with a C3'-endo ribose puckering mode. Pyrimidine and purine deoxyribonucleosides are found primarily with C2'-endo sugar ring puckers, with pyrimidines preferring the less sterically hindered anti orientation. Purine nucleosides may reside in the +sc or ap ranges for both C2'-endo and C3'-endo puckering modes. In pyrimidine nucleosides, the preferred conformation about the C4'-C5' bond is +sc regardless of sugar pucker.

1.3.2 Solution-State Techniques

Nucleosides in the liquid state behave as dynamically averaged mixtures of rapidly interconverting conformers. A variety of spectroscopic methods have been

utilized to probe the conformational characteristics and intermolecular interactions of nucleosides in solution: NMR, IR and UV absorption, and circular dichroism [1, 9-11]. Details about molecular conformation and pseudorotational parameters are most readily deduced from NMR data. Three NMR parameters have been used to estimate conformational characteristics and intermolecular interactions in nucleosides: chemical shifts, time-averaged spin-spin vicinal coupling constants (^3J) and spin-lattice relaxation times (T_1). The orientation of the base relative to the sugar moiety has been estimated from NMR spin relaxation times, double resonance NOE methods, and ^{13}C-^1H coupling constants [12]. NMR and CD spectroscopic data suggest that in solution nucleosides undergo a rapid interconversion between syn and anti orientations. However, only rough estimates of the relative orientation about the glycosidic bond can be made using these techniques. Scalar vicinal coupling constants are particularly useful because they can be related to the dihedral torsion angles through modified forms of the Karplus relation [13-15]. A ratio of vicinal ^1H coupling constants, $^3J_{1'2'}$ and $^3J_{3'4'}$, can be used to evaluate equilibrium populations for N and S conformers [2]. An analogous treatment of $^3J_{4'5'}$ and $^3J_{4'5''}$ establishes the conformation of the exocyclic 5'-oxygen relative to the ribose ring [16]. The valid application of these idealized empirical equations for determination of furanoside ring conformation, especially in biomacromolecules, has recently been disputed by Zhu and Harbison et al. [17, 18]. The use of J-coupling to analyze sugar ring conformation is based on applying simplified models derived for furanose derivatives to large, slowly tumbling macromolecules. It has been shown that the information derived from interpretation of scalar ^1H-^1H coupling data may be inaccurate, because it does not take into account the effects of cross-relaxation that are unavoidable for macromolecular systems in the long correlation time limit.

1.4 Solid-State NMR Spectroscopy

Solid-state NMR is a powerful complement to X-ray crystallography and solution-state spectroscopic techniques for determination of molecular conformation. A wealth of information about anisotropic interactions (such as the chemical shift and the homo- and heteronuclear dipolar couplings) is contained in the solid-state NMR signal. In the liquid state, these anisotropic interactions are substantially averaged by rapid molecular tumbling, so generally only time-averaged quantities can be measured. Solid-state NMR is particularly useful for probing conformational permutations in systems that are not always tractable by more traditional methods. This technique requires neither the preparation of pristine single crystals, nor is dependent on a molecule's solubility characteristics. Different types of solid-state NMR experiments can be used to investigate various structural and dynamical aspects of samples in a variety of physical conditions, ranging from refined single crystal or polycrystalline states to amorphous, heterogeneous powders. Although solid-state NMR can yield valuable information about structure, numerous technical difficulties have prevented its widespread application to biological systems. The techniques for obtaining high-resolution solid-state NMR spectra will be discussed in more detail in Chapters 2 and 3.

The application of solid-state NMR for structure elucidation of nucleosides and nucleic acids has focused primarily on high molecular weight DNA oligomers [19, 20]. Early reports of ^{13}C CP-MAS spectra on calf thymus DNA fibers indicated that A and B forms of DNA show quite different chemical shifts in the sugar region due to the difference in deoxyribose ring puckers [21]. C3' and C5' resonances were shifted upfield by 7.5-10 ppm in A-DNA relative to B-DNA. These chemical shift changes could be correlated with proportions of North (C3'-endo) and South (C2'-endo) puckering modes. Phosphorus-31 MAS spectra of A- and B-type DNA were found to be very similar, exhibiting a complete absence of resolution among the phosphorus nuclei. However, it was determined from static powder pattern and CP-

MAS sideband patterns (for the overlapped ^{31}P resonances), that the chemical shielding tensor principal values of sodium and lithium B-DNA were subtly different. Harbison and coworkers have also utilized two-dimensional natural abundance ^{13}C CP-MAS experiments on oriented fibrous DNA to measure the base and sugar ring chemical shielding tensors and orientations relative to the fiber axis [22, 23]. Nitrogen-15 CP-MAS spectroscopy was conducted by Opella and coworkers to study E. coli DNA that had been grown on a medium containing $^{15}NH_4SO_4$ as its sole nitrogen source [24]. The spectra produced 15 resolved chemical shift resonances resulting from chemically distinct nitrogen nuclei. These authors further simplified the spectrum, using the heteronuclear dipolar coupling between ^{15}N and ^{1}H nuclei as a selection mechanism [25]. Recently, dipolar recoupling techniques from this laboratory have been implemented to measure internuclear ^{13}C-^{13}C distances and orientations in a doubly carbon labeled dT7-dT8 segment of the B-DNA dodecamer, $[d(CGCGAATTCGCG)]_2$. The details of these studies will be discussed in greater detail in Chapter 5.

1.5 Localized Dynamics in Nucleic Acids

Many approaches have been applied to the study of nucleic acid dynamics. Some of these methods are carried out in the solution state and others under amorphous, hydrated conditions. Some of the techniques include: high-resolution solution-state NMR, solid-state deuterium NMR, fluorescence polarization anisotropy, dynamic light scattering, X-ray diffraction, electron paramagnetic resonance, and molecular dynamics. The reader is referred to several review articles covering experimental and theoretical aspects of DNA dynamics [25-28]. The technique that is utilized in this dissertation for the measurement of local internal motions has been solid-state ^{2}H NMR. An extensive review of deuterium dynamics in DNA has been

published by Alam and Drobny [25]. The advantages of solid-state ^2H NMR as a probe of internal dynamics in DNA oligonucleotides will be discussed in Chapter 2.

1.6 DNA Methylation

Sequence-specific recognition of nucleic acids by proteins is vital in the regulation of numerous biological processes. We are particularly interested in understanding those structural and dynamical features of nucleic acids that may contribute to the sequence-specific recognition by proteins that exhibit enzymatic activities. Methyltransferases and restriction endonucleases are two examples of this class of proteins. Modification of DNA by methylation occurs in both prokaryotes and eukaryotes. Enzymatic transfer of a methyl group from S-adenosyl-L-methionine (AdoMet) to the N6 position of adenosine and the C5 or N4 position of cytidine nucleotides shortly after replication is the most common form of biological DNA modification [29]. These modified bases are depicted in Figure 1.7. Methylation of cytosine and adenosine in prokaryotes is involved primarily in restriction-modification systems that serve as immune responses to phage infection. DNA methylation in prokaryotes is also known to be involved in regulating the initiation of DNA replication.

Restriction enzyme-modification systems provide a clear example where methylation of DNA inhibits cleavage by the corresponding endonuclease. The DNA dodecamer, $[d(CGCGAATTCGCG)]_2$, is being used as our model system for studying the structural and dynamical aspects of protein-DNA recognition. This DNA dodecamer sequence is of particular biological interest because it contains the palindromic EcoRI restriction endonuclease recognition site, G↓AATTC (the arrow indicates the enzyme cutting site between G4 and A5). The EcoRI restriction enzyme (31,000 Dalton: 276 amino acids) binds its cognate DNA sequence as a dimer. Each subunit hydrolyzes the phosphodiester bond of one of the palindromic strands in the presence of Mg^{2+}, leaving a 5'-phosphate [30, 31]. This six base-pair sequence is also recog-

nized by the EcoRI methyltransferase, which transfers a methyl group from AdoMet to the N6 position of the adenine residue at the central ApT junction shortly after DNA replication, preventing degradation of the bacterial host DNA by the EcoRI endonuclease [32].

Brennan and coworkers investigated the effect of base analogue substitutions on protein-DNA interactions involved in the recognition of the six base pair sequence, d(GAATTC), by the EcoRI restriction and methyltransferase enzymes using steady-state kinetics [31, 32]. This investigation confirmed that methylation of the exocyclic amino group of the central adenine in the sequence, $[d(GGAATTCC)]_2$, inhibits cleavage by the EcoRI endonuclease. The Brennan study also showed that introduction of either 5-bromocytosine or 5-methylcytosine at the cytosine position prevents cleavage by the restriction enzyme. Although these two analogue substitutions are examples of conservative alterations that do not disrupt hydrogen bonding contacts between the DNA and the protein, the absence of reactivity indicates that the endonuclease is in close proximity to the 5 position of cytosine during the cleavage reaction. These same base modifications did not inhibit EcoRI methyltransferase activity, suggesting that the modification methylase is not in close proximity to the substrate in this region of the major groove of the recognition sequence.

In higher eukaryotes, methylation at the C5 position of cytosine is the only reported methylation site [29, 33]. In vertebrates, the methylation of cytosine bases occurs predominately at CpG dinucleotide steps. Approximately 70% of the CpG steps are methylated in humans [34]. The CpG sequences are unevenly distributed in the genome and are concentrated in regions called "CpG islands". These CpG islands (which are approximately 1000-2000 nucleotide pairs long) generally surround the promoters of housekeeping genes. The exact function of DNA methylation in eukaryotic cells is not fully understood, and methylation has been implicated in various cellular processes: transcription, genomic imprinting, developmental regulation, mutagenesis, transposition, DNA repair, X-inactivation, and chromatin organization.

Additionally, abnormal methylation patterns have been correlated to human genetic disorders such as cancer and fragile X syndrome [29, 33, 35, 36].

The structure and mobility of various nucleotides in the EcoRI enzyme binding site (underlined section) of the DNA dodecamer, [d(CGCGAATTCGCG)]$_2$, have been extensively studied by X-ray crystallography and solution- and solid-state NMR. The findings of these investigations are summarized in the next section. The goal of these studies has been to understand the mechanism for the specificity between the EcoRI restriction and methylase proteins and their cognate DNA binding, cleavage, and modification sites. This DNA dodecamer sequence also possesses two CpG dinucleotide steps directly adjacent to the enzyme binding site. Consequently, this well-studied sample can serve as a model system for understanding the structural and dynamical consequences of cytosine methylation at CpG steps, which have been shown to be vitally important for eukaryotic systems.

1.7 The Dickerson Sequence, [d(CGCGAATTCGCG)]$_2$

The single-crystal X-ray structure of a synthetic dodecanucleotide, [d(CGCGAATTCGCG)]$_2$, by Dickerson and Drew has formed the basis for numerous structural studies of DNA [37]. This was the first example of a single-crystal X-ray structure of a synthetic DNA oligonucleotide in the biologically relevant right-handed B-form. Examination of the crystal structure revealed that the conformation of the DNA helix was highly dependent on base sequence, and variations in sugar and backbone conformation could induce changes in base-pair stacking. The possibility of sequence-specific structural variations was a radical departure from the concept of an ideal Watson-Crick B-DNA double helix.

A detailed analysis of sugar-backbone torsion angles for each of residue in the sequence by Dickerson and Drew indicated that sugar conformations ranged from C3'-exo to O4'-endo, with purine sugars preferring a C2'-endo pucker and pyrimidine

sugars preferring an O1'-endo conformation. This trend was preserved for symmetry-related pairs, despite the presence of an overall 19° bend in the helix axis. Furthermore, the authors determined that the orientation of the base about its glycosyl (χ) bond was closely correlated with the δ torsion angle, where the δ angle defines the puckering mode of the furanose ring. Several important observations were made about the sequence, T8-C9-G10, contained in two places in the palindromic dodecamer [38]. One of these was that the C9 base was shown to "slip" from under T8 and stack more efficiently over G10. This results in a broad step from T8 to C9 and a narrow step between C9 to G10. The C9-G4 base-pair must compensate by opening out into the minor groove, possibly weakening the hydrogen bond that normally exists between G4:O6 and C9:N4. Lomonossoff et al. have observed from kinetic studies that this widened TpC step is the preferred point for cutting by the DNAase I endonuclease [39]. It was proposed by Dickerson and Drew that the T8-C9 "slip" widens the TpC step and leaves the TpC sugar-phosphate bond exposed, thus making it more susceptible to cleavage by the DNAase I enzyme [38].

The structure and dynamics of the Dickerson dodecamer have also been studied extensively by solution-state NMR spectroscopy [17, 40, 41]. While the solution-state NMR structure did not detect the global bend in the helical axis, many similarities were seen in base-pair orientation (i.e., inclination, tip, propeller twist and buckle). The solution-state and x-ray structure have the same trend in sugar ring conformation, except for the lower sugar pseudorotation phase values for the C3 residue in the X-ray structure. Additionally, the minor groove at the T8, C9, and the G10 steps was not found to be as narrow as in the X-ray structure. The solution-state structure also did not reveal the anomalous backbone conformations that were observed for G4 and G10 in the X-ray structure. Zhu attributed these discrepancies in the minor groove width and in the backbone structure to crystal packing forces in the X-ray structure. The "splay" in the C9-G4 base pair was not directly mentioned in the solution-state NMR structure.

Bax and Lerner investigated the local sugar mobility of individual nucleotides in the Dickerson sequence by measuring solution-state NMR scalar (J) coupling constants [42]. This work utilized a modified Karplus-type equation to calculate dihedral angles from the scalar ^{1}H-^{1}H coupling data. The dihedral angles were then used to calculate populations of North (C3'-endo) and South (C2'-endo) conformations using the principles of pseudorotation. The Bax and Lerner study suggested that the sugar ring conformations of some residues exhibit a more rapid interconversion between conformers while others remain more rigid. Specifically, the sugar rings of C3, T7, and C9 were thought to exhibit increased exchange between North and South conformers. Exhaustive solid-state ^{2}H dynamics investigations of localized sugar, backbone, and base motions in the Dickerson dodecamer from this laboratory have indicated that both C3 and C9 show unusual large amplitude motions at biologically relative hydration levels [43]. The details of these ^{2}H studies will be discussed in greater detail in Chapter 8.

1.8 EcoRI Protein-DNA Complex

The crystal structure of the complex between the EcoRI endonuclease and the DNA oligonucleotide, $[d(TCGCGAATTCGCG)]_2$, was solved by McClarin and coworkers [44]. The complex consists of a distorted DNA double helix and a protein dimer composed of identical subunits related by a twofold axis of rotational symmetry. There is intimate contact between the major groove of the DNA and the protein, while the minor groove is clearly exposed to solvent. Twelve hydrogen bonds are responsible for the sequence specificity of the enzyme for the hexanucleotide sequence, GAATTC. Additionally, the protein is in proximity to the DNA backbone over a span of 10 base pairs, which includes the enzyme binding site. It has been proposed that recognition of the DNA by the EcoRI protein is due to a combination of both di-

rect readout (via protein-base contacts within the binding site) and indirect readout (via protein-phosphate contacts both within and adjacent to the binding site) [45, 46].

Several structural features of the complex are particularly noteworthy. The DNA retains its Watson-Crick base pairing throughout the 12 paired bases. However, the DNA is kinked in the recognition complex. These kinks (designated as "neokinks") are induced and stabilized by the binding of the protein and are not found in the native DNA dodecamer. A type I neokink between A6 and T7 results in a 25° unwinding of the double helix which increases the separation of the backbones and widens the major groove to permit insertion of the protein. A negative roll angle between the central base pairs (-57°) compared with the free DNA (-6°) results in a complete unstacking of the base pairs [47]. Additionally, neokinks are also induced between C3pG4 and C9pG10, which do not introduce a net unwinding of the DNA helix. These are referred to by the authors as type II neokinks. However, the backbone associated with nucleotides on either side of G4 and G10 are in unusual, extended conformations. The G4-A5 phosphate-phosphate distance is 7.3Å, and the C9-G10 phosphate-phosphate distance is 7.4Å. Both of these distances are longer than expected in B-DNA. There is no direct reference in the EcoRI complex crystal structure of what happens to the unusual structural perturbations ("slip" and "splay") at the T8-C9-G10 segment which were seen in the crystal structure of the native DNA dodecamer.

1.9 Structural Consequences of Methylation on CpG Structure

The biological consequences of cytosine methylation may arise from alterations in local DNA conformation, in addition to direct protein-methyl group interactions. Several reports on the effect of cytosine methylation on the structure at CpG steps exist in the literature. It is known that the presence of methylcytosine stabilizes the DNA double helix as evidenced by an increase in the melting temperature of the

DNA [29, 48]. Although cytosine methylation alters the chemical structure of the base by increasing its size and changing electron densities in the pyrimidine ring, methylation does not perturb Watson-Crick hydrogen bonding nor has it been found to substantially alter the global B-conformation of the DNA [49]. However, Garcia and Hagerman showed that cytosine methylation can modulate the net curvature of an A-tract containing DNA based on electrophoretic mobility studies [50]. Heinemann and coworkers asserted from an X-ray diffraction study that methylation of ^{5Me}CC in the B-DNA decamer, [d(CCAGGC^{5Me}CTGG)]$_2$, resulted in only very slight structural rearrangements relative to an unmethylated control sequence [51]. This investigation was complicated by differences in the crystalline conditions and space groups of the methylated and unmethylated analogues. In a more recent study by Ollila and co-workers on the sequence specificity of CpG mutational hotspots in the vertebrate genome, it was found that the 5' cytosine in CpG dinucleotides with flanking 5'-pyrimidine and 3'-purine bases (i.e. TCGA and TCGG) were the most frequently mutated tetranucleotides [52]. These researchers also propose that the DNA may possess local structural alterations due to the 5'-dT-dC-dG-purine-3' sequence that could affect protein-DNA interactions in the major groove.

Lefebvre et al. utilized solution-state ^{1}H and ^{31}P NMR to probe the structural differences in two related octamer duplexes, d(CATCGATG)$_2$ and d(CAT^{5Me}CGATG)$_2$ [49]. Chemical shift (^{31}P and ^{1}H) and NOE data were compiled in an effort to understand the structural basis for the increase (+4°C) in melting temperature of the methylated relative to the unmethylated DNA sequence. The phosphorus backbone was shown to be sensitive to cytosine methylation as evidenced by substantial downfield-shifted ^{31}P resonances for the central cytidine nucleotide. Proton chemical shifts indicated that Watson-Crick base-pairing was not significantly altered upon methylation, and both oligonucleotides retained their B-DNA conformation. However, deviations in the H1' and H2' chemical shifts for the T3 and C4 residues in d(CAT^{5Me}CGATG)$_2$ were suggestive of differing orientations of the pyrimidine ring

in the two samples. The gain in thermal stability was attributed to improved base stacking in the analogue containing the methylated CpG step [49].

The other major effect of cytosine methylation is to enhance the probability that a stretch of DNA will undergo a B-Z transition in poly(dG-^{5Me}dC)·(dG-^{5Me}dC) [53]. Behe and Felsenfeld studied the effects of methylation on the B-Z transition using circular dichroism and UV absorption and demonstrated that this transition occurs at much lower salt concentrations than for the unmethylated dG-dC polymer. Thermodynamic, X-ray, and solution-state NMR investigations have indicated that B-Z transitions occur in vitro and may be important in eukaryotic gene expression and recombination [1].

1.10 Brominated and Methylated Dickerson DNA Crystal Structures

Because bromine and methyl groups are structurally homologous, with similar van der Waals radii (1.95-2.00 Å), the X-ray crystal structure for the Dickerson dodecamer heavy-atom derivative (containing 5-bromocytosine at the dC9 position) is of particular relevance in this investigation [54]. The single crystal structure of [d(CGCGAATT^{5Br}CGCG)]$_2$ in 60% methylpentanediol was shown to undergo a reversible bending/unbending phase transition as a function of temperature (7°↔20°C). Introduction of bromine at the dC9 residue reduced the 19° bend observed in the original Dickerson crystal structure to 14°. This apparent "stiffening" effect was attributed to the presence of the bulky bromine atom in the major groove, which blocks further curvature of the helix. This straightening of the helix was even more pronounced in the MPD7 structure, which was solved for this same dodecamer at 7° C in a slightly higher alcohol concentration [54].

The X-ray diffraction coordinates for the methylated derivative, [d(CGCGAATT^{5Me}CGCG)]$_2$, have only recently been deposited in the Protein Data Bank, so no detailed structural analysis of that DNA dodecamer is currently available

[55]. A reduction in the overall bend of the helix was also noted by Salisbury for the singly methylated C9 derivative and to an even greater extent in the crystal structure of a doubly methylated species, $[d(CG^{5Me}CGAATT^{5Me}CGCG)]_2$. A visual inspection of the methylated dodecamer X-ray coordinates reveals the presence of only minor structural perturbations in the vicinity of the dT8-dC9-junction. Most notably, there appears to be a slight flattening of the propeller twist of the dC9-dG4 base pair (Figure 1.8).

1.11 Dissertation Outline

This dissertation is comprised of solid-state NMR experiments that probe both local structure and dynamics in nucleosides and in a methylated DNA dodecanucleotide. After a discussion of the relevant NMR theory and general synthetic and experimental procedures (Chapters 2, 3, and 4), there are four chapters explaining the experimental results. Chapter 5 describes the application of a dipolar recoupling experiment (Dipolar Recoupling with A Windowless Sequence, DRAWS) to two selectively ^{13}C-labeled cytidine monomers and to the DNA dodecanucleotide, $[d(CGCGAATT^{5Me}CGCG)]_2$, which contains ^{13}C isotopes at the C2 positions of both the dT8 and ^{5Me}dC9 nucleotides. This sample and its control sequence (without the methyl modification at 5 position of dC9) were constructed for the purpose of probing the effect of base methylation on the structure at the dT8-dC9 step. A fluorinated analogue of the methylated dodecamer was also synthesized which contains 5-fluoro-2'-deoxyuridine and 5-fluoro-2'-deoxycytidine at the dT8 and dC9 positions, respectively. The motivation for using fluorinated DNA derivatives is outlined in Chapter 5. A series of internuclear ^{19}F-^{19}F and ^{13}C-^{13}C distance measurements were made on these DNA samples at biologically relevant hydration levels. Chapter 6 describes applications of two-dimensional dipolar recoupling experiments (RFDR and DRAWS) for the chemical shift assignment of uniformly ^{13}C, ^{15}N labeled deoxynucleosides and

ribonucleosides in both polycrystalline and amorphous forms. This chapter focuses in particular on the use of the chemical shift parameter to probe molecular geometry. Chapter 7 presents results for selectively and uniformly labeled ribonucleosides using a variant of the DRAWS experiment that selects for double quantum coherence (DQ-DRAWS). This experiment is particularly sensitive to the relative orientations of the nuclei in the molecule. Due to this angular dependence, double quantum spectra serve as a useful probe of molecular conformation in the solid-state. Chapter 8 focuses on solid-state ^{2}H NMR spectroscopy of a methylated DNA dodecanucleotide with the sequence, $[d(CGCGAATT^{5Me}CGCG)]_2$. The internal dynamics of this DNA dodecamer, selectively deuterated on either the furanose ring, the backbone, or the base moieties of the dC9 nucleotide, were investigated as a function of hydration level. These studies are a first step towards understanding the nebulous relationship between the effect of cytosine methylation, DNA flexibility, and the importance of CpG steps in prokaryotes and eukaryotes.

1.12 Notes to Chapter 1

[1] Saenger, W., *Principles of Nucleic Acid Structure*, ed. C.R. Cantor. 1984, New York: Springer-Verlag New York, Inc.

[2] Davies, D.B. and Danyluk, S.S. (1974) *Biochemistry*, **13** (21), p. 4417.

[3] Sundaralingam, M. (1969) *Biopolymers*, **7**, p. 821.

[4] Kilpatrick, J.E., Pitzer, K.S., and Spitzer, R. (1947) *J. Am. Chem. Soc.*, **69**, p. 2483.

[5] Altona, C. and Sundaralingam, M. (1972) *J. Am. Chem. Soc.*, **94** (23), p. 8205.

[6] Dickerson, R.E., *DNA Structures*. Methods in Enzymology: Part A Synthesis and Physical Analysis of DNA, ed. D.M.J. Lilley and J.E. Dahlberg. Vol. 211. 1992, Harcourt Brace Jovanovich Publishers: San Diego. 67.

[7] Kopka, M.L., Fratini, A.V., Drew, H.R., and Dickerson, R.E. (1983) *J. Mol. Biol.*, **163**, p. 129.

[8] Arnott, S., Hukins, D.W., and Dover, S.D. (1972) *Biochem. Biophys. Res. Commun.*, **48**, p. 1392.

[9] Bloomfield, V.A., Crothers, D., and Tinoco, I., *Physical Chemistry of Nucleic Acids*. 1974, New York: Harper & Row.

[10] Altona, C., *High resolution NMR studies of nucleic acids*, in *Methods in Structural Molecular Biology*, D.B. Davies, W. Saenger, and S.S. Danyluk, eds. 1981, Plenum Press: London. p. 161.

[11] Davies, D.B. (1978) *NMR Spectrosc.*, **12**, p. 135.

[12] Ludemann, H.D. and Westhof, E., *Solution Conformations of purine (β) nucleosides and analogs*, in *Nuclear Magnetic Resonance Spectroscopy in Molecular Biology*, B. Pullman, ed. 1978, D. Reidel Publishing Company: Dordrecht, Holland. p. 41.

[13] Haasnoot, C.A., De Leeuw, F.A., and Altona, C. (1980) *Tetrahedron*, **36**, p. 2783.

[14] de Leeuw, F.A. and Altona, C. (1983) *J. Comp. Chem.*, **4** (3), p. 428.

[15] Karplus, M. (1959) *J. Chem. Phys.*, **30** (1), p. 11.

[16] Hruska, F.E., Wood, D.J., Mynott, R.J., and Sarma, R.H. (1973) *FEBS Lett.*, **31**, p. 153.

[17] Zhu, L., *Ph.D.* Dissertation, 1994, University of Washington; Zhu, L., Reid, B.R., Kennedy, M., and Drobny, G.P. (1994) *J. Magn. Reson. Series A*, **111**, p. 195.

[18] Harbison, G.S. (1993) *J. Am. Chem. Soc.*, **115**, p. 3026.

[19] Opella, S.J., Hexem, J.G., Frey, M.H., and Cross, T.A. (1981) *Phil. Trans. R. Soc. Lond.*, **A** (299), p. 665.

[20] Juang, C., Tang, P., and Harbison, G.S., eds. *Solid-State NMR of DNA*. Methods in Enzymology. Vol. 261. 1995, Academic Press.

[21] Santos, R.A., Tang, P., and Harbison, G.S. (1989) *Biochemistry*, **28**, p. 9372.

[22] Harbison, G.S. and Spiess, H.W. (1986) *Chem. Phys. Lett.*, **124**, p. 128.

[23] Harbison, G.S., Vogt, V.D., and Spiess, H.W. (1987) *J. Chem. Phys.*, **86**, p. 1206.

[24] Opella, S.J. and Morden, K.M., *Dynamic Properties of Biomolecular Assemblies*, S.E. Harding and A.J. Rowe, eds. 1989, The Royal Society of Chemistry: Cambridge. p. 196.

25] Alam, T.A. and Drobny, G.P. (1991) *Chem. Rev.*, **91**, p. 1545.

[26] Robinson, B.H. and Drobny, G.P. (1995) *Annu. Rev. Biophys. Biomol. Struct.*, **24**, p. 523.

[27] Schurr, J.M., Fujimoto, B.S., P., W., and Song, L., *Fluorescence Studies of Nucleic Acids: Dynamics, Rigidities, and Structures*, in *Biochemical Applications*, J.R. Lakowicz, Editor. 1992, Plenum Press: New York. p. 137.

[28] Holbrook, S.R. and Kim, S.H. (1984) *J. Mol. Biol.*, **173**, p. 361.

[29] Adams, R.L. (1990) *Biochem. J.*, **265**, p. 309.

[30] Jack, W.E., Rubin, R.A., Newman, A., and Modrich, P., eds. *Gene Amplification and Analysis*. Vol. 1. 1981, Elsevier/North-Holland: New York. 165.

[31] Brennan, C.A., Van Cleve, M.D., and Gumport, R.I. (1986) *J. Biol. Chem.*, **261** (16), p. 7270.

[32] Brennan, C.A., Van Cleve, M.D., and Gumport, R.I. (1986) *J. Biol. Chem.*, **261** (16), p. 7279.

[33] Ahmad, I. and Rao, D. (1996) *Critical Reviews in Biochemistry and Molecular Biology*, **31** (5-6), p. 361.

[34] Bird, A.P. (1996) *Cancer Surveys*, **28**, p. 87.

[35] Cedar, H. (1988) *Cell*, **53**, p. 3.

[36] Ramsahoye, B.H., Davies, C.S., and Mills, K.I. (1996) *Blood Reviews*, **10**, p. 249.

[37] Dickerson, R.E. and Drew, H.R. (1981) *Proc. Natl. Acad. Sci. (USA)*, **78**, p. 7318.

[38] Dickerson, R.E. and Drew., H.R. (1981) *J. Mol. Biol.*, **149**, p. 761.

[39] Lomonosoff, G.P., Butler, P.J.G., and Klug, A. (1981) *J. Mol. Biol.*, **149**, p. 745.

[40] Nerdal, W., Hare, D.R., and Reid, B.R. (1989) *Biochemistry*, **28**, p. 1008.

[41] Ott, J. and Eckstein, F. (1985) *Biochemistry*, **24**, p. 2530.

[42] Bax, A. and Lerner, L. (1988) *J. Magn. Reson.*, **79**, p. 429.

[43] Hatcher, M.E., Mattiello, D.L., Orban, J., and Drobny, G.P. (1997) *J. Am. Chem. Soc.*, accepted.

[44] McClarin, J.A., Frederick, C.A., Wang, B., Greene, P., Boyer, H.W., Grable, J., and Rosenberg, J.M. (1986) *Science*, **234**, p. 1526.

[45] Lesser, D.R., Kurpiewski, M.R., and Jen-Jacobson, L. (1990) *Science*, **250**, p. 776.

[46] Ollis, D.L. (1987) *Chem. Rev.*, **87**, p. 981.

[47] Lesser, D.R., Kurpiewski, M.R., Waters, T., Connolly, B.A., and Jen-Jacobson, L. (1993) *Proc. Natl. Acad. Sci. (USA)*, **90**, p. 7548.

[48] Collins, M. and Myers, R.M. (1987) *J. Mol. Biol.*, **198**, p. 737.

[49] Lefebvre, A., Mauffret, O., El Antri, S., Lescot, E., and Fermandjian, S. (1995) *Eur. J. Biochem.*, **299**, p. 445.

[50] Hodges-Garcia, Y. and Hagerman, P.J. (1992) *Biochemistry*, **31**, p. 7595.

[51] Heinemann, U. and Alings, C. (1991) *EMBO J.*, **10** (1), p. 35.

[52] Ollila, J., Lappalainen, I., and Vihinen, M. (196) *FEBS Lett.*, **396**, p. 119.

[53] Behe, M. and Felsenfeld, G. (1981) *Proc. Natl. Acad. Sci. (U.S.A.)*, **78**, p. 1619.

[54] Fratini, A.V., Kopka, M.L., Drew, H.R., and Dickerson, R.E. (1982) *J. Biol. Chem.*, **257** (24), p. 14686.

[55] Partridge, B.L. and Salisbury, S.A., *Structural Studies on Nucleic Acids, Ph.D. Dissertation*, 1996, Cambridge University.

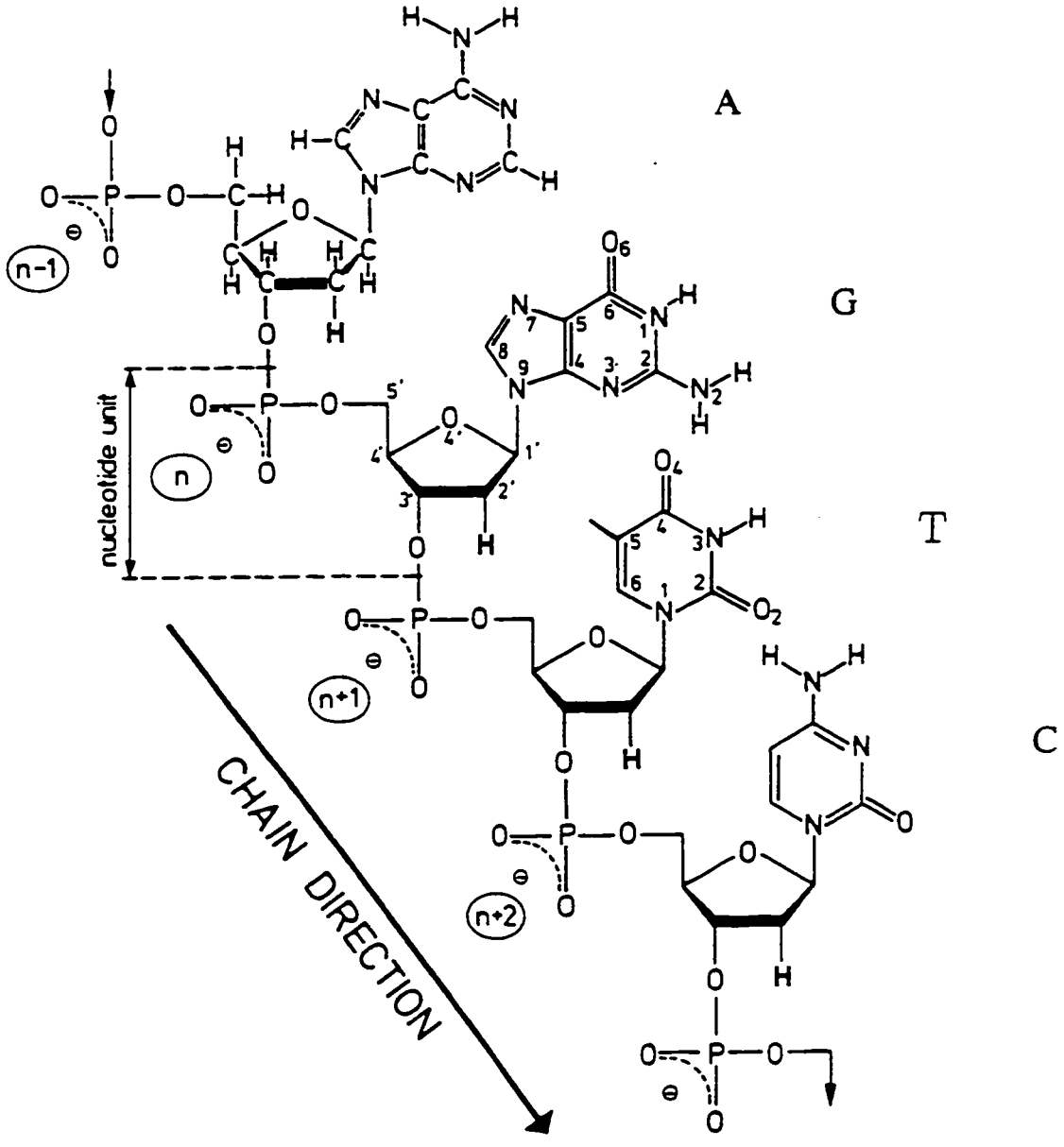

Figure 1.1: Representation of a polynucleotide chain containing the deoxynucleosides: deoxyadenosine (A), deoxyguanosine (G), thymidine (T), and deoxycytidine (adapted from [1]).

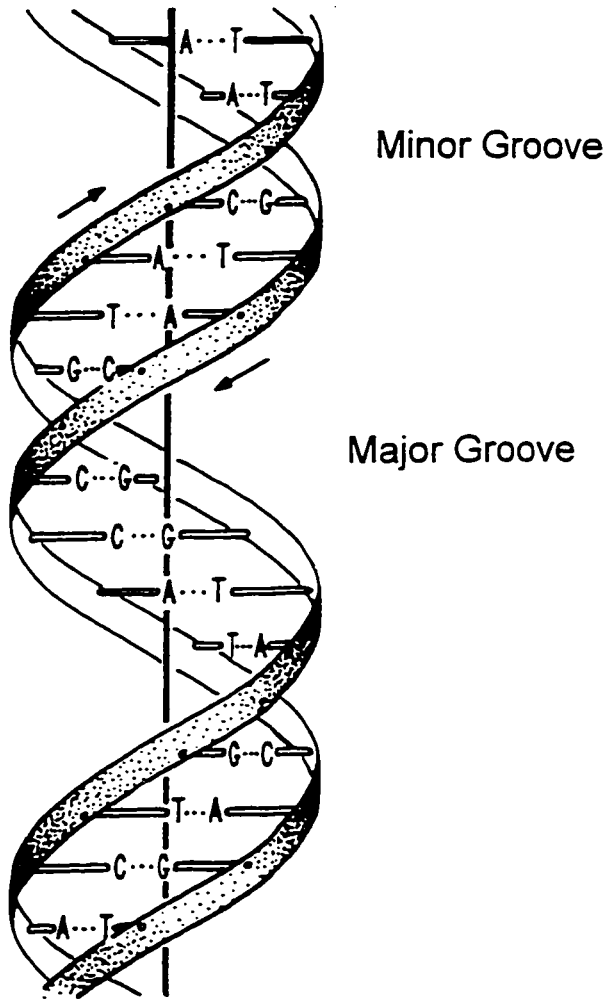

Figure 1.2: Schematic representation of the DNA double helix. The sugar-phosphate backbones are depicted as ribbons. Base-pairs (A-T and G-C) are depicted as horizontal bars (adapted from [1]).

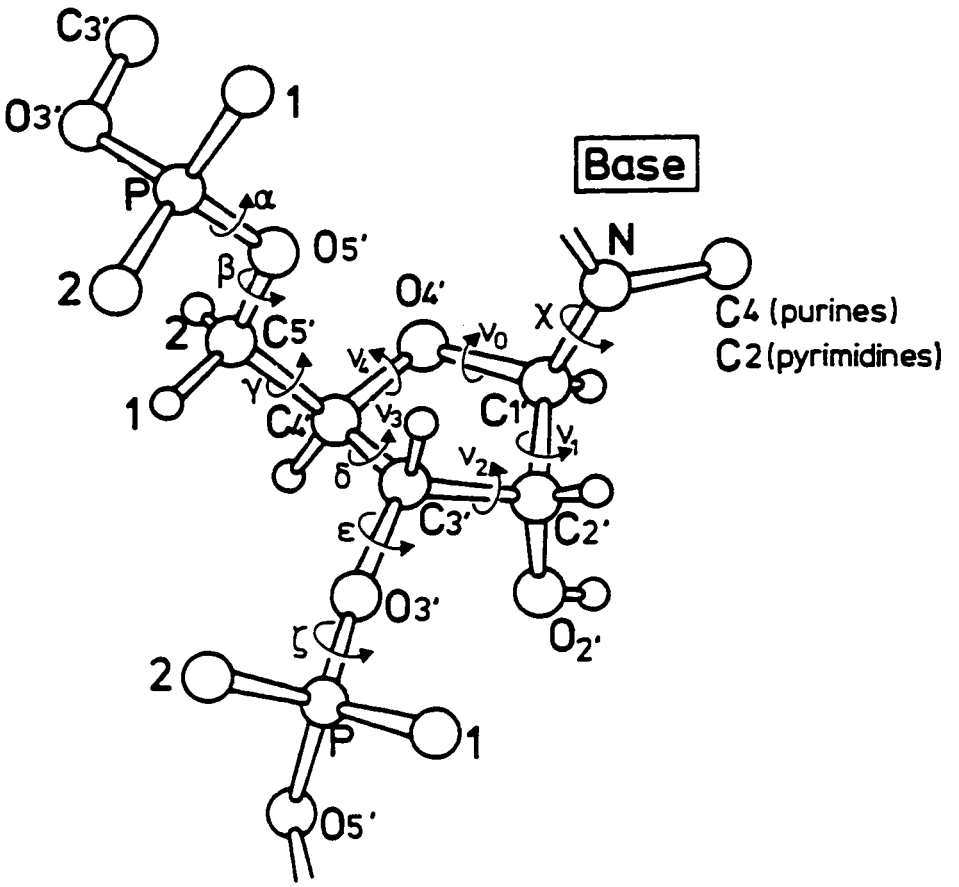

Figure 1.3: Atomic numbering scheme and definition of torsional angles for a polynucleotide chain (adapted from [1]).

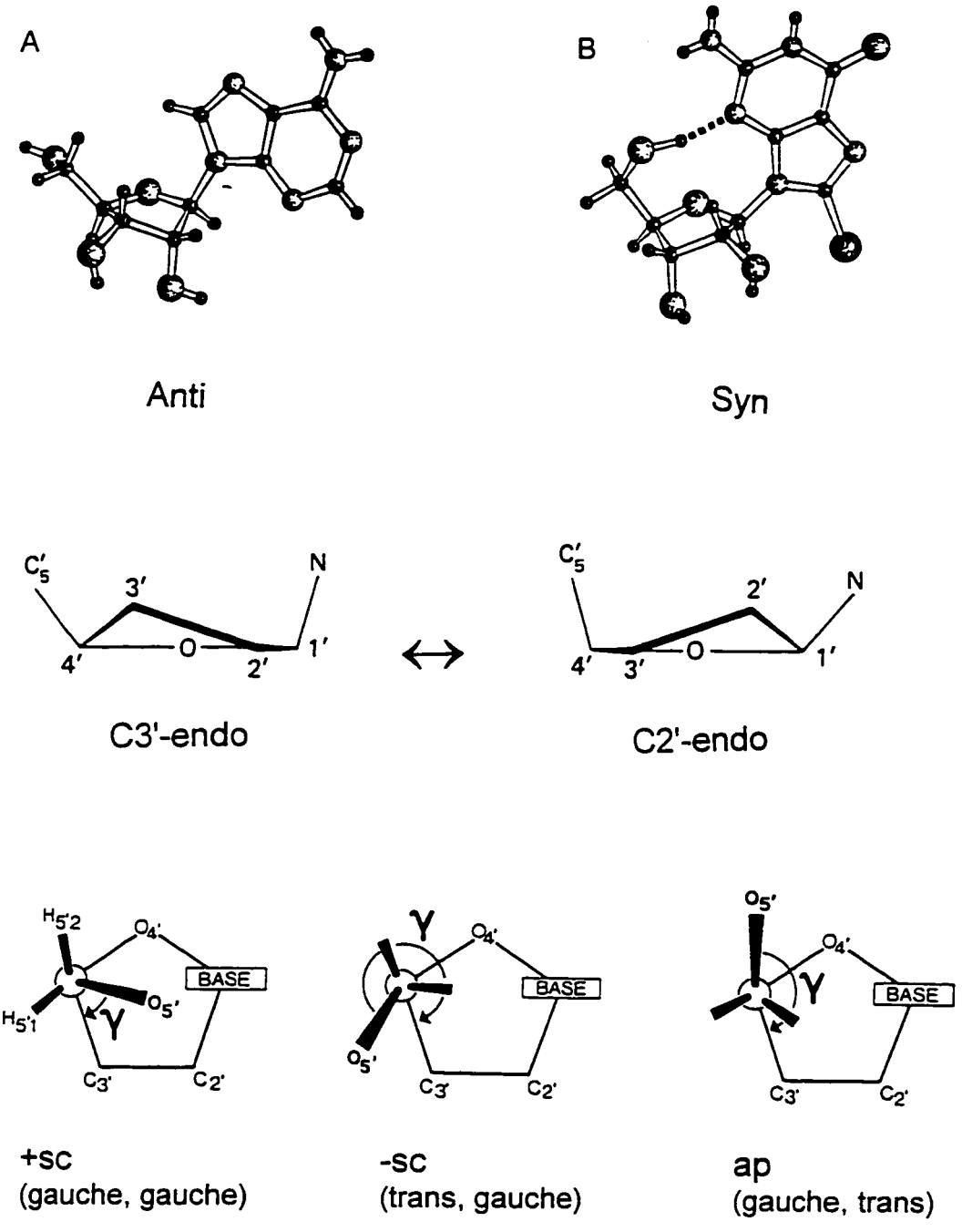

Figure 1.4: A) Adenosine in the anti form with a C3'-endo pucker. B) 8-bromoguanosine in the syn form with a C2'-endo pucker. C) Interconversion of furanose rings between C3'-endo and C2'-endo sugar ring conformations. C1'-O4'-C4' plane is perpendicular to the page. D) Definition of torsion angle ranges about the C4'-C5' bond, viewed in the C5' → C4' direction (adapted from [1]).

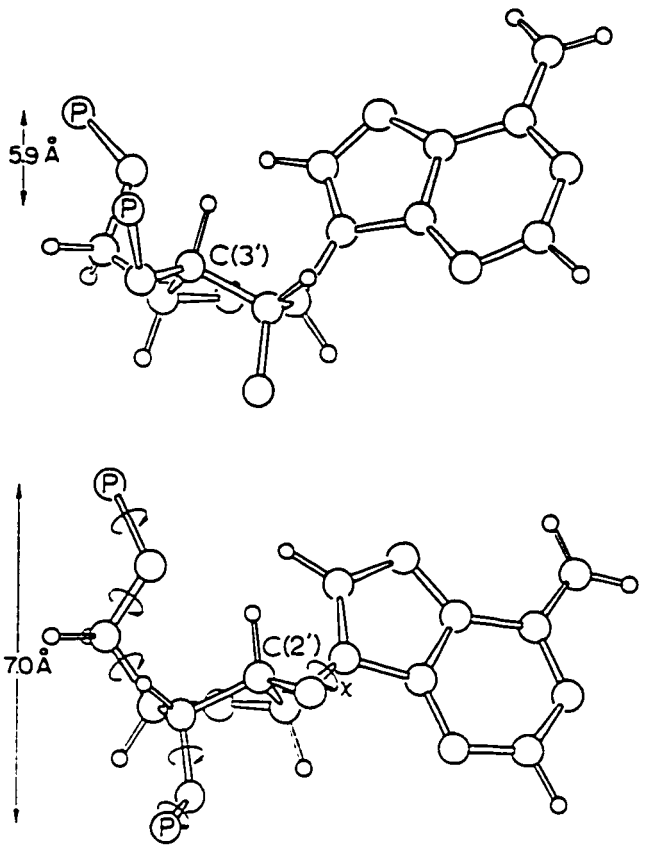

Figure 1.5: The two preferred nucleotide conformations: C3'-endo (top) and C2'-endo (bottom) conformations for A- and B-type polynucleotide helices, respectively (adapted from [1]). Phosphate-phosphate distances are given in Å.

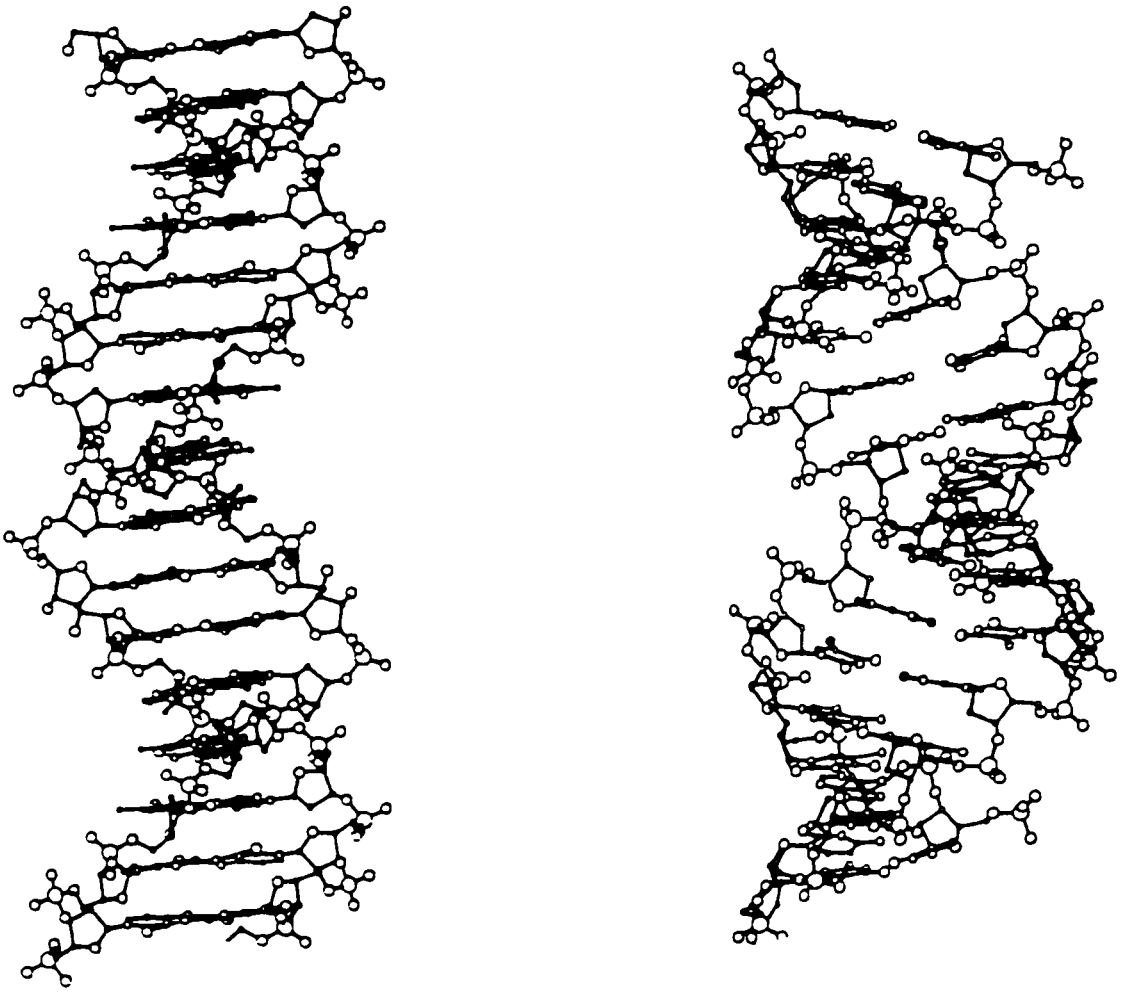

Figure 1.6: Structure of A-DNA (right) and B-DNA (left) generated from the stacked crystal structures of $[d(GGTATACC)]_2$ and $[d(CCAACGTTGG)]_2$, respectively (adapted from [6]).

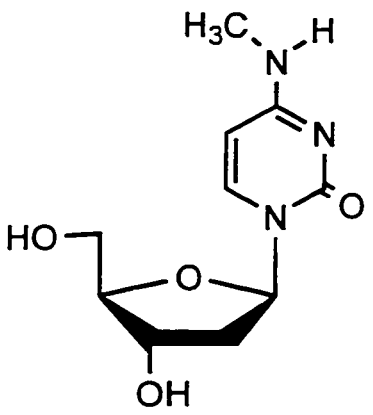

A

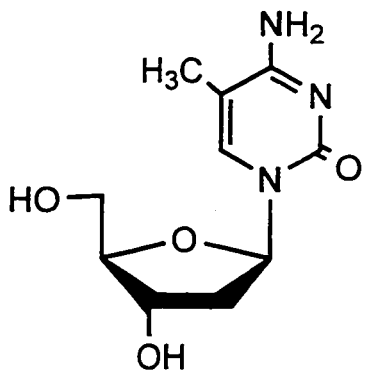

B

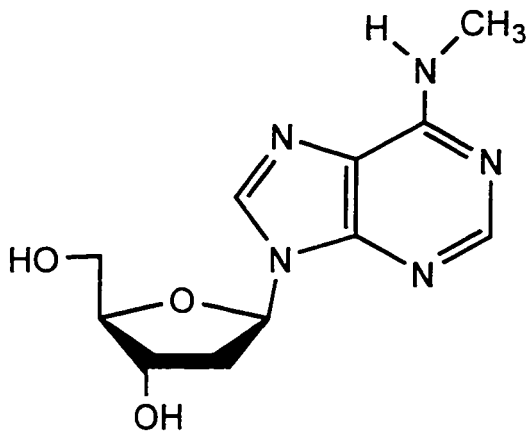

C

Figure 1.7: Structures of methylated nucleosides: A) N4-methyl-2'-deoxycytidine, B) C5-methyl-2'-deoxycytidine, and C) N6-methyl-2'-deoxyadenosine.

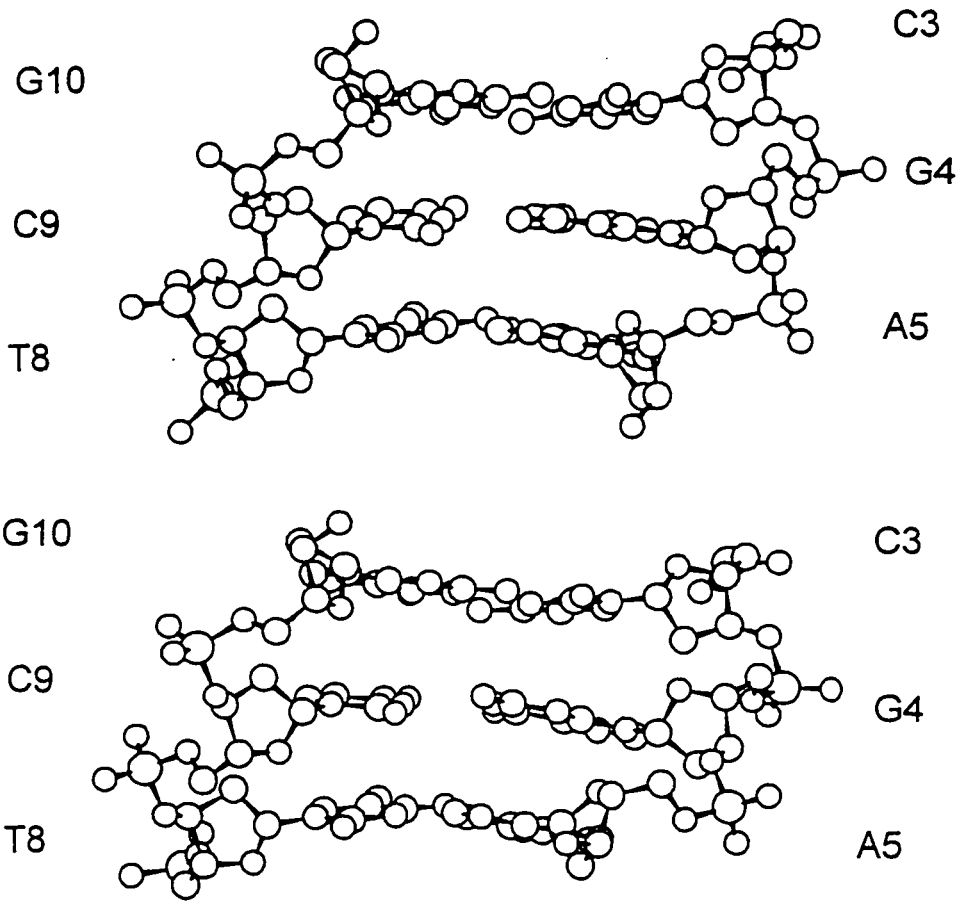

Figure 1.8: d(T8-C9-G10)•d(C3-G4-A5) segment of the B-DNA dodecamers, $[d(CGCGAATT^{5Me}CGCG)]_2$ (top) and $[d(CGCGAATTCGCG)]_2$ (bottom) obtained from Protein Data Bank X-ray coordinates. Note the minor structural changes at the G4-C9 base pair.

Chapter 2
Nuclear Magnetic Resonance Theory

This chapter reviews the basic nomenclature and quantum mechanical principles for spin-1/2 and spin-1 systems required to understand the experimental results in later sections of the dissertation. The reader is referred to several excellent texts on the subject of nuclear magnetic resonance for a more thorough discussion of these topics [1-5]. The chapter begins with a formal treatment of the internal and external NMR interactions that are relevant for spin-1/2 and spin-1 nuclei. Sections 2.5-2.7 discuss the concept of coherence in NMR and two experimental techniques, cross-polarization and magic angle spinning. Later sections of the chapter will briefly outline the effect of dynamics on NMR interactions and observables.

2.1 NMR Interactions

The Hamiltonian for an NMR spin system can be written as the sum of terms

$$H = H_{external} + H_{internal} \qquad [2.1]$$

The interaction with the external magnetic fields ($H_{external}$) includes the Zeeman interaction with the static magnetic field and the interaction with the radio frequency magnetic field of the pulse. The interaction with the internal fields ($H_{internal}$) involves couplings to other spins (homonuclear and heteronuclear dipolar interactions) or coupling to the local environment (chemical shift and quadrupolar interactions).

2.2 Interaction with Static Magnetic Field

Magnetic resonance is a phenomenon that arises due to the intrinsic property of certain nuclei and other subatomic particles called spin. Spin is a source of angular momentum that is governed by the laws of quantum mechanics. Spin angular momentum endows a particle with a magnetic moment, which can be represented by the vector quantity, $\vec{\mu}$,

$$\vec{\mu} = \gamma_I \hbar \vec{\mathbf{I}} \qquad [2.2]$$

The magnetic moment is related to the total angular momentum by the gyromagnetic ratio, γ_I. When placed into a magnetic field, $\vec{B}_0$, the spin acquires an energy given by the Zeeman Hamiltonian

$$H_Z = -\gamma_I \hbar \vec{B}_0 I_z = -\omega_0 I_z \qquad [2.3]$$

where, ω_0 is called the Larmor frequency. $\vec{B}_0$ is defined to be along the z axis of the laboratory coordinate system and is the dominant contribution to the total Hamiltonian at high field. The eigenvalues of the Hamiltonian are $E \pm m\gamma\hbar B_0$, where m = I, I-1, ... -I. For spin-1/2 nuclei (I=1/2), $E \pm \frac{1}{2}\gamma\hbar B_0$, resulting in two possible energy levels (i.e. eigenstates). The two energy eigenstates are also referred to as the $|\uparrow>$ and $|\downarrow>$ basis states. $|\uparrow>$ and $|\downarrow>$ are the low and high energy states that correspond to two particular orientations of $\vec{\mu}$ relative to the static magnetic field. The energy level diagram for a spin-1/2 nucleus under the Zeeman interaction is shown in Figure 2.1.

2.3 Density Matrix

The description presented thus far is for a single nucleus in a static magnetic field. However, a typical NMR sample consists of many magnetic moments, which are referred to as an ensemble. Prior to an NMR experiment, the ensemble is considered to be in thermal equilibrium with the net magnetization vector aligned in the z direction. For a macroscopic ensemble in thermal equilibrium, the populations of each energy level may be described by the Boltzmann spin density matrix

$$\rho = \frac{\exp(-\beta H)}{Tr\{\exp(-\beta H)\}} \qquad [2.4]$$

where, $\beta = \hbar / kT$ and H is the static Hamiltonian. The initial density matrix (in the high temperature limit) is $\rho(0) = I_z$.

2.4 Propagators

The observable in NMR is the transient response of a system of nuclear magnetic moments, under the influence of the system's Hamiltonian, following a disturbance from equilibrium. The equation for the time evolution of the density matrix in the laboratory frame is governed by the Liouville von Neumann equation,

$$\frac{d}{dt}\rho(t) = -i\left[H(t), \rho(t)\right] \qquad [2.5]$$

The solution to Equation [2.5] for a Hamiltonian that is not explicitly time-dependent is simply

$$\rho(t) = \exp(-\tfrac{i}{\hbar} Ht)\rho(0)\exp(\tfrac{i}{\hbar} Ht) \qquad [2.6]$$

The initial state advances in time under the influence of the propagators, $U(t) = \exp(-\frac{i}{\hbar} Ht)$. The formal solution to Equation [2.5] for a time-dependent Hamiltonian assumes the form

$$\rho(t) = D\exp\left(-\frac{i}{\hbar}\int_0^t H(t')dt'\right)\rho(0)\exp\left(\frac{i}{\hbar}\int_0^t H(t')dt'\right) \qquad [2.7]$$

$$\text{where, } U(t) = \exp\left(-\frac{i}{\hbar}\int_0^t H(t')dt'\right)$$

Evaluation of propagators for systems in which the Hamiltonians are time-dependent is complicated by the fact that the Hamiltonian at one time does not necessarily commute with the Hamiltonian at another time. Consequently, the factors in these integrals must be ordered consistently via the Dyson time-ordering operator D in Equation [2.7] [6].

An extensive literature exists for finding approximations to propagators which contain non-commuting Hamiltonians [1, 2]. One approach is Average Hamiltonian Theory (AHT), which postulates that the propagator (expressed in a reference frame that is "toggling" with the r.f. pulses) governing the system may be approximated by a simple exponential operator, $U(t) = \exp(-i\overline{H}t)$, where the effective Hamiltonian is independent of time:

$$\overline{H} = \overline{H}^{(0)} + \overline{H}^{(1)} + \overline{H}^{(2)} + \ldots \qquad [2.8]$$

This infinite series is known as the Magnus expansion [7]. The zeroth order term in the series,

$$H^{(0)} = \frac{1}{\tau_c}\int_0^{t_c} \overline{H}_{\text{int}}(t)dt \qquad [2.9]$$

represents the average of the internal Hamiltonian over a suitably chosen cycle. Higher order terms act as corrections to this leading term. Chapter 3 will present AHT results for several of the r.f. pulse sequences utilized in this dissertation.

2.5 Interactions with Oscillating Magnetic Fields

To generate an NMR signal, and consequently to gain information about chemical structure and dynamics, the ensemble of spins must be perturbed from its equilibrium state. The simplest method of excitation is to apply a time-dependent linearly polarized radio-frequency magnetic field perpendicular to B_0 at a frequency close to the Larmor frequency. The Hamiltonian (for irradiation along the y axis) that describes how transverse magnetization interacts with an oscillating field is given by

$$H_1 = -2\omega_1 I_y \cos\omega t \qquad [2.10]$$

where, $\omega_1 = \gamma_I B_1$ and B_1 is the radio-frequency amplitude [2]. The equation of motion can be most readily solved by transforming into a reference frame that is rotating at the Larmor frequency.

$$H^*(t) = (\omega - \omega_0) I_z + \exp(-i\omega t I_z) H_1(t) \exp(-i\omega t I_z) \qquad [2.11]$$

Evaluation of Equation [2.11], using the properties of exponential operators results in the following expression for the "rotating frame" Hamiltonian,

$$H^*(t) = -\omega_1 I_y - \omega_1 I_y \sin 2\omega t - \omega_1 I_x \sin 2\omega t \qquad [2.12]$$

The truncated form of the rotating frame Hamiltonian is obtained by neglecting rapidly oscillating time-dependent terms in Equation [2.12],

$$H^*(t) = -(\Delta\omega I_z + \omega I_y) \qquad [2.13]$$

where, $\Delta\omega = \omega_0 - \omega$ is the offset from resonance. For the situation where irradiation is performed on-resonance ($\Delta\omega = 0$), the system develops in the rotating frame as

$$\rho(t) = \exp(-iI_y w_1 t) I_z \exp(iI_y \omega_1 t) = I_z \cos(\omega_1 t) - I_x \sin(\omega_1 t) \qquad [2.14]$$

If the r.f. field is applied for a given time, $t=\pi/2$, initial z-magnetization will be completely rotated into x-magnetization.

The situation described above is the most rudimentary example of how a system can be perturbed from equilibrium. A redistribution of populations and the formation of coherence can be generated by the application of a multitude of intricate radio-frequency pulse sequences. While the system remains perturbed (i.e. before the system can relax back to its equilibrium state), the response of the local spin interactions to the transient excitation induces a voltage in the sample coil tuned to the Larmor frequency and is recorded as a free induction decay (FID). The frequency, amplitude, and decay of each oscillation conveys information about the system, its relaxation properties, and its chemical environment. Fourier transformation of the FID results in a frequency domain NMR spectrum. The nature of these local spin interactions is the focus of the next section.

2.6 Interactions with Internal Fields

Upon transformation into the rotating frame, the internal Hamiltonian for a spin-1/2 nuclei becomes [5]

$$H_{internal} = H_{off} + H_C + H_J + H_Q + H_D + H_{SR} \qquad [2.15]$$

H_{off} accounts for any offset from resonance. For spin ≥ 1 (e.g. deuterium), the term H_Q must be included to account for the coupling of the electric quadrupole moment of a nonspherical distribution of nuclear charge with an electronic field gradient. H_C (chemical shift), H_Q, and H_{SR} (spin-rotation) depend on the spin operators for a single nucleus. In comparison, H_D (dipole-dipole) and H_J (scalar) depend on the spin operators for two spins. In the solid-state, we can neglect the minor contribution to the internal Hamiltonian that arises from a coupling of the nuclear spin with the moment produced by the angular momentum of the molecule (H_{SR}). An internal Hamiltonian may be expressed in general form as a scalar operator [2].

$$H_{internal} = \mathbf{I} \cdot \tilde{\mathbf{A}} \cdot \mathbf{S} = \left(I_x, I_y, I_z\right) \begin{pmatrix} A_{xx} & A_{xy} & A_{xz} \\ A_{yx} & A_{yy} & A_{yz} \\ A_{zx} & A_{zy} & A_{zz} \end{pmatrix} \begin{pmatrix} S_x \\ S_y \\ S_z \end{pmatrix} \qquad [2.16]$$

Both **I** and **S** are vector operators (specified by three components), whereas $\tilde{\mathbf{A}}$ is a second-rank Cartesian tensor (3 x 3 matrix). The coupling tensor $\tilde{\mathbf{A}}$ gives both the magnitude and direction of the local field. The internal fields are generally small compared to the externally applied Zeeman field, and only those components parallel or antiparallel to B_0 (i.e. components that commute with the Zeeman interaction) can affect the spins significantly. These components that commute with the I_z operator are called *secular* interactions. The effect of secular, internal interactions is to impart fine structure to the Zeeman energy levels by adding or subtracting small contributions to B_0. The coupling tensor $\tilde{\mathbf{A}}$ can be rotated into a special frame of reference in which the tensor is diagonal. This reference frame is referred to as the principal axis system (PAS). The diagonal components of the matrix in the PAS are called principal elements. The PAS can be different for the different internal interactions. The transformation of $\tilde{\mathbf{A}}$ in coordinate space into the PAS can be accomplished by a rotation

described by the Euler angles (α, β, γ). The conventions for rotations of 3 x 3 matrices are given in Appendix B of Mehring [2].

2.6.1 Spherical Tensors

Sometimes it is more convenient mathematically to deal with spin interactions in the form of irreducible spherical tensors. This is especially true when performing rotations or other unitary transformations. The relationship between spherical tensors and the Cartesian matrix representation of anisotropic spin interactions is described in detail elsewhere [2, 8]. In the spherical tensor representation, the spin interaction Hamiltonian in Equation [2.15] becomes

$$H_{\lambda} = C^{\lambda} \sum_{l=0}^{2} \sum_{m=-l}^{+l} (-1)^{m} R_{l-m}^{\lambda} T_{lm}^{\lambda} \qquad [2.17]$$

where, λ=C, Q, J, D, SR, or the Zeeman interaction. C^{λ} is a collection of constants, which depends on the spin interaction. R_{lm} and T_{lm} are spherical tensors of rank l with $2l$+1 components, which represent the geometrical and spin variables of the Hamiltonian, respectively. Terms containing T_{00} give the isotropic contribution to the NMR spectrum. The angular dependence of the line position in the NMR spectrum is contained in terms containing T_{20} [8]. The secular spin interaction Hamiltonian can be written as

$$H_{\lambda} = C^{\lambda} T_{20}^{\lambda} \sum_{m=-2}^{2} \rho_{2m}^{\lambda} D_{m,0}^{(2)}(\alpha^{\lambda}, \beta^{\lambda}, \gamma^{\lambda}) \qquad [2.18]$$

where, the Euler angles (α, β, γ) describe the transformation from the PAS into the desired reference frame. $D_{m,0}^{(2)}(\alpha,\beta,\gamma)$ are the Wigner rotation matrix elements, and ρ_{2m}^{λ} are the irreducible coupling tensor components in the PAS [8].

2.6.2 Chemical Shielding

The nucleus is generally embedded within a distribution of electric current resulting from the nearby electrons. When such a current distribution is placed in an external magnetic field, additional currents, and therefore additional magnetic fields, will be induced. The anisotropic interaction of a nuclear magnetic moment with internal fields of this kind is described by the chemical shielding (chemical shift) Hamiltonian

$$H_C = \gamma \mathbf{I} \cdot \tilde{\sigma} \cdot \mathbf{B_0} \qquad [2.18]$$

where, $\tilde{\sigma}$ is the chemical shift anisotropy (CSA) tensor associated with a particular spin. The chemical shift parameter is highly sensitive to local electronic environment and, consequently, to molecular conformation. The diagonal form of the CSA tensor in the PAS is

$$\tilde{\sigma}_{PAS} = -\gamma \begin{pmatrix} \sigma_{xx} & 0 & 0 \\ 0 & \sigma_{yy} & 0 \\ 0 & 0 & \sigma_{zz} \end{pmatrix} \qquad [2.20]$$

The diagonal elements are called the CSA principal tensor elements. Six numbers are required to fully define the CSA tensor: three principal tensor elements and three Euler angles which describe the orientation of the PAS with respect to the crystal or molecular frame.

2.6.3 Scalar Coupling

Two nuclei may interact indirectly through the electrons in an intervening chemical bond via the scalar (J) coupling. The Hamiltonian is bilinear in the spin an-

gular momentum operator, because two nuclei (j and k) are involved in the interaction.

$$H_J = \mathbf{I}_i \cdot \tilde{\mathbf{J}} \cdot \mathbf{I}_j \qquad [2.21]$$

Scalar interactions are especially important in liquid-state systems. The rapid molecular orientation averages the second rank tensor interaction, leaving only the isotropic component of $\tilde{\mathbf{J}}$. Because the scalar coupling is small (generally ≤ 100 Hz for two coupled ^{13}C nuclei), this interaction is not a significant contribution to the solid-state NMR spectrum.

2.6.4 Quadrupole Coupling

The nuclear quadrupolar coupling pertains only to nuclei with nonspherical charge distribution ($I \geq 1$) and involves the electric quadrupole moment of the nucleus and the electric field of the surrounding electrons. Specifically, the quadrupolar interaction involves the interaction between the electric quadrupole moment of the nucleus and the electric field gradient. For spin=1 nuclei, such as deuterium, the internal Hamiltonian is dominated by the quadrupolar interaction. The Hamiltonian for the quadrupolar interaction is given by

$$H_Q = \frac{eQ}{2I(2I-1)\hbar} \mathbf{I} \cdot \tilde{\mathbf{V}} \cdot \mathbf{I} \qquad [2.22]$$

where, $\mathbf{I}$ is the nuclear spin vector and $\tilde{\mathbf{V}}$ is the second-rank, traceless electric field gradient (EFG) tensor. The tensor $\tilde{\mathbf{V}}$ can be interpreted classically as the tensor of the second derivatives of the electric potential at the nuclear site [8]. The symbol, eQ, represents the nuclear quadrupole moment, which is an intrinsic property of the nu-

cleus, regardless of its chemical environment. Alternatively, the secular, quadrupolar Hamiltonian can be rewritten in irreducible spherical tensor notation,

$$H_Q = \frac{eQ}{2\hbar}\mathbf{T}_{20}^{Q}\mathbf{R}_{20}^{Q} \qquad [2.23]$$

expressed in the laboratory frame. For the quadrupolar interaction, only the second-rank coupling components are non-zero. Expressing the coupling tensor, $\mathbf{R}_{20}^{Q}$, in terms of the tensors in the PAS yields the following expression for the orientation-dependent interaction Hamiltonian,

$$H_Q = \frac{eQ}{2\hbar}\sqrt{\frac{3}{2}}\,eq\mathbf{T}_{20}^{Q}\,[3\cos^2\theta - 1 + \eta\sin^2\theta\cos 2\phi] \qquad [2.24]$$

θ and ϕ are the two angles that define the direction of the magnetic field vector, B_0, in the PAS of the EFG tensor. The PAS for the quadrupolar interaction is generally the frame of reference where the z-axis lies along the C-D bond of the molecule. In Equation [2.24], the coupling strength of the nucleus to the electric field gradient tensor is represented by the factor eq. η is referred to as the static asymmetry parameter. Both eq and η are related to the Cartesian components of the EFG tensor $\tilde{\mathbf{V}}$ in the PAS

$$\tilde{\mathbf{V}}_{\mathbf{PAS}} = \begin{pmatrix} V_{xx} & 0 & 0 \\ 0 & V_{yy} & 0 \\ 0 & 0 & V_{zz} \end{pmatrix} \qquad [2.25]$$

with. $\eta = (V_{xx} - V_{yy})/V_{zz}$ and $eq = V_{zz}$. We are specifically concerned in this investigation with axially symmetric coupling tensors (η = 0), which is a valid assumption for a deuteron bonded to an aliphatic carbon.

A spin-1 nucleus in a static magnetic field is a three-level system with transition frequencies occurring at $\pm\,\omega_0$ under the influence of the Zeeman interaction. The quadrupolar interaction can be viewed as a first-order perturbation of the Zeeman interaction [9]. The transition frequencies in the presence of an orientation-dependent H_Q occur at $\pm\,\omega_Q$ about the Zeeman frequency ω_0, where

$$\omega_Q = \frac{3\pi}{4}\left(\frac{e^2qQ}{h}\right)[3\cos^2\theta - 1 + \eta\sin^2\theta\cos 2\phi] \qquad [2.26]$$

The quantity (e^2qQ/h) is referred to as the static quadrupolar coupling constant (QCC). The energy level diagram for a spin-1 nucleus in a high magnetic field and as a result of the quadrupolar perturbation is presented in Figure 2.2. The resulting spectrum consists of two spectral lines centered about ω_0 at $\pm\,\omega_Q$. The separation between these two lines is linearly dependent on coupling strength (eq). Therefore, the separation between the lines is proportional to the V_{zz} component of the EFG tensor. The effect of motional processes on the static QCC will be addressed in Section 10.

2.6.5 Dipole-Dipole Interaction

Dipole-dipole coupling occurs when a magnetic dipole moment of one nucleus (j) interacts with the dipole moment of another nucleus (k). The secular dipolar Hamiltonian takes the form

$$H_D = 2\gamma_j\gamma_k\hbar\mathbf{I}_j\cdot\tilde{\mathbf{D}}\cdot\mathbf{I}_k \qquad [2.27]$$

$$H_D = \frac{\gamma_j\gamma_k\hbar}{r_{jk}^3}\frac{1}{2}(3\cos^2\theta_{jk} - 1)[2I_{zj}I_{zk} - \frac{1}{2}(I_{+j}I_{-k} + I_{-j}I_{+k})]$$

Because $\tilde{\mathbf{D}}$ is a traceless, symmetric coupling tensor, the dipolar interaction has axial symmetry with no isotropic component. The magnitude of the dipolar coupling is dependent on geometric parameters such as the internuclear distance (r) and the angle between the internuclear vector and the main magnetic field (θ). Homonuclear dipolar couplings for ^{13}C and ^{19}F nuclei are generally on the order of hundreds of Hertz.

2.7 Coherence

The idea of coherence is an important concept in NMR spectroscopy. In Section 2.1 we addressed the effect of applying a 90° pulse to an ensemble of spin-1/2 nuclei initially in thermal equilibrium. The result was a rotation of the net magnetization from the z-axis into the transverse plane. In quantum mechanical terms, this amounts to producing an equally weighted, coherent superposition of the $|\uparrow>$ and $|\downarrow>$ energy states. Alternatively, application of a 180° pulse would rotate the magnetization vector to the negative z-axis. The effect of a 180° pulse is to invert the population from a lower energy state to a higher energy state, without creating any coherence. Figure 2.3 compares the effect of applying a 90° and a 180° pulse on a two-level system. In macroscopic systems, coherent superpositions are established separately for individual two-level systems. Coherence can be thought of as the net interference between these two-level systems over the entire ensemble.[5] The order of coherence is the number of energy quanta between the basis states. Only single quantum coherences can be detected directly in NMR.

Now consider a system in which the two nuclei are no longer independent due to an internal coupling of the type discussed in Section 2.6.5. There are four possible quantized energy levels for such a system (Figure 2.4) and each level may be populated. It is now possible to have transitions and coherences that involve both spins simultaneously in addition to the single quantum coherences involving only one spin. These are referred to as zero-quantum (ZQ) and double-quantum (DQ) coherent

states. The creation and subsequent detection of DQ coherence, in particular, will play an important role in the experiments presented in later portions of this dissertation.

2.8 Magic Angle Spinning (MAS)

The NMR spectrum of static, powdered solid sample typically results in kilohertz-wide lines with very low signal-to-noise, even at very high magnetic fields. In solids, molecular motion is restricted, and the anisotropic components of the NMR interactions are preserved. In liquids, the anisotropic contributions to the internal NMR interactions are averaged by rapid molecular tumbling, and only the isotropic chemical shifts and scalar couplings are retained in the NMR spectrum. The solid-state NMR spectrum of a powder or polycrystalline sample is due to a superposition of transitions from many randomly oriented crystallites. Representations of powder lineshapes for spin-1/2 and spin-1 case are presented in Figure 2.5.

Rapid mechanical rotation of a solid-state sample greatly reduces the anisotropic interactions that dominate the solid-state NMR spectrum. Second-rank tensorial interactions are dependent on terms of the form, $3\cos^2\theta - 1$. By rotating the sample about an axis tilted by a "magic" angle of 54.7° ($3\cos^2\theta - 1 = 0$) relative to the external magnetic field, the broad powder spectrum is reduced to an isotropic peak that is surrounded by a manifold of spinning sidebands, separated by the rotor frequency [10, 11]. At very high spinning speeds, only the isotropic components of the tensorial interactions survive. As a result of magic angle spinning, all interactions with zero trace ($\tilde{\boldsymbol{D}}$ and $\tilde{\boldsymbol{V}}$) vanish, and only the isotropic components of the chemical shift and scalar coupling remain. Figure 2.6 illustrates the effect of rapid rotation at the magic angle on a spin-1/2 powder lineshape.

Herzfeld and Berger demonstrated that the ratios of sideband and centerband intensities were related to the chemical shift anisotropies [12]. The principal values

for the chemical shift tensor can be extracted from the MAS spectrum and used to reconstruct the anisotropic powder lineshape using numerical simulations. Section 4.11 describes the practical aspects of calculating chemical shift principal values from MAS spectra.

2.9 Cross-Polarization (CP)

When magic angle spinning is combined with cross-polarization (CP-MAS), it is possible to obtain well resolved NMR spectra of low γ spin-1/2 nuclei such as ^{13}C and ^{15}N [13, 14]. Cross-polarization is useful for enhancing the sensitivity of magnetically dilute nuclei (*S*) by utilizing the magnetization of the abundant proton spin (*I*) reservoir. Figure 2.6 presents the r.f. pulse sequence for the CP experiment. Hartmann-Hahn cross-polarization experiment involves three parts:

1) $\pi/2$ pulse on the *I* channel to establish transverse magnetization.
2) Spin-locking of *I* magnetization along y axis.
3) Irradiation of *S* with rf amplitude $\omega_{1S} = \omega_{1I}$ (Hartmann-Hahn condition).

During the CP contact time, *I*-*S* coupling appears strong in the doubly rotating frame, and magnetization is transferred between the subsystems. High power proton decoupling is necessary to remove the heteronuclear dipolar coupling between the observed nuclei (spin-1/2) and the surrounding protons. The advantages of CP are twofold: 1) CP increases the signal for rare spin-1/2 nuclei, and 2) T_1 relaxation for the protons governs the T_1 relaxation time for the *S* nuclei.

2.10 Motional Processes

Although rapid molecular tumbling is minimized in amorphous or polycrystalline samples, dynamical processes are still important even in the solid-state. This is

especially true for partially hydrated systems. Solid-state deuterium NMR can be used to probe the effects of dynamics directly by observing changes in the quadrupolar echo lineshape parameters and relaxation rates. Solid-state deuterium NMR has several advantages which make it particularly suited for the study of dynamics [15]. Because deuterium is a spin-1 nucleus, the interaction of the electric quadrupolar moment with the surrounding electric field gradients dominates the NMR spectrum. Furthermore, the quadrupolar interaction is a single nucleus property, so few structural assumptions are required when analyzing the relaxation or lineshape data. Deuterium is also considered a relatively non-perturbing isotopic probe when used as a replacement for hydrogen. Finally, the dynamic range of deuterium NMR is large (10^4-10^{10} Hz). Slower motions (10^4-10^6 Hz) are most effectively probed through the use of quadrupolar echo lineshape and spin-alignment echoes. Relaxation measurements are more sensitive to faster time-scale dynamics (10^6-10^{10} Hz).

Changes in lineshape characteristics are also important in spin-1/2 systems in which the chemical shift anisotropy dominates the NMR spectrum (e.g. ^{19}F, ^{31}P). Molecular motions may also significantly perturb the effects of dipolar recoupling pulse sequences, such as those discussed in Chapter 3. For example, if the system is sampling between two conformations, and these motions are fast on the NMR time scale, we can only measure an averaged distance between the two interchanging conformers. Dipolar recoupling experiments may be further complicated due to short transverse (T_2) relaxation times that produce rapid dephasing of the spins.

2.10.1 Relaxation

The recovery of magnetization to equilibrium is induced by external sources of magnetic couplings, collectively referred to as the "lattice" [3]. Relaxation in NMR depends on the spatial or temporal fluctuation of these local magnetic fields. Fluctuating magnetic fields produce fluctuating torque that reorients the magnetiza-

tion. Relaxation is generally introduced by motions such as translation, rotation, and vibrations. However, internal couplings can also affect relaxation [8]. In solution, transitions between nuclear spin levels are induced by the randomly fluctuating magnetic fields that are generated as the molecules undergo Brownian motion. In solids, the spins dephase due to differences in resonance frequencies before relaxation due to motion can occur.

The two most significant relaxation parameters are the spin-lattice or longitudinal relaxation time (T_1) and the spin-spin or transverse relaxation time (T_2). The longitudinal relaxation time represents the rate at which the net magnetization returns to equilibrium along the z-axis. The transverse relaxation time describes the rate at which the net magnetization in the x-y plane is lost. Relaxation can be most easily described by including empirical damping terms into the Bloch equations of motion [5].

$$\frac{d\rho_{xy}}{dt} = -i\omega\rho_{xy} - \frac{\rho_{xy} - \rho_{xy}(eq)}{T_2} \qquad [2.28]$$

$$\frac{d\rho_z}{dt} = -\frac{\rho_z - \rho_z(eq)}{T_1} \qquad [2.29]$$

where, $\rho_z(eq) = \beta_I I_z$ and $\rho_{xy}(eq) = 0$, respectively. The solutions to Equations [2.28] and [2.29] are

$$\rho_{xy}(t) = \rho_{xy}(0)\exp(-i\omega t)\exp(-t/T_2) \qquad [2.30]$$

$$\rho_z(t) = \beta_I I_z\left[1 - \exp(-t/T_1)\right] \qquad [2.31]$$

Relaxation with a T_1 time constant reestablishes the equilibrium population distribution. Due to an absence of rapid molecular motions, T_1's in solids are generally very long (many seconds to minutes). Damping due to transverse relaxation processes results from two processes: 1) variation in Larmor frequencies for nuclei in different portions of the sample as a result of field inhomogeneities, and 2) random processes which tend to realign the nuclei within each portion of the sample to reestablish thermal equilibrium. Both processes contribute to the finite resonance linewidth. The large linewidths exhibited by solid-state samples imply very short transverse relaxation times (on the order of several ms).

2.10.2 Deuterium Lineshape Theory

The solid-state ^2H powder lineshape can provide valuable information about anisotropic motions. Molecular motions can modulate the orientational dependent transition frequencies, ω_Q, in Equation [2.26]. Any large amplitude motion of the C-D bond (which defines the V_{zz} axis in the PAS) will decrease the effective strength of the coupling, *eq*, and narrow the resulting spectrum. This effect is illustrated schematically in Figure 2.8.

Dynamics can be divided into three motional regimes: static, fast limit, and intermediate exchange limit. If motion is slow on the time scale of ω_Q^{-1}, there is minimal distortion of the classic Pake doublet spectrum (Figure 2.5). Spectra in this limit are referred to as static lineshapes. It is possible to measure QCC_{static} and η_{static} from the static quadrupolar echo line shape. A more general theory must be invoked for dynamics with rates comparable to the quadrupolar coupling constant. In this motional regime, spectral features can become highly distorted. In the intermediate motional regime, it becomes necessary to calculate the spectrum for continuous dynamics with a diffusion operator or discrete dynamics utilizing a jump matrix [16].

The theory for describing intermediate ^2H exchange lineshapes has been developed in detail by Barbara et al. and Wittebort et al.[17, 18]

The spectral lineshape, in the limit where motions are fast compared to QCC (> 170 kHz), is motionally averaged. The spectrum depends only on the equilibrium distribution of molecular orientations, $P(\Omega)$, and is independent of the exchange rate [9]. In the fast motion limit, the resonant frequency can be described by averaged (effective) quadrupolar coupling constants (QCC_{eff}) and asymmetry parameters (η_{eff}). Replacement of the averaged parameters into Equation [2.26] yields the following expression for the resonance frequency of a single crystallite,

$$\omega_Q = \frac{3\pi}{4}\left(\frac{e^2qQ}{h}\right)_{eff}[3\cos^2\theta - 1 + \eta_{eff}\sin^2\theta\cos 2\phi] \qquad [2.32]$$

For discrete processes, the eigenfrequencies of H_Q are an orientation-dependent average weighted by $P(\Omega)$,

$$\overline{V}_{ij} = \sum_k P(\Omega_k)V_{ij}(\Omega_k) \qquad [2.33]$$

where, $\Omega(\alpha, \beta, \gamma)$ are the Euler angles describing the orientation of the EFG tensor [18]. The powder lineshape is a superposition of spectral lines with frequencies calculated from the averaged Hamiltonian,

$$\overline{H} = \sum_{j=1}^{N} p_{eq}(j)H_Q^j \qquad [2.34]$$

where, j is the number of crystallites, and H_Q^j is given by Equation [2.24] [19]. $p_{eq}(j)$ is the equilibrium probability for an orientation of the crystal-fixed coordinate system

(C) relative to the PAS (P) reference frame for the *j*th site. The orientation dependent frequency for a system that is motionally averaged is

$$\omega = \pm\sqrt{\tfrac{3}{2}}\frac{eQ}{2\hbar}\sum_{j=1}^{N} p_{eq}(j)\sum_{an=-2}^{2}\rho_{2n}^{Q} D_{na}^{2}(\Omega_{PC}) D_{a0}^{2}(\Omega_{CL}) \qquad [2.35]$$

Rotation through the Euler angles $\Omega_{PC} = (\alpha_{PC}, \beta_{PC}, \gamma_{PC})$ rotates the principal axis system into coincidence with the crystal-fixed coordinate system, C. $\Omega_{CL} = (\alpha_{CL}, \beta_{CL}, \gamma_{CL})$ brings the C system into coincidence with the laboratory frame, L. ρ_{2n}^{Q} are the irreducible coupling tensor elements in the PAS. For an axially symmetric coupling, ρ_{2n}^{Q} is zero unless n=0. Upon transformation into spherical polar coordinates, the resonant frequency for an axially symmetric coupling tensor undergoing an N-site libration in the fast exchange limit is given as

$$\omega = \pm\sqrt{\tfrac{3}{2}}\frac{eQ}{2\hbar}\rho_{20}\sum_{j=1}^{N} p_{eq}(j) P_2(\cos\Theta_{PL}^{j}) \qquad [2.36]$$

where, Θ_{PL}^{j} is the angle between the magnetic field direction and the symmetry axis of the EFG tensor in the PAS. $P_2(\cos\Theta_{PL}^{j})$ is the second Legendre polynomial ($P_2(\cos\Theta_{PL}^{j}) = \frac{1}{2}(3\cos^2\Theta - 1)$). Equation [2.36] can be used to calculate the resonant frequency corresponding to each orientation of B_0 in the C system for any model of rapid molecular reorientations. The procedure to derive expressions for unequal site populations $p_{eq}(j)$ is to diagonalize $\overline{\mathbf{V}}$ in Equation [2.33]. Expressions for $\overline{\mathbf{V}}$ for a variety of motional models (discrete jump and diffusive) which have proved to be particularly useful in the interpretation of quadrupolar echo lineshapes of DNA have been developed by Wittebort and coworkers [18].

2.10.3 Quadrupolar Relaxation

For systems with quadrupolar coupling, Zeeman relaxation is dominated by fluctuations of the orientation-dependent quadrupolar interaction resulting from molecular motions. The relaxation rates of quadrupolar nuclei depend on the orientation of the principal axis coordinate system (PAS) with respect to the static magnetic field. The anisotropy in Zeeman relaxation rates across the powder pattern gives an indication of possible motions that may be contributing to the relaxation rate. The general form of the Zeeman quadrupolar relaxation rate is

$$\frac{1}{T_1} = \frac{\omega_Q^2}{3}[J_1^Q(\omega_0) + 4J_2^Q(2\omega_0)] \qquad [2.37]$$

where, $\omega_Q = 3e^2qQ/4\hbar$.[19] The spectral density function, $J_m^Q(\omega_0)$, is related to the autocorrelation function by the cosine Fourier transform,

$$J_m^Q(\omega_0) = 2\int_0^\infty C_m^Q(t)\cos(\omega t)dt \qquad [2.38]$$

where the autocorrelation function, $C_m^Q(t)$, is

$$C_m^Q(t) = \frac{\left\langle R_{2m}^{Q*} = (0)R_{2m}^Q = (t)\right\rangle}{(\rho_{20}^Q)^2} \qquad [2.39]$$

The autocorrelation function describes the orientation dependent fluctuations of the EFG tensor. The brackets denote an ensemble average. The R_{2m}^Q terms are the elements of the irreducible coupling tensor expressed in the laboratory frame. Correla-

tion functions have been constructed for a variety of motional models (e.g., discrete jump or continuous diffusion) that are particularly useful to describe relaxation phenomenon in DNA oligonucleotides. Expression for these correlation functions have been developed in detail elsewhere [19-23].

2.11 Notes to Chapter 2

[1] Haeberlen, U., *High Resolution NMR in Solids, Selective Averaging*. 1976, New York: Springer Verlag.

[2] Mehring, M., *Principles of High Resolution NMR in Solids*. 1983, New York: Springer Verlag.

[3] Slichter, C.P., *Principles of Magnetic Resonance*, 3rd ed. 1990, New York: Springer Verlag.

[4] Abragam, A., *Principles of Nuclear Magnetism*. 1961, New York: Oxford University Press.

[5] Munowitz, M., *Coherence and NMR*. 1988, New York: John Wiley & Sons, Inc.

[6] Dyson, F.J. (1949) *Phys. Rev.*, **75**, p. 486.

[7] Magnus, W. (1954) *Comm. Pure and Appl. Math.*, **7**, p. 649.

[8] Spiess, H.W., *NMR Basic Principles and Progress*. Vol. 15. 1978, Berlin/Heidelberg/New York: Springer-Verlag.

[9] Alam, T.A. and Drobny, G.P. (1991) *Chem. Rev.*, **91**, p. 1545.

[10] Andrew, E.R., Bradbury, A., and Eades, R.G. (1958) *Nature*, **182**, p. 1659.

[11] Maricq, M.M. and Waugh, J.S. (1979) *J. Chem. Phys.*, **70**, p. 3300.

[12] Herzfeld, J. and Berger, A. (1980) *J. Chem. Phys.*, **73**, p. 6021.

[13] Hartmann, S.R. and Hahn, E.L. (1962) *Phys. Rev.*, **133**, p. 2042.

[14] Stejskal, E.O., Schaefer, J., and McKay, R.A. (1977) *J. Magn. Reson.*, **25**, p. 569.

[15] Alam, T.M., Orban, J., and Drobny, G.P. (1991) *Biochemistry*, **30**, p. 9229.

[16] Alam, T.M. and Drobny, G.P. (1990) *J. Am. Chem. Soc.*, **29**, p. 3421.

[17] Barbara, T.M., Greenfield, M.S., Vold, R.L., and Vold, R.R. (1986) *J. Magn. Reson.*, **69**, p. 311.

[18] Wittebort, R.J., Olejniczak, E.T., and Griffin, R.G. (1987) *J. Chem. Phys.*, **86** (10), p. 5411.

[19] Torchia, D.A. and Szabo, A. (1982) *J. Magn.Reson.*, **49**, p. 107.

[20] Wittebort, R.J. and Szabo, A. (1978) *J. Chem. Phys.*, **69**, p. 1722.

[21] Allison, S.A. and Schurr, J.M. (1979) *Chem. Phys.*, **41**, p. 35.

[22] Langowski, J., Fujimoto, B.S., Wemmer, D.E., Benight, A.S., Drobny, G.P., Shibata, J.H., and Schurr, J.M. (1985) *Biopolymers*, **24**, p. 1023.

[23] Vold, R.L. and Vold, R.R., in *Adv. Magn. and Opt. Reson.* 1991, Academic Press: San Diego.

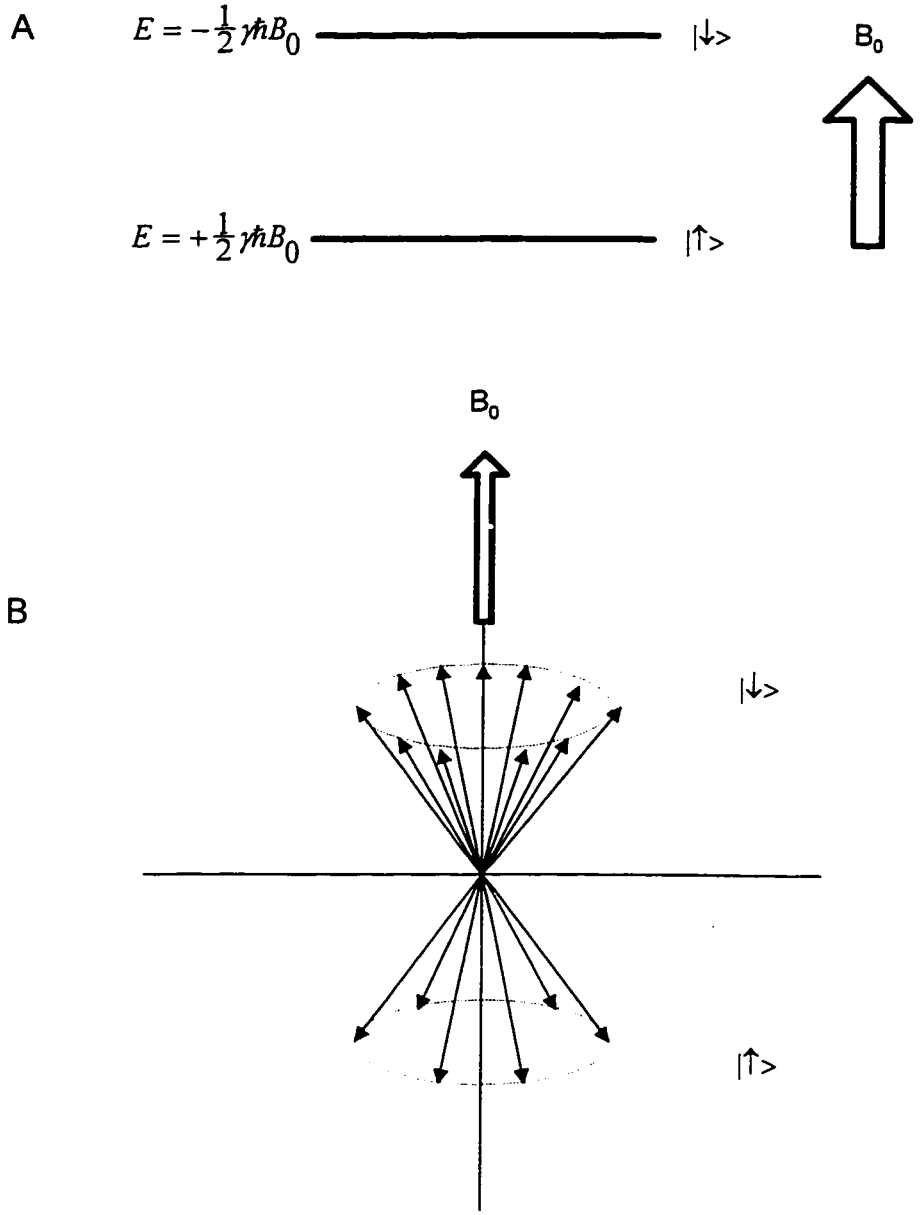

Figure 2.1: A) Energy level splitting due to the Zeeman interaction for a spin-1/2 nucleus. The low and high energy states are designated as |↑> and |↓>, respectively, and are separated by an energy, $E = \pm\gamma\hbar B_0$. B) Two-cone representation illustrating the precession of a single spin-1/2 magnetic moment (depicted as arrows) in a static magnetic field.

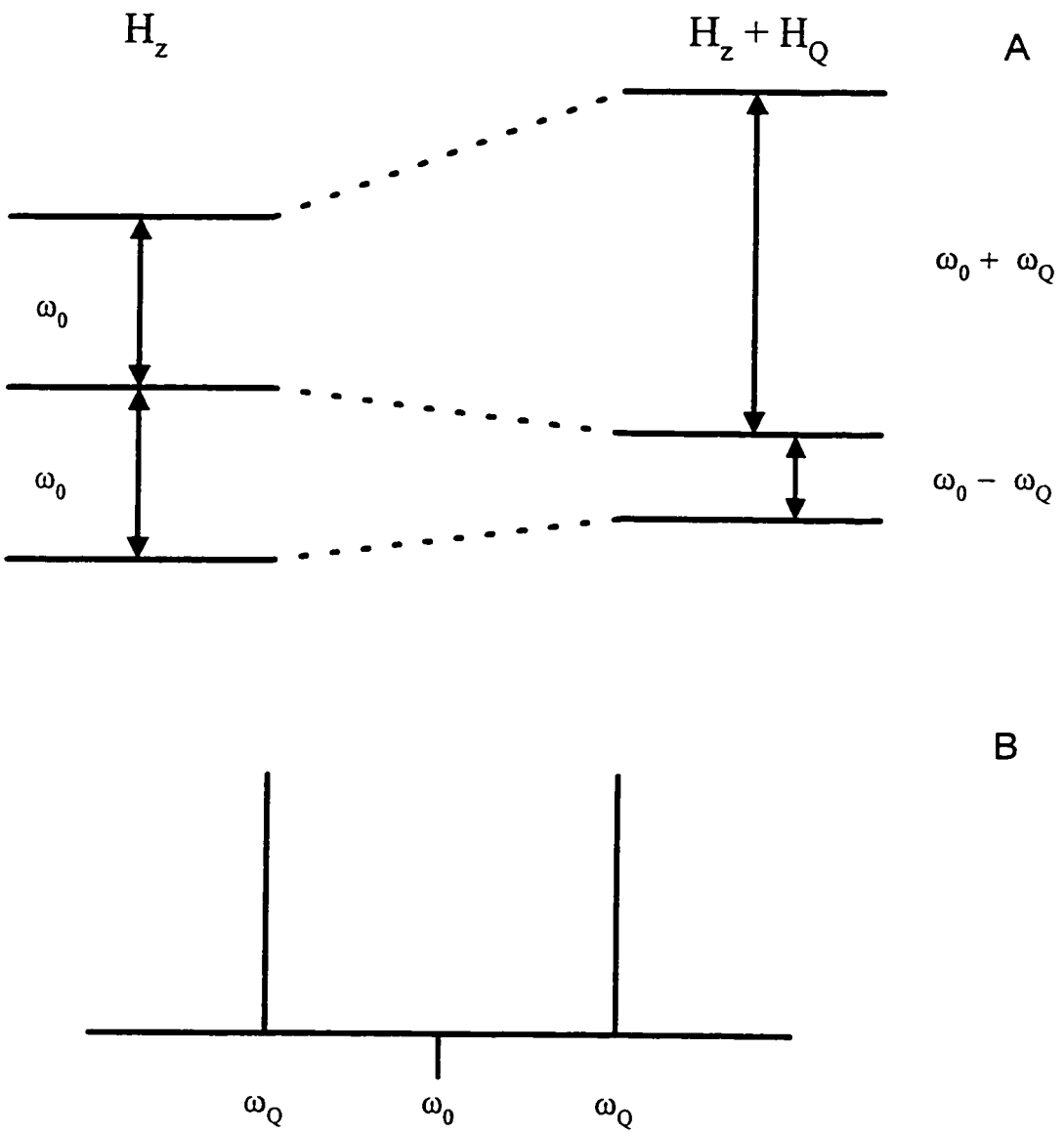

Figure 2.2: A) The effect of the first-order quadrupolar perturbation on the energy levels of a spin I=1 nucleus in a high magnetic field. The quadrupolar interaction H_Q splits the degenerate transition due to the Zeeman interaction. B) The resulting spectrum for a single value of the quadrupolar interaction at $\omega_0 \pm \omega_Q$ (adapted from ref. [9])

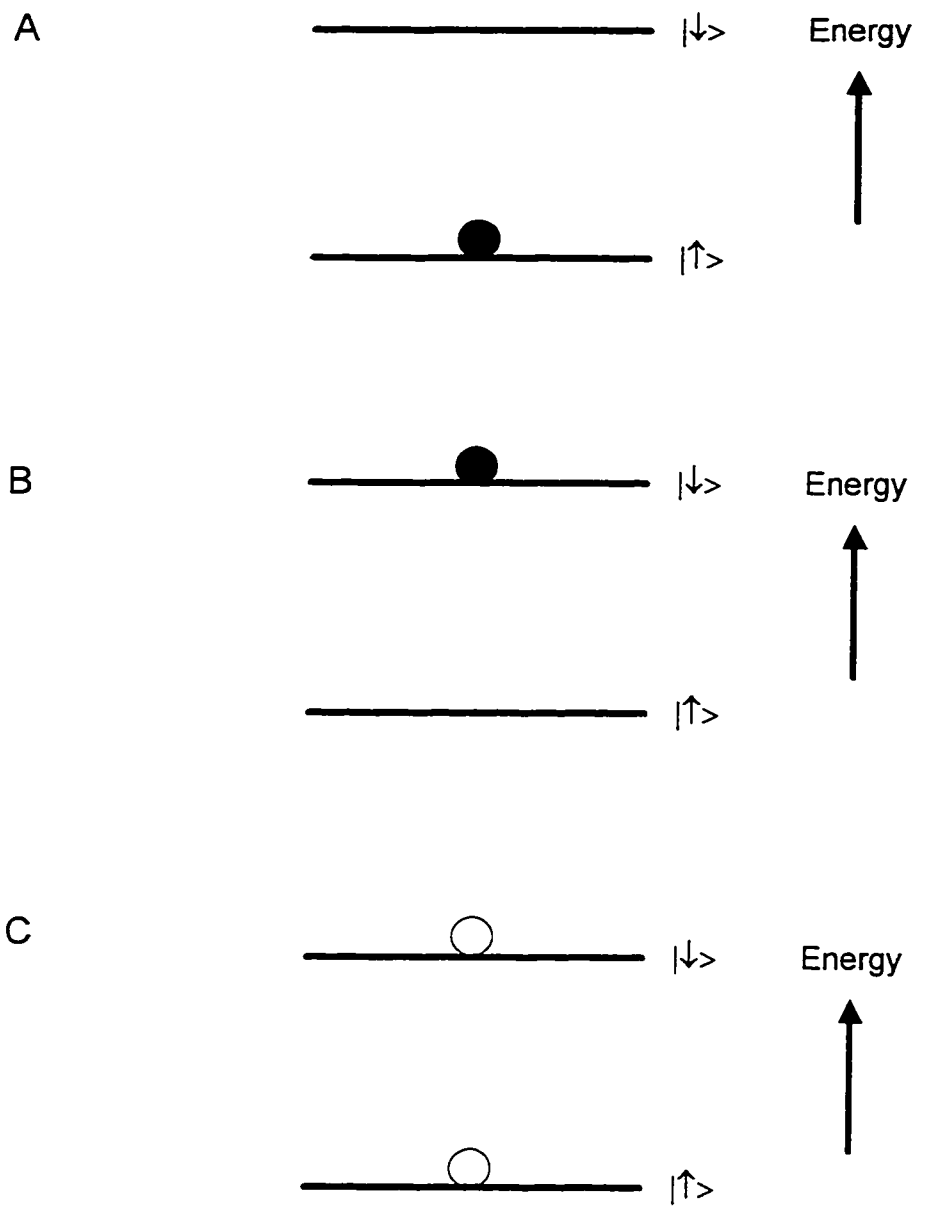

Figure 2.3: Quantum mechanical representation for a single quantum coherence in a spin-1/2 system. A) Spin in lower energy state (e.g. at equilibrium) with magnetization vector pointing along B_0. B) Spin in higher energy state (e.g. after application of a 180° pulse) with magnetization vector pointing opposite to B_0. C) Coherent superposition of energy states created after a 90° pulse to a spin system with its magnetization vector initially along the +z axis.

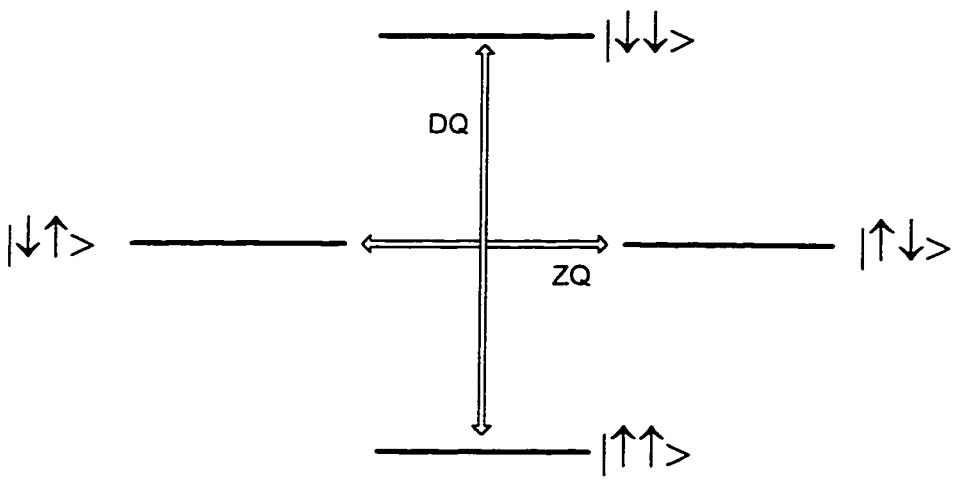

Figure 2.4: Quantized energy level diagram for two coupled spin-1/2 nuclei. A double quantum coherence is a coherent superposition between the |↑↑> and |↓↓|> energy states. A zero quantum coherence is a coherent superposition between the |↑↓> and |↓↑>energy states.

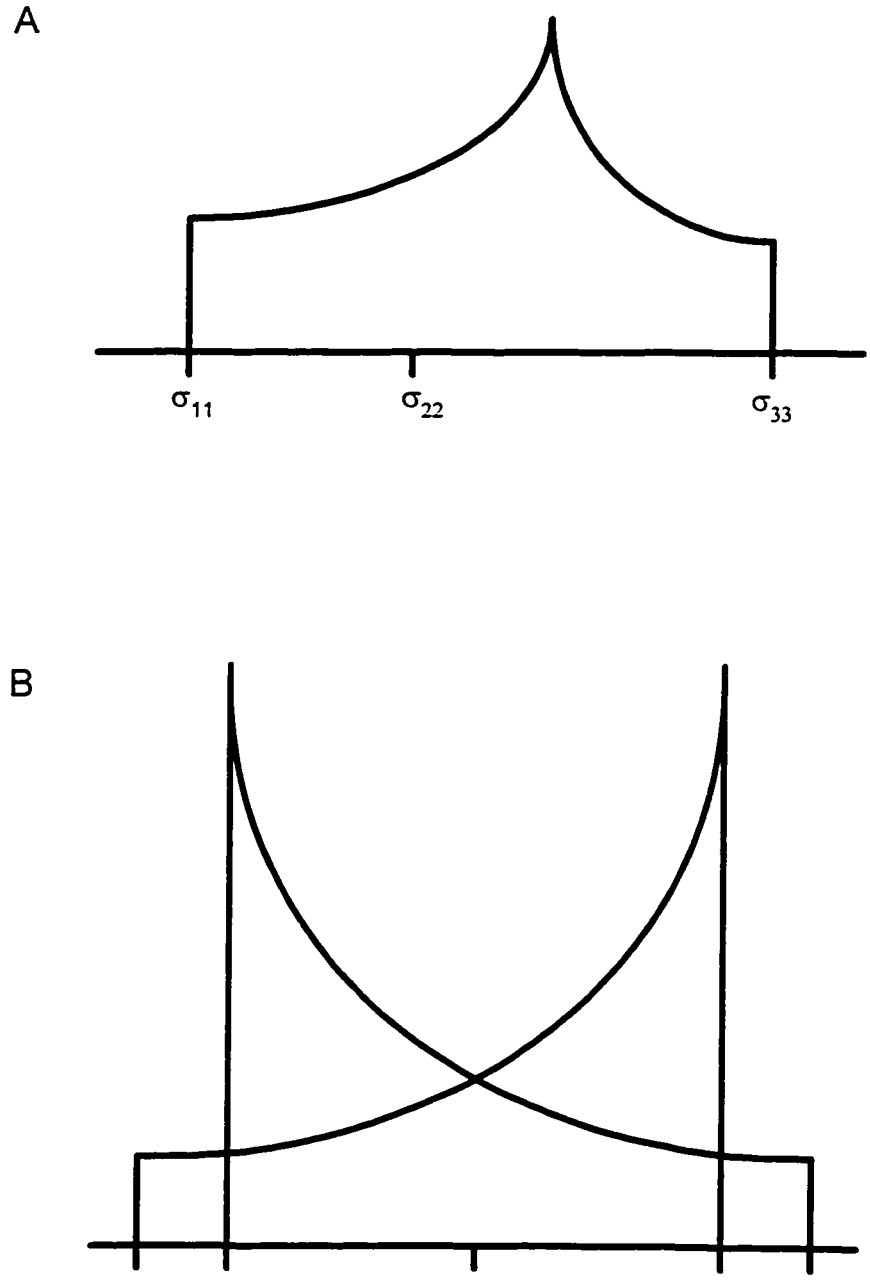

Figure 2.5: Schematic representation of powder line shapes. A) Arbitrary second rank tensor (e.g. chemical shift). CSA principal tensor components are given below spectrum. B) Axially symmetric second rank coupling tensor (e.g. dipolar coupling between two spin-1/2 spins or quadrupolar coupling).

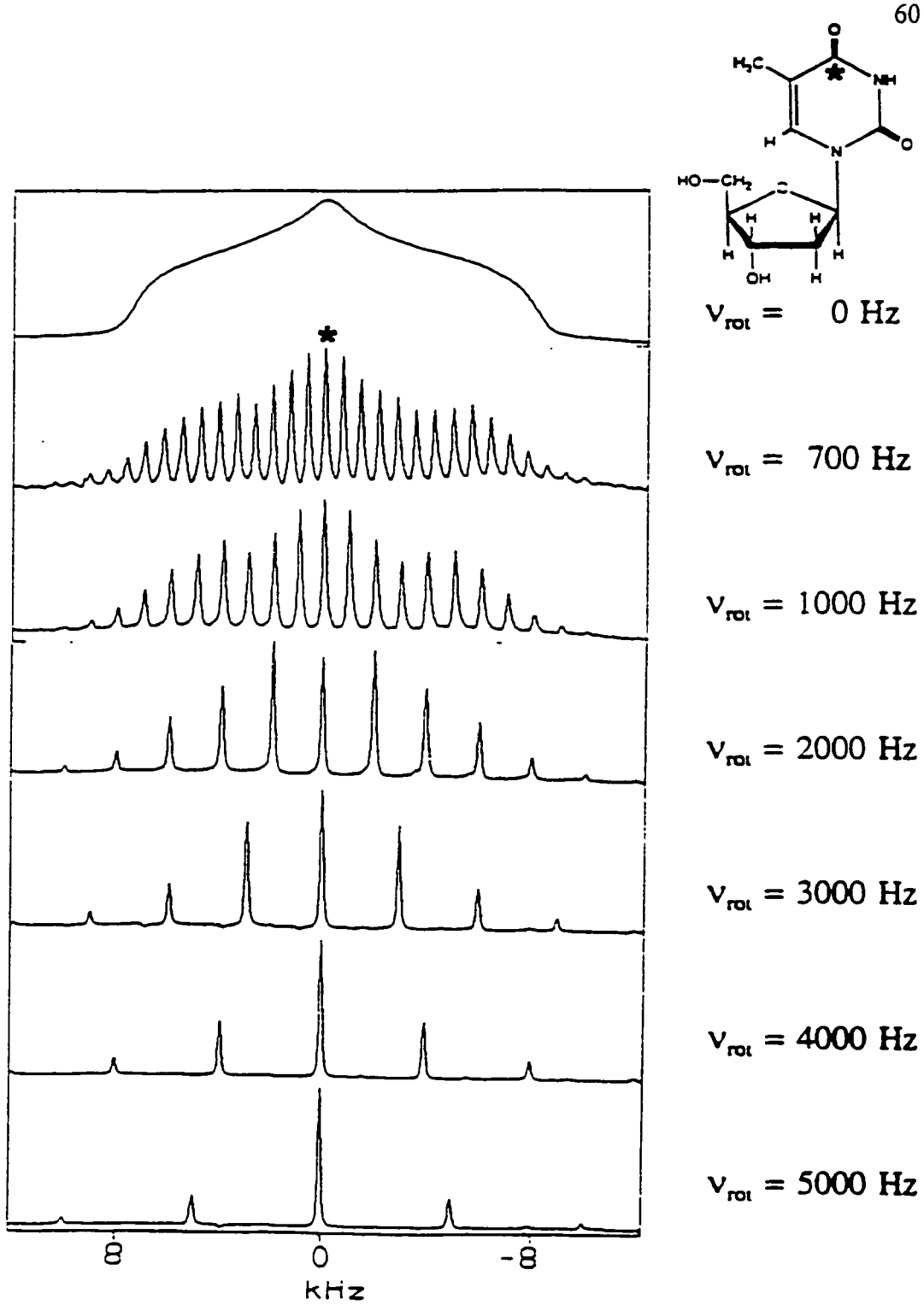

Figure 2.6: Experimental CP-MAS spectra of [4-^{13}C] thymidine monomer taken at several different spinning speeds. The rotor frequency (ν_{rot}) is given in Hertz. The isotropic peak is indicated with an asterisk (adapted from ref. [56]).

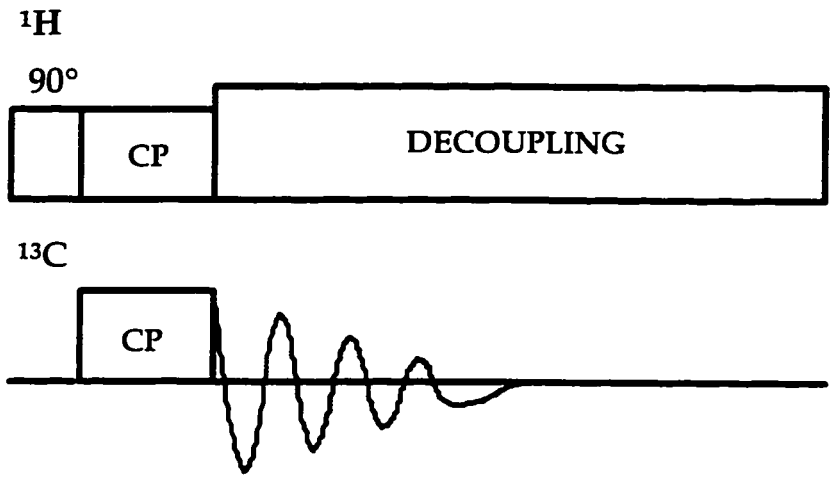

Figure 2.7: Radio-frequency pulse sequence for cross-polarization experiment.

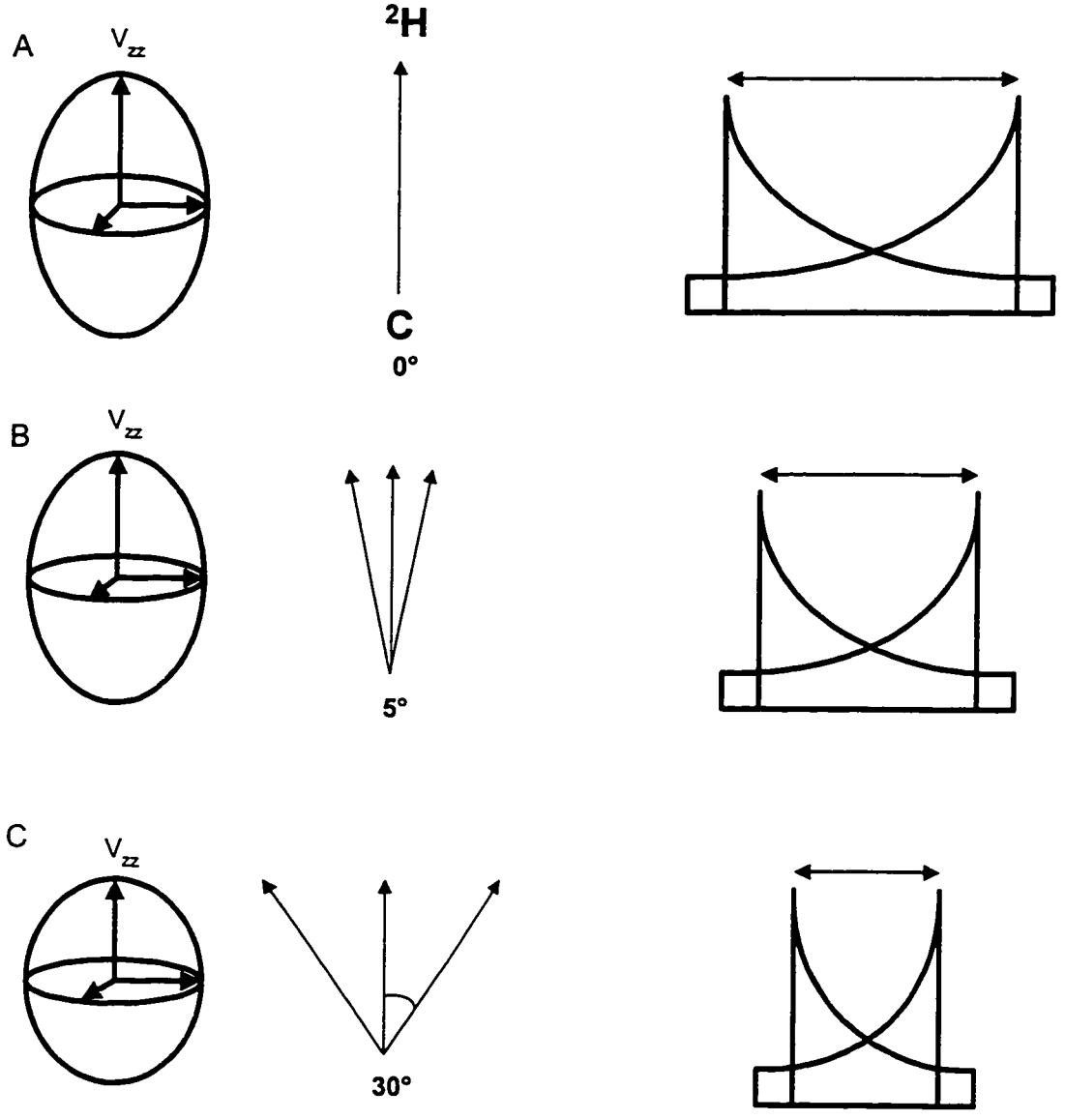

Figure 2.8: Schematic representation of the effect of motion of the carbon-^{2}H bond on the EFG tensor and ^{2}H lineshape. A) Static interaction. B) The result of small amplitude motional averaging. C) The result of large amplitude motional averaging (adapted from ref [69]).

Chapter 3
Dipolar Recoupling

3.1 Introduction

While CP-MAS affords spectral simplification and an increase in signal-to-noise, precious structural information that is contained in the anisotropic interactions is lost. The extent that homonuclear dipolar couplings are averaged by MAS depends on the relative magnitude of the coupling strength and the spinning frequency. It was realized that the averaging of the dipolar coupling could be interrupted by introducing carefully timed radio frequency pulses, thereby allowing one to measure a portion of the original coupling while preserving all other advantages of MAS [1]. Radiofrequency pulse sequences that reinstate the dipolar coupling are termed "dipolar recoupling" experiments. Since the dipolar interaction between two spins is proportional to $(\gamma_j \gamma_k \hbar)/r^3$, where r is the internuclear distance, the dipolar coupling provides a sensitive probe of molecular conformation. Dipolar recoupling experiments fall into two categories: 1) those that reinstate the dipolar coupling between heteronuclear spin pairs (e.g. ^{13}C-^{15}N and ^{31}P-^{13}C) and 2) those that recouple the dipolar interaction between homonuclear spin pairs (e.g. ^{13}C-^{13}C, ^{31}P-^{31}P, and ^{19}F-^{19}F). This dissertation is concerned exclusively with homonuclear dipolar recoupling experiments.

Numerous homonuclear dipolar recoupling methods have been developed, and the particular advantages and drawbacks of each have been extensively reviewed in the literature [1-3]. Three different dipolar recoupling pulse sequences have been utilized in this dissertation: Dipolar Recoupling with a Windowless Sequence (DRAWS), Double Quantum (DQ) DRAWS and Radio Frequency Dipolar Recoupling (RFDR). The DRAWS and DQ-DRAWS pulse sequences were developed by

members of this laboratory and have been discussed in several recent papers and Ph.D. dissertations [2, 4, 5]. DRAWS has been successfully implemented for the measurement of ^{13}C-^{13}C distances up to 5.0 Å in isotopically labeled peptides, nucleosides, and DNA oligonucleotides displaying a variety of CSA tensor properties [2] [3]. DRAWS can reinstate dipolar couplings over a broad spectral range with efficient suppression of CSA and offset effects at moderate r.f. powers and does not appear to be particularly sensitive to r.f. inhomogeneity. Furthermore, DRAWS is virtually independent of the mutual orientation of the CSA tensor for the dipolar-coupled ^{13}C-^{13}C spin pair (in contrast to the RFDR pulse sequence). Double quantum (DQ) DRAWS is a variation of the DRAWS pulse sequence that is useful for obtaining angular information and is described in Section 3.7. The RFDR pulse sequence was developed by Bennett and coworkers and is discussed in Section 3.3 [6]. The following sections will describe the theory, experimental implementation, and information content available from the one-dimensional and two-dimensional pulse sequences that were utilized in this study.

3.2 Dipolar Recoupling with A Windowless Sequence (DRAWS)

The DRAWS pulse sequence was designed as an improvement to the DRAMA (Dipolar Recovery At the Magic Angle) experiment developed by Tycko [7]. The DRAMA r.f. pulse sequence is shown in Figure 3.1. Two 90° pulses per rotor period interrupt the averaging of dipolar coupling due to MAS over a rotor cycle. A 180° pulse is applied once every two rotor periods to refocus spin evolution due to the chemical shift interaction. The DRAMA experiment is quite sensitive to CSA and off-resonance effects. Therefore, it is best suited for homonuclear spin pairs with small chemical shift differences. The DRAWS pulse sequence is shown for comparison in Figure 3.1. The two 90° pulses (centered at $\tau_r/4$ and $3\tau_r/4$) are the same as in DRAMA. However, the 90° pulses are of phase y. The 90° pulses impart a time

dependence to the spin Hamiltonian which recouples the dipolar interaction. Phase-alternated 360° x-pulses are applied between the 90° pulses. These serve to suppress the chemical shift while the phase alternation helps compensate for r.f. field inhomogeneity and other pulse imperfections. The basic DRAWS sequence is repeated using a 4-rotor cycle supercycle, $R\overline{R}\overline{R}R$. Transverse magnetization is observed stroboscopically every 4 rotor cycles and the amplitude monitored as a function of the number of DRAWS supercycles applied to the system.

The theory of dipolar recoupling via the DRAWS pulse sequence has been developed by Gregory et al. and Mehta et al. using both Average Hamiltonian Theory (AHT) and Floquet Theory [2, 3, 8]. Only the results from the Average Hamiltonian theory will be presented here. The zeroth-order average dipolar Hamiltonian for DRAWS irradiation using the product operator basis is

$$\overline{H}_D^{(0)} = \frac{d}{17\pi}[c_{xx-yy}(I_xS_x - I_yS_y) + c_{zz}(3I_zS_z - \mathbf{I}\cdot\mathbf{S}) \qquad [3.1]$$

where, $d = \hbar\gamma^2 / r^3$ (in units of radians/second) is the static dipolar coupling. Expressions for $c_{xx\text{-}yy}$ and c_{zz} are functions of (α, β, γ), the Euler angles that orient the PAS of the dipolar tensor in the rotor frame. Expressions for $c_{xx\text{-}yy}$ and c_{zz} are given by Gregory et al.[2] AHT also reveals that DRAWS does not completely eliminate the chemical shift interaction after a single application of the pulse sequence. However, addition of the $R\overline{R}\overline{R}R$ supercycle shown in Figure 3.1 suppresses the chemical shift effects to zeroth order.

The effect of the I_xS_x term is to rotate the initial state after cross-polarization, $\rho(0) = I_y + S_y$, into antiphase I_xS_z and I_zS_x states by the end of one rotor period,

$$\rho(t) = \exp(-ikI_xS_x)(I_y + S_y)\exp(ikI_xS_x) = (I_y + S_y)\cos(kt) + (I_xS_z - I_zS_x)\sin(kt)$$

$$\text{where, } k = \frac{d_{IS}}{17\pi}c_{xx-yy} \qquad [3.2]$$

consisting of non-observable single quantum magnetization. The I_zS_z term in Equation [3.1] has a similar effect, and the I_yS_y term commutes with the initial state, $\rho(0) = I_y+S_y$. After four rotor periods, the system has evolved into an *-Iy-Sy* state. After eight rotor periods, the system once again returns to the *Iy+Sy*. Figure 3.2 illustrates the effect of the I_xS_x term on the initial I_y state. Within each rotor period, antiphase magnetization also alternates with double quantum (DQ) magnetization $I_xS_y + I_yS_x$. The production and subsequent detection of DQ magnetization has proved to be useful for obtaining angular information in nucleic acids. Chapter 7 and Section 3.7 will further describe the details of these experiments.

3.3 Radio Frequency Driven Dipolar Recoupling (RFDR)

The RFDR (Radio Frequency Driven Dipolar Recoupling) experiment is another example of a broadband dipolar recoupling pulse sequence that is useful for measuring internuclear distances over a large spectral width and over a broad range of spinning speeds [6]. The RFDR pulse sequence uses a single π pulse per rotor period to drive magnetization exchange between coupled, chemically shifted spin-1/2 nuclei via a longitudinal mixing scheme. The relevant internal Hamiltonian for a homonuclear spin pair under RFDR is composed of terms for the chemical shifts, dipolar interactions, and the external r.f. π pulses. The zeroth order average Hamiltonian for one rotor period (neglecting CSA) is given by

$$\overline{H} = \overline{d}(I_x S_x + I_y S_y) \qquad [3.3]$$

$$\overline{d} = \frac{2}{\pi} \sum_{m=1,2} d_m \frac{\omega_\Delta / \omega_R}{\omega_\Delta^2 / \omega_R^2 - m^2} (-1)^{m-1} \sin\left(\pi \omega_\Delta / \omega_R\right)$$

where, **d** is the dipolar coupling, which depends on spinning speed (ω_r) and isotropic chemical shift (ω_Δ) . The magnitude of $\overline{H}$ is maximum when $\omega_\Delta = \omega_r$. A drawback of RFDR for quantitative distance measurement is its dependence on chemical shift tensor orientation. Additionally, RFDR cannot be used to measure distances between spins with degenerate chemical shifts. Due to these drawbacks, we have decided not to utilize the one-dimensional RFDR experiment in this dissertation. However, RFDR has been useful as a mixing sequence in a two-dimensional dipolar recoupling experiment. The two-dimensional RFDR experiment will be discussed in Section 3.6.

3.4 Two-Dimensional Experiments

Three different two-dimensional dipolar recoupling NMR experiments have been performed in this study for the purposes of gaining distance, angular, and spectral assignment information in selectively and multiply ^{13}C labeled spin systems: DRAWS, RFDR, and double-quantum (DQ) DRAWS. The general format of a two-dimensional experiment is presented as a block diagram in Figure 3.3. There are four distinct time periods: preparation (t), evolution (t_1), mixing (t'), and detection (t_2). The time dependence of the spin system for these four periods is governed by the propagators, U(t), $\exp(-iH_1 t_1)$, V(t'), and $\exp(-iH_2 t_2)$ [9]. The first excitation period creates a non-equilibrium condition that evolves under the Hamiltonian H_1 for a time t_1 with modes of coherence oscillating at the eigenfrequencies ω_1. During the mixing period, V(t') converts the system back to a state of observable magnetization which can then be detected during t_2. This new distribution evolves under the Hamil-

tonian H_2 for a time t_2 oscillating at frequencies ω_2. The full response during the evolution period is recorded over several hundred points by incrementing the values of t_1 (illustrated in Figure 3.3B). The signal detected in t_2 is encoded with information concerning the frequency, amplitude, and phase of whatever magnetization modes were present earlier. In the two-dimensional experiments that were used in this dissertation, the pulse train was turned off during the evolution and detection periods. Fourier transform with respect to both t_1 and t_2 produces a two-dimensional spectrum which correlates eigenfrequencies in the evolution period and eigenfrequencies in the detection period. Components that oscillate at the same frequencies in t_1 and t_2 appear as auto-peaks along the diagonal. Components that oscillate at different frequencies in the t_1 and t_2 time periods appear as crosspeaks.

3.5 Two-Dimensional DRAWS

The DRAWS technique has only recently been extended into a full two dimensional, phase-sensitive experiment for the correlation of homonuclear chemical shifts and has already been successfully applied to the spectral assignment and measurement of multiple interatomic distances in ^{13}C labeled amino acids and nucleosides [2, 3, 5]. 2D-DRAWS, like the solution-state 2D-NOESY (Nuclear Overhauser Effect Spectroscopy) experiment, is useful for correlating the chemical shifts of multiple dipolar coupled nuclei [10]. The cross-peak intensities observed in two-dimensional DRAWS experiments give an indication of the distance between the two dipolar coupled ^{13}C nuclei. Cross-peak buildup curves have also been generated for mutually coupled, multi-spin (≥ 3) systems for distance measurement [5]. However, spin diffusion is an important complication in the accurate determination of distances in multi-spin systems when the network of coupled nuclei cannot be treated as isolated two-spin systems.

A characteristic signature of the two-dimensional transverse DRAWS experiment is alternation of negative and positive cross-peaks depending on the number of ^{13}C nuclei involved in magnetization transfer during the mixing time. The theoretical origin of this sign change is discussed extensively by Kiihne and coworkers [11]. Correlations between nuclei engaged in direct internuclear coherence transfer are negative (i.e., nearest neighbors). At longer mixing times, a sign change results upon magnetization transfer through a mutually coupled intermediate spin. Positive cross-peaks to next nearest neighboring sites indicate this indirect transfer of magnetization (spin diffusion). We will illustrate how this feature proves invaluable in the spectral assignment of complicated spin systems. This positive-negative pattern is also a feature when the MELODRAMA (MElding of spin-LOcking and DRAMA) pulse sequence is used as a mixing sequence in a two-dimensional correlation experiment [12]. Sun and coworkers attributed negative crosspeaks to the double quantum nature of the recoupled dipolar Hamiltonian created by the MELODRAMA pulse sequence. The two-dimensional RFDR experiment, in comparison, does not possess this characteristic phase alternation, and structural information is based purely on distinguishing differences in relative cross-peak intensity [6].

The two-dimensional DRAWS pulse sequence is shown in Figure 3.4. The CP mixing period is followed by a t_1 evolution time which consists of a 4-step TOSS pulse sequence, a free precession period, and a time reversed TOSS pulse sequence (SSOT) [13, 14]. During the t_1 time period, dipolar couplings are averaged by MAS. MAS also induces a time dependence into the chemical shift interaction. The application of the TOSS-SSOT (TOtal Suppression of Sidebands) sequence during t_1 averages the anisotropic modulations in t_1 by rendering the MAS chemical shift Hamiltonian time independent. The TOSS-SSOT pulse sequence suppresses sidebands in the indirectly detected dimension and allows transverse magnetization to evolve solely under the influence of the isotropic chemical shifts.

Evolution of the spin system under the 2D-DRAWS pulse sequence can be most readily accomplished using the density matrix formalism. The initial state of the system (after cross-polarization) is $\rho(0) = I_x + S_x$. For simplicity, only the I_x term will be considered here. The density matrix is propagated in time according to Equation [2.5], where H is time-independent during the time t. The MAS chemical shift Hamiltonian as a result of the TOSS-SSOT sequence is

$$H_C = -\Omega_I I_z - \Omega_S S_z \qquad [3.4]$$

Under the influence of this time-independent Hamiltonian, the density matrix at the end of the t_1 evolution period is given by

$$\rho(t_1) = I_x \cos\Omega_I t_1 + I_y \sin\Omega_I t_1 \qquad [3.5]$$

During the mixing period, dipolar recoupling is achieved by the DRAWS pulse sequence (Figure 3.1). The time-independent, zeroth order DRAWS Hamiltonian is given in Equation [3.1]. At the end of the mixing period, the density matrix can be calculated from Equation [3.5],

$$\rho(\tau + t_1) \approx e^{i\overline{H}_D^{(0)}\tau} \rho(t_1) e^{-i\overline{H}_D^{(0)}\tau} \qquad [3.6]$$

To simplify the calculation, Equation [3.6] is converted into the tilted pseudospin ½ basis, in which the dipolar Hamiltonian in Equation [3.1] is fully diagonal [15].

$$\overline{H}_D^{(0)} = (3\alpha - \beta) I_z^{13} + 2\beta I_z^{12} = (3\alpha + \beta) I_z^{12} + (3\alpha - \beta) I_z^{23} \qquad [3.7]$$

Using this form of the Hamiltonian yields the following expression for the density matrix,

$$\rho(t_1+\tau)=[I_x\cos\beta\tau\cos\left(\tfrac{3\alpha+\beta}{2}\right)\tau-S_x\sin\beta\tau\sin\left(\tfrac{3\alpha+\beta}{2}\right)\tau-2I_yS_z\cos\beta\tau\sin\left(\tfrac{3\alpha+\beta}{2}\right)\tau-2I_zS_y\sin\beta\tau\cos\left(\tfrac{3\alpha+\beta}{2}\right)\tau]\cos\Omega_I t_1+[I_y\cos\beta\tau\cos\left(\tfrac{3\alpha-\beta}{2}\right)\tau-S_y\sin\beta\tau\sin\left(\tfrac{3\alpha-\beta}{2}\right)\tau+2I_xS_z\cos\beta\tau\sin\left(\tfrac{3\alpha-\beta}{2}\right)\tau-2I_zS_x\sin\beta\tau\cos\left(\tfrac{3\alpha-\beta}{2}\right)\tau]\sin\Omega_I t_1 \qquad [3.8]$$

The four linear terms in the above equation correspond to the observable components of the magnetization. The I_x and I_y terms correspond to the autopeaks, and negative S_x and S_y terms correspond to the developing negative crosspeaks. The four remaining bilinear terms are antiphase states that represent the mechanism of dipolar magnetization transfer.

After the mixing period, there is a mixture of sine and cosine components, which must be separated in order to obtain pure phase peaks. A 180° pulse is applied just prior to the mixing period to change the sign of the phase accumulated during t_1. This causes an effective reversal of the t_1 precession (i.e. time reversal). Time reversal can only be accomplished exactly when the time-dependence introduced by MAS is removed from the t_1 period by the TOSS-SSOT couple. The mixing period is followed by another TOSS pulse sequence which serves to suppress spinning sidebands in the t_2 time domain. The two signals are then combined, and the resulting expression, which includes the effects of chemical shift precession during t_2 is

$$\begin{aligned}&\rho^{comb}(t_1+\tau+t_2)=\\&[I_x\cos\beta\tau\cos\left(\tfrac{3\alpha+\beta}{2}\right)\tau-2I_yS_z\cos\beta\tau\sin\left(\tfrac{3\alpha+\beta}{2}\right)\tau]\cos\Omega_I t_1\cos\Omega_I t_2\\&+[I_y\cos\beta\tau\cos\left(\tfrac{3\alpha+\beta}{2}\right)\tau+2I_xS_z\cos\beta\tau\sin\left(\tfrac{3\alpha+\beta}{2}\right)\tau]\cos\Omega_I t_1\sin\Omega_I t_2\\&-[S_x\sin\beta\tau\sin\left(\tfrac{3\alpha+\beta}{2}\right)\tau+2I_zS_y\sin\beta\tau\cos\left(\tfrac{3\alpha+\beta}{2}\right)\tau]\cos\Omega_I t_1\cos\Omega_S t_2\\&-[S_y\sin\beta\tau\sin\left(\tfrac{3\alpha+\beta}{2}\right)\tau-2I_zS_x\sin\beta\tau\cos\left(\tfrac{3\alpha+\beta}{2}\right)\tau]\cos\Omega_I t_1\sin\Omega_S t_2\end{aligned} \qquad [3.9]$$

The net effect of the TOSS-SSOT couple in the t_1 time period and TOSS in the t_2 time period is to produce amplitude-modulated, pure phase peaks in the two dimensional spectrum, which are devoid of spinning sidebands in both dimensions. Phase sensitive detection is accomplished by combining a second set of two experiments in which $\sin\Omega_I t_1$ terms are observed.

Crosspeaks in the two-dimensional DRAWS experiment are negative for directly dipolar coupled nuclei. However, for longer distances, the sign of the crosspeak is positive. This sign change indicates that the crosspeak between the two nuclei is dominated by an indirect transfer of magnetization (i.e. spin diffusion) through a mutually coupled nucleus. Comparison of the time behavior of 1-D DRAWS decay curves and the build-up of 2-D crosspeak volumes indicates that the 2-D experiment is viable for distance measurement if the system can be separated into a series of isolated two-spin interactions. In multi-spin systems ($\geq$ 3 nuclei), the two-spin approximation is not necessarily valid, and the quantitative interpretation of crossspeak intensities for distance measurement has severe limitations [5].

3.6 Two-Dimensional RFDR

The RFDR method has also been extended into a phase sensitive two-dimensional chemical shift correlation experiment (Figure 3.4). The theory of the two-dimensional RFDR experiment has been discussed in detail by both Bennett and Mitchell [6, 16]. In the 2D-RFDR experiment, the mixing period contains the SEDRA (Simple Excitation for the Dephasing of Rotational-echo Amplitudes) cycle of one π pulse per rotor period developed by Gullion and Vega [17]. The CP mixing period is followed by a t_1 evolution time which consists of a TOSS-t_1-SSOT pulse sequence. This portion of the pulse sequence is identical to the t_1 period in the 2D-DRAWS experiment discussed in Section 3.5. After the t_1 period, a 90° pulse restores transverse magnetization to the z axis. Depending on the phase of the 90°

pulse, either the sine or cosine component of the transverse magnetization will be rotated to the z axis. The phase of the 90° pulse is altered in a second experiment to detect the other component. This set of two experiments is necessary for phase-sensitive detection. Any remaining transverse components are removed by phase cycling. During the mixing time, τ_{mix}, the RFDR pulse sequence serves to drive longitudinal magnetization exchange between dipolar coupled spins, resulting in the formation of crosspeaks. Another non-selective 90° pulse returns longitudinal magnetization into the transverse plane. This is followed by another TOSS pulse sequence which serves to suppress spinning sidebands in the t_2 time domain. The two-dimensional matrix is then Fourier transformed in both dimensions. Distance information can be obtained from the buildup of the RFDR crosspeak intensities over a series of mixing times. These measurements are dependent on the principal values of the chemical shift tensor, the relative orientation of the chemical shift and dipolar tensors, the sample rotation frequency, and the zero-quantum relaxation rate. In multi-spin systems, crosspeak buildup rates from RFDR (as is the case for DRAWS) are complicated by the effects of spin diffusion.

3.7 Double Quantum DRAWS

Double quantum (DQ) DRAWS is a two-dimensional dipolar recoupling experiment that is useful for determining orientational information [18]. Angular information is an important complement to distance measurement for molecular structure determination. Most recoupling techniques create either zero- (ZQ) or double-quantum (DQ) coherence between the dipolar coupled nuclei [7, 12, 19, 20]. As was mentioned in Section 3.2, the DRAWS pulse sequence produces double quantum coherence between the two nuclei of a dipolar coupled spin pair which oscillates with antiphase magnetization. This double quantum coherence may be selected by varying the phase of the r.f. pulses and the receiver in successive experiments. The results are

added so as to accumulate signal which has passed through the desired double quantum state [4]. Other orders of coherence will add destructively over the course of the phase cycle.

A detailed theoretical treatment of the DQ-DRAWS pulse sequence using Average Hamiltonian Theory and Floquet Theory has been given elsewhere [8, 18]. The DQ-DRAWS pulse sequence that was utilized in this investigation is depicted in Figure 3.5. A cross-polarization period is followed by DRAWS irradiation, which is applied synchronously with the sample spinning. The preparation time is, therefore, equal to an integral number of rotor cycles. Application of the DRAWS pulse sequence during the preparation period produces both double quantum and antiphase magnetization, which oscillate rapidly in response to the r.f. irradiation. By the end of a pulse cycle, transverse magnetization is converted into antiphase magnetization, with no net production of double quantum coherence. A 90° pulse at the conclusion of the preparation period rotates the antiphase magnetization into a double-quantum coherence state which evolves during the t_1 period. The t_1 period is incremented regularly over several hundred experiments. When the experiment is used for double quantum filtering, the t_1 period is fixed at 1μs [18]. The application of DQ-filtered DRAWS to DNA oligonucleotides will be discussed in Chapter 7. DRAWS irradiation during the mixing period recouples the dipolar interaction. The recoupled dipolar interaction is introduced directly into the double quantum spinning sideband intensities. The preparation sequence, in contrast, affects only the intensity of the overall spectrum. At the conclusion of the mixing period, the double quantum magnetization has been converted into single quantum magnetization that can be observed during the t_2 time period. Longer mixing times are needed to create multiple quantum coherence between more weakly dipolar coupled nuclei that correspond to longer internuclear distances.

The DQ-DRAWS experiment produces a two-dimensional matrix that can be processed with a double Fourier transform. Projections along each of the two axes

give one dimensional spectra. The projection along the ω_2 axis is the single quantum spectrum that is due to evolution during the t_2 time period. The single-quantum spectrum is identical to the normal CP-MAS spectrum. The projection along the ω_1 axis contains information due to evolution in the t_1 time period. This is referred to as the double quantum projection and contains information about the angular relationship between the spins. The DQ isotropic shift appears as a single line at the sum of the two single quantum isotropic chemical shifts (depicted in Figure 3.5) and is surrounded by a manifold of spinning sidebands separated by the rotor frequency. Chapter 7 presents DQ-DRAWS results for several selectively and uniformly labeled nucleosides and describes how we can obtain orientational information from the spinning sidebands of the DQ spectrum.

3.8 Notes to Chapter 3

[1] Griffiths, J.M. and Griffin, R.G. (1993) *Anal. Chim. Acta*, **283**, p. 1081.

[2] Gregory, D.M., Mitchell, D.J., Stringer, J.A., Kiihne, S., Shiels, J.C., Callahan, J., Mehta, M.A., and Drobny, G.P. (1995) *Chem. Phys. Lett.*, **246**, p. 654.

[3] Mehta, M.A., Gregory, D.M., Kiihne, S., Mitchell, D.J., Hatcher, M.E., Shiels, J.C., and Drobny, G.P. (1996) *Solid State Nuclear. Magn. Reson.*, **7**, p. 211.

[4] Gregory, D.M., *Ph.D. Dissertation*, 1996, University of Washinton.

[5] Kiihne, S.R., *Ph.D. Dissertation*, 1998, University of Washington.

[6] Bennett, A.E., Ok, J.H., Vega, S., and Griffin, R.U. (1992) *J. Chem. Phys.*, **96**, p. 8634.

[7] Tycko, R. and Dabbagh, G. (1990) *Chem. Phys. Lett.*, **173** (5-6), p. 461.

[8] Gregory, D.M., Mehta, M.A., Shiels, J.C., and Drobny, G.P. (1997) *J. Chem. Phys.*, **107** (1), p. 28.

[9] Munowitz, M., *Coherence and NMR*. 1988, New York: John Wiley & Sons, Inc.

[10] Jeener, J., Meier, B.H., Bachmann, P., and Ernst, R.R. (1979) *J. Chem. Phys.*, **71**, p. 4546.

[11] Kiihne, S.R., Mehta, M.A., Stringer, J.A., Gregory, D.M., Shiels, J.C., and Drobny, G.P. (1997) *J. Phys. Chem.*, in press.

[12] Sun, B.Q., Costa, P.R., Kociski, D., Lansbury, P.T., and Griffin, R.G. (1995) *J. Chem. Phys.*, **102** (2), p. 702.

[13] Geen, H. and Bodenhausen, G. (1992) *J. Chem. Phys.*, **97** (5), p. 1.

[14] Dixon, W.T. (1982) *J. Chem. Phys.*, **77** (4), p. 1800.

[15] Weintraub, O. and Vega, S. (1993) *J. Magn. Reson. A*, **105**, p. 245.

[16] Mitchell, D.J., *Ph.D. Dissertation*, 1996, University of Washington.

[17] Gullion, T. and Vega, S. (1992) *Chem. Phys. Lett.*, **194** (4,5,6), p. 423.

[18] Gregory, D.M., Wolfe, G.M., Jarvie, T.P., Shiels, J.C., and Drobny, G.P. (1996) *Mol. Phys.*, **89** (6), p. 1835.

[19] Lee, Y.K., Kurur, N.D., Helmle, M., Johannessen, O.G., Nielsen, N.C., and Levitt, M.H. (1995) *Chem. Phys. Lett.*, **242**, p. 304.

[20] Nielsen, N.C., Creuzet, F., Griffin, R.G., and Levitt, M.H. (1992) *J. Chem. Phys.*, **96**, p. 5668.

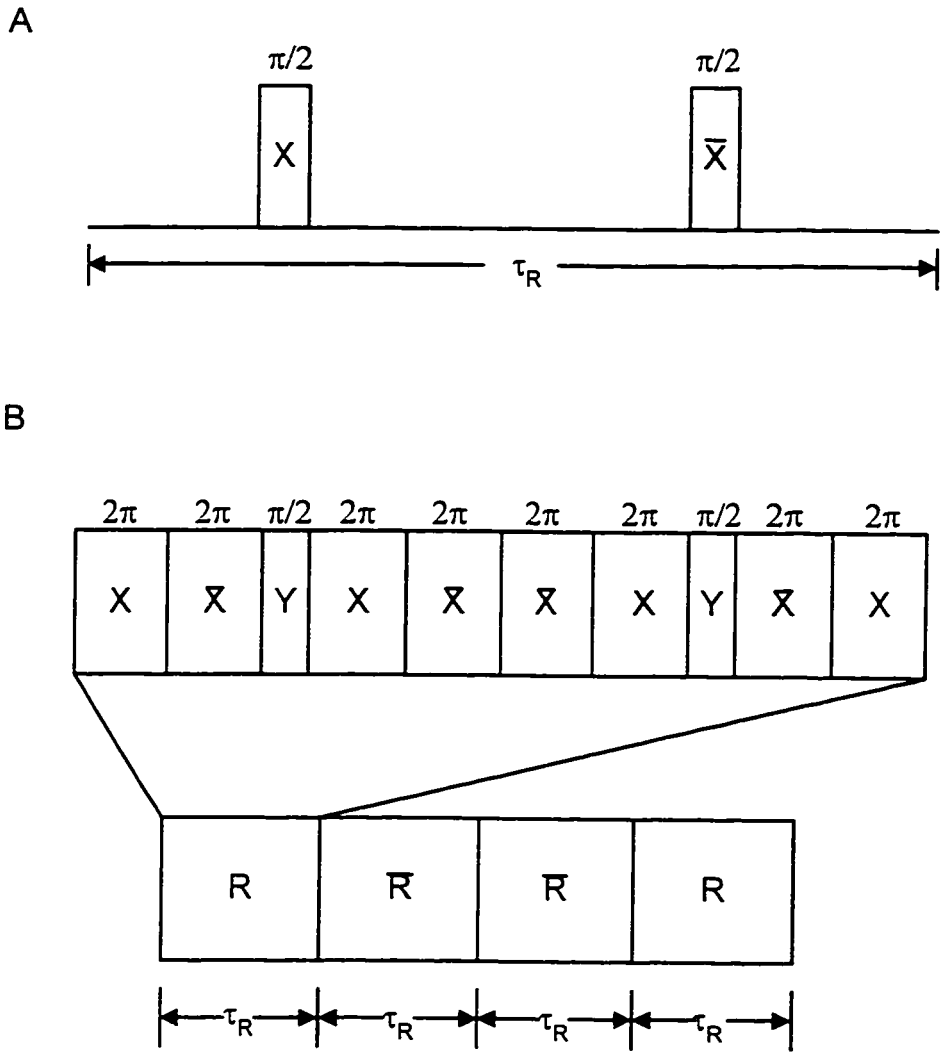

Figure 3.1: Dipolar recoupling r.f. pulse sequences (only ^{13}C channel shown). (A) DRAMA pulse sequence for one rotor period. $\overline{X}$ indicates a negative 90° X pulse. (B) DRAWS pulse sequence for one rotor period and DRAWS supercycle for four rotor periods. All X and $\overline{X}$ pulses are 360° pulses. R indicates the one rotor cycle DRAWS sequence. $\overline{R}$ indicates the one rotor cycle DRAWS sequence with the phases of all pulses reversed.

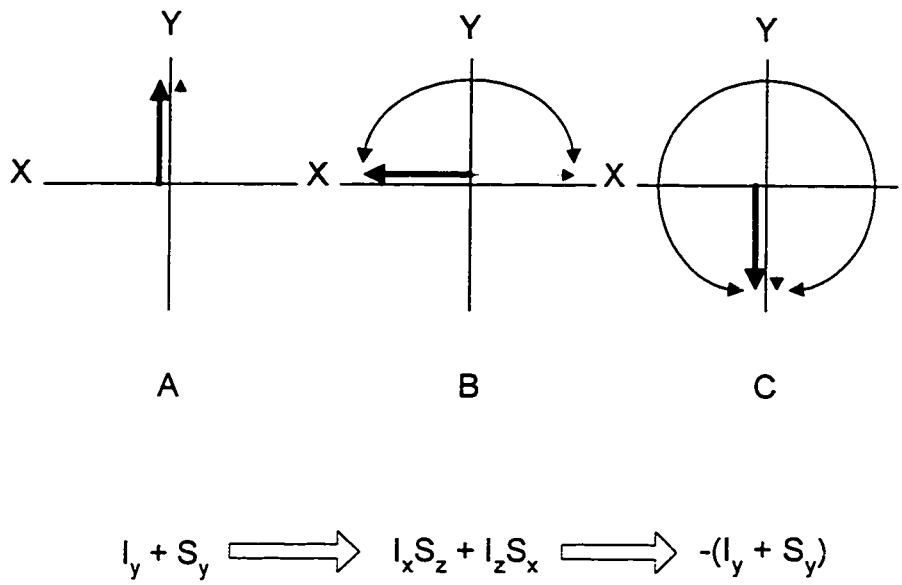

Figure 3.2: Formation of antiphase magnetization during the DRAWS pulse sequence. An initial $I_y + S_y$ state (A) is rotated into antiphase magnetization ($I_xS_z + I_zS_x$) by the end of each rotor period (B). Only the I_y spin is depicted here. After four rotor periods, Y magnetization is rotated back to the z axis ($-I_y-S_y$) (C), while antiphase magnetization alternates with double quantum magnetization, $I_xS_y + I_yS_x$ (adapted from ref. [4]).

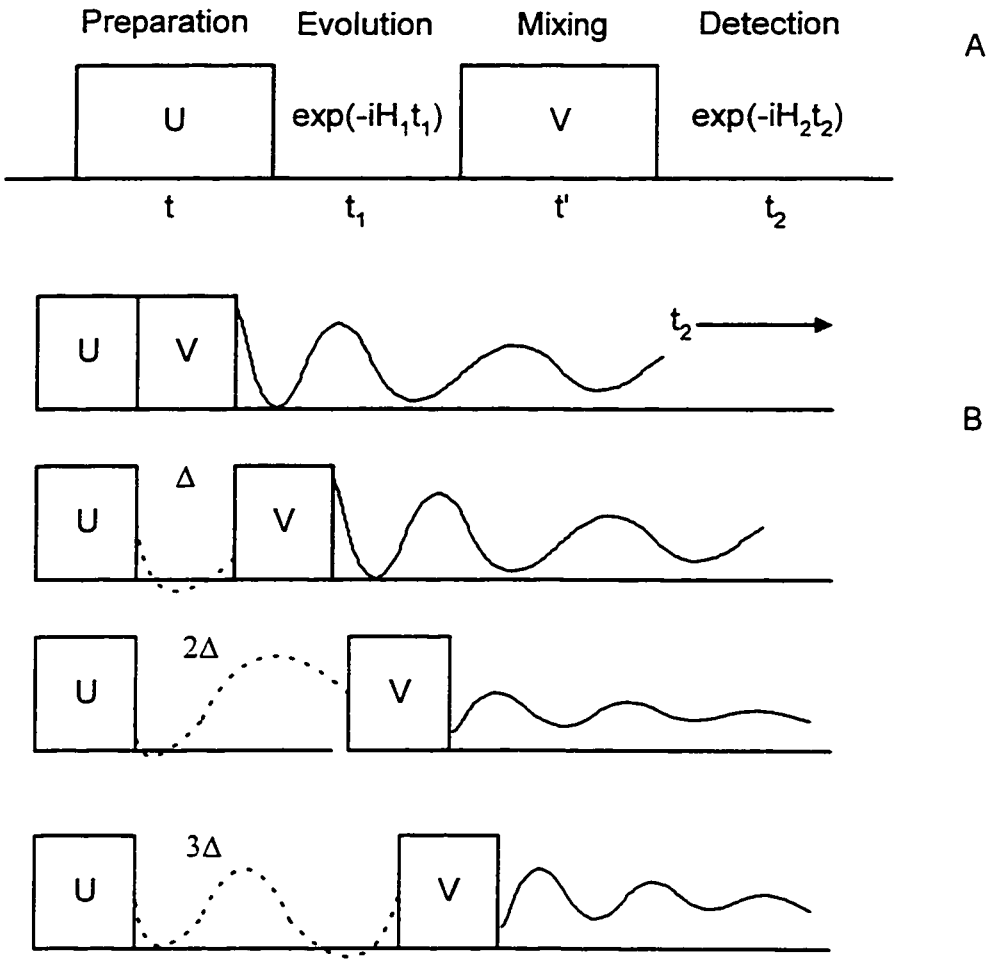

Figure 3.3: (A) Block diagram for a two-dimensional experiment. FID is recorded during the detection period, t_2. (B) Repetitions of the experiment over a series of regularly incremented values of t_1 (represented by Δ). For each value of t_1, the signal detected during t_2 changes according to what has happened previously. The preparation and mixing periods are reapplied without change for each experiment (adapted from ref. [9]).

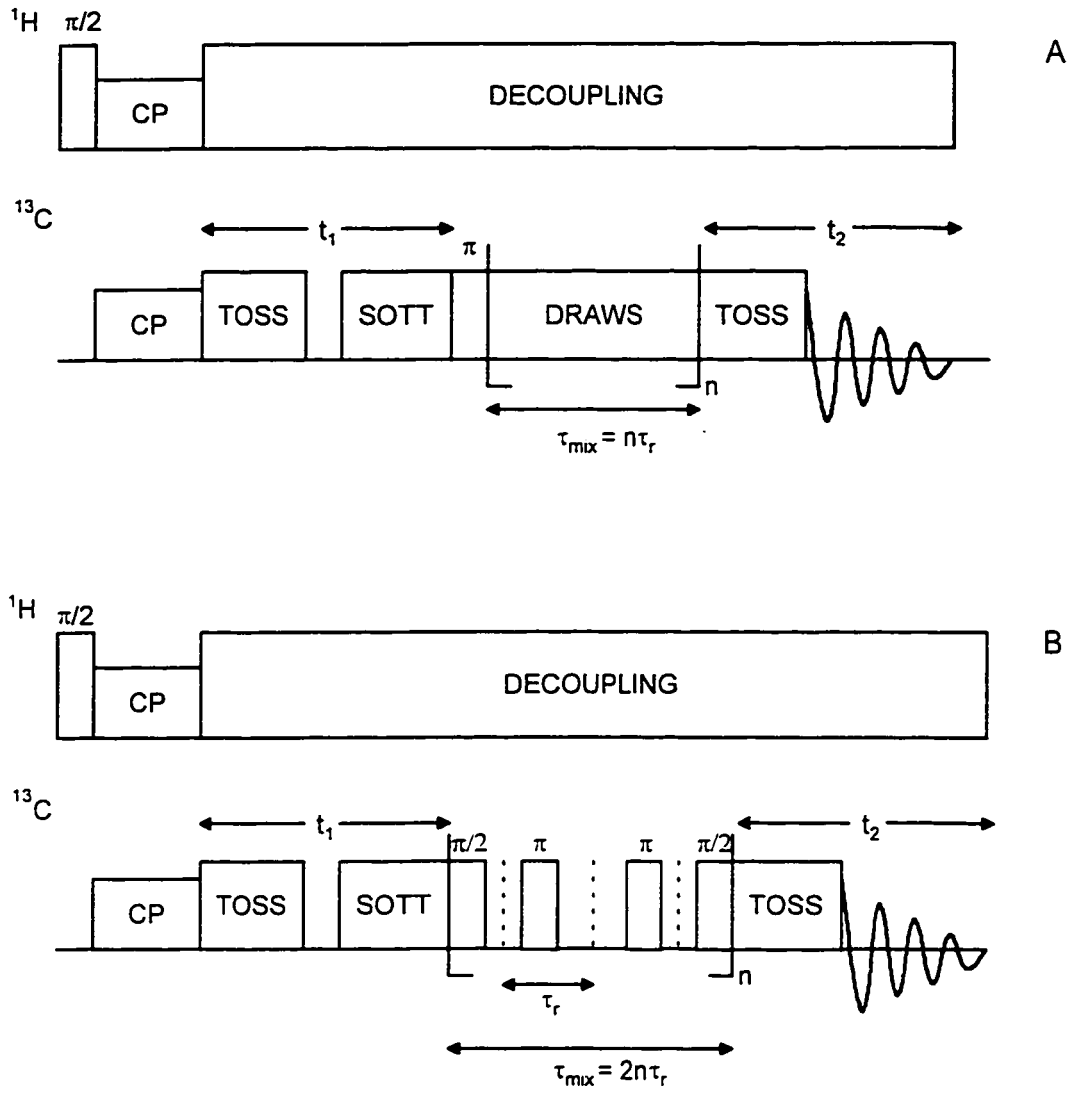

Figure 3.4: Two-dimensional dipolar recoupling r.f. pulse sequences. 2D-DRAWS (A) and 2D-RFDR (B). See text for details.

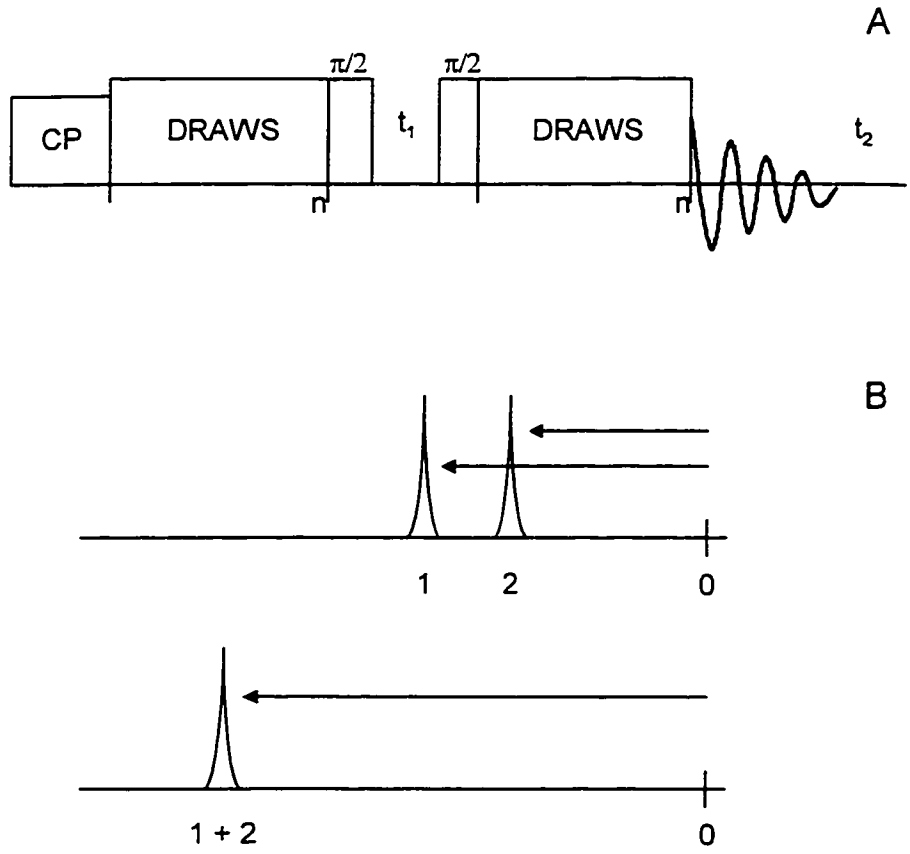

Figure 3.5: (A) R.f. pulse sequence for DQ-DRAWS experiment. Only the ^{13}C channel is shown. The DRAWS period represents a four-step supercycle of the one rotor period DRAWS sequence. n refers to number of repetitions of DRAWS and is held fixed during the experiment. (B) Representation of single and double quantum spectra for two coupled spins. In the single quantum spectrum, lines occur at the chemical shifts of the two spins (1 and 2). In the double quantum spectrum, one line occurs at the sum (1+2) of the chemical shifts.

Chapter 4
Materials and Methods

4.1 Preparation of Selectively ^{13}C, ^{15}N, and ^{2}H Labeled Nucleosides

This section contains chemical and biochemical synthetic protocols for the preparation of the selectively ^{13}C, ^{15}N, and ^{2}H labeled nucleoside and deoxynucleoside monomers studied during the course of this investigation. Procedures are presented for the synthesis of [2"-^{2}H]-2'-deoxythymidine, [2-^{13}C, 1,3-$^{15}N_2$]-thymine, [2-^{13}C, 1,3-$^{15}N_2$]-2'-deoxythymidine, [2-^{13}C, 1,3-$^{15}N_2$]-2'-deoxyuridine, [2,2'-$^{13}C_2$]-, [2,1'-$^{13}C_2$]-,[2,2',5'-$^{13}C_3$]-, and [2, 1',3'-$^{13}C_3$]-cytidine, and 4-(1,2,4-triazol-1-yl)-2'-deoxythymidine-5'-O-(dimethoxytrityl)-3'-O-(N,N-diisopropyl)-β-cyanoethylphosphoramidite.

4.1.1 [2"-^{2}H]-2'-deoxythymidine. [2"-^{2}H]-2'-deoxythymidine was prepared using the method of Robins et al. with some minor modifications in solvents and purification procedures [1]. The synthetic scheme for this reaction is presented in Figure 4.1. Ribothymidine was reacted with 1,3-dichloro-1,1,3,3-tetraisopropyldisiloxane (TPDS-Cl_2) and pyridine to produce the selectively 3',5' protected nucleoside derivative. Phenoxythiocarbonylation of the 2' hydroxyl group, AIBN-initiated homolytic deoxygenation with tri-n-butyltin deuteride, and deprotection with tetra-n-butylammonium fluoride yielded the 2'-deuterated deoxynucleoside. TPDS-Cl_2, 4-N,N-dimethylaminopyridine (DMAP), triethylamine (TEA), trifluoroacetic acid (TFA), tri-n-butyltin deuteride (n-Bu_3SnD), phenylchlorothionoformate (PTC-Cl), 2,2'-azobis-(2-methyl-propionitrile) (AIBN), adenosine, and tetra-n-butyl ammonium fluoride

(TBAF) were purchased from Aldrich Chemical Company. Ribothymidine was purchased from Sigma Chemical Company.

3',5'-O-TPDS-ribothymidine. Ribothymidine (0.9120g, 3.5mmol) was vacuum pumped overnight. Dry pyridine (50ml) was introduced into the reaction vessel under an argon atmosphere with stirring. The temperature was raised to 75°C in order to fully dissolve the nucleoside. This prewarming step appears to be essential for successful TPDS protection. Once dissolved, 1.25ml (1.1 eq) TPDS-Cl_2 were added to the reaction and stirred for 2 hours at 75°C. The reaction was then stirred overnight at room temperature. The reaction progress was monitored by TLC (95% CH_2Cl_2/5% CH_3OH). Once complete, the solution was transferred to a separatory funnel and extracted with H_2O. The organic layer was washed sequentially with HCl (1M), saturated $NaHCO_3$, and saturated NaCl. The organic layer was dried over $MgSO_4$ and evaporated to dryness. This series of sequential washes is referred to as the standard processing procedure. The resulting residue was purified via silica gel column chromatography (60% EtOAc/40% hexane). The product (1.28g, 2.6mmol, 67% yield) was evaporated to dryness. 6.5 equivalents DMAP (2.019g, 16.5mmol) were added to the dried product and the reaction mixture stored overnight under vacuum before continuing onto the next step.

2'-O-phenoxythiocarbonyl-3', 5'-O-TPDS-thymidine. 65ml of dry methylene chloride were added to the reaction mixture under an argon atmosphere via dry syringe and stirred. Once dissolved, the reaction cooled in an ice bath and 2.8 equivalents of PTC-Cl (1ml, 7.2mmol) were added. The reaction was stirred for 1 hour, removed from the ice bath and stirred for an additional 3 hours. The reaction progress was monitored by TLC (80% EtOAc/20% hexane). Upon completion, the reaction mixture was evaporated to dryness and washed using the standard processing procedure. The resulting residue was purified via silica gel column chromatography using 40%

EtOAc/60% hexane as the effluent. The product (1.36g, 2.1mmol, 82% yield) was dried and 0.7 equivalents (0.247g, 1.5 mmol) AIBN were added. The reaction mixture was stored under vacuum overnight.

3', 5'-O-TPDS-[2"-^{2}H]-2'-thymidine. 60ml freshly sparged toluene was added to the protected nucleoside under an argon atmosphere via dry syringe. Eight equivalents of fresh n-Bu_3SND (5g, 17.0mmol) were added and the reaction stirred for 30 minutes at room temperature. The temperature was raised to 75°C and stirred for 2 hours. The reaction progress was monitored via TLC (80% EtOAc/20% hexane). Upon completion, the solvent was evaporated and the residue purified on a silica column with a two-step gradient (40% EtOAc/60% hexane followed by 60% EtOAc/40% hexane), yielding 980mg (2.0mmol, 95% yield) of 3',5'-O-TPDS-[2"-^{2}H]-2'-thymidine. The product was stored under vacuum overnight.

[2"-^{2}H]-2'-thymidine. 3', 5'-O-TPDS-[2"-^{2}H]-2'-thymidine was dissolved in THF (50ml). 2ml of TBAF in 1M THF were added and the reaction stirred at 75°C for 2 hours until the reaction mixture turned dark yellow. Upon completion, the solvent was rotary evaporated and partitioned between H_2O and diethyl ether. The aqueous layer was collected and evaporated to dryness. The crude product was purified via silica gel column chromatography with the following gradient: 100% chloroform (2x bed volume), 10% CH_3OH/90% $CHCl_3$ (1x bed volume), 15% CH_3OH/85% $CHCl_3$ (2x bed volume), 20% CH_3OH/80% $CHCl_3$ (1x bed volume). The final yield of [2"-^{2}H]-2'-deoxythymidine was 0.450g (1.85mmol, 53% overall yield). Sample purity and percentage deuteration (>95%) were monitored by ^{1}H NMR. In particular, the H1' triplet (6.2 ppm) reduces to a doublet (6.2 ppm), and the multiplet at δ 2.0-2.5 ppm exhibits a reduction in signal intensity upon deuteration.

4.1.2 [2-^{13}C, 1, 3-$^{15}N_2$]-thymine. Methods to prepare [2-^{13}C, 1,3-N_2]-thymine from 2-bromopropionic acid, sodium cyanide, and ^{13}C,$^{15}N_2$ urea were combined from the procedures of Redwine et al. and Boxer et al. [2, 3]. The reaction scheme for the preparation of thymine via these procedures appears in Figure 4.2. [2-^{13}C, 1,3-N_2]-thymine was prepared in sufficient quantities for enzymatic glycosylation (Section 4.1.3). ^{13}C,$^{15}N_2$ urea was purchased from Cambridge Isotope Laboratories. 2-bromopropionic acid, sodium cyanide, basic alumina, and PtO_2 were purchased from Aldrich Chemical Company. H_2 gas was purchased from Matheson.

Sodium 2-bromopropionate. The 2-bromopropionic acid sodium salt was prepared by adding 4.2g (39.7mmol) Na_2CO_3 to 6.3g (39.4mmol) 2-bromopropionic acid in 90ml dry CH_2Cl_2. Methylene chloride was passed down a column of basic alumina to remove residual traces of HCl just prior to use. The mixture was stirred for 2.5 hours at 50°C. The resulting white precipitate was filtered off and washed three times with ether and dried to yield 9.8g (56mmol) of sodium 2-bromopropionate.

2-Cyanopropionic acid. 9.8g sodium 2-bromopropionate and 2.74g (56mmol) of sodium cyanide were dissolved in 13 ml of 0.5M NaOH/H_2O and the reaction stirred at 50°C for 2.5 hours. After cooling, the reaction mixture was acidified (pH 1.2) with 20% HCl. The product was extracted from the aqueous phase by washing three times with EtOAc. The organic extracts were combined and dried over $MgSO_4$, filtered, and rotovaped to yield 3.32g (34mmol) of a light yellow oil.

2-Cyanopropionyl-1-^{13}C-urea-$^{15}N_2$. 3.67g (61mmol) ^{13}C, $^{15}N_2$-urea, 5.72g (56mmol) acetic anhydride, and 3.32g of 2-cyanopropionic acid was stirred vigorously at 85°C (water bath) under an argon atmosphere for 1 hour. The reaction was rotovaped to a white solid and recrystallized from hot water.

[2-^{13}C-1, 3-$^{15}N_2$]-thymine. 0.50g of PtO_2 and 20ml of water were added to a vacuum tube and the mixture freeze-pump-thawed three times. After the last freezing step, the vessel was purged with N_2, followed by H_2. While stirring, the vessel was connected to H_2 gas, allowing the catalyst to be under an atmosphere of H_2 overnight. 1.50g (10.4mmol) of 2-cyanopropionylurea was dissolved in 20ml of hot glacial acetic acid and injected through a septum into the vacuum flask. After the mixture was stirred under a H_2 for 72 hours at 73°C (oil bath), the catalyst was filtered off, and the filtrate was rotovaped to a white solid. The product was recrystallized from water two times to yield 0.66g of pure white crystals. ^{1}H NMR in DMSO-d_6 indicated that the product was virtually pure thymine: δ 1.70 ppm (3H, s, CH_3), δ 7.25 ppm (1H, s, CH).

4.1.3 [2-^{13}C, 1, 3-$^{15}N_2$]- and [6,α_3-$^2H_4$]-thymidine. Methods to prepare labeled thymidine monomers enzymatically from thymine were adapted from the procedures of Krenitsky et al.[4, 5] Enzymatic transglycosylation of [6,α_3-$^2H_4$]-thymine (Cambridge Isotope Laboratories) and [2-^{13}C, 1,3-N_2]-thymine, using 2'-deoxyadenosine as the glycosyl donor, yielded [6,α_3-$^2H_4$]-thymidine, and [2-^{13}C, 1,3-N_2]-thymidine, respectively (Figure 4.3).

5.5g of 2'-deoxyadenosine and 1.0g of thymine were dissolved in 150ml 10mM K_2HPO_4 buffer (pH 9.5). The mixture was heated in a water bath until all solids remained fully dissolved. The solution was then titrated to pH 7.4 with 10mM KH_2PO_4 (pH 4.75). The reaction mixture was left to equilibrate overnight at 37°C in a shaker bath. 0.4ml of thymine phosphorylase (1500units) (Sigma) and 0.8ml of purine nucleoside phosphorylase (Sigma) (93units) were added and the mixture allowed to incubate for four to ten days at 37°C. The reaction progress was monitored by TLC (80% chloroform/20% CH_3OH). Upon completion, the solution was rotary evaporated to a white solid. The solid was dissolved in 200ml hot methanol and allowed to cool overnight at 4°C. The reaction mixture was filtered and the supernatent isolated. The remaining white solid was subjected to a second recrystallization from hot

methanol. The eluants from both recrystallizations (containing thymidine product, as well as thymine and 2'-deoxyadenosine starting material) were combined and purified via silica gel column chromatography. A 2" x 16" silica gel column (200-400 mesh, 60Å) was prepared and equilibrated with chloroform. The reaction mixture was loaded onto the silica gel as a slurry in chloroform and covered with a layer of sand. Thymine and thymidine were eluted with the following solvent gradient: 200ml 10% EtOH/90% $CHCl_3$, 800-1200ml 10% MeOH/90% $CHCl_3$. The final yield of thymidine was 0.412g (21% yield).

4.1.4 [2-^{13}C, 1, 3-$^{15}N_2$]-2'-deoxyuridine. The procedures of Bhat and Hubbard were modified by Jerome Shiels and applied to the synthesis of [2-$^{13}C_2$, 1,3-N_2]-deoxyuridine from [2-$^{13}C_2$, 1,3-N_2]-uracil by Henry Zebroski [6, 7]. Condensation of silated [2-^{13}C, 1,3-$^{15}N_2$]-uracil with 3',5'-ditoluyl chlorodeoxyribose, followed by crystallization and deprotection, resulted in the β-anomer of [2-^{13}C, 1,3-$^{15}N_2$]-uridine. The reaction scheme for the preparation of 2'-deoxyuridine is presented in Figure 4.4. [2-$^{13}C_2$, 1,3-N_2]-uracil was purchased from Cambridge Isotope Laboratories. 2-deoxy-D-erythro-pentose, 1,1,1,3,3,3-hexamethyldisilazane (HMDS), and trimethylsilyl chloride (TMS-Cl) were purchased from Aldrich Chemical Company.

Methyl 2-deoxy-3,5-di-O-p-toluoyl-D-erythro-pentoside. 13.6g (0.1mol) of 2-deoxy-D-erythro-pentose was added to 243 ml of methanol. 27ml of a 1% solution of HCl in methanol was added to the above solution and kept in a stoppered flask for 12-15 minutes. The reaction was stopped by adding 5g of silver carbonate with vigorous stirring. The reaction mixture was filtered and the clear solution was evaporated to a clear syrup under reduced pressure. Residual methanol was removed with repeated evaporations with small volumes of dry pyridine. The syrup was dissolved in 80ml of pyridine and cooled in an ice bath. To this solution was quickly added 34g (0.22mol) of p-toluoyl chloride, and the reaction stirred at 0°C for one hour. The reaction mix-

ture was gradually warmed to 40-50°C and stirred for 2-12 hours at room temperature. The mixture was poured into 300ml crushed ice with stirring. When the ice had melted, the product was extracted into three 150ml portions of ether. The combined ether extracts were successively washed with water, dilute sulfuric acid (1-5%), and aqueous sodium hydrogen carbonate. Evaporation of the extract under reduced pressure yielded a yellowish syrup.

2-Deoxy-3, 5-di-O-p-toluoyl-D-erythro-pentosyl chloride. The above syrup was dissolved in 40ml of glacial acetic acid, and to this solution was added 80ml of glacial acetic acid presaturated with dry HCl at 10°C. HCl is passed into the solution for 10 minutes, whereupon the chloride solidified to form a thick, crystalline mass. After 30 minutes, the crystals were filtered and washed with dry ether. The crystals (m.p. 109°C) were then suspended in dry ether, filtered off, and stored in a vacuum desiccator containing soda-lime and phosphorus pentaoxide to prevent anomerization of the α-chlorosugar.

3', 5' Ditoluyl-2-^{13}C-1, 3-$^{15}N_2$-2'-deoxyuridine. 1.0g of [2-^{13}C-1,3-N_2]-uracil and 35ml of HMDS/35 ml of TMS-Cl (1:1) were refluxed under an argon atmosphere overnight. The next day, the solution was homogenous, and ammonium chloride had condensed on the condenser. Excess HMDS/TMS-Cl. HMDS/TMS-Cl were either removed by distillation in vacuo directly from the reaction vessel or evaporated under aspirator pressure and reduced heat. Both methods yielded a yellowish oil. 7ml of dry chloroform was added via a dry syringe, and the solution was pulled into the syringe. This was then added to a fresh solution of 3.1g 2-deoxy-3,5-di-O-p-toluoyl-D-erythro-pentosyl chloride in 40ml dry chloroform. The mixture remained homogenous (indicating that no water was present) and stirred 3 hours or overnight. The mixture was rotovaped down to a white/yellow foam , dissolved in boiling ethanol, and cooled slowly. White crystals were filtered off yielding 1.82g of the pure β anomer.

[2-^{13}C-1, 3-$^{15}N_2$]-2'-deoxyuridine. 1.82g of 3',5' ditoluyl-2-^{13}C-1,3-$^{15}N_2$-uridine was refluxed with 200mg of MeONa and 75ml of MeOH. Completion (3-14 hours) was monitored by TLC (90% chloroform/10% methanol). Recrystallization from EtOAc and a small amount of methanol afforded 0.682g (2.8mmol, 31% yield) of [2-^{13}C-1,3-$^{15}N_2$]-deoxyuridine.

4.1.5 [2,2'-$^{13}C_2$]-, [2, 1'-$^{13}C_2$]-,[2,2',5'-$^{13}C_3$]-, [2, 1',3'-$^{13}C_3$]-cytidine. Cytidine nucleosides with specific ^{13}C enrichment at C2, C1', C2', C3', and C5' were prepared by Henry Zebroski in five steps using the methods compiled by Kline and Serianni without further modification (Figure 4.5) [8]. The syntheses of [2, 2'-$^{13}C_2$], [2, 1'-$^{13}C_2$], [2, 2', 5'-$^{13}C_3$], and [2, 1', 3'-$^{13}C_3$] cytidine were achieved using the identical procedure but with different combinations of D-[^{13}C] ribose and [2-^{13}C] cytosine. D-[2, 5-$^{13}C_2$], D-[1, 3-$^{13}C_2$], D-[2-^{13}C], and D-[1-^{13}C] ribose (Omicron Biochemicals) was converted into a mixture of methyl-α and β-D-ribofuranosides as described by Barker and Fletcher [9]. The methyl-β-D-^{13}C labeled ribofuranoside anomer was converted to 1-O-acetyl-O-benzoyl-β-D-^{13}C labeled ribofuranoside (ABR) utilizing the techniques of Recondo and Rinderknecht [10]. N4 protected acetyl cytosine was prepared from [2-^{13}C] cytosine (Isotec) using the procedure of Codington and Fox [11]. Silyation of the N4 protected acetyl [2-^{13}C] cytosine base with hexamethyldisilazane, condensation with ^{13}C labeled ABR, and removal of the acyl protecting groups with methanolic ammonia was accomplished using the methods of Vorbrüggen with some modifications to yield the desired β-cytidine anomer [12].

4.1.6 4-(1,2,4-Triazol-1-yl)-2'-deoxythymidine (2'-deoxyuridine)-5'-O-(dimethoxytrityl)-3'-O-(N,N-diisopropyl)-β-cyanoethylphosphoramidite. 4-Triazole-2'-deoxynucleoside-3'-CED phosphoramidite derivatives were prepared following procedures of Cowart et al. and incorporated into a DNA oligonucleotide via standard solid-state DNA synthesis [13]. The same procedure worked equally well for the

preparation of the 2'-deoxyuridine-4-triazole derivative. Treatment of the protected DNA oligomer in concentrated ammonia resulted in conversion of the 4-triazole derivative to the 5-methylcytidine (or cytidine) nucleotide. The reaction scheme is presented in Figure 4.6. 1,2,4-Triazole, $POCl_3$, and triethylamine (TEA) were purchased from Aldrich Chemical Company. Anhydrous acetonitrile was purchased from Biogenex. TEA was distilled from ninhydrin prior to use. All reactions were conducted under an argon atmosphere, ensuring strictly anhydrous conditions at all times.

537 mg (0.75 mmol) of protected thymidine (or uridine) phosphoramidite and 1.164 g (17 mmol) of 1,2,4,-triazole were dried overnight under reduced pressure (vacuum pump). 2.4 ml of triethylamine and 7.5 ml of acetonitrile were added and the reaction vessel chilled on ice. 138 μL (1.5 mmol) $POCl_3$ was added dropwise and the reaction stirred at room temperature for 7h (or overnight) producing a thick bright yellow broth. The conversion was monitored by TLC (r_f = 0.62, 0.69, diastereomeric mixture) on silica gel (45% dichloromethane, 45% ethyl acetate, 10% triethylamine), absorbance measurement (λ_{max} 267 nm → λ_{max} 328 nm), and ^{1}H NMR. The product appeared as an bright blue spot on TLC under short-wave UV light. The 2'-deoxyuridine derivative appeared as a dark purple spot under short-wave UV light. The reaction mixture was poured into 150 ml of ethyl acetate and 30 ml of triethylamine and washed with 5% aqueous sodium carbonate (2 x 150 ml). The organic phase was separated, dried over Na_2SO_4, and concentrated in vacuo to a light yellow syrup. The product was chromatographed on a silica gel column (2.5 cm x 15 cm) with 45% dichloromethane, 45% ethyl acetate, 10% triethylamine yielding a colorless glass. The product was azeotroped three times from anhydrous acetonitrile prior to DNA synthesis resulting in 0.418 g (70 % yield) of pure 4-(1,2,4-triazol-1-yl)-5-methyl-5'-O-(dimethoxytrityl)-2'-deoxythymidine-3'-O-(N,N-diisopropyl)-β-cyanoethylphosphoramidite. ^{1}H 200 MHz ($CDCl_3$), characteristic resonances are at δ 9.22 (s, 1H), 8.34 (d, 2H, J=14 Hz), 9.02 (s, 1H), 7.1-7.4 (m, 9H), 6.78 (m, 4H), 6.29 (q,

1H, J=6 Hz), 2,58 (t, 1H, J=5 Hz), 2.39 (t, 1H, J = 5 Hz), 1.85 (d, 3H, J = 3 Hz), and 1.42 (m, J=12 Hz). ^{31}P 200 MHz (CH_3CN), δ 148.45 (relative to H_3PO_4).

4.2 Biosynthesis of Uniformly ^{13}C, ^{15}N Labeled Nucleosides

Preparation of uniformly ^{13}C, ^{15}N labeled ribonucleosides was accomplished using the protocols developed by Batey et al. [14] E.coli bacteria were grown in isotopically enriched minimal growth media, their nucleic acids harvested, RNA and DNA separated and enzymatically degraded to deoxynucleosides and nucleosides, and purified by reverse-phase HPLC. A flow-chart outlining the steps described below appears in Figure 4.7. The following section describes procedures and quantities based on a 1L cell culture. This procedure was repeated numerous times to yield sufficient quantities for solid-state NMR work (5-38mg). 98% ^{13}C-glucose and 98% ^{15}N-ammonium sulfate was purchased from Isotec. Nuclease P1, RNase-free DNase I, and calf intestinal phosphatase (CIP) were purchased from Boehringer Mannheim. Lysozyme chloride was purchased from Sigma. Affi-gel 601 boronate-derivatized polyacrylamide gel affinity resin was purchased from Bio-Rad. DEAE Sephadex ion-exchange resin was purchased from Pharmacia. Dialysis tubing (1500 MW cutoff) was purchased from Spectrum. Nanopure H_2O (nH_2O) water was used in all procedures. All glassware, pipette tips, and polyethylene bottles were autoclaved for 30 minutes prior to use. Basic biochemical techniques and standard abbreviations can be found in the text, *Molecular Cloning: A Laboratory Manual* [15].

Reverse phase HPLC was used to monitor hydrolysis of DNA and RNA during the P1 Nuclease digestion, nucleotide dephosphorylation by calf intestinal phosphatase, and for collection of nucleosides. HPLC analysis was performed using a 7.8 x 300mm Waters C-18 Delta Pak semi-preparative column with a flow rate of 4ml/minute and detection at 260nm using a step-wise linear gradient with (A) 10mM ammonium acetate (pH 6.0 with glacial acetic acid) and (B) 60% acetonitrile/H_2O.

The retention times for each of the nucleoside monomers (in minutes) is rC (4), rU (6), rG (12.5), rA (21), dC (5.5), dT (16), dG (14), dA (21).

4.2.1 Cell growth. Uniformly labeled ^{13}C and ^{15}N nucleic acids were grown on a minimal salts media containing (per liter): KH_2PO_4 (13.6g), $MgSO_4 \cdot H_2O$ (0.25g), $CaCl_2 \cdot 2H_2O$ (15mg), Na_2EDTA (30mg), $FeCl_3 \cdot 6H_2O$ (25mg), $CuSO_4 \cdot 5H_2O$ (240μg), $MnSO_4 \cdot 5H_2O$ (180μg), ZnSO4 $\cdot 7H_2O$ (27μg), $CoCl_2 \cdot 6H_2O$ (27μg). 975ml KH_2PO_4 (pH 7.0 with KOH) was prepared in a 4L culture flask and autoclaved. All other salts were added as filter sterilized solutions to the cooled KH_2PO_4 solution just prior to use. $(^{15}NH_4)_2SO_4$ (0.5g) and $^{13}C_6$-glucose (1.0g) were dissolved in 5ml nH_2O, filter-sterilized, and added to the minimal media solution. 5ml of centrifuged LB media (500 ml, 5g Bacto-tryptone, 2.5g Bacto-Yeast extract, 5g NaCl, pH 7 with NaOH) were inoculated with single colonies of E. coli [strain BL21(DE3)] and incubated 12-14 hours at 37°C with vigorous shaking (300 rpm). Minimal media was inoculated with 5ml overnight (O/N) E.coli culture and incubated 14-15 hours at 37°C with vigorous shaking. Cells were harvested by centrifugation at 4500 rpm in GS3 rotor for 30 minutes. Each liter culture yielded approximately 2.5-3.5g of wet packed cells.

4.2.2 Lysis. Wet packed cells were resuspended in 30ml of lysozyme buffer (250mM Tris·Cl (pH 8.0), 100mM NaCl, 50mM Na_3EDTA). 2.5mg lysozyme chloride was added per 1g wet packed cells and incubated on ice for 20 minutes. Dissolved cells were lysed with four to five 30 second pulses, monitoring A_{260}, A_{280}, and A_{600} readings after each sonication cycle using a Heat Systems Ultrasonic Processor (Model W-225). An alternative lysis method was implemented in later preparations. Approximately 3g of wet packed cells were suspended in an equal volume of STE buffer (0.1M NaCl, 10mM Tris·Cl (pH, 8.0), 1mM EDTA (pH 8.0)). The resuspended cells were added to a mixture of 90ml STE buffer and 5ml 10% SDS at 37°C for 10 minutes with vigorous shaking.

4.2.3. Nucleic Acid Extraction. Lysed cells were transferred to a 250ml centrifuge bottle. For a 30ml solution, 30ml equilibrated phenol (preheated to 65°C) and 30ml chloroform/isoamyl alcohol (24:1) solution were added, stirred at 65°C for 30 minutes, and centrifuged in a GSA rotor for 10 minutes at 8K. Phenol containing 0.1% 8-hydroxyquinoline (w/v) was equilibrated against STE buffer to a pH > 7.8. The top layer (aqueous phase) was removed (taking care not to disrupt the protein layer), transferred to a 250ml centrifuge bottle, and stored at 4°C. 30ml STE buffer was added to the organic phase, vortexed briefly to resuspend the white protein layer, and emulsified for two minutes in a Waring blender. The mixture was then centrifuged as described above, and the aqueous layer was added to the initial pool. Another 30 ml volume of STE buffer was added to the organic phase, vortexed briefly, emulsified for 2 minutes, and centrifuged. The pooled aqueous layers were partitioned between two 250ml centrifuge bottles and combined with an equal volume of chloroform/isoamyl alcohol. The solution was vortexed one minute and centrifuged at 8K for 20 minutes. The top layer was removed and transferred to a 500 ml centrifuge bottle.

4.2.4 Isopropanol Precipitation. 1/10 volume of 3M NaOAc (pH 5.2) and one volume isopropyl alcohol were added to the aqueous extract and stored at -20°C O/N. After centrifuging the solution in a GS3 rotor at 6K for 30 minutes, the white nucleic acid (NA) pellets were air dried to evaporate any residual solvent. NA pellets were stored at -20°C until ready for the next step. The NA pellets were dissolved in nH_2O and transferred to dialysis tubing (1500 MW cutoff). NA's were dialyzed against H_2O for 2-3 days to eliminate excess EDTA and other impurities that were found to inhibit later enzyme digests. Following dialysis, NA's were lyophilized to dryness and stored at -20°C. Nucleic acids were resuspended in TE buffer (10mM Tris·Cl (pH 8.0), 1mM EDTA). A 1L cell preparation yielded approximately 2000-3000 A_{260} units of nucleic acids.

4.2.5 Nucleic Acid Hydrolysis. Total nucleic acids were degraded to monophosphates by the enzymes DNase I and nuclease P1 using the procedure outlined by Zimmer et al.[16] The purified NA's (1200 A_{260} units in 25ml TE buffer) were brought to 10mM $MgCl_2$. 100 units of DNase I were added and the reaction mixture incubated for 1 hour at 37°C. The solution was denatured in a boiling water bath for 10 minutes and cooled in ice for 10 minutes. The solution was then brought to 50mM NaOAc (pH 5.2) and 0.1mM $ZnCl_2$. 6 units P1 Nuclease were added and the reaction mixture incubated at 55°C for 1 hour. The nucleic acids were denatured a second time, another 6 units of P1 Nuclease added, and the solution incubated at 55°C for an additional hour. Reaction progress was monitored by HPLC using 20μg injections (1 A_{260} unit ≈ 40μg ss DNA/RNA). After the second reaction, the enzymes were heat inactivated at 85°C for 2 minutes. The reaction mixture was then lyophilized to dryness.

4.2.6 DEAE chromatography. Nucleotides were exchanged into 1M trietylammonium bicarbonate (TEABC) at pH 9.5 by loading total NMP's onto a 8cm x 2.5cm DEAE-Sephadex G25 column (bicarbonate form) [16]. To prepare the ion-exchange column, 7g of DEAE Sephadex resin was hydrated in with 200ml of 0.2M NaCl for 10-15 minutes. The solution was decanted, and 200 ml of resin buffer (1000ml, 10mM KH_2PO_4, 1mM Na_3EDTA, pH 8.0) were added. The resin was swelled for one day at room temperature. The resin buffer was decanted and 200ml cold 1M TEABC (pH 9.5) were added and the slurry equilibrated to 4°C. 1M TEABC, pH 9.5, was prepared by bubbling CO_2 through 141ml triethylamine in 700ml H_2O (while submersed in an ice bath) until the pH drops to 9.5. The total volume of the solution was brought to 1L. TEABC was decanted, an equal volume fresh TEABC was added, and the resin poured into a 2.5cm x 20cm glass column. The resin was rinsed with one column volume of TEABC until the flow-though was pH 9.5. The total nucleotide monophosphates (NMP's) were resuspended in 10ml 1M TEABC. The NA's were

loaded onto the equilibrated DEAE column and eluted with 1M TEABC (pH 9.5), collecting 5ml fractions until the A_{260} readings fell to 0.2 or below. The nucleotide fractions were pooled and loaded directly onto a cis-boronate affinity column. In later procedures, it was determined that the DEAE column was probably not necessary. The total nucleotide pool (after PI Nuclease digestion) could be dissolved in 10 ml 1M TEABC (pH 9.5) and loaded directly onto the cis-boronate affinity column.

4.2.7 Boronate affinity chromatography. The deoxyribonucleotides (dMP's), salts, and other impurities were separated from the ribonucleotides (rMP's) using cis-boronate affinity chromatography. Boronates form covalent complexes with 1,2 cis-diols at high pH that are readily hydrolyzed at low pH. Binding of rMP's requires high ionic strength, high pH (>9.0), and low temperatures (~4°C). The dMP's were collected as flow-through, and the rMP's eluted from the column with CO_2-acidified water (pH 4-5). To prepare the boronate affinity column, 10 g of resin was hydrated in 200 ml TE buffer (10 mM Tris HCl, pH 8.0, 1 mM EDTA, pH 8.0) overnight at room temperature. The buffer was decanted and 200 ml TE buffer were added to the resin. The resin was equilibrated to 4°C and poured into a 2.5cm x 20cm glass column and rinsed with three column volumes of 1M TEABC (pH 9.5). The pH of the flow through was checked prior to use. The total NMP pool was dissolved in 10ml 1M TEABC and loaded onto the column. The column was rinsed with 1M TEABC, while collecting 5ml fractions containing the dMP's, until the A_{260} readings of the eluant dropped below 0.1. The rMP's were eluted by washing the column with acidified H_2O (pH 4-5), while continuing to collect 5ml fractions. The acidified water was prepared by bubbling CO_2 through H_2O (while submersed in an ice bath) until the pH drops to 4-5. The resin volume changes drastically with this change in pH. Elution of rMP's was continued until the A_{260} reading fell to below 0.1. The fractions containing dMP's and rMP's were each pooled, rotary evaporated to dryness, and pumped O/N under reduced pressure.

4.2.8 Enzymatic Dephosphorylation. The rMP and dMP fractions were each converted individually into nucleosides by enzymatic dephosphorylation with calf intestinal phosphatase (CIP). Each fraction was resuspended in 2ml H_2O and 1/10 volume of CIP buffer (500mM Tris·Cl, pH 8.5, 1mM EDTA, pH 8.5). 2 units CIP/25μg nucleotide were added and the reaction mixture incubated 30 minutes at 37°C, followed by another 2 units and continued incubation for 30 minutes. Dephosphorylation was monitored by HPLC (20μg injections). Because the dMP fraction may contain salts (such as excess EDTA) and impurities after the boronate column separation, the dephosphorylation reaction may become inhibited. Addition of $MgCl_2$ to the reaction will chelate excess EDTA. This problem does not exist for the rMP fraction.

4.2.9 Reverse-Phase HPLC. Digested nucleosides were separated by reverse-phase HPLC, concentrated by rotary evaporation and lyophilized repeatedly to remove trace amounts of residual volatile HPLC salts. Isotopic enrichment (>95%) and chemical purity were verified by ^{1}H, ^{13}C, and ^{15}N solution-state NMR. Representative solution-state ^{13}C spectra for each of the ribonucleoside monomers are presented in Figures 4.8 and 4.9.

4.3 Preparation of Phosphoramidite Derivatives

5'-(dimethoxytrityl)-)-3'-O-(N,N-diisopropyl)-β-cyanoethyl-2'-deoxynucleoside phosphoramidite derivatives were prepared from 2'-deoxythymidine, 2'-deoxyuridine, and u-^{13}C,^{15}N-2'-deoxycytidine using the procedures compiled in *Oligonucleotide Synthesis*, edited by M.J. Gait [17]. The only modification to the procedure was the use of 2-cyanoethyl-N,N-diisopropylchlorophosphoramidite as the phosphitylating agent. Synthetic protocols for the preparation of phosphoramidite derivatives have also been described thoroughly in the Ph.D. dissertation by Mary Hatcher [18]. The [5'/5"-$^{2}H_{1:1}$]-5'-O-(dimethoxytrityl)-2'-deoxythymidine-3'-CED

phosphoramidite was prepared by Dr. John Orban as described previously [19]. Purity of phosphoramidite derivatives was determined by ^{1}H and ^{31}P NMR (δ 148 ppm (d) ($CHCl_3$) relative to 5% phosphoric acid) prior to DNA synthesis. 5'-O-(dimethoxytrityl)-5-fluoro-2'-deoxyuridine-3'-[(2-cyanoethyl)-(N,N-diisopropyl)]-phosphoramidite and O4-(2,4,6-trimethylphenyl)-5'-O-(dimethoxytrityl)-5-fluoro-2'-deoxyuridine-3'-[(2-cyanoethyl)-(N,N-diisopropyl)]-phosphoramidite derivatives were purchased from Glen Research and incorporated into DNA oligonucleotides without further purification.

4.4 Preparation and Purification of Synthetic DNA Oligonucleotides

Phosphoramidite derivatives were incorporated at specific positions in the DNA oligonucleotide via standard solid-state DNA synthesis using a Model 394 DNA/RNA synthesizer (Applied Biosystems). All DNA samples used in this study were of the following sequence: $[d(CGCGAATTCGCG)]_2$. Generally, two to four 10μmol syntheses were pooled to provide enough material for a single solid-state NMR sample (~40-100mg). Each 10μmol DNA synthesis was deprotected by incubation at 55°C in concentrated ammonia for 2-4 days. Purification was performed on 10 μmole batches by ethanol precipitation (2x), (1ml H_2O, 100μl 0.5M NaCl, 3ml EtOH), followed by G-25 Sephadex (Pharmacia, Inc.) gel-exclusion chromatography. Fractions with positive A_{260} readings were collected and analyzed for failure sequences via denaturing polyacrylamide gel electrophoresis (20% polyacrylamide, 7M urea). A final desalting step was performed on the pure DNA by G-10 Sephadex (Pharmacia, Inc.) column chromatography. Purity of synthetic DNA oligonucleotides was assayed by one- and two-dimensional ^{1}H NMR. The oligonucleotides were salted with 10% NaCl (w/w).

Deuterated DNA samples were lyophilized three times from deuterium depleted water and packed into a 5 mm solid-state Kel-F NMR sample holder. The ab-

sorption of water was accomplished by equilibration of the DNA samples for 3-4 weeks in saturated salt solutions (containing deuterium depleted water) for specific hydration ranges [20]. The water content was monitored gravimetrically to determine values for W (moles of water/moles of nucleotide). The carbon labeled DNA samples were lyophilized and packed into a 5 mm solid-state Kel-F NMR sample rotor. The fluorine labeled DNA samples were lyophilized and packed in a 5mm solid-state Vespel NMR sample rotor. The absorption of water for carbon and fluorine labeled DNA samples was accomplished as outlined above using saturated salt solutions containing nanopure water. The following DNA oligonucleotides were synthesized for this investigation:

5-Methyl-dC9-[5'/5"-^{2}H]-[d(CGCGAATTC*GCG)]$_2$. [5'/5"-^{2}H]-4-(1,2,4-triazol-1-yl) -2'-deoxythymidine-5'-O-(dimethoxytrityl)-3'-O-β-CED-phosphoramidite was incorporated into DNA at the dC9 position.

5-Methyl-dC9-[2"-^{2}H]-[d(CGCGAATTC*GCG)]$_2$. [2"-^{2}H]-4-(1,2,4-triazol-1-yl)-2'-deoxythymidine-5'-O-(dimethoxytrityl)-3'-O-β-CED-phosphoramidite was incorporated into DNA at the dC9 position.

5-Methyl-dC9-[6,α_3-^{2}H$_4$]-[d(CGCGAATTC*GCG)]$_2$. [6,α_3-^{2}H$_4$]-4-(1,2,4-triazol-1-yl)-2'-deoxythymidine-5'-O-(dimethoxytrityl)-3'-O-β-CED-phosphoramidite was incorporated into DNA at the dC9 position.

5-Fluoro-dT8-[d(CGCGAATT*CGCG)]$_2$. 5-fluoro-5'-(dimethoxytrityl)-2'-deoxyuridine-3'-CED phosphoramidite was incorporated into DNA at the dT8 position.

5-Fluoro-dT8, 5-Fluoro-dC9-[d(CGCGAATT*C*GCG)]$_2$. The doubly fluorinated DNA oligonucleotide was synthesized by introducing 5-fluoro-5'-(dimethoxytrityl)-2'-

deoxyuridine-3'-CED phosphoramidite at the dT8 position and 4-TMP-5'-(dimethoxytrityl)-2'-deoxyuridine-3'-CED phosphoramidite at the dC9 position.

[2-^{13}C]-T8, [2-^{13}C]-5-Methyl-C9-[d(CGCGAATT*C*GCG)]$_2$. [2-^{13}C-1,3-$^{15}N_2$]-4-(1,2,4-triazol-1-yl)-2'-deoxythymidine-5'-O-(dimethoxytrityl)-3'-O-β-CED-phosphoramidite was incorporated at the dC9 position, and [2-^{13}C-1,3-$^{15}N_2$]-2'-deoxythymidine-5'-O-(dimethoxytrityl)-3'-O-β-CED-phosphoramidite was incorporated at the dT8 position.

[2-^{13}C]-T8, [2-^{13}C]-C9-[d(CGCGAATT*C*GCG)]$_2$. [2-^{13}C-1,3-$^{15}N_2$]-4-(1,2,4-triazol-1-yl)-2'-deoxuridine-5'-O-dimethoxytrityl-3'O-β-CED-phosphoramidite was incorporated at the dC9 position, and [2-^{13}C-1,3-$^{15}N_2$]-2'-deoxythymidine-5'-O-dimethoxytrityl-3'O-β-CED-phosphoramidite was incorporated at the dT8 position.

[u-^{13}C,^{15}N]-C9-[d(CGCGAATTC*GCG)]$_2$. Uniformly ^{13}C,^{15}N labeled 2'-deoxycytidine-5'-O-dimethoxytrityl-3'O-β-CED-phosphoramidite was incorporated at the dC9 position. The phosphoramidite was cut with 80% unlabeled 2'-deoxycytidine phosphoramidite in order to have sufficient material for DNA synthesis.

4.5 Nucleoside Crystallization

Nucleosides were studied either as amorphous lyophilized powders or crystallized in known conformations based on previous X-ray crystallographic studies. Uridine (5mg ^{13}C,^{15}N labeled/ 40mg unlabeled) was crystallized via slow room temperature evaporation from ethanol (25ml) which was maintained at 37°C for 7 days in the form of colorless plates [21]. Cytidine (23mg ^{13}C,^{15}N labeled/40 mg unlabeled) was crystallized via slow room temperature evaporation from a 50/50 mixture of EtOH/water [22]. Adenosine (30mg ^{13}C, ^{15}N labeled/30mg unlabeled) was crystal-

lized by slow room temperature evaporation from an aqueous solution (5ml) in the form of long, colorless needles [23]. Guanosine (38mg $^{13}C,^{15}N$ labeled/40mg unlabeled) was dissolved in hot water and crystallized by slow evaporation at 70°C [24, 25]. Guanosine dihydrate was prepared by hydration of the crystalline material in a chamber containing a saturated solution of CH_3COOK (20% relative humidity). 2'-Deoxyadenosine monohydrate, 2'-deoxycytidine-5'-monophosphate monohydrate, 2'-deoxycytidine hydrochloride, and thymidine were crystallized according to previously published literature procedures [26-29].

4.6 X-Ray Crystallography

Single crystal x-ray diffraction studies were conducted on a portion of the polycrystalline NMR samples for adenosine, cytidine, and uridine to confirm the unit cell dimensions and structure of each nucleoside in the crystalline state. The unit cell dimensions and structures for each monomer were in close agreement with those reported in the previously published crystal structures. Data collection was performed using an Enraf-Nonius KappaCCD x-ray diffractometer. Intensities were measured using Mo Kα radiation (λ=0.7107 Å) at 161 K by rotation about the φ axis in 1° increments over 90° with 15 seconds per frame for uridine and over 180° with 30 seconds per frame for adenosine. Data reduction and calculations were performed on a Silicon Graphics workstation using the maXus software package (MacScience, Japan).

4.6.1 Adenosine. A crystalline needle of dimensions 0.29 x 0.03 x 0.03 mm was used in this study. The three dimensional crystal structure of adenosine was determined from the intensities of 647 reflections. The crystal was monoclinic with space group $P2_1$ with two molecules per unit cell (Z=2). The unit cell dimensions were determined from least squares fit to 100 reflections with a=4.784 Å, b=10.217 Å,

c=11.691 Å, β=99.602°. Least-squares refinement of coordinates and anisotropic thermal factors yielded an R factor of 0.049. The conformation of the ribose ring was C3'-endo, the torsion angle about the glycosidic bond was anti, and the conformation about the C4'-C5' bond was gauche-gauche.

4.6.2 Uridine. A 0.16 x 0.09 x 0.08 mm crystalline platelet was found to be monoclinic with space group P_{21} and two molecules (A and B) per unit cell (Z=4). The three dimensional crystal structure of uridine was determined from the intensities of 2784 reflections. The unit cell dimensions were determined from least squares fit to 148 reflections with a=4.925 Å, b=14.723 Å, c=13.885 Å, β=95.706°. Least-squares refinement of coordinates and anisotropic thermal factors yielded an R factor of 0.047. The conformations of the two independent molecules were shown to have very similar conformations. The ribose rings were both puckered with C3'-endo, and the conformations about the glycosidic bond were both anti. The conformation about the C4'-C5' bond was gauche-gauche for both molecules in the asymmetric unit cell.

4.6.3 [2,1'-$^{13}C_2$]-Cytidine. The unit cell dimensions were determined for [2,1'-$^{13}C_2$]-cytidine and were found to be in agreement with those from the previously published crystal structure by Furberg and coworkers [30]. The crystal was orthorhombic with space group $P2_12_12_1$ and contained four molecules per unit cell (Z=4) and unit cell dimensions a=13.93, b=14.75, c=5.10 Å. Due to the small size of the crystal, the full structure was not solved for this sample. However, Furberg et al. report that the C3' is displaced from the plane of the ribose ring by 0.5Å (C3'-endo). The relative orientations of the pyrimidine and ribose correspond to an anti conformation of the nucleoside. The crystal structure also indicates the presence of a weak intramolecular C-H O interaction between C6 and O5', which are separated by a distance of only 3.24 Å. The authors also report the presence of a weak intermolecular C-H···O interaction between C5 and O5' of a neighboring molecule (3.35Å).

4.7 Solution-State NMR Spectroscopy

One-dimensional ^{1}H, ^{31}P, ^{19}F, ^{15}N, and ^{13}C NMR spectra were collected on either a Bruker AC-200 or WM500 NMR spectrometer. Two-dimensional ^{1}H NOESY experiments were conducted on a Bruker AM-500 spectrometer and all data processed off-line using the FELIX (version 2.10) software from Biosym Technologies, Inc. Phase-sensitive two-dimensional NOESY spectra were collected at a sample temperature of 300 K. The data sets were collected in TPPI mode with 2048 complex data points in t_2, 800 data points in t_1, 32 scans per t_1 increment, and a sweep width of 6000 Hz. The carrier frequency was placed on the residual HDO resonance. Proton chemical shifts were referenced relative to the residual HDO solvent peak (4.6 ppm). NOESY spectra were collected at a mixing time of 150 ms with a 2.5 s relaxation delay. The NOESY data sets were baseline corrected and apodized with a sine-squared 90° phase-shifted function to 400 points in t_2 and 800 points in t_1.

4.8 Solid-State NMR Spectroscopy

This dissertation includes solid-state NMR data for a variety of different nuclei (^{13}C, ^{15}N, ^{19}F, and ^{2}H) resulting from the application of several different r.f. pulse sequences. Each NMR experiment is designed to probe a unique feature of nucleic acid structure or dynamics. Certain experiments, such as CP-MAS and two-dimensional dipolar recoupling methods, are most suited for examining the chemical shift interaction. One-dimensional dipolar recoupling experiments, such as DRAWS, are useful for measuring internuclear distances between spin-1/2 nuclei. The modulation of molecular dynamics and relaxation in spin $\geq$ 1 systems can be monitored over a wide range of time scales by application of quadrupolar echo and inversion recovery experiments.

4.8.1 Solid-State ^{13}C NMR Spectroscopy. Solid-state ^{13}C NMR experiments were performed on home-built NMR spectrometers operating at ^{13}C Larmor frequencies of 100.6 MHz and 125.75 MHz. To obtain ^{13}C data at 125.75 MHz, a Doty Scientific double channel (^{13}C-^{1}H) probe equipped with a 5mm spinner assembly was used. Spin rate was regulated to ± 5Hz with a home-built spin rate controller. To obtain ^{13}C data at 100.6 MHz, a Doty Scientific triple channel (^{1}H-^{15}N-X) probe equipped with a 5mm spinner assembly was used. In all experiments, proton irradiation frequencies were 50 kHz during cross-polarization and were raised to 90-120 kHz during decoupling. Cross-polarization contact times were 2ms.

4.8.1.1 One-Dimensional DRAWS Experiments. For experiments utilizing DRAWS in the mixing period, ^{13}C rf power levels were matched to the $t_r = 17\pi/2$ condition during DRAWS mixing. A standard tune-up procedure was used to minimize pulse imperfections [31]. In general, 1D-DRAWS data was collected at a spinning speed of 4901 Hz with a ^{13}C power level of 41.6kHz. Relaxation delays were 7s and 15s for lyophilized and crystalline material, respectively. For 1D-DRAWS experiments, normalized signal intensity is plotted as a function of the numbers of repetitions of the DRAWS mixing period. Each point in a DRAWS decay curve is obtained by integration over all peaks (i.e., fundamentals and sidebands). For measurements where error estimates are reported, the DRAWS experiment was performed 4-5 times.

4.8.1.2 DRAWS Control Experiment. A control experiment was also conducted to measure contributions to the DRAWS magnetization exchange curve other than the dipolar coupling between the two labeled nuclei. These contributions include 1) coupling to naturally abundant ^{13}C nuclei in the vicinity of the isotopically enriched spin pair, 2) incomplete suppression of the chemical shift, 3) incomplete proton decoupling, and 4) transverse relaxation effects which are present independent of the

DRAWS pulse sequence [32]. A phenomenological damping rate was derived from simulation of the control experiment by varying the $\left(T_2^{SQ}\right)^{-1}$ parameter in the DRAWS simulation program. There are two possible methods for conducting a DRAWS control experiment. One option is to perform the DRAWS experiment on a singly labeled sample. This approach was used to determine the single quantum damping rate for the fluorinated dU8-dC9 DNA oligonucleotide. However, this method is not always possible due to unavailability of the singly labeled sample. Another option is to perform the control experiment on the doubly labeled sample of interest. For resolved chemical shifts, the control experiment can be conducted by first preparing an initial state, $\rho(0) = I_y - S_y$ using the TOSS-τ-deTOSS pulse sequence [33]. The standard DRAWS experiment is then performed on the sample, with only this modification in the initial state of the system. It was shown previously that both the I_y+S_y and $I_y - S_y$ experiments produced comparable decay curves, suggesting that the TOSS-τ-deTOSS method is a valid control experiment [32]. This strategy was used in measuring ^{13}C distances in the doubly labeled cytidine monomer samples.

4.8.1.3 Natural Abundance Background. Data from selectively labeled ^{13}C samples also need to be corrected for the presence of naturally abundant ^{13}C nuclei to suppress the effect of intermolecular couplings. ^{13}C is 1.1% naturally abundant. The monomer samples were diluted to 10% with unlabeled material, so approximately 10% of the signal was due to spins at natural abundance. The presence of this background signal exhibits itself in the decay curve as a "pedestal effect", in which the normalized signal intensity does not drop below 0.10. To compensate for the presence of these naturally abundant ^{13}C nuclei, a correction to the observed signal intensity must be included. The following formula was used to correct for this effect,

$$P = \frac{R - b \cdot U}{1 - b} \qquad [4.1]$$

where, P is the processed data, R is the normalized data from the labeled sample, U is the normalized data from the control experiment, and b is the fraction of signal which is due to spins at natural abundance.

4.8.2 Two-Dimensional Chemical Shift Correlation Experiments. For experiments utilizing DRAWS in the mixing period, ^{13}C r.f. power levels were matched to the $t_r = 17\pi/2$ condition during DRAWS mixing. A standard tune-up procedure was used to minimize pulse imperfections [31] In general, 2D-DRAWS data was collected at a spinning speed of 4901 Hz with a ^{13}C power level of 41.6kHz. Relaxation delays were 7s and 15s for lyophilized and crystalline material, respectively. 64 scans and 256 complex t_1 increments were collected for each 2-D DRAWS spectrum. One DRAWS supercycle (n=1; 0.832 ms) during the mixing period assured that coherence transfer would occur between carbons within one or two bond lengths. Two and three cycles of DRAWS were also implemented to illustrate the presence of coherence transfer pathways arising from indirect relay effects. Phase-sensitive two-dimensional RFDR spectra were also acquired for each ribonucleoside monomer using one cycle of RFDR (n=1: 1.32ms) in the mixing period. All 2D data sets were processed in hypercomplex mode using the FELIX NMR processing software program (BIOSYM Technologies) [34]. RFDR and DRAWS data sets were zero-filled to 1024 points in both dimensions. The t_2 dimension was apodized with a 90° phase-shifted sine squared window function. The t_1 dimension was apodized with either a 90° phase-shifted sine squared or kaiser window function. All shifts were referenced to an external CCl_4 standard (96.5 ppm relative to TMS). Carbon-13 assignments were made by 1-D and 2-D solution-state NMR and verified by two-dimensional solid-state NMR.

4.8.3 Two-Dimensional DQ-DRAWS Experiments. Two-dimensional DQ-DRAWS data were collected at a ^{13}C frequency of 100.6 MHz at a spinning speed of 4525 Hz or 4901 Hz with a ^{13}C power level of 38.5 kHz or 41.7 kHz, respectively.

Slow-spinning spectra were also acquired at a spinning speed of 2525 Hz, using a ^{13}C power level of 38.5 kHz and doubling the number of 360° pulses per rotor period. Relaxation delays of 7s and 15s were applied to lyophilized and crystalline material, respectively. 64-128 scans and 160 complex t_1 increments were collected for each spectrum, unless stated otherwise. One DRAWS supercycle during the mixing period was implemented for all uniformly ^{13}C,^{15}N labeled monomers. Phase cycling was used to eliminate signal which did not pass through a double quantum state during the evolution period [35]. DQ-DRAWS data sets were processed in hypercomplex mode using the FELIX NMR processing software program (BIOSYM Technologies). Both dimensions were zero-filled to 1024 points. The t_2 dimension was apodized with a 90° phase-shifted sine squared window function. The t_1 dimension was apodized with either a 90° phase-shifted sine squared or kaiser window function. All shifts were referenced to an external CCl_4 standard (96.5 ppm relative to TMS). The one-dimensional DQ-DRAWS spectrum was obtained by selective projection of ω_2 columns.

4.8.4 Solid-State ^{15}N NMR Spectroscopy. One-dimensional ^{15}N CP-MAS experiments were conducted on each of the u-^{13}C,^{15}N ribonucleosides. CP-MAS experiments were performed on a home-built NMR spectrometer operating at a Larmor frequency of 40 MHz using a Doty Scientific triple channel (1H-15N-X) probe equipped with a 5mm spinner assembly. In all experiments, proton frequencies were 50kHz during both cross-polarization and were raised to 90-100kHz during decoupling. Cross-polarization contact times were 2ms. Relaxation delays were 7 and 15s for lyophilized and crystalline material, respectively. All data was collected at a spin rate of 4000-5000 Hz. All ^{15}N chemical shifts were referenced to an external $NH_4^+Cl^-$ standard (-38.5 ppm).

4.8.5 Solid-State ^{19}F NMR Spectroscopy. Solid-state ^{19}F NMR experiments were conducted on home-built NMR spectrometer operating at a Larmor frequency of 188.198 MHz (200MHz ^{1}H frequency). Data was collected using a home-built high-efficiency triple channel (^{1}H-^{13}C-^{19}F) probe equipped with a 5mm spinner assembly [36]. Spin rate was regulated to ± 5Hz with a home-built spin rate controller. For experiments utilizing DRAWS, ^{19}F r.f. power levels were matched to the $t_r = 17\pi/2$ condition, as described above. Typically, ^{19}F fields were adjusted to 22-36kHz, with spinning speeds ranging from 3289-4500Hz. During all DRAWS experiments, proton frequencies were adjusted to ~120 kHz during decoupling. No cross-polarization was used in these experiments. In place of cross-polarization, a 90° pulse was applied to the fluorine channel prior to application of the DRAWS pulse sequence. Recycle delays for amorphous, hydrated DNA samples were 3-8 seconds. The integrated intensities were normalized to the intensity obtained from a standard MAS spectrum with no DRAWS applied. No correction for natural abundance background was required for fluorinated DNA samples. The DRAWS control experiment was conducted on a singly ^{19}F labeled DNA oligonucleotide, $[d(CGCGAAT^{5F}UCGCG)]_2$. For measurements where error estimates are reported, the DRAWS experiment was performed 4 times. T_2 relaxation times were measured by application of the Carr-Purcell XY8 pulse sequence developed by Guillion and coworkers [37]. A transverse relaxation time was extrapolated from a single-exponential fit to the decaying echo signal intensity.

4.8.6 Solid-State ^{2}H NMR Spectroscopy. All ^{2}H NMR experiments were conducted on a home-built spectrometer (11.7 Tesla) with a deuterium resonant frequency of 76.775 MHz equipped with a ENI LPI-10 radio frequency amplifier. 90° pulse times were generally 1.5-2.5μs. These high power pulses were necessary to excite the entire spectral width (200 kHz) of the deuterated DNA samples. A high efficiency home-built single-channel ^{2}H probe was used for these experiments. The line

shape data were collected using a quadrupole echo pulse sequence with phase-shifted 90° pulses (90ϕ -τ_1-$90_{\phi\pm90°}$-τ_2-acquire) using an eight-step phase cycle [38]. The delay between the two 90° pulses was 40μs, and the dwell time was 200ns. Data acquisition began prior to the echo maximum and the time domain data was left-shifted prior to Fourier transformation. Spin-lattice relaxation times, T_{1Z}, were determined using an inversion recovery pulse sequence, which incorporated a 180° composite pulse to ensure broadband excitation [39]. To obtain powder-averaged spin-lattice relaxation times, $\langle T_{1Z} \rangle$, the integrated intensity of the powder spectrum was monitored as a function of recovery time. Data from these experiments were analyzed using a non-linear least squares fitting routine [40]. All lineshape and relaxation data were collected at room temperature.

4.9 ^{13}C and ^{19}F One-Dimensional DRAWS Simulations

DRAWS magnetization exchange curves are fit to calculated simulations to determine an internuclear distance. Numerical simulation of the ^{13}C and ^{19}F one-dimensional DRAWS decay curves was accomplished using software developed in this laboratory [32, 41, 42]. All simulations of the experimental DRAWS data were performed on a DEC Alpha workstation. Fitting a DRAWS magnetization exchange curve requires the optimization of several parameters: the dipolar coupling, the principal chemical shift tensor values and orientations, the single quantum (T_2^{SQ}) transverse relaxation time, and the double quantum (T_2^{DQ}) transverse relaxation time. Information about the chemical shift tensors and the single quantum relaxation time can be derived empirically. Unfortunately, it is difficult to determine T_2^{DQ} independently. Consequently, simulation of a DRAWS decay curve requires a two parameter fit, in which the internuclear distance and the double quantum transverse relaxation rate $\left(T_2^{DQ}\right)^{-1}$ are the two adjustable parameters.

The simulation calculates the time evolution of the density matrix when it is subjected to the DRAWS pulse sequence. This involves solving the equation,

$$\rho(t) = D\exp(-\tfrac{i}{\hbar}\int_0^t H(t')dt')\rho(0)(\tfrac{i}{\hbar}\int_0^t H(t')dt') \qquad [4.2]$$

where, D is the Dyson time ordering operator. Because *H(t')* does not commute with itself at different times, it is necessary to approximate a solution for the propagator

$$U(t) = (-\tfrac{i}{\hbar}\int_0^t H(t')dt') \qquad [4.3]$$

numerically. The integral that appears in this expression for the propagator may be rewritten as a Riemann sum,

$$U(t) \approx \prod_{m=1}^{N} \exp\left(-\tfrac{i}{\hbar} H(m\cdot\Delta t)\Delta t\right) \qquad [4.4]$$

The time increment, Δt, used in these simulations is generally 2-3μs. The program computes the propagator for a single crystallite over the course of the DRAWS super-cycle ($4\tau_r$). Each propagator is then multiplied in a time-ordered fashion. Typically, 2000-4000 randomly oriented crystallites are powder averaged in each simulation. The trace of the propagated density matrix with the desired observable (generally, I_y+S_y), yields a value that can be compared with the experimental, normalized signal intensity.

When a powder average is performed, initial magnetization decay is followed by small oscillations about zero. The oscillations in DRAWS magnetization decay curves are damped by relaxation effects and are not always observed experimentally. Relaxation effects are included into the simulations by multiplying the appropriate terms in the density matrix by an exponential factor after every time step. A damping

rate is measured by varying $\left(T_2^{SQ}\right)^{-1}$ in the DRAWS simulation of the singly labeled or I_y - S_y control data, as described in Section 4.8.1.2. This same rate is then used in subsequent simulations to model the decay of I_y+S_y amplitude under DRAWS irradiation.

The DRAWS pulse sequence also produces double quantum coherence between two dipolar coupled nuclei. Double quantum and antiphase states continuously alternate during the course of the DRAWS experiment. While the double quantum state exists, it will undergo transverse relaxation. The time constant for this decay is denoted T_2^{DQ}. The result of double quantum relaxation is to overdamp the DRAWS decay curves for weak dipolar couplings. These double quantum relaxation effects can be modeled with an exponential decay in the simulations.

The second parameter that is varied in the DRAWS simulation is the dipolar coupling. The static dipolar coupling between two nuclei, I and S, in energy units, is written

$$d_{IS} = \frac{\mu_0 \gamma_I \gamma_S \hbar^2}{4\pi r^3} \qquad [4.5]$$

where, μ_0 is the permeability of free space, $\mu_0 = 4\pi \times 10^{-7} N / A^2$ [32]. Dividing this equation by Planck's constant converts the units of this equation into frequency units. For ^{13}C (γ=6.7283), Equation [4.5] becomes

$$d_{IS} = \frac{7.59814 \times 10^{-27} (m^3)(s^{-1})}{r^3} \qquad [4.6]$$

4.10 Chemical Shift Tensor Principal Values

Chemical shift tensor principal values were obtained from fitting the sideband intensities from CP-MAS experiments using the method developed by Herzfeld and

Berger [43]. CSA tensor values are reported using the convention,

$$|\sigma_{zz} - \sigma_{iso}| \geq |\sigma_{xx} - \sigma_{iso}| \geq |\sigma_{yy} - \sigma_{iso}|$$

$$\text{where,} \quad \sigma_{iso} = \tfrac{1}{3}\left(\sigma_{zz} + \sigma_{yy} + \sigma_{xx}\right) \qquad [4.7]$$

is the isotropic chemical shift [44]. The width of the spectrum is described by the anisotropy parameter, $\delta = \sigma_{zz} - \sigma_{iso}$. The shape of the spectrum is described by the asymmetry parameter (which ranges from 0 to 1),

$$\eta = \frac{\sigma_{yy} - \sigma_{xx}}{\sigma_{zz} - \sigma_{iso}} \qquad [4.8]$$

The three Euler angles required to orient the principal axis system with respect to the crystal or molecular frame must be obtained experimentally. The Euler angles required by the DRAWS simulation program orient the PAS system relative to a common dipolar frame. The values reported in this dissertation for thymidine and cytidine tensors were derived either from dipolar modulation experiments or deduced from X-ray crystal structures [32, 45]. Orientations of the PAS relative to the crystal frame were obtained by rotation of a separate axis system relative to the crystal structure using the InsightII software package (Biosym Technologies). It has been shown that DRAWS is much less sensitive to CSA tensor orientation than rotational resonance and RFDR. DRAWS becomes even less sensitive to this effect as the r.f. power is increased.

4.11 Notes to Chapter 4

[1] Robins, M.J., Wilson, J.S., and Hansske, F. (1983) *J. Am. Chem. Soc.*, **105** (12), p. 4059.

[2] Redwine, C.M. and Whaley, T.W. (1979) *J. Label. Comp. Radiopharm.*, **16**, p. 1529.

[3] Williamson, J.R. and Boxer, S.J. (1988) *Nuc. Acids Chem.*, **16**, p. 1529.

[4] Krenitsky, T.A., Rideout, J.L., Chao, E.Y., Koszaika, G.W., Gurney, F., Crouch, R.C., Cohn, N.K., Wolberg, G., *et al.* (1986) *J. Med. Chem.*, **29**, p. 138.

[5] Diaz, R. (1998), personal communication.

[6] Bhat, C.C. (1968) *Synthetic Procedures in Nucleic Acid Chemistry*, **1**, p. 521.

[7] Hubbard, A.J., Jones, A.S., and Walker, R.T. (1984) *Nuc. Acids Res.*, **12**, p. 6827.

[8] Kline, P.C. and Serianni, A.S. (1989) *J. Am. Chem. Soc.*, **112**, p. 7373.

[9] Barker, R. and Fletcher Jr., H.G. (1961) *J. Org. Chem*, **26**, p. 4605.

[10] Recondo, E.F. and Rinderknecht, G.L. (1959) *Chim. Acta.*, **42**, p. 1171.

[11] Codington, F. and Fox, J.J. (1963) *Meth. Carbohyd. Res.*, **2**, p. 113.

[12] Vorbrüggen, H., Krolikiewicz. K., and Bennua, B. (1981) *Chem. Ber.*, **114**, p. 1234.

[13] Cowart, M., Gibson, K.J., Allen, D.J., and Benkovic, S.J. (1989) *Biochemistry*, **28**, p. 1975.

[14] Batey, R.T., Inada, M., Kujawinski, E., Puglisi, J.D., and Williamson, J.R. (1992) *Nuc. Acids Res.*, **20** (17), p. 4515.

[15] Sambrook, J., Fritsch, E.F., and Maniatis, T., eds. *Molecular Cloning: A Laboratory Manual*. 1989, Cold Spring Harbor Press: Cold Spring Harbor, New York.

[16] Zimmer, D.P. and Crothers, D.M. (1995) *Proc. Natl. Acad. Sci. (USA)*, **92**, p. 3091.

[17] Gait, M.J., ed. *Oligonucleotide Synthesis: A Practical Approach.* . 1984, IRL Press Limited: Oxford, England.

[18] Hatcher, M.E.. *Ph.D. Dissertation*, 1996, University of Washington.

[19] Alam, T.M., Orban, J., and Drobny, G.P. (1991) *Biochemistry*, **30**, p. 9229.

[20] Weast, R.C., ed. *Handbook of Chemistry and Physics.* 60th ed. 1979, CRC: Boca Raton, FL.

[21] Green, E.A., Rosenstein, R.D., Shiono, R., and Abraham, D.J. (1975) *Acta Cryst.*, **B31**, p. 102.

[22] Furberg, S. (1950) *Acta Cryst.*, **3**, p. 325.

[23] Lai, T.F. and Marsh, R.E. (1972) *Acta Cryst.*, **B28**, p. 1982.

[24] Sugawara, Y., Iimura, Y., Iwasaki, H., Urabe, H., and Saito, H. (1994) *J. Biomol. Struct. Dynam.*, **11** (4), p. 721.

[25] Thewalt, U., Bugg, C.E., and Marsh, R. (1970) *Acta Cryst.*, **B26**, p. 1089.

[26] Young, D.W., Tollin, P., and Wilson, H.R. (1969) *Acta Cryst.*, **B25**, p. 1423.

[27] Subramanian, E. and Hunt, D.J. (1970) *Acta Cryst.*, **B26**, p. 303.

[28] Viswamitra, M.A., Reddy, B.S., Lin, G.H.Y., and Sundaralingam, M. (1971) *J. Am. Chem. Soc.*, **93**, p. 4565.

[29] Watson, D.G., Sutor, D.J., and Tollin, P. (1965) *Acta Cryst.*, **19**, p. 111.

[30] Furberg, S., Petersen, C.S., and Rømming, C. (1965) *Acta Cryst.*, **18**, p. 313.

[31] Burum, D.P., Linder, M., and Ernst, R.R. (1981) *J. Magn. Reson.*, **43**, p. 463.

[32] Gregory, D.M., *Ph.D. Dissertation*, 1996, University of Washinton.

[33] Geen, H., Levitt, M.H., and Bodenhausen, G. (1992) *Chem. Phys.Lett.*, **200**, p. 350.

[34] States, D.J., Haberkorn, R.A., and Ruben, D.J. (1982) *J. Magn. Reson.*, **48**, p. 286.

[35] Gregory, D.M., Mehta, M.A., Shiels, J.C., and Drobny, G.P. (1997) *J. Chem. Phys.*, **107** (1), p. 28.

[36] Stringer, J.A. and Drobny, G.P. (1998) *Rev. Sci. Instr.*, accepted.

[37] Gullion, T. and Conradi, M. (1990) *J. Magn. Reson.*, **89** (3), p. 479.

[38] Griffin, R.G. (1981) *Methods in Enzymology*, **72**, p. 108.

[39] Tycko, R. (1983) *Phys. Rev. Lett.*, **51**, p. 775.

[40] DeFontaine, D.L., Ross, D.L., and Ternai, B. (1975) *J. Magn. Reson.*, **18**, p. 276.

[41] Mitchell, D.J., *Ph.D. Dissertation*, 1996, University of Washington.

[42] Mehta, M.A., Gregory, D.M., Kiihne, S., Mitchell, D.J., Hatcher, M.E., Shiels, J.C., and Drobny, G.P. (1996) *Solid State Nuclear Magn. Reson.*, **7**, p. 211.

[43] Herzfeld, J. and Berger, A. (1980) *J. Chem. Phys.*, **73**, p. 6021.

[44] Haeberlen, U., *High Resolution NMR in Solids. Selective Averaging*. 1976, New York: Springer Verlag.

[45] Kiihne, S.R., *Ph.D. Dissertation*, 1998, University of Washington.

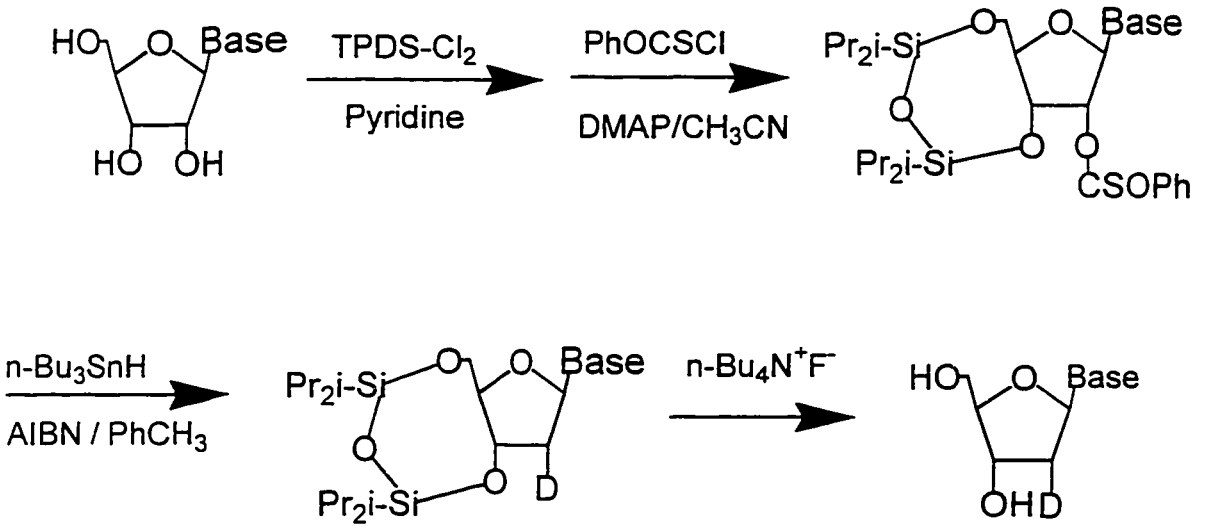

Figure 4.1: Reaction scheme for synthesis of [2"-^{2}H]-2'-deoxythymidine.

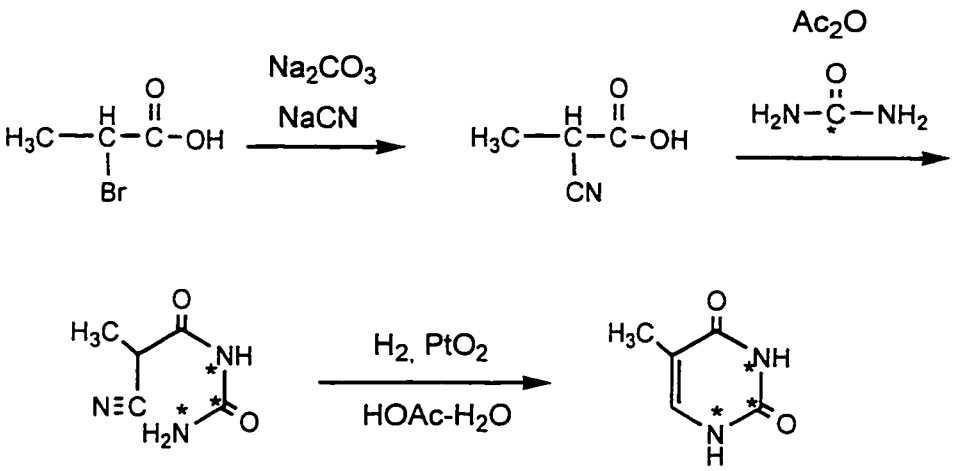

Figure 4.2: Reaction scheme for synthesis of [2-^{13}C, 1, 3-$^{15}N_2$]-thymine.

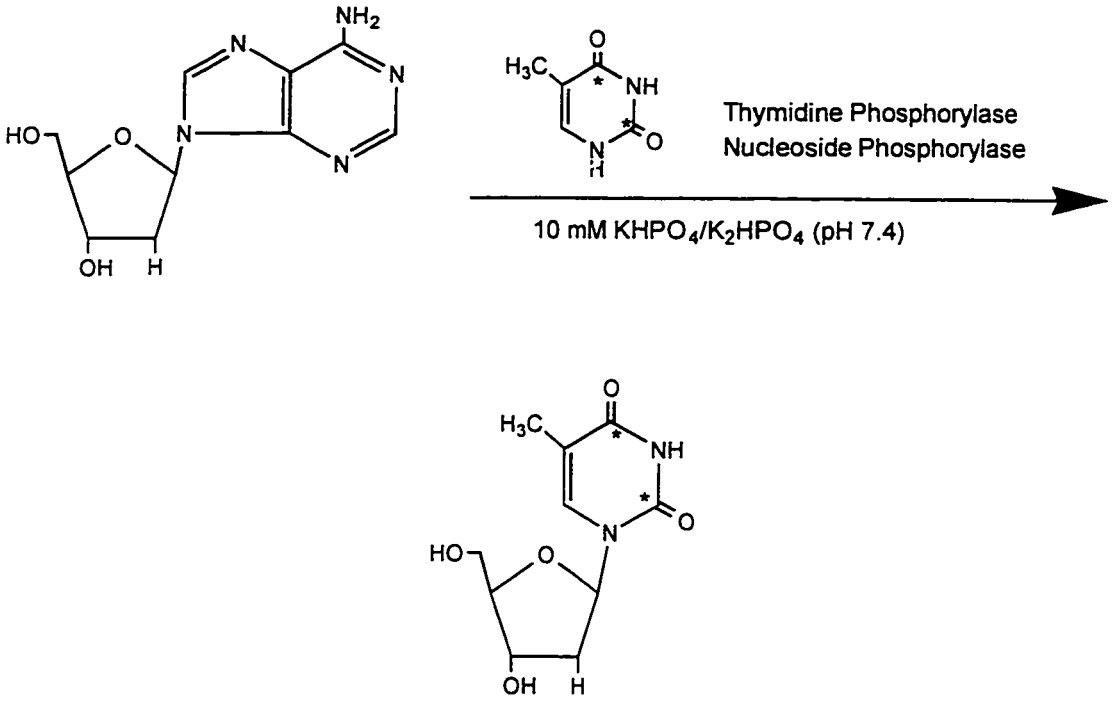

Figure 4.3: Reaction scheme for enzymatic synthesis of [2-^{13}C, 1, 3-$^{15}N_2$] thymidine from adenosine and [2-^{13}C, 1, 3-$^{15}N_2$] thymine.

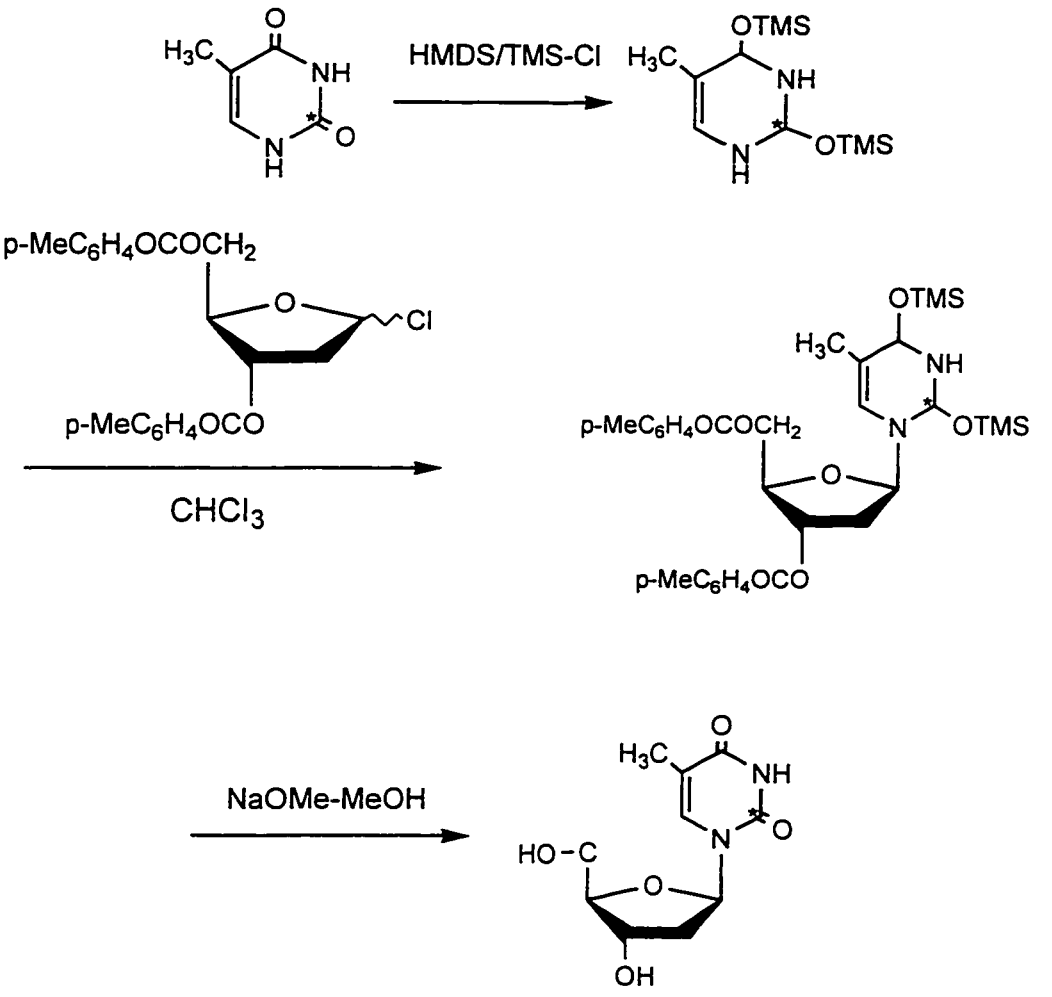

Figure 4.4: Reaction scheme for preparation of [2-^{13}C, 1, 3-$^{15}N_2$]-2'-deoxyuridine.

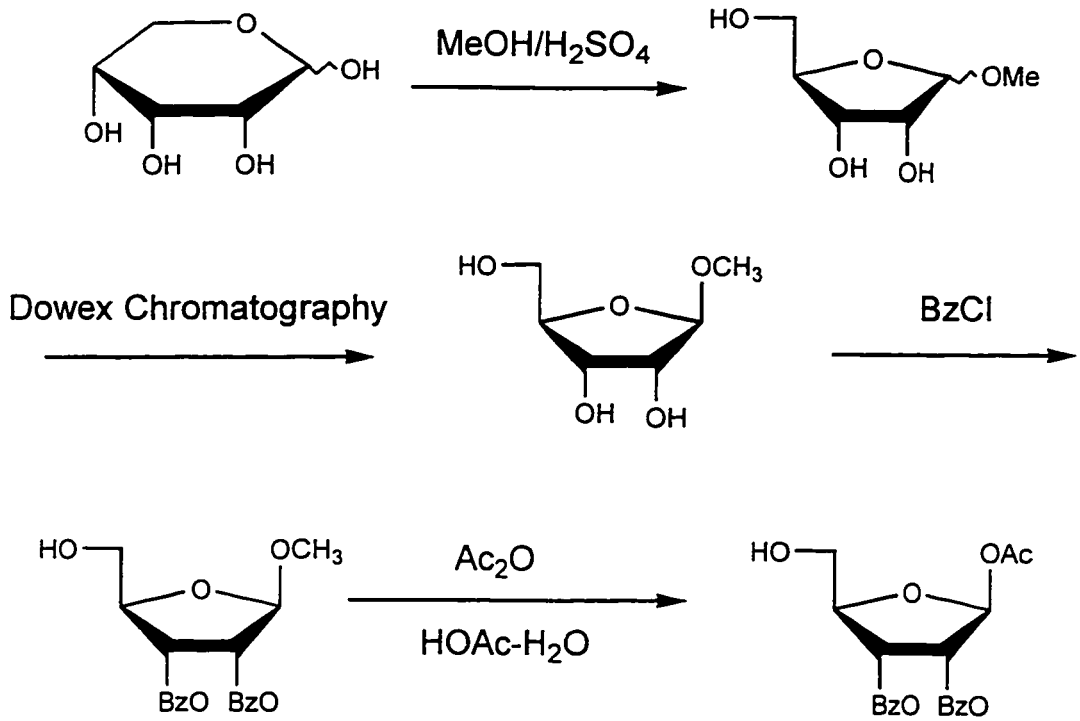

Figure 4.5: Reaction scheme for preparation of selectively ^{13}C enriched cytidine: (A) preparation of 1-O-Acetyl-2,3,5-tri-O-benzoyl-β-D-[^{13}C]-ribofuranoside (ABR) and (B) condensation of ABR with N4-acetyl cytosine.

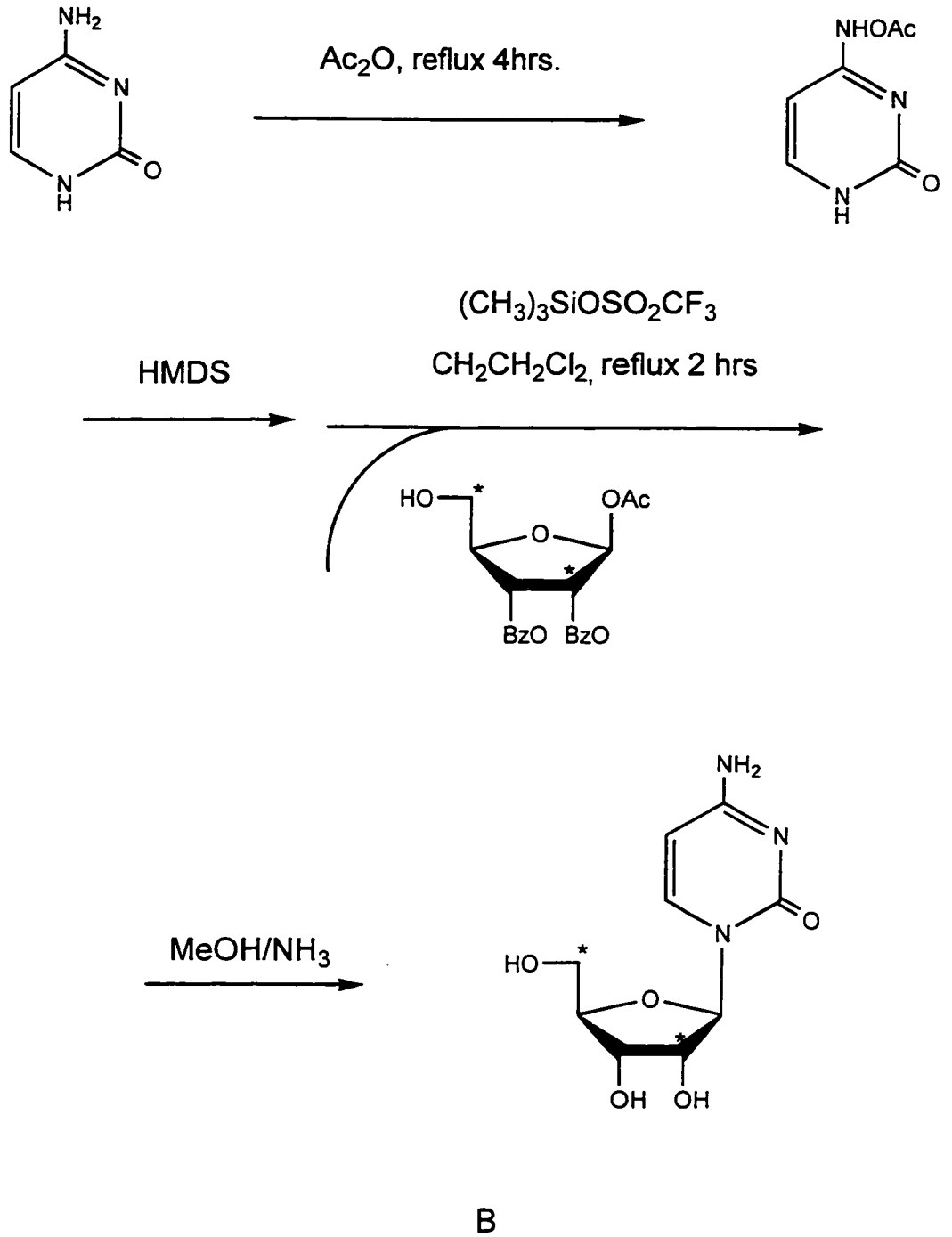

B

Figure 4.5 (continued)

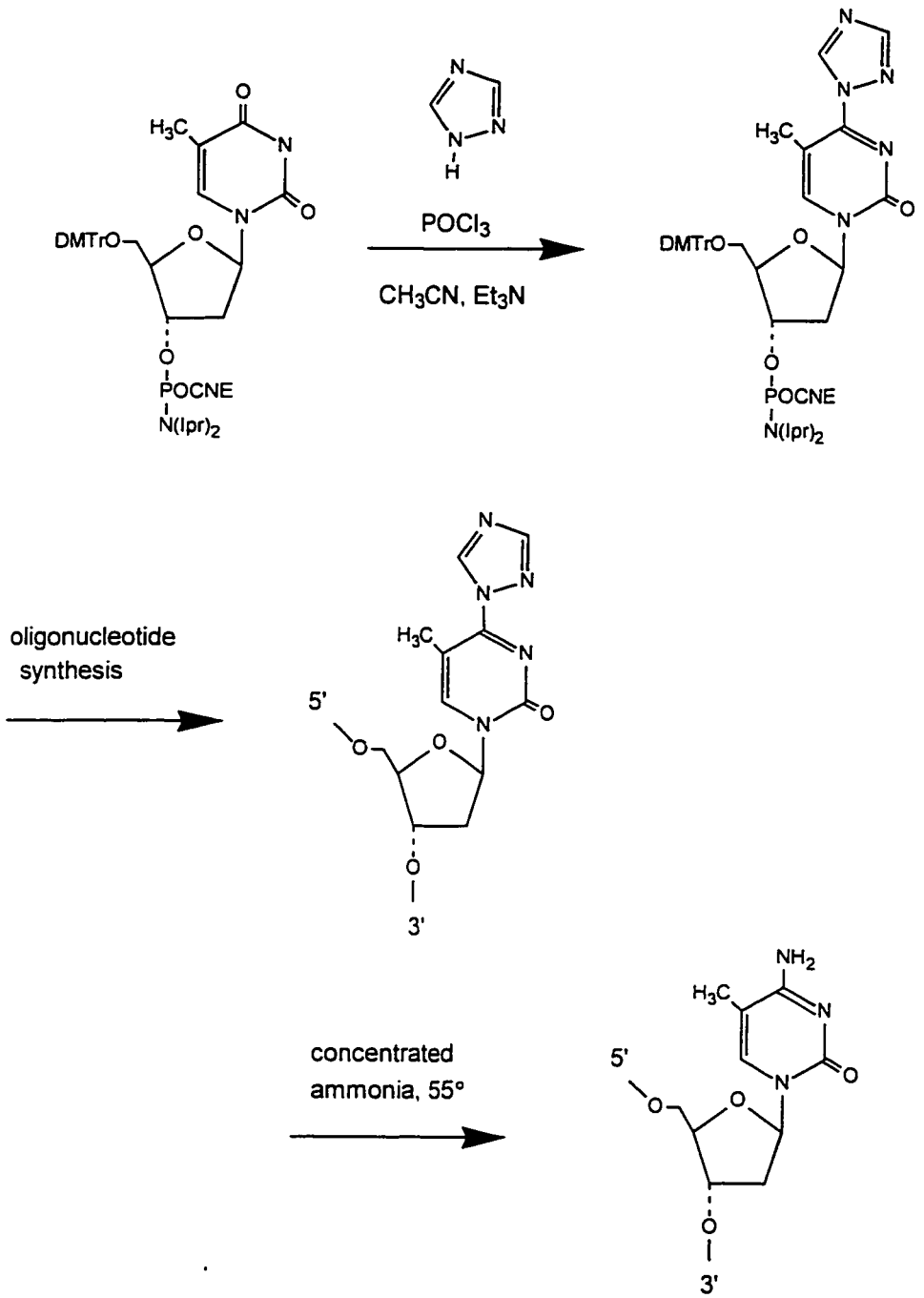

Figure 4.6: Reaction scheme for preparation of 4-(1,2,4-triazoyl-1-yl)-thymidine-5'-O-(dimethoxytrityl)-3'-O-(N,N-diisopropyl-β-cyanoethyl-phosphoramidite.

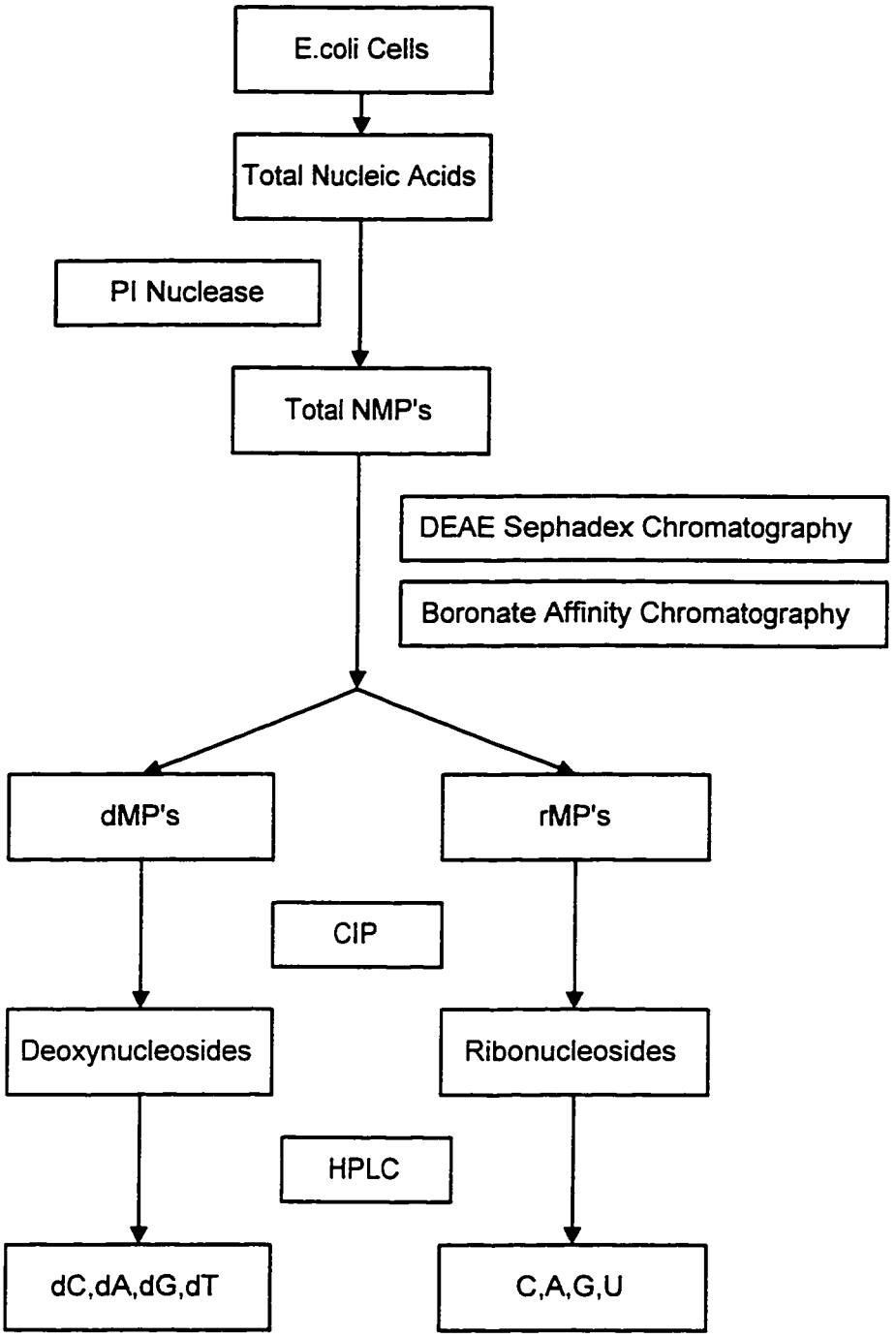

Figure 4.7: Flowchart for the biosynthesis of uniformly ^{13}C,^{15}N labeled nucleosides.

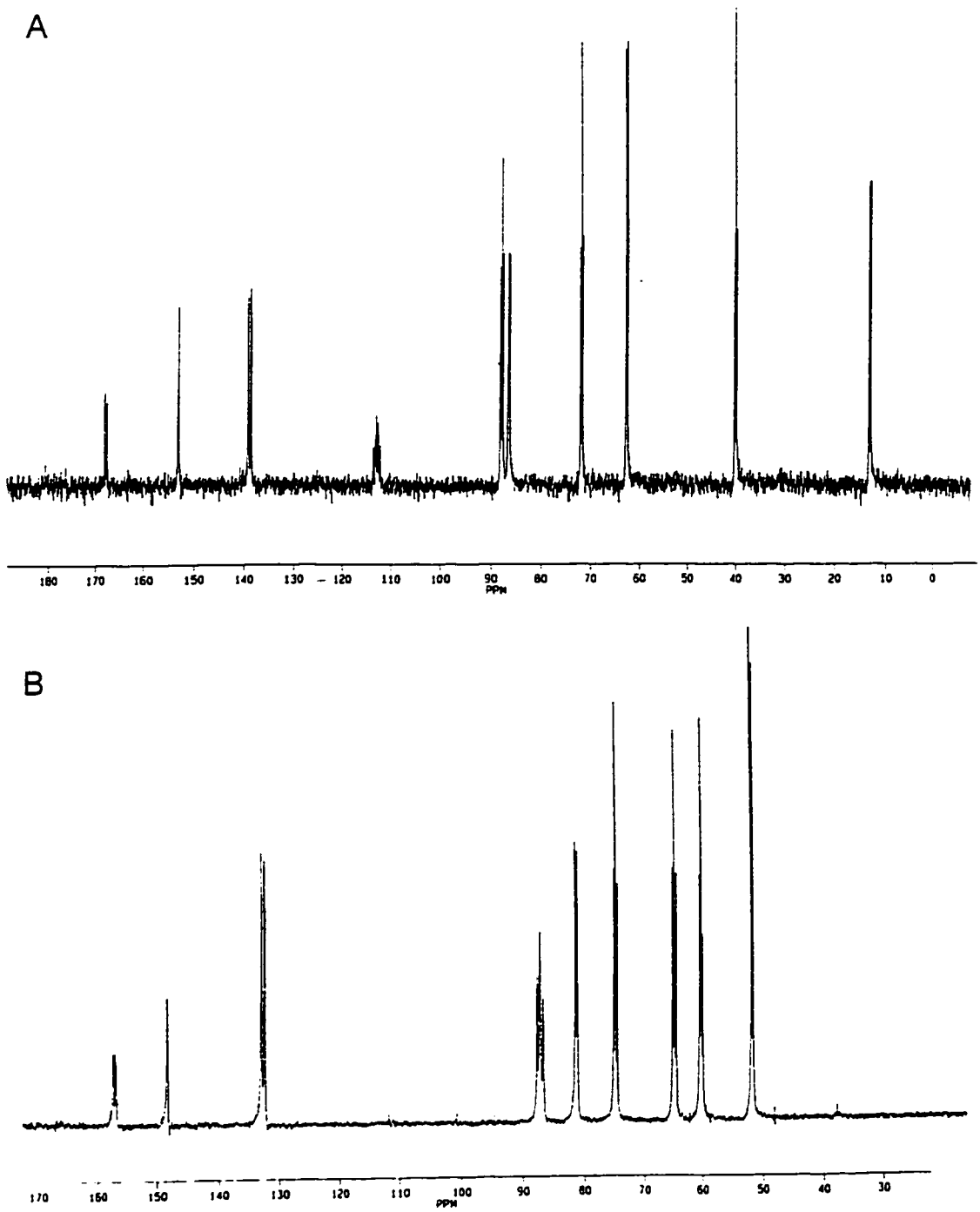

Figure 4.8: Solution-state ^{13}C spectra of thymidine (A) and cytidine (B). Assignments given in Table 6.4.

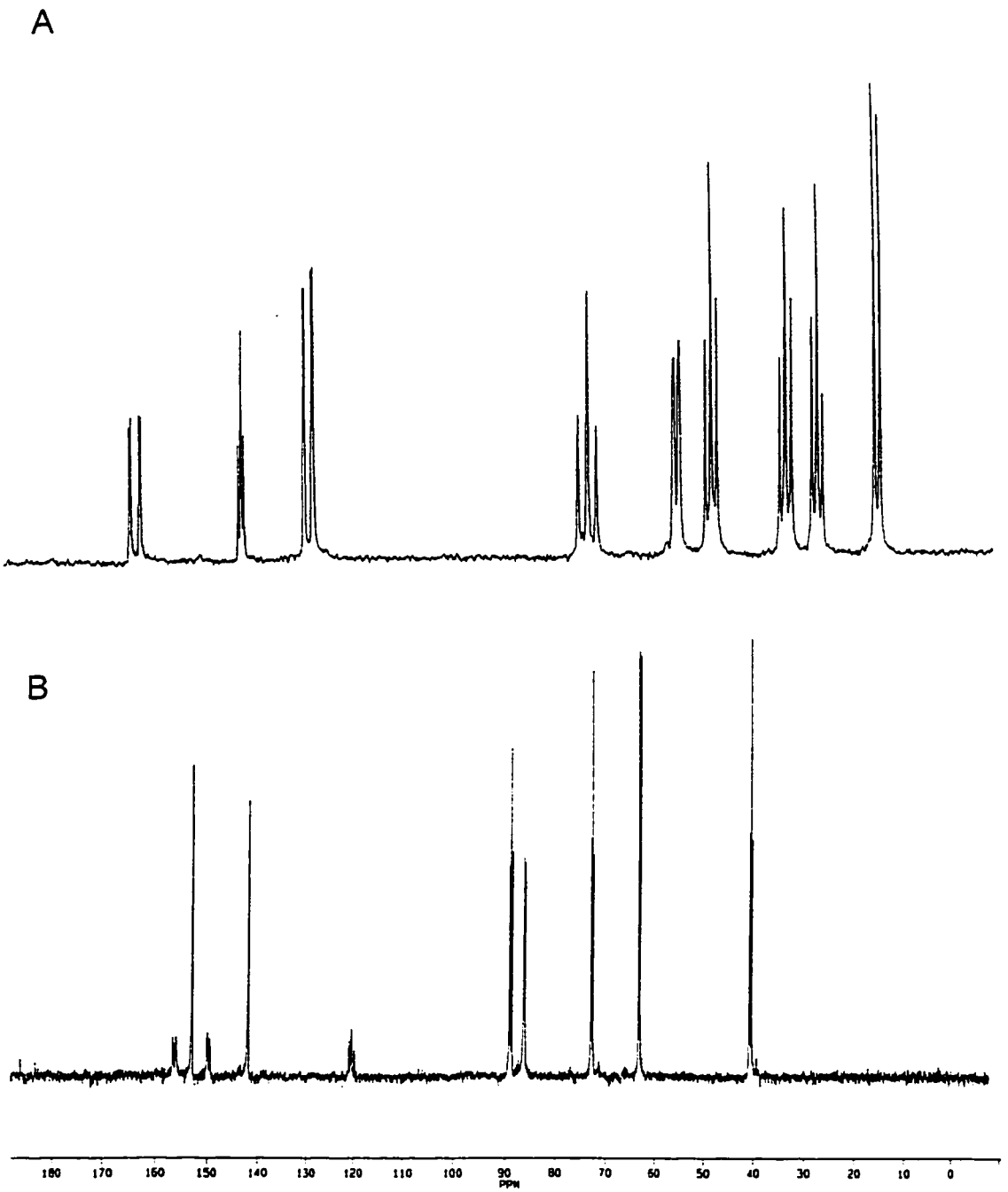

Figure 4.9: Solution-state ^{13}C spectra of uridine (A) and 2'-deoxyadenosine (B). Assignments given in Table 6.4.

Chapter 5
One-Dimensional DRAWS Results

5.1 Introduction

This chapter presents data for ^{13}C-^{13}C and ^{19}F-^{19}F distance measurements in nucleosides and DNA oligonucleotides obtained using the DRAWS dipolar recoupling experiment. The first section of the chapter describes the results for two doubly carbon labeled cytidine monomers and provides the first example of how dipolar recoupling methods can be implemented to monitor sugar ring conformation in nucleosides. The following sections of the chapter cover applications of the DRAWS technique to selectively carbon and fluorine labeled DNA oligonucleotides. These measurements were directed toward probing the structure at the dT8-^{5Me}dC9 step of the DNA dodecamer, [d(CGCGAAT$\underline{T}^{5Me}\underline{C}$GCG)]$_2$ (underlined nucleotides). The goal of these studies has been to monitor the effect of base methylation on the unusual structural features (i.e. T8-C9 "slip" and C9-G4 "splay") that were noted by Dickerson and Drew in their X-ray diffraction study of the DNA dodecanucleotide, [d(CGCGAATTCGCG)]$_2$ (see Section 1.7) [1]. Figure 5.1 illustrates the dT8-^{5Me}dC9 dinucleotide segment, taken from the X-ray structure of the ^{5Me}dC9 dodecamer of the same sequence [2].

One of the biological consequences of cytosine methylation may be to influence the action of proteins through alterations in local DNA conformation. Although cytosine methylation affects the chemical structure of the base by increasing its size and changing electron densities in the pyrimidine ring, methylation has not been found to substantially alter the global B-conformation of the DNA in the liquid- or crystalline state (see Section 1.9). A comparison of the ^1H-^1H NOESY spectra for the

Dickerson dodecamer and the methylated dC9 analogue (in 200mM NaCl, 50mM sodium phosphate, 0.8mM EDTA, pH 7.0) attest to the relatively non-perturbing influence of the 5-methylcytosine residue on the geometry of the DNA dodecanucleotide, $[d(CGCGAATTCGCG)]_2$. Major conformational changes in the DNA helix would evidence themselves as disruptions in the sequential assignment pathway and the crosspeak intensities of the aromatic-H1'/H5 and aromatic-H2', H2" regions of the ^{1}H-^{1}H NOESY spectrum [3]. These regions of the NOESY data sets for the methylated and unmethylated species are presented in Figures 5.2 and 5.3. A cursory inspection of these spectra maintains that, apart from a slight chemical shift change for the ^{5Me}C9 protons, there is essentially no distortion in the sequential assignment pathway for the methylated DNA dodecamer.

The distance measurements presented in the subsequent sections of this chapter for DNA oligonucleotides are a first attempt at probing the structure of a methylated TpC step using solid-state NMR dipolar recoupling techniques. DNA measurements were conducted on amorphous, lyophilized powders under hydration conditions ranging from 66-84% RH, which corresponds to 5.2-14.7 waters per nucleotide (i.e. 120-353 H_2O molecules per DNA dodecamer). The hydration levels utilized in this investigation (apart from 66% RH) are comparable to those found in the X-ray diffraction studies. The original Dickerson dodecamer crystal structure produced reflections from 80 bound solvent molecules or approximately 280 solvent molecules per asymmetric unit (i.e. $W \approx 11$-12) [4]. In comparison, the bromine heavy-atom derivative of the Dickerson dodecamer, $[d(CGCGAATT^{5Br}CGCG)]_2$, contained 422 solvent molecules (i.e. $W \approx 17$-18) [5]. The 5-methyl-dC9 analogue solved by Partridge and Salisbury produced reflections from 55 bound waters, which is slightly less than for the original dodecamer (i.e. $W \approx 9$-10) [2]. Relevant internuclear distances were measured in all three of these crystal structures and serve as a useful comparison for the data in the present work.

5.2 Using Dipolar Coupling to Probe Structure in the Solid-State

Because the dipolar interaction is proportional to $1/r^3$, where r is the internuclear distance, it is possible to obtain distance information from dipolar recoupling experiments, such as DRAWS (see Chapter 3). The quantitative measurement of distances and orientations from dipolar recoupling techniques is performed by direct comparison of experimental results with quantum mechanical simulations and is independent of empirically derived models. Numerical simulation of the DRAWS data requires chemical shift tensor principal values, the spinning rate, the internuclear distance, and the r.f. field strength, and two empirical damping constants, T_2^{SQ} and T_2^{DQ} (see Section 4.9). Only the asymmetry and anisotropy of the tensors are included as input parameters. Additionally, CSA tensor orientations have been omitted in the simulations, since previous work by Gregory and coworkers has demonstrated the relative insignificance of tensor orientations on the outcome of DRAWS distance measurements [6].

Numerous applications of the DRAWS pulse sequence for measurement of interatomic ^{13}C-^{13}C distances in deoxynucleoside monomers, amino acids, and DNA oligonucleotides have been reported in the literature. One DRAWS study that is particularly pertinent to the present investigation was conducted by Gregory and coworkers on a series of five different doubly ^{13}C labeled DNA dodecamers of the sequence, $[d(CGCGAA\underline{TT}CGCG)]_2$, in which the dT7-dT8 dinucleotide step contained several different combinations of ^{13}C labeled nuclei [6]. Relevant results for the $^{13}C_2$-$^{13}C_2$ and $^{13}CH_3$-$^{13}CH_3$ labeled compounds (taken for DNA in frozen, buffered solution) from that study are given in Table 5.1. Examination of the measured solid-state NMR distances reveals that they are comparable to those in the previous solution-state NMR and X-ray structures of this dodecanucleotide (Tables 5.1 and 5.2) [1, 7].

Recent technological advances have now made it feasible to measure internuclear distances in fluorinated samples [8]. Substitution of 5-fluoro-2'-deoxyuridine

for thymidine is a common practice in biochemical applications [9]. The advantages of this approach for structural investigations in DNA are two-fold: 1) Fluorinated phosphoramidite derivatives may be purchased commercially, making synthesis of fluorinated DNA relatively straightforward, and 2) the high sensitivity of ^{19}F nuclei makes distance and orientational measurements in nucleic acids experimentally viable. This improvement in signal-to-noise is a distinct advantage for dipolar recoupling measurements. One question that raises concern is whether the presence of fluorine in place of a methyl group alters the structural and chemical properties of the DNA. Introduction of fluorine at the 5-position on thymine as a replacement for the 5-methyl group is known to perturb the chemical properties of the pyrimidine heterocycle [10]. Fluorine is the most electronegative atom of the halogen series with a size similar to hydrogen (1.35Å and 1.2Å, respectively), while the van Waal's radius of a methyl group (1.95Å) is more similar to bromine (2.0 Å). UV spectroscopic melting experiments by Habener and coworkers have shown that duplexes containing A-^{5F}U base pairs were slightly more stable than duplexes containing A-T base pairs [10]. Fluorine may also alter normal Watson-Crick hydrogen bonding and base stacking by changing the dipole moment of the base [11]. In order to address the effect of replacing the methyl groups with fluorine on local DNA geometry, a complementary ^{19}F and ^{13}C DRAWS study was undertaken for the DNA dodecamer, [d(CGCGA^{5F}U^{5F}UCGCG)]$_2$, in which the methyl groups on dT7 and dT8 were substituted with fluorine atoms [12]. The ^{13}C-^{13}C distance measurements were conducted on amorphous, hydrated powders at 75% and 81% RH. The results of these distance measurements were comparable to those determined for DNA in frozen, buffered solutions by Gregory et al., suggesting that the amorphous, hydrated DNA samples were in a similar physical state. The results for the fluorinated analogue (at 75% and 81 % RH) suggest that introduction of fluorine in place of a methyl group does not noticeably perturb the local structure at the dT7-dT8 step of this particular DNA dodecanucleotide (see Table 5.1). Examination of the data in Tables 5.1 and 5.2

also indicates that there is reasonably good agreement between the DRAWS and X-ray derived distances for distances measured at the dT7-dT8 step.

In a related solution-state NMR structure of the DNA octamer, $[d(GGAAT^{5F}\underline{U}CC)]_2$, containing 5-fluorouracil (as an analogue for thymidine), Stolarski and coworkers revealed that the DNA adopted a normal B-form helical conformation and that the 5-fluorouracil residue exhibited standard Watson-Crick hydrogen bonding to the cross-strand adenine residue [9]. This DNA sequence is particularly relevant to our work as it also contains the EcoRI restriction enzyme binding site. Consequently, the NMR structure by Stolarski et al. serves as a direct solution-state corollary to the solid-state NMR investigation discussed above. The absence of major structural perturbations in the DNA octanucleotide in the liquid-state further corroborates our solid-state NMR data indicating that substitution of 5-fluorouridine for thymidine does not significantly alter the conformation of the DNA.

5.3 DRAWS Distance Measurements in [2,1'-$^{13}C_2$] and [2,1'-$^{13}C_2$] Cytidine

DRAWS distance measurements were carried out on polycrystalline [2, 1'-$^{13}C_2$] and [2, 1'-$^{13}C_2$] cytidine in order to define the conformation of the furanose ring and the orientation of the cytosine heterocycle about the glycosidic bond. The NMR samples contained 10mg of ^{13}C labeled material and 90mg of unlabeled cytidine monomer. The natural abundance background signal was corrected according to Equation [4.1]. Principal tensor elements were calculated from a series of CP-MAS spectra on the doubly labeled compounds using a Herzfeld-Berger spinning sideband analysis [13]. These values are presented in Table 5.3. Tensor elements for C3' and C5' were also measured from the [2, 1', 3'-$^{13}C_3$] and [2, 2', 5'-$^{13}C_3$] cytidine monomers and are included in Table 5.3 for completion. An I_y-S_y DRAWS control experiment was conducted on each of the doubly labeled monomers to yield single quantum damping constants (T_2^{SQ}).

5.3.1 [2,1'-$^{13}C_2$]-Cytidine

Figure 5.4 presents spectra taken at different time points during the course of the DRAWS experiment, illustrating the decay of magnetization for an increasing number of repetitions of the DRAWS mixing time. The DRAWS and I_y-S_y control magnetization decay curves for [2, 1'-$^{13}C_2$]-cytidine are presented in Figures 5.6A and 5.5, respectively. A fit to the control data was achieved by varying only the single quantum relaxation rate for each carbon atom in the simulation program. The C2 and C1' carbon nuclei decayed with a rate of 160 s^{-1} and 280 s^{-1}, respectively. This discrepancy in relaxation rates was attributed to the effects of insufficient decoupling for the aliphatic C1' proton. A double-quantum $\left(T_2^{DQ}\right)^{-1}$ relaxation rate of 600 s^{-1} was included in the simulation of the DRAWS data to achieve agreement at longer DRAWS mixing times. Simulation of the DRAWS data yielded a distance between C2 and C1' of 2.4 ± 0.2 Å. This measurement agrees reasonably well with the distance of 2.46 Å reported in the original X-ray crystal structure of cytidine by Furberg et al. [14]

5.3.2 [2,2'-$^{13}C_2$]-Cytidine

The DRAWS magnetization decay curve for [2,2'-$^{13}C_2$]-cytidine is presented in Figure 5.6. An I_y-S_y DRAWS control experiment was conducted on the doubly labeled monomer to yield T_2^{SQ} values of 9.1 and 4.8 ms for C2 and C2', respectively (Figure 5.7). A double quantum damping constant of 4 ms was required to fit the data at longer time points. Simulation of the DRAWS data yields a distance of 3.1 ± 0.2 Å, which is in good agreement with the crystallographic distance of 3.19 Å reported by Furberg and coworkers. The DRAWS simulation parameters for [2,2'-$^{13}C_2$]- and [2,1'-$^{13}C_2$]-cytidine are compiled in Table 5.4. The distance measurements

obtained from the two cytidine isotopomers confirm that the furanose ring is puckered in the C3'-endo conformation. For cytidine to be in a C2'-endo pucker with an anti orientation, the internuclear distance between C2 and C2' would be approximately 3.71 Å. The error in our measurements is sufficiently small to allow for discrimination between the C2'- and C3'-endo sugar ring conformations. The unit cell dimensions (confirmed for the 2,1'-cytidine NMR sample) matched those from the previous X-ray diffraction study and confirmed that the nucleoside resides in a C3'-endo sugar ring pucker and an anti base orientation (see Section 4.6.3).

5.4 DRAWS Results for [5-^{19}F]-dU8, [5-^{19}F]-dC9 DNA Dodecamer

The DRAWS experiment was used to measure the internuclear distance between two ^{19}F nuclei (substituted for the 5-methyl group of thymidine and 5-methylcytidine) at adjacent dT8-^{5Me}dC9 nucleotides (underlined residues) in the DNA dodecamer, [d(CGCGAAT^{5F}U^{5F}CGCG)]$_2$. The 4651 Hz MAS spectrum for 38.3 mg of [5-^{19}F]-dU8, [5-^{19}F]-dC9 DNA dodecamer at a hydration level of W=12.7 (75% RH) appears in Figure 5.8. The MAS spectrum reveals that the fluorine resonances are overlapped. The DRAWS magnetization decay curves for 55.3 mg of a singly fluorinated dodecamer, [d(CGCGAAT^{5F}UCGCG)]$_2$, labeled at the 8 position with 5-fluoro-2'-deoxyuridine at W = 7.4 and for the doubly labeled ^{5F}dU8-^{5F}C9 DNA at W=12.7 are presented in Figure 5.9. These experiments were performed at a spinning speed of 4651Hz with a ^{19}F field of 38.2 kHz. CSA tensor values were determined by Herzfeld Berger analysis as described previously: σ_{11}=-42.8ppm, σ_{11}=-16.7ppm, σ_{11}=-59.56ppm (relative to isotropic shift = 0ppm) [8]. Simulation of the DRAWS control experiment on the singly fluorine labeled DNA yielded a T_2^{SQ} value of 2.5 ms. Simulation of the DRAWS data at this hydration level resulted in a distance of 5.0 ± 0.2 Å. A double quantum damping rate of 1200 Hz (830 ms) was required to fit

the data at longer time points. Table 5.5 contains the DRAWS simulation parameters for the fluorinated dodecamers.

The corresponding 4425Hz MAS spectrum and the DRAWS decay curve at 81% relative humidity (W=14.7) are given in Figures 5.8 and 5.10, respectively. The MAS spectrum reveals that the linewidths for the DNA are considerably narrower upon increased hydration (i.e. a reduction from 958 Hz to 447 Hz resulting from the transition in hydration level from 75% to 81% RH). These reduced linewidths suggest the onset of motional averaging and/or a decrease in sample heterogeneity (i.e. phase transition). The DRAWS distance measurement was conducted at a spinning speed of 4425 Hz using a 37.6 kHz ^{19}F field. For mixing times up to 7.2 ms, the data indicate an internuclear ^{19}F-^{19}F distance of 5.0 ± 0.2 Å with a T_2^{DQ} constant of 500 ms and a single quantum relaxation time of 2.6 ms (Figure 5.10). It is primarily the DQ damping constant, not the distance, that appears to be affected by the increase in water content, indicating that no further structural change occurred at the dT8-dC9 dinucleotide junction. Attempts to collect DRAWS data for the fluorinated DNA at 84% RH were unsuccessful. A T_2 measurement on the DNA revealed that the central isotropic peak exhibited a faster magnetization decay rate than the spinning sidebands (Figure 5.11). This effect was observed for both the singly ^{5F}dU8 and doubly ^{5F}dU8, ^{5F}dC9 labeled analogues. We have tentatively interpreted this result to be a consequence of there being a more mobile component (with signal intensity primarily contributing at the isotropic chemical shift) and a less mobile component in the sample. In the presence of motion, the DRAWS experiment causes rapid loss of signal intensity after several milliseconds, preventing the measurement of accurate internuclear distances.

5.5 DRAWS Results for [2-^{13}C]-dT8, [2-^{13}C]-5-Methyl-dC9 DNA Dodecamer

The DRAWS technique was used to measure the internuclear distance between two ^{13}C labels at the carbonyl (C2) position of adjacent dT8 and ^{5Me}dC9 nu-

cleotides in the DNA dodecanucleotide, [d(CGCGAATT^{5Me}CGCG)]$_2$ (underlined residues). Data was collected for 58.3 mg of the doubly [2-^{13}C] labeled compound at 66% RH, corresponding to W=5.2. The CP-MAS spectrum at 4525 Hz for this sample appears in Figure 5.12. Inspection of the spectrum reveals that the C2 carbon resonances are only minimally resolved at this hydration level and are treated as one degenerate peak in the calculations. Due to chemical shift degeneracy, the I_y-S_y control experiment could not be applied to this doubly labeled oligonucleotide. An alternative pulse sequence (designated as DRAWSX) was utilized for the control experiment on the doubly labeled DNA sample. This version of the DRAWS pulse sequence (shown in Figure 5.13) has proved to be a viable alternative to the I_y-S_y or singly labeled control experiments for samples with degenerate chemical shifts [15]. DRAWS data was collected at a spinning speed of 4525 Hz and a ^{13}C r.f. field of 38.46 kHz. DRAWSX data was collected at a spinning speed of 2331 Hz using this same carbon power level. Figure 5.14 compares the DRAWS dephasing curves and simulations for both experiments. CSA tensor values for the C2 carbon of dT8 were based on previous measurements for a singly [2-^{13}C] labeled thymidine monomer: σ_{11}= 98 ppm, σ_{22}= 124 ppm, σ_{33}=229 ppm (relative to TMS) [6]. The tensor values for the C2 of the ^{5Me}dC9 residue were based on those obtained for the [2,1'-$^{13}C_2$] cytidine monomer (Table 5.3). Previous results from this laboratory have indicated that the CSA principal tensor values remain relatively unaffected upon incorporation of the monomer into a DNA oligonucleotide [16]. Simulation of the DRAWSX decay curve yielded a T_2^{SQ} of 14.3 ± 2.0 ms. This value is slightly faster than the previous DRAWS measurement obtained for a singly $^{13}C_4$ labeled DNA hexadecamer in frozen solution (20.8 ms) [6]. Simulation of the DRAWS data for the DNA at 66% RH was accomplished using a 14.3 ms single quantum damping rate, a dipolar coupling corresponding to 3.5 ± 0.2 Å, and an empirical double quantum relaxation time of 2.5 ms. The DRAWS simulation parameters for the carbon labeled DNA oligonucleotides are compiled in Table 5.5. Numerous attempts to collect DRAWS data at

75% RH (W=8.2) were made. Due to the increased water content, probe detuning and loss of the CP match condition prevented the collection of DRAWS data at either 4.7 or 9.4 Tesla.

5.6 Conclusion

These preliminary DRAWS measurements indicate that methylation of the 5 carbon of dC9 in the DNA dodecamer, [d(CGCGAATT^{5Me}CGCG)]$_2$, produces very little distortion of the local geometry at the dT8-dC9 dinucleotide junction. This result corroborates the findings of previous structural studies on the effect of cytosine methylation on local DNA geometry (see Sections 1.9 and 5.2). The fluorine DRAWS data suggests a slight increase in the ^{5F}dU8 and ^{5F}dC9 distance ($\leq$ 0.5Å) relative to the native dodecamer. In the native dodecamer X-ray structure, the dC9-H5 to dT8-CH_3 distance is 4.57 Å for one strand and 4.79 Å for the complementary strand. The same distance in the solution-state NMR structure is 4.50 Å, which is intermediate between the analogous distance in the ideal A- and B-forms of the DNA [7]. However, the data at 75% and 81 % RH closely resembles the ideal B-DNA distance (4.91 Å) for adjacent methyl groups at a dT8-^{5Me}dC9 dinucleotide step.

It is also of interest to compare the DRAWS data with distances derived from crystal structures for the methylated (MC9) and brominated (MPD 7 and MPD 20) dC9 derivatives (Tables 5.1 and 5.2). Within each crystal structure, the symmetry of the two strands is broken, producing two sets of internuclear distances. This break in symmetry is most likely the result of crystal packing forces. Partridge and Salisbury's X-ray diffraction study of the methylated analogue indicates that the dC9-CH_3 is separated by 4.60 Å or 4.70 Å from the methyl group of dT8. Judging from this structure alone, it appears that methylation incurs no perturbation of the dT8-dC9 CH_3-CH_3 distance. The X-ray structure for the MPD 20 derivative indicates a 0.5 Å reduction in the 5-Br to dT8-CH_3 distance (4.28 Å) of one strand relative to the dC9-H5 to dT8-

CH_3 distance in the native DNA. However, this distance in strand 2 is slightly longer (4.62 Å).

In contrast, the carbon data at 66% RH suggests that the C2-C2 distance between dT8 and ^{5Me}dC9 (3.5 ± 0.2 Å) is slightly shorter than the comparable distance in the native DNA (3.94 and 3.97 Å). The MC9 derivative, in comparison, only indicates a very minor decrease in this distances (approximately 0.2 Å). The MPD 20 heavy-atom derivative has slightly longer ^{5Br}dC9-C2 to dT8-C2 distances (3.88 Å or 3.95 Å) than the methylated analogue. The discrepancies between the amorphous powder and crystalline DNA samples are not entirely surprising since the crystallization conditions for the 5-methylcytidine and bromine derivatives were considerably different than the conditions used to prepare the samples in this study.

It is not apparent, gauging from the scatter in internuclear distances among the three crystal structures and our DRAWS measurements, whether cytosine methylation distorts base stacking of the dT8pdC9 junction. It is likely that the effect of methylation on local structure is so minor as to be imperceptible given the current resolution (and the effects of crystal packing forces) of the solid-state NMR and crystallographic data. In order to definitively determine the mutual orientation (base stacking) of these two pyrimidine rings, it would be necessary to conduct five additional dipolar coupling measurements using a series of doubly labeled DNA oligonucleotides [17]. An alternative is to conduct a single double quantum DRAWS measurement on the doubly dT8-$^{13}C_2$, ^{5Me}dC9-$^{13}C_2$ labeled DNA sample (see ref. [57]). A future direction of this project is to conduct the DQ-DRAWS experiment as well as repeat the DRAWS measurements in frozen solution for both the unmethylated $^{13}C_2$-dT8, $^{13}C_2$-dC9 control sequence, [d(CGCGAATTCGCG)]$_2$ and the methylated dC9 dodecamer. By carrying out the measurements in frozen solution, it will be possible to minimize motional processes that can complicate the collection of DRAWS data at higher hydration levels. These additional distance and orientational measurements will be neces-

sary to make any firm conclusions about the effect of methylation on the dT8-dC9 step.

5.7 Notes to Chapter 5

[1] Dickerson, R.E. and Drew, H.R. (1981) *Proc. Natl. Acad. Sci. (USA)*, **78**, p. 7318.

[2] Partridge, B.L. and Salisbury, S.A., *Structural Studies on Nucleic Acids, Ph.D. Dissertation*, 1996, Cambridge University.

[3] Wüthrich, K., *NMR of Proteins and Nucleic Acids*, New York: John Wiley & Sons, Inc.

[4] Drew, H.R., Wing, R.M., Takano, T., Broka, C., Tanaka, S., Itakura, K., and Dickerson, R.E. (1981) *Proc. Natl. Acad. Sci. (USA)*, **78** (4), p. 2179.

[5] Kopka, M.L., Fratini, A.V., Drew, H.R., and Dickerson, R.E. (1983) *J. Mol. Biol.*, **163**, p. 129.

[6] Mehta, M.A., Gregory, D.M., Kiihne, S., Mitchell, D.J., Hatcher, M.E., Shiels, J.C., and Drobny, G.P. (1996) *Solid State Nuclear Magn. Reson.*, **7**, p. 211.

[7] Zhu, L., *Ph.D. Dissertation*, 1994, University of Washington.

[8] Stringer, J.A., unpublished results.

[9] Stolarski, R., Egan, W., and James, T. (1992) *Biochemistry*, **31**, p. 7027.

[10] Habener, J.F., Vo, C.D., Le, D.B., Gryan, G.P., and Ercolani, L. (1988) *Proc. Natl. Acad. Sci. (USA)*, **85**, p. 1735.

[11] Coll, M., Saal, D., Frederick, C.A., Rich, A., and Wang, A. (1989) *Nucleic Acids Res.*, **17**, p. 911.

[12] Merritt, M.M. (1998), unpublished results.

[13] Herzfeld, J. and Berger, A. (1980) *J. Chem. Phys.*, **73**, p. 6021.

[14] Furberg, S. (1950) *Acta Cryst.*, **3**, p. 325.

[15] Long, J. and Kiihne, S.R. (1998), unpublished results.

[16] Gregory, D.M., *Ph.D. Dissertation*, 1996, University of Washinton.

[17] Gregory, D.M., Mehta, M.A., Shiels, J.C., and Drobny, G.P. (1997) *J. Chem. Phys.*, **107** (1), p. 28.

Table 5.1: Internuclear Distances (Å) for T_7-T_8, T_8-C_9 and T_8-$^{5Me}C_9$ Labeled $[d(CGCGAATTCGCG)]_2$

Spin Pair	W	Ideal A-DNA	Ideal B-DNA	Solution[d]	DRAWS
C_2-C_2 (T7/T8)	a	4.56	3.99	3.84	3.9 ± 0.2
C_2-C_2 (T8/C9)	---	4.56	3.98	3.77	b
C_2-C_2 (T8/MC9) (66%)	5.2	4.56	3.98	3.77	3.5 ± 0.2
C_2-C_2 (T8/MC9) (75%)	8.2	---	---	---	c
CH_3-CH_3 (T8/MC9)	---	4.11	4.91	4.50	---
CH_3-CH_3 (T7/T8)	a,e	3.80	4.75	4.27	4.8 ± 0.3
F_5-F_5 (T7/T8) (75%)	b	---	---	---	4.7 ± 0.2
F_5-F_5 (T7/T8) (81%)	b	---	---	---	4.9 ± 0.2
F_5-F_5 (T8/MC9) (75%)	12.7	---	---	---	5.0 ± 0.2
F_5-F_5 (T8/MC9) (81%)	14.7	---	---	---	5.0 ± 0.2

[a]Frozen solution (see ref [6]). [b]Quantity to be measured. [c]Quantity not measurable. [d]Solution values from Zhu (see ref. [7]). [e]Quantity measured at 75% RH and 81% RH.

Table 5.2: Internuclear Distances (Å) for T_7-T_8, T_8-C_9 and T_8-$^{5Me}C_9$ Labeled $[d(CGCGAATTCGCG)]_2$

Spin Pair	Dickerson Crystal		MC9 Crystal[a]		MPD 7 Crystal[a]		MPD 20 Crystal[b]	
Strand	1	2	1	2	1	2	1	2
C_2-C_2 (T8/MC9)	---	---	3.71	3.83	4.01	4.16	3.88	3.95
C_2-C_2 (T7/T8)	4.00	4.07	4.19	3.95	4.14	3.90	4.18	4.09
C_2-C_2 (T8/C9)	3.94	3.97	---	---	---	---	---	---
CH_3-CH_3 (T8/MC9)	4.79[c]	4.57[c]	4.70	4.60	4.37	5.03	4.28	4.62
CH_3-CH_3 (T7/T8)	4.66	4.52	4.83	4.71	5.02	4.34	4.27	4.59

[a]Taken from PDB coordinates (266D) (ref. [2]). [b]MPD 7 (7°C) is straight. MPD 20 (20°C) is bent 14° (see ref. [5]).
[c]Value measured from dT8-CH_3 to dC9-H5.

Table 5.3: Chemical Shift Principal Tensor Values and Orientations

	σ_{11}	σ_{22}	σ_{33}	σ_{iso}	α	β	γ
C2	214.00	155.8	93.1	154.3	268°	137°	235°
C1'	111.3	89.3	65.8	88.8	131°	128°	12°
C2'	55.2	70.6	89.9	71.9	227°	65°	163°
C3'	31.8	58.8	97.9	62.8	59°	169°	100°
C5'	26.7	51.7	90.5	56.3	37°	133°	347°

$|\sigma_{33}-\sigma_{iso}| \geq |\sigma_{11}-\sigma_{iso}| \geq |\sigma_{22}-\sigma_{iso}|$ values relative to TMS. Angles related the PAS of the chemical shift tensor to the crystal frame by the rotations $R(\alpha, \beta, \gamma)$ (see Section 4.10 for details).

Table 5.4: DRAWS Simulation Parameters for Cytidine Monomer

Spin-Pair	Distance (Å)	T_2^{SQ} (ms)	T_2^{DQ} (ms)
C2-C1'	2.4 ± 0.2	---	1.7
C2	---	10.0	---
C1'	---	5.0	---
C2-C2'	3.1 ± 0.2	---	4.0
C2	---	8.7	---
C2'	---	4.5	---

Table 5.5: DRAWS Simulation Paramters for DNA Oligonucleotides

Spin-Pair	W	Distance (Å)	T_2^{SQ} (ms)	T_2^{DQ} (ms)
^{5F}dU8-^{5F}dC9 DNA				
75% RH	12.7	5.0 ± 0.2	2.5	0.83
81% RH	14.7	5.0 ± 0.2	2.6	0.50
84% RH	16.1	*	*	*
dT8-^{5Me}dC9 DNA				
66% RH	5.2	3.5 ± 0.2	14.3 ± 0.2	2.5
75% RH	8.2	*	*	*

*Quantity not measured.

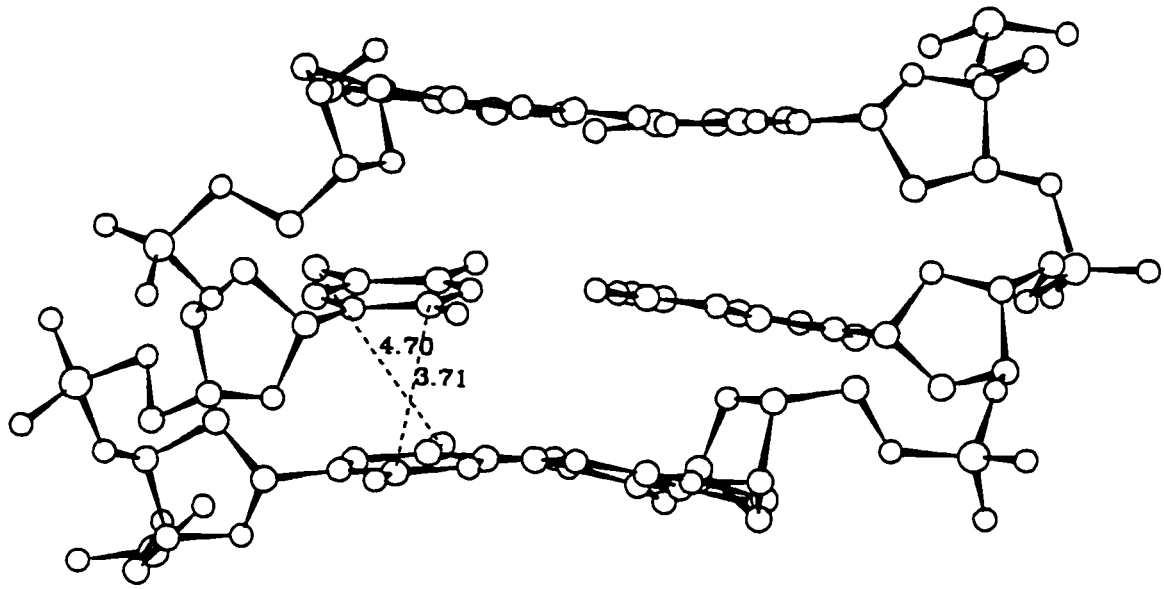

Figure 5.1: dT8-^{5Me}dC9 step in the crystal structure of the dodecanucleotide, [d(CGCGAATT^{5Me}CGCG)]$_2$. Internuclear distances between dT8-C_2 and ^{5Me}dC9-C_2 (3.71 Å) and the dT8-CH_3 and ^{5Me}dC9-CH_3 (4.70 Å) appear as dashed lines.

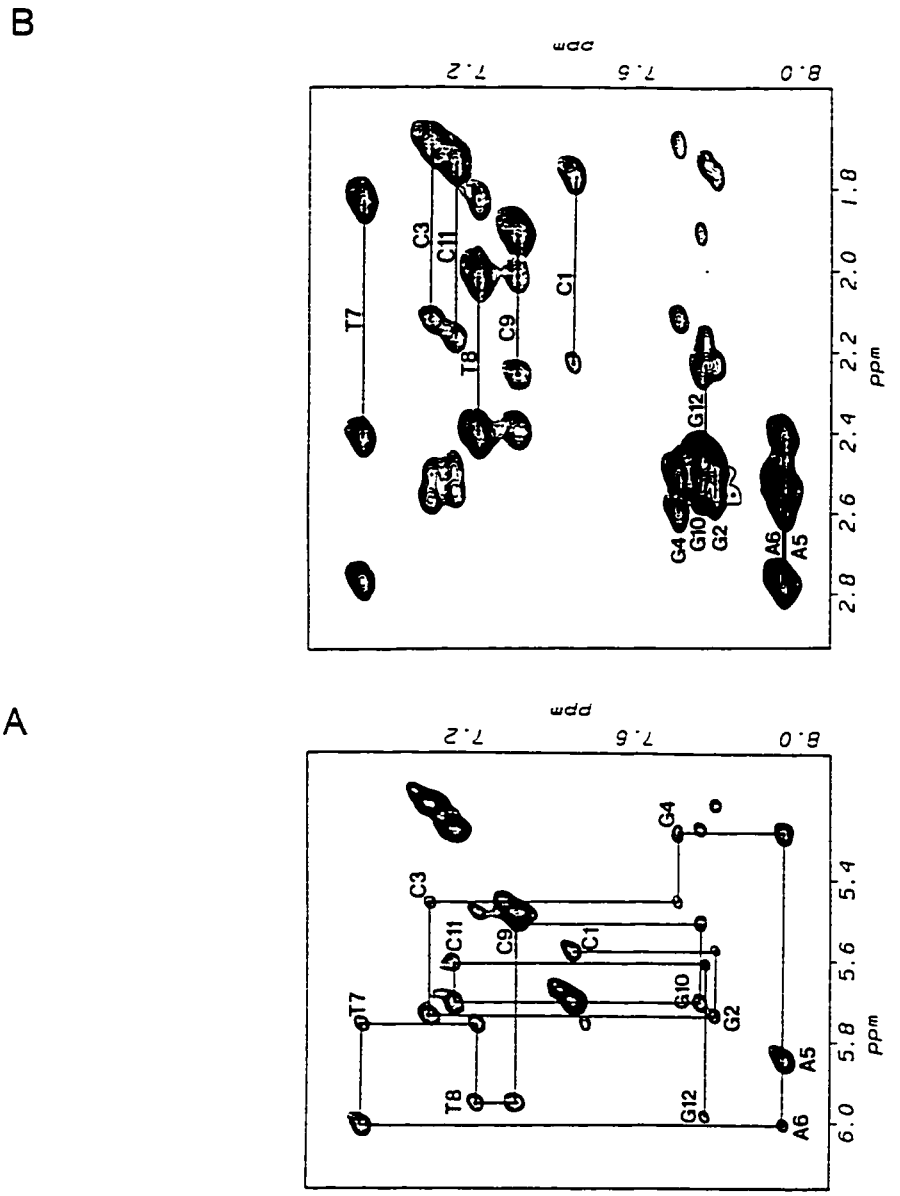

Figure 5.2: Sequential assignment of the H6/H8-H1' (A) and H6/H8-H2'/H2" (B) regions of the 120 ms ^{1}H-^{1}H NOESY spectrum of $[d(CGCGAATTCGCG)]_2$.

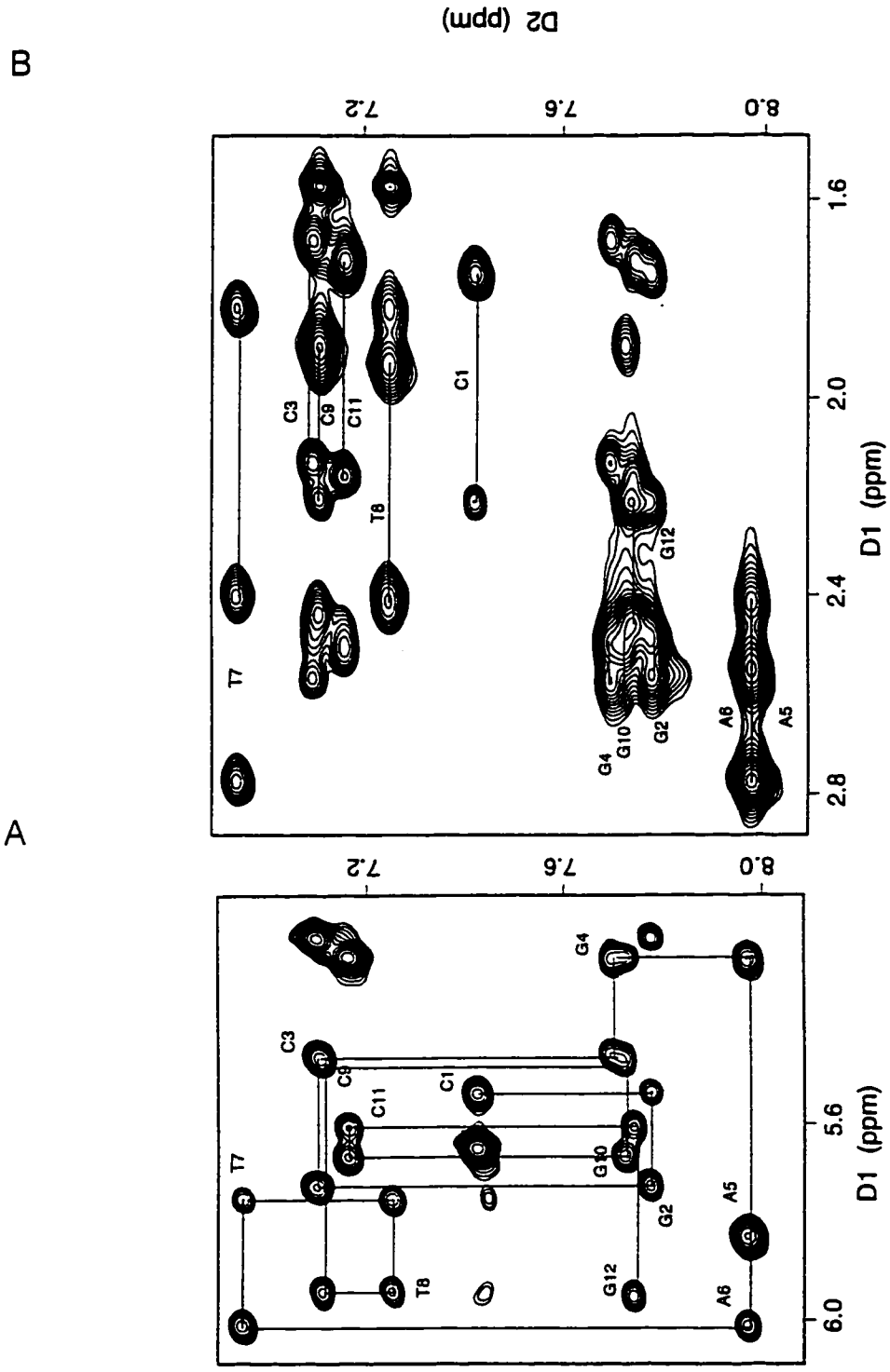

Figure 5.3: Sequential assignment of the H6/H8-H1' (A) and H6/H8-H2'/H2" (B) regions of the 150 ms ^{1}H-^{1}H NOESY spectrum of [d(CGCGAATT^{5Me}CGCG)]$_2$.

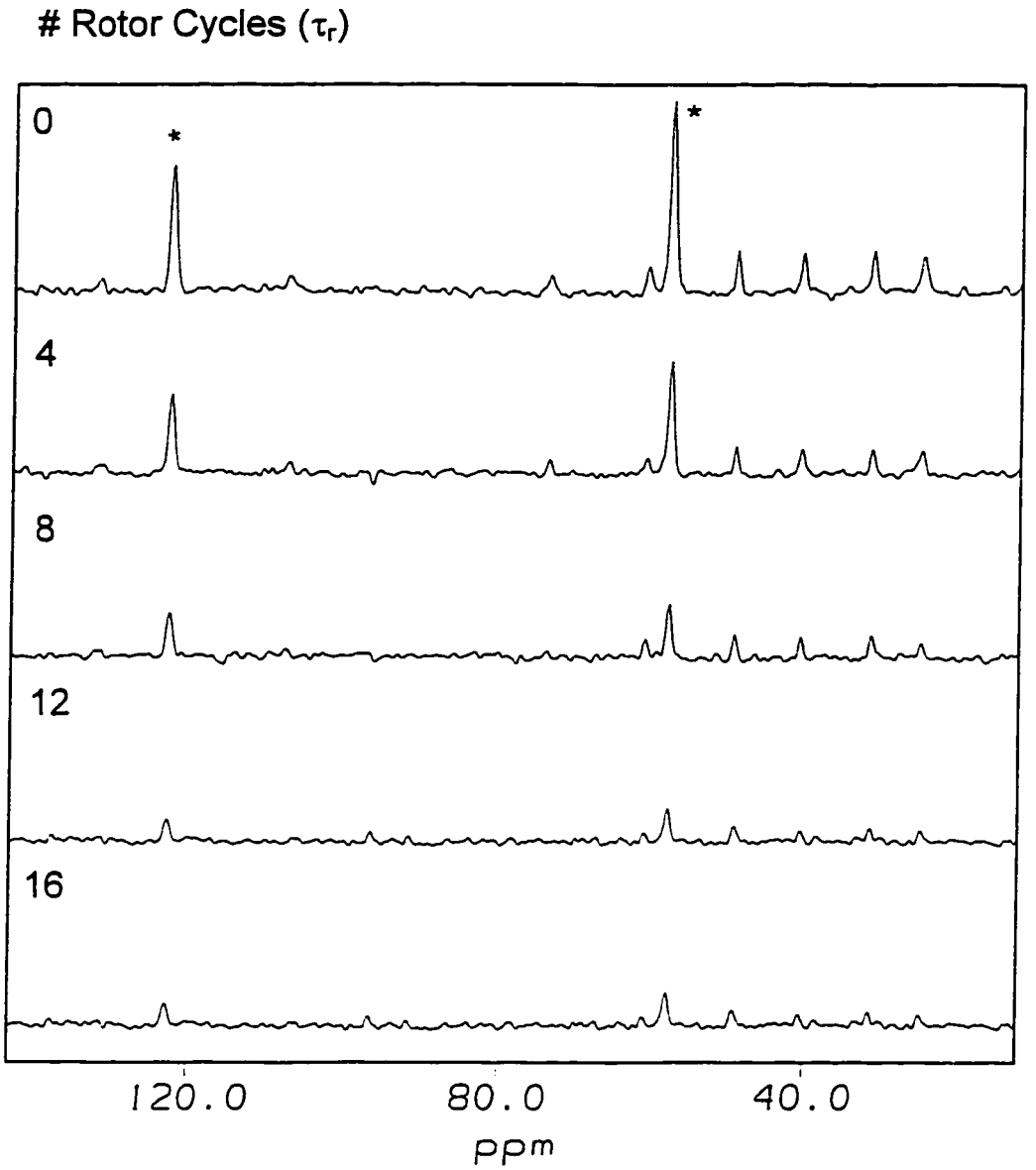

Figure 5.4: Experimental DRAWS results for [2,1'-$^{13}C_2$] cytidine at a spinning speed of 4901Hz. Spectra are shown for different numbers of DRAWS mixing periods to illustrate the decay of Iy+Sy magnetization as a function of increasing number of rotor cycles. Spectra are normalized to the τ_r=0 data set. The isotropic C2 (downfield) and C1' (upfield) chemical shifts are marked with an asterisk. The spectra are integrated to produce a DRAWS dephasing curve.

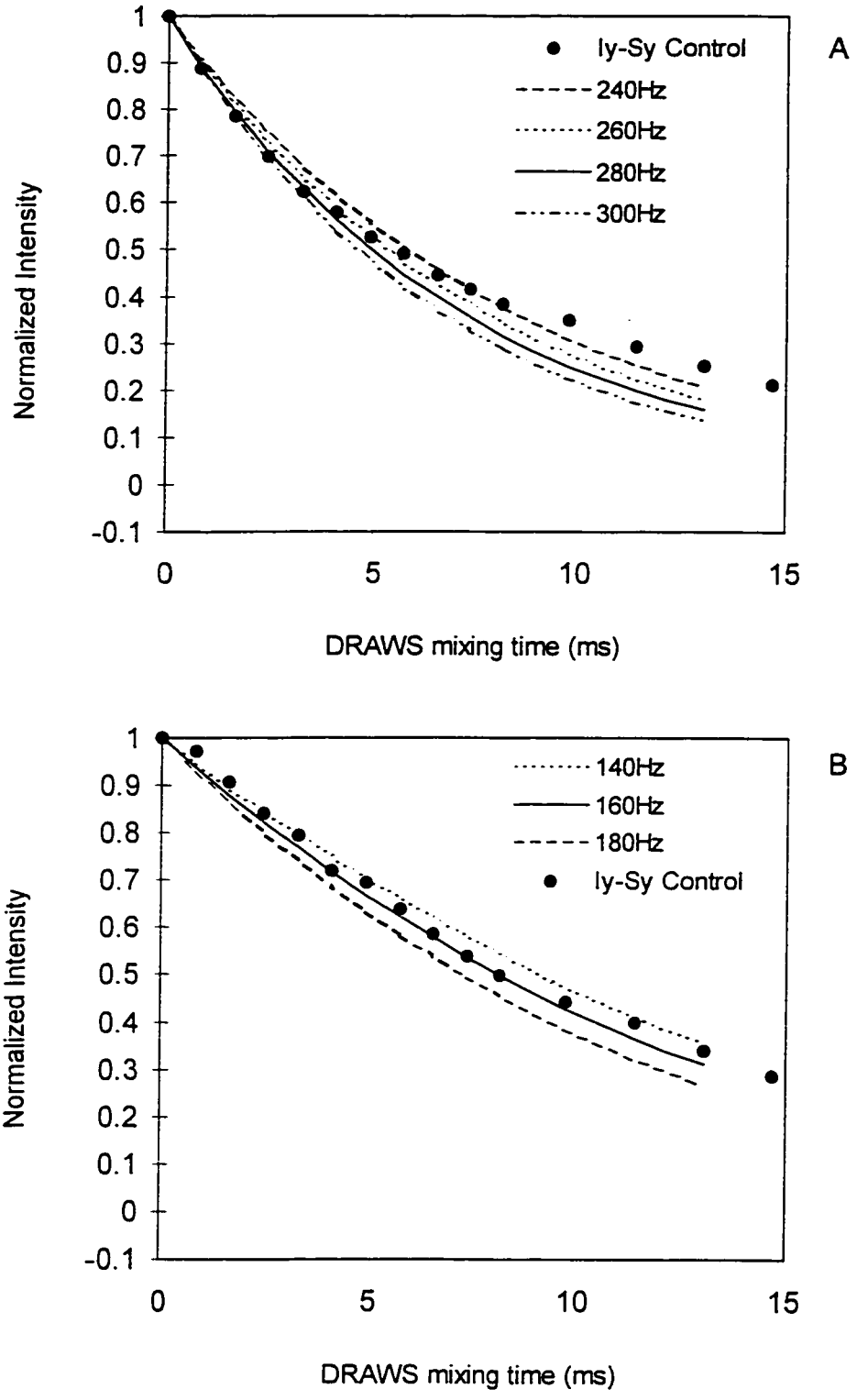

Figure 5.5: Iy-Sy control experiments and simulations for [2,1'-$^{13}C_2$] cytidine: (A) C1' decay curve fit with a SQ damping rate of 280 Hz. (B) C2 decay curve fit with a SQ damping rate of 160 Hz.

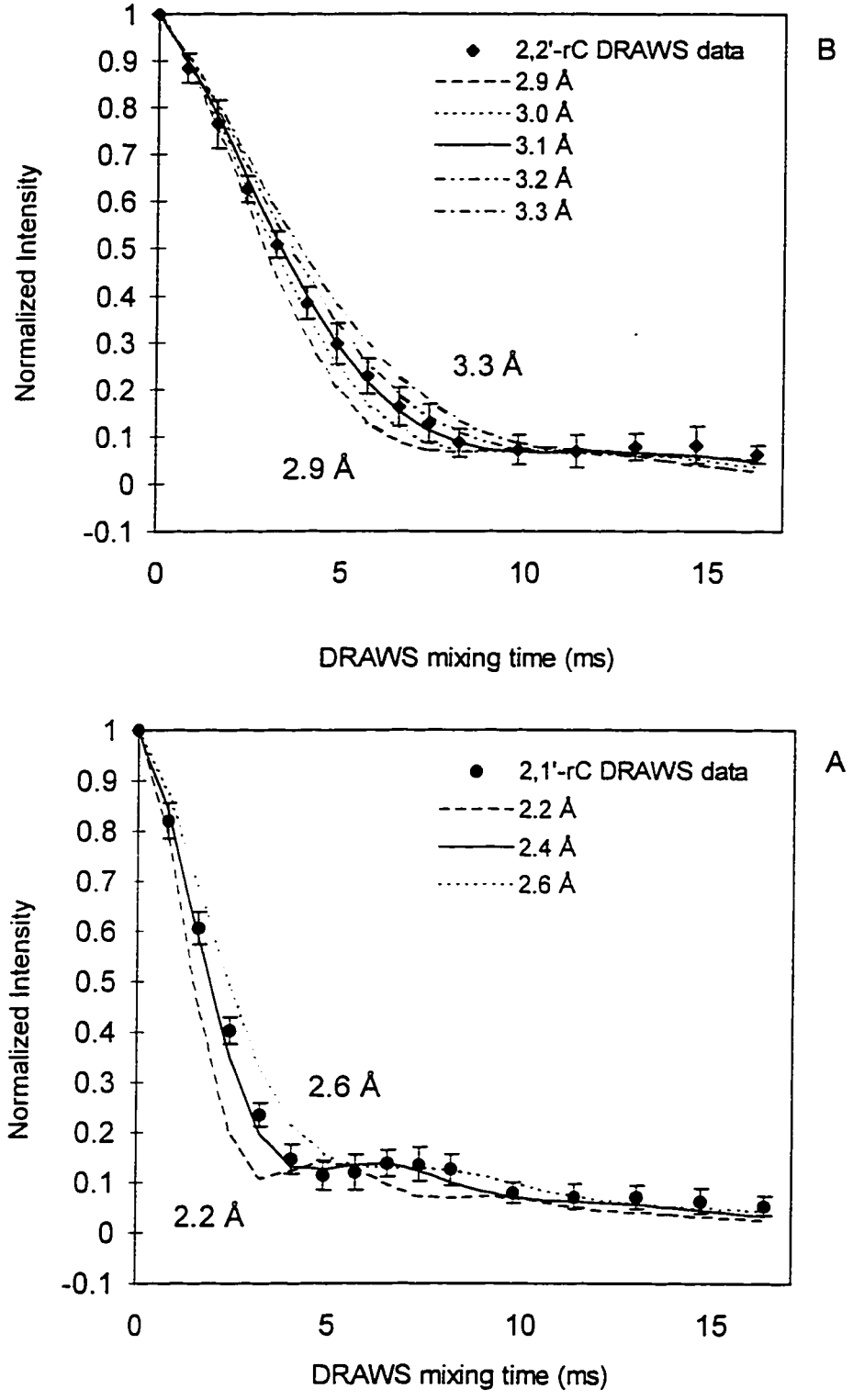

Figure 5.6: DRAWS experiments and simulations: (A) [2,1'-$^{13}C_2$] cytidine data fit with a distance of 2.4 ± 0.2 Å and a DQ damping rate of 600 Hz, (B) [2,2'-$^{13}C_2$] cytidine data fit with a distance of 3.1 ± 0.2 Å and a DQ damping rate of 250 Hz.

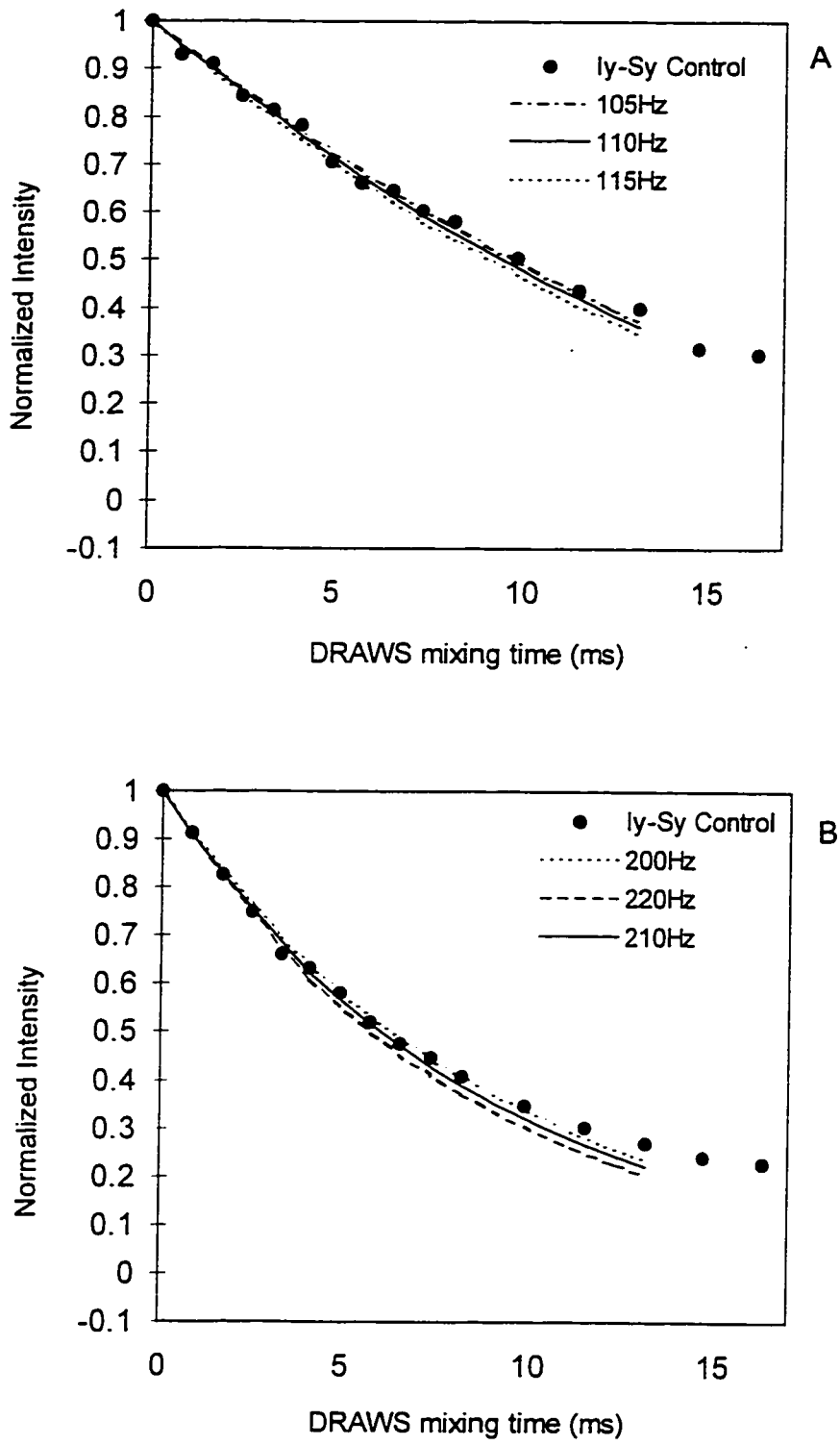

Figure 5.7: Iy-Sy control experiments and simulations for [2,2'-$^{13}C_2$] cytidine: (A) C2 decay curve fit with a SQ damping rate of 110 Hz. (B) C2' decay curve fit with a SQ damping rate of 210 Hz.

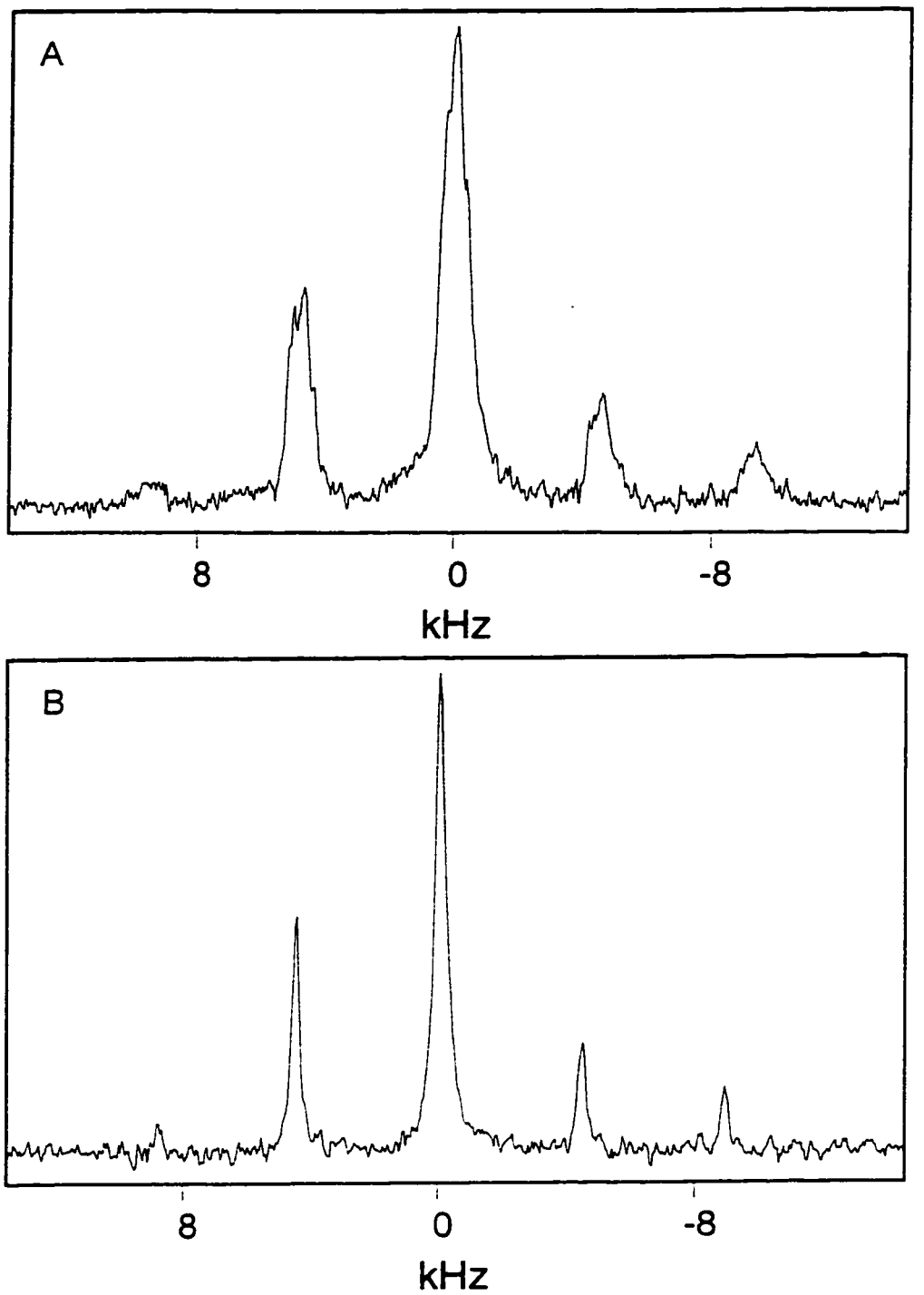

Figure 5.8: MAS spectra of ^{5F}dU8, ^{5F}dC9 dodecamer at 75% RH (A) and 81% RH (B), taken at 4651 Hz and 4425 Hz, respectively. A reduction in linewidths from 958 Hz to 447 Hz accompanied the increase in hydration from 12.7 to 14.7 waters per nucleotide.

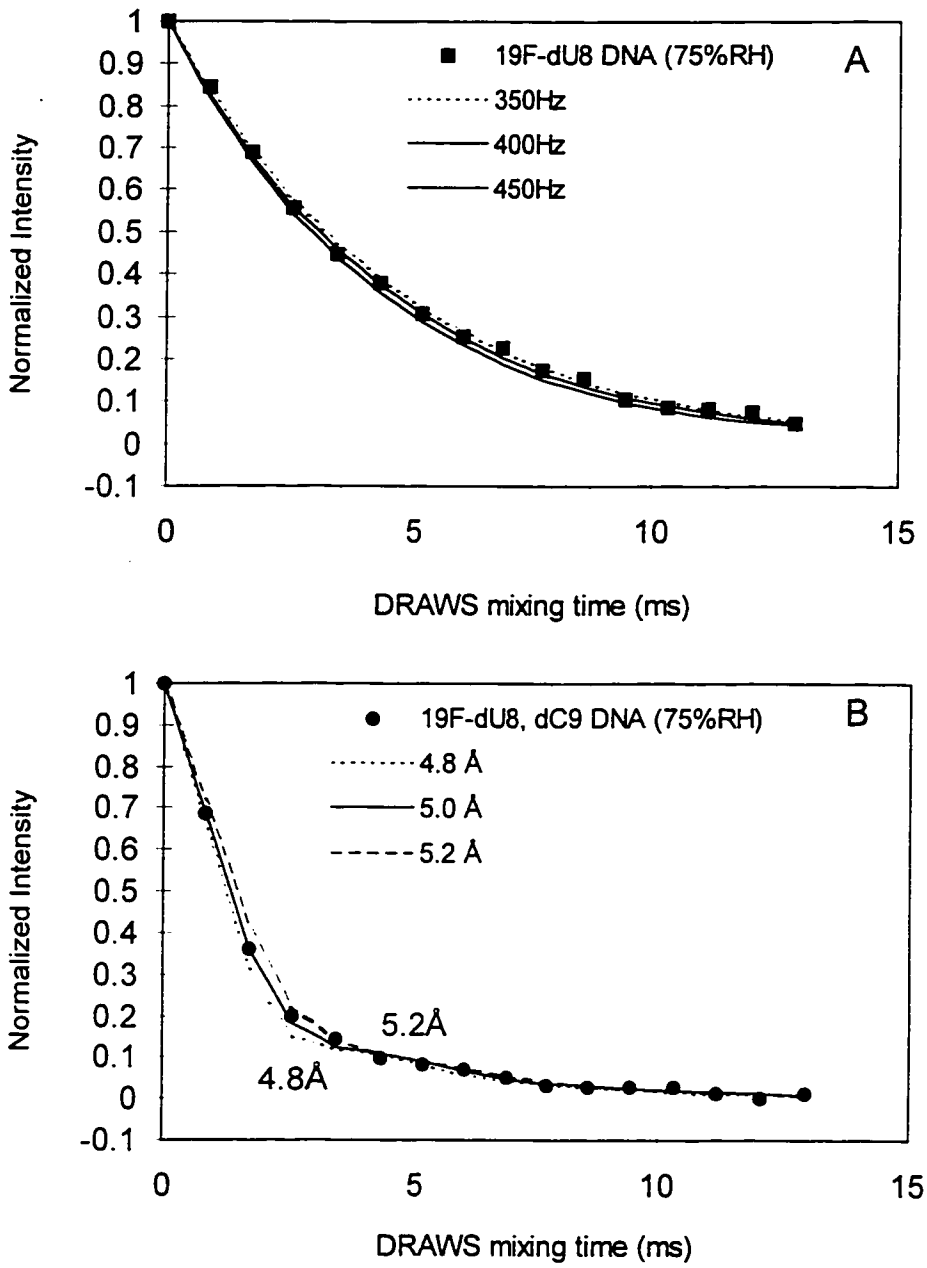

Figure 5.9: (A) DRAWS control experiment and simulations for ^{5F}dU8 dodecamer at 75% RH. Decay curve fit with a SQ rate of 400 Hz. (B) DRAWS experiment and simulations for ^{5F}dU8,^{5F}dC9 dodecamer at 75% RH at 4651Hz. Decay curve fit with a dipolar coupling constant corresponding to 5.0 ± 0.2 Å.

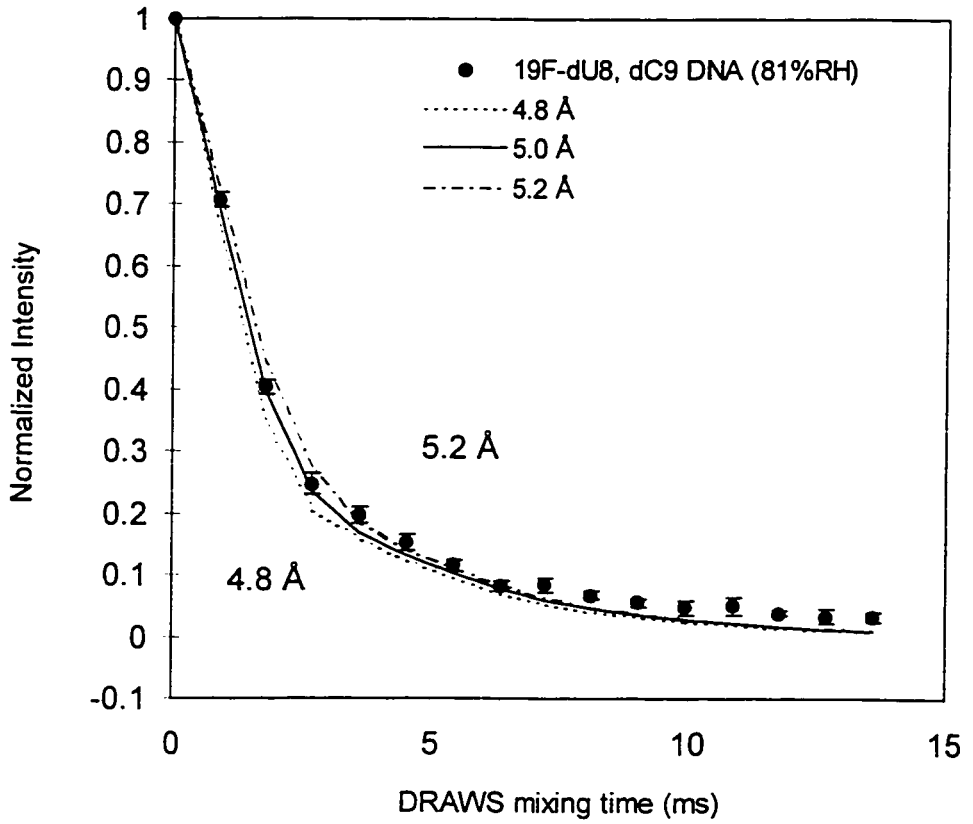

Figure 5.10: Experimental and simulated DRAWS magnetization decay curves for ^{5F}dU8,^{5F}dC9 dodecamer (81% RH) collected with a spin rate of 4425 Hz. Experimental data was fit with a dipolar coupling constant of 750-950 Hz, which corresponds to 5.0 ± 0.2 Å. SQ and DQ damping constants of 2.6 ms and 500 ms were included in the simulation.

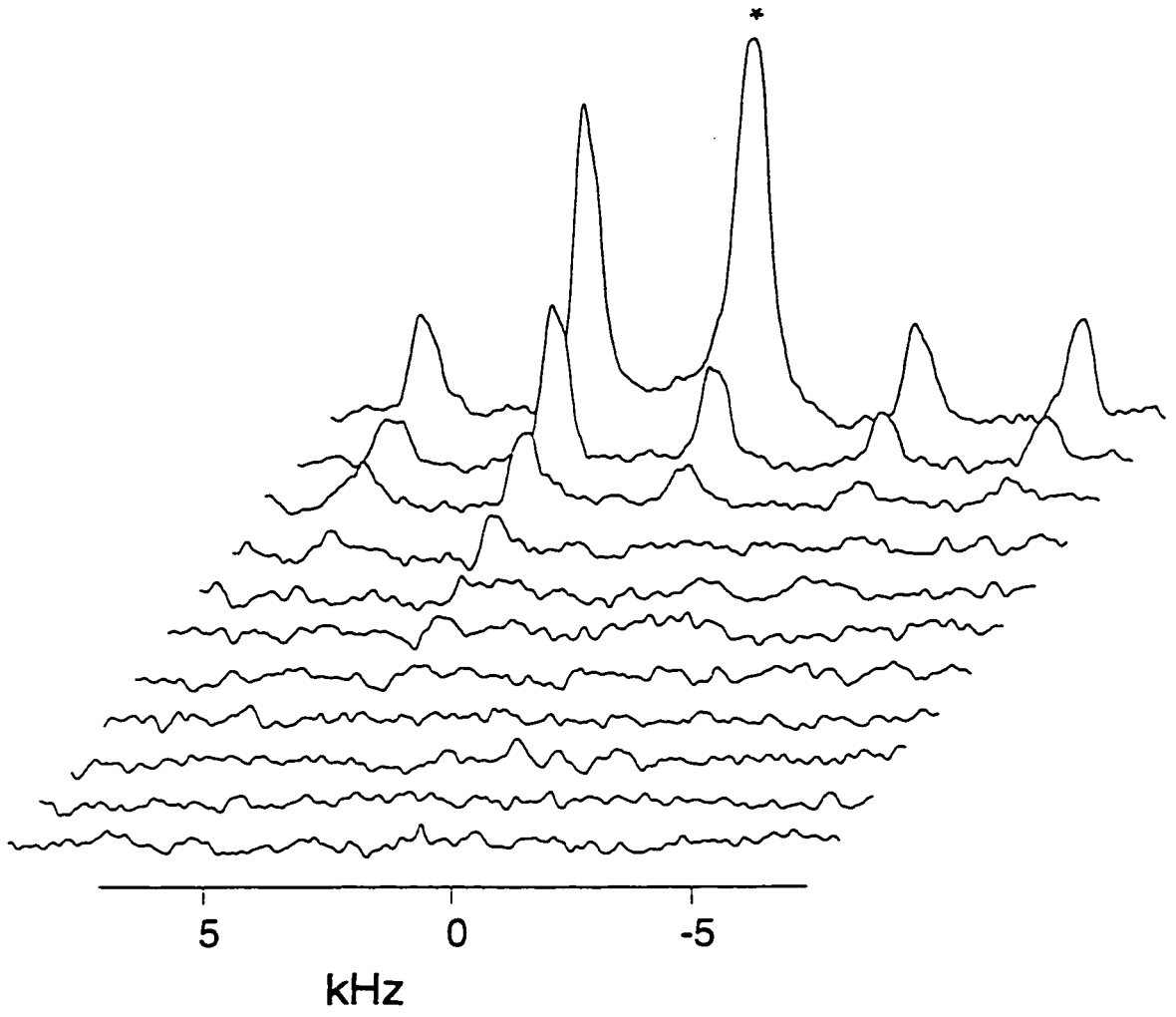

Figure 5.11: Experimental T_2 echo data for ^{5F}dU8, ^{5F}dC9 dodecamer at 84% RH taken at 5680 Hz. The central isotropic peak (labeled with an asterisk) and the sidebands decay with different time constants. The decay of signal intensity for the isotropic peak was fit to a single exponential with a time constant of 1.6 ± 0.2 ms. The decay of sideband intensities was fit to a single exponential with a T_2 of 2.6 ± 0.2 ms. Spectra are plotted in reverse order so as not to obscure decaying peaks.

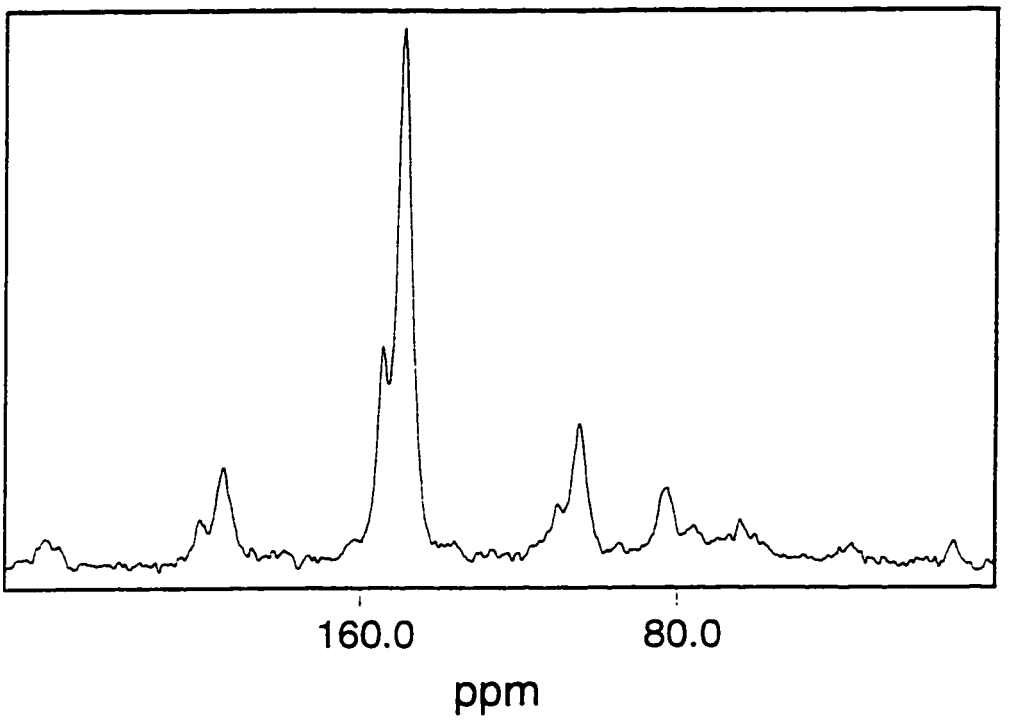

Figure 5.12: 4525 Hz CP-MAS spectrum of the DNA dodecamer, $[d(CGCGAATT^{5Me}CGCG)]_2$, containing ^{13}C labeled C2-thymidine at dT8 and a C2 labeled 5-methylcytidine at dC9 at a hydration level of 66% RH. The resonances of the C2 labeled carbon atoms are only partially resolved.

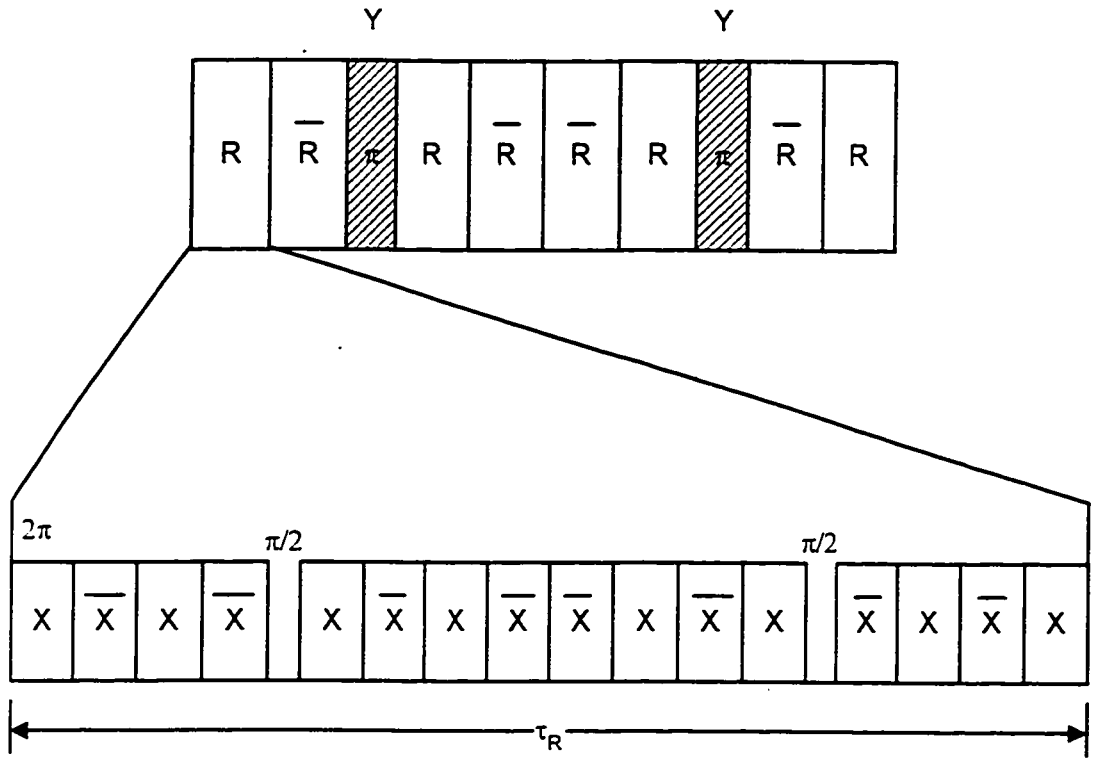

Figure 5.13: DRAWSX control experiment pulse sequence for one rotor period. The phasing follows the description given in Figure 3.1. A delay equivalent to the length of a 90° pulse occurs after the first four 360° and after the next eight 360° pulses. The DRAWSX control experiment supercycle includes a 180° pulse after two and six repetitions of the supercycle.

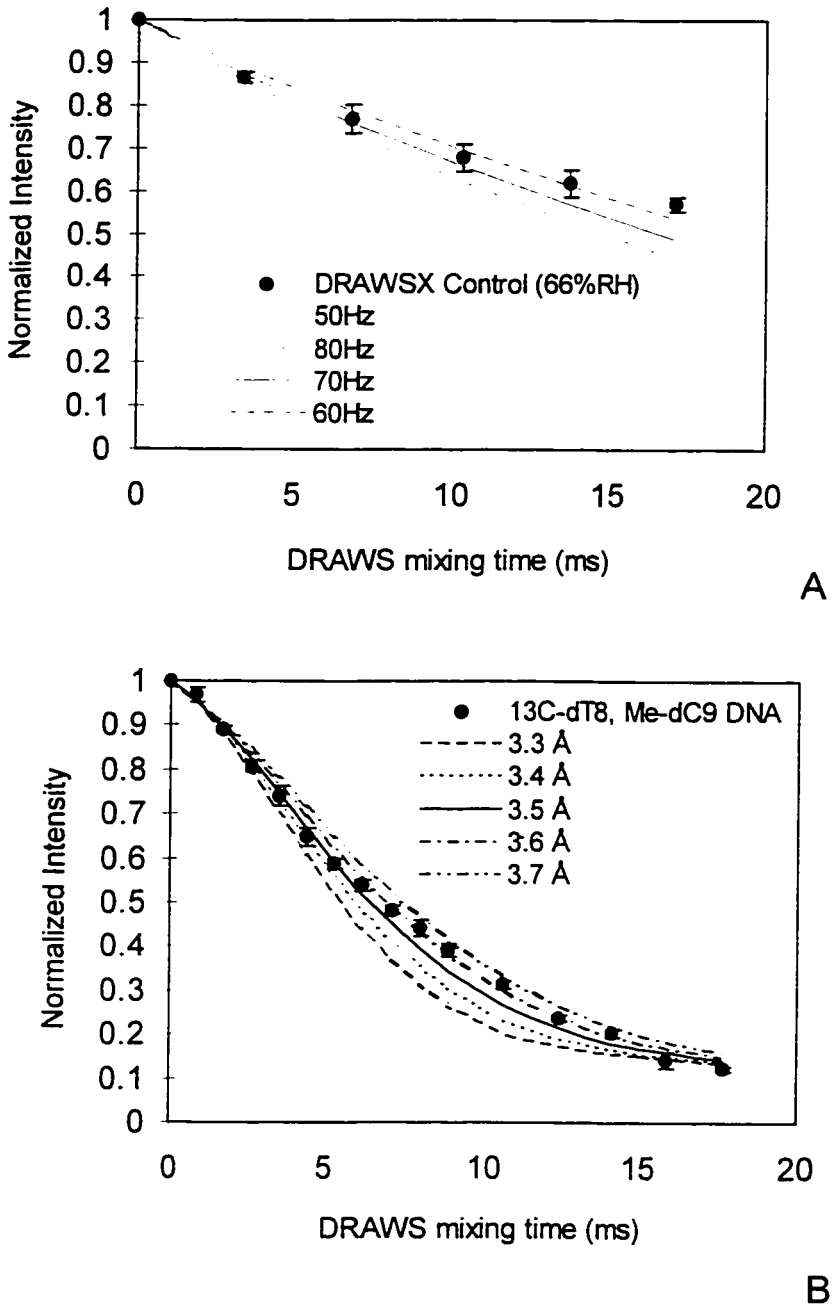

Figure 5.14: Experimental and simulated DRAWS magnetization decay curves for [2-^{13}C]-dT8, [2-^{13}C]-^{5Me}dC9 DNA dodecamer (66% RH). (A) DRAWSX control experiment was conducted at a spinning speed of 2331 Hz and fit with a SQ decay constant of 14.3 ms. (B) Experimental DRAWS data was collected at a spin rate of 4525 Hz. DRAWS decay curve was fit with a dipolar coupling constant of approximately 177 Hz, corresponding to an internuclear distance of 3.5 ± 0.2 Å. A DQ damping rate of 400 Hz was included in the simulation to fit later time points.

Chapter 6
Two-Dimensional Dipolar Recoupling Results

6.1 Chapter Overview

This chapter presents results from two-dimensional dipolar recoupling experiments for the ^{13}C chemical shift assignment of uniformly ^{13}C, ^{15}N labeled cytidine, uridine, adenosine, guanosine, 2'-deoxyguanosine, and thymidine in the solid-state. Spectral assignments and observations are based on a combination of two-dimensional Radio Frequency Driven Dipolar Recoupling (RFDR) and Dipolar Recoupling with a Windowless Sequence (DRAWS), one-dimensional CP-MAS, and X-ray diffraction experiments for both amorphous and polycrystalline samples. One-dimensional ^{13}C CP-MAS spectra of several crystalline forms of the 2'-deoxycytidine and 2'-deoxyadenosine appear in this chapter, as well. Additionally, ^{15}N CP-MAS spectra were collected and assigned for each of the ribonucleosides. The ^{13}C and ^{15}N chemical shift data is compiled in Tables 6.1, 6.2, and 6.3. The corresponding solution-state ^{13}C and ^{15}N chemical shift values appear in Tables 6.3 and 6.4. The chapter concludes with a brief commentary about the multiple conformations that can be achieved by nucleoside monomers in homogenous and heterogeneous environments.

6.2 Using Chemical Shift to Probe Structure in the Solid-State

Both the anisotropic and isotropic ^{13}C NMR chemical shift are highly sensitive to perturbations in the local electronic environment surrounding the observed nucleus. Numerous single crystal NMR studies have shown that the magnitude and orientation of the anisotropic ^{13}C chemical shift tensor can provide highly detailed

structural information [1]. Because the local molecular geometry is deduced by relating the principal axis system of the chemical shift tensor in the molecular frame, these measurements are quite sensitive to subtle changes in local molecular conformation and hydrogen bonding. Such single crystal investigations require the preparation of pristine single crystals, preferably devoid of conformational disorder, and the existence of favorable symmetry properties to make this a viable technique. Single crystal NMR studies of various carbohydrates (e.g. glucose, erythritol, and methyl glycosides) have been reported in the literature [2-4]. However, due to the experimental difficulties of this approach, no such measurements have been performed on nucleoside monomers to our knowledge.

The isotropic chemical shift parameter can also be highly indicative of molecular configuration in the solid-state [5]. As was discussed in Chapter 2, solid-state NMR techniques such as CP-MAS can be used to average the anisotropy of the chemical shielding interaction, revealing only the isotropic chemical shift. The CP-MAS technique has been applied to numerous carbohydrates over recent years [5-7]. These investigations have revealed the remarkable degree of conformational flexibility that is realized by carbohydrates in the solid-state. Santos et al. have successfully used solid-state ^{13}C MAS in conjunction with cross-polarization to monitor isotropic chemical shifts for different 2'-deoxynucleoside conformations [8]. CP-MAS NMR spectra were collected and assigned for a series of deoxynucleosides and deoxynucleotides, crystallized in a variety of biologically relevant forms, in order to correlate chemical shifts with the known furanose ring conformation. It was found that 3'-endo conformers have 3' and 5' chemical shifts significantly upfield from the C2'-endo and C3'-exo conformers. These researchers attributed C3' and C5' upfield chemical shifts (~5 ppm) in C3'-endo deoxynucleoside derivatives to steric interactions between the axial 3' proton and the base and 5' carbon on the endo side of the furanose ring. These effects are illustrated in Figure 6.1, which presents the CP-MAS spectra for 2'-deoxycytidine hydrochloride and 2'-deoxycytidine-5'-phosphate monohydrate. Note

the upfield-shifted C3' and C5' chemical shifts for the hydrochloride derivative, which is known to reside in the C3'-endo conformation in the crystalline state [9]. The 2'-deoxycytidine-5'-phosphate monohydrate C3' and C5' chemical shift resonances are indicative of a sugar ring in the C2'-endo/C3'-exo conformation [10, 11]. Differences in the C1' and C4' chemical shifts are also evident in these spectra, with significantly better resolution between these resonances for the C3'-exo conformers. Santos and coworkers have suggested that large C1' chemical shift changes in the CP-MAS spectra of 2'-deoxynucleosides could be related to changes in the glycosidic torsion angle. Although no complementary study has been published on ribonucleosides, it may be assumed that isotropic chemical shifts should also be indicative of differences in the conformation of the ribose sugar ring. The results in the following sections will provide evidence that this is indeed the case.

6.3 Two-Dimensional Chemical Shift Correlation Experiments

Polycrystalline nucleosides generally produce ^{13}C CP-MAS spectra with well-resolved chemical shifts in both the sugar ring and aromatic regions of the spectrum. However, this is not necessarily the case for samples in heterogeneous environments (i.e. lyophilized samples). Sample heterogeneity results in chemical shift dispersion from the presence of multiple molecular conformations. This phenomenon is especially true for high molecular weight systems, in which poor chemical shift resolution complicates the spectral assignment. Consequently, natural abundance CP-MAS studies of large biomacromolecules have been hindered due to insufficient resolution. Ultimately, we would like to monitor the effect of local conformational changes on NMR parameters such as the chemical shift and the dipolar coupling of the individual nucleoside constituents in high molecular weight oligonucleotides.

One method used to improve resolution is with a two-dimensional NMR technique. Two-dimensional NMR has been widely applied to biomacromolecules in the

solution-state, but comparatively few reports on biological systems in the solid-state exist in the literature. This is primarily due to the technical difficulties of the technique and the requirement for isotopically enriched samples. The two-dimensional experiments that have been implemented in this dissertation correlate chemical shift resonances for dipolar coupled ^{13}C nuclei in the presence of MAS. An overview of these phase-sensitive two-dimensional dipolar recoupling methods appears in Chapter 3. The subsequent sections of this chapter present one- and two-dimensional NMR results for the chemical shift assignment (^{13}C and ^{15}N) of each of the naturally occurring nucleosides in the solid-state.

6.3.1 Cytidine

Figure 6.2 shows the one-dimensional CP-MAS spectrum of polycrystalline cytidine. The relatively narrow and unsplit crosspeaks indicate the presence of only one molecular conformation in the crystal asymmetric unit, in accordance with published X-ray crystallography data [12, 13]. The X-ray structure of cytidine indicates that the molecule resides in a C3'-endo sugar conformation and an anti orientation about the glycosidic bond. The carbon skeleton for the furanose moiety can be readily traced by inspection of the 1 cycle DRAWS data set (Figure 6.3). Correlations with directly coupled neighboring carbon atoms yield strong, negative cross-peaks: C1' (88.8 ppm) is correlated with C2' (71.9 ppm), C2' with C3' (62.8 ppm), C3' with C4' (80.1 ppm), and C4' with C5' (56.3 ppm). This initial assignment can be confirmed by inspection of the 2 cycle DRAWS spectrum (Figure 6.4). Additionally, positive crosspeaks (indicated by boxed connectivities) due to indirect relay effects are distinguishable in both data sets. The C1'-C3' and C3'-C5' sugar ring connectivities appear as strong positive crosspeaks, while the C2'-C4' correlation is slightly weaker. Two weak negative connectivities between C1'-C4', C2'-C5', and C2-C2' are evidence of longer range couplings. The RFDR spectra (for 1 and 2 RFDR mixing periods) are

shown for comparison in Figures 6.5 and 6.6, respectively. Crosspeak intensities in the crowded sugar ring region are quite intense after two RFDR mixing cycles for both directly bonded and next nearest neighboring ^{13}C nuclei, quickly complicating the spectrum.

The C2 carbon (154.3 ppm) may be identified by a strong negative cross-peak to C1' (88.8 ppm) in the two cycle DRAWS data set. Additionally, there is a weak positive connectivity between the aromatic C2 nucleus and C2' on the ribose ring. This connectivity is also apparent in the two cycle RFDR spectrum. The negative crosspeak to the C2 resonance in the aromatic region of the spectrum is especially strong, suggesting a connectivity with a second carbonyl atom, C4 (164.0 ppm). The remaining unassigned resonance (at 138.9 ppm) that is correlated to C4 has been assigned to C6. The two cycle RFDR data set also reveals weak crosspeaks between C2-C5 and C4-C5. The directly bonded C6 and C5 (92.0 ppm) atoms show only a very weak crosspeak in the two cycle RFDR or DRAWS data sets. The low intensity of the C5 and C6 resonances, which is also apparent in the CP-MAS spectrum, may be due to insufficient proton decoupling. The weak C4-C6 crosspeak may also be attributed to the low intensity of the C6 nucleus. Upon lyophilization, the 1-D CP-MAS spectrum of the cytidine monomer indicated only minimal discrepancies between amorphous and crystalline states (data not shown). The sugar ring resonances were only very slightly broadened, and neither significant chemical shift changes nor increased chemical shift dispersion was apparent for any of the carbon atoms in the pyrimidine heterocycle.

6.3.2 Uridine

The CP-MAS spectra for polycrystalline and lyophilized uridine appear in Figure 6.7. Comparison of these spectra reveals that there is little difference (apart from discrepancies in the number of rotational sidebands) between the isotropic

chemical shifts of the uridine monomer in lyophilized and crystalline forms. The uridine monomer in both samples clearly exhibits two sets of ^{13}C resonances. The uridine X-ray structure (see Section 4.6) reveals that there are two similar molecules per asymmetric unit cell, each with a C3'-endo furanose ring pucker [14]. Both molecules in the unit cell are also known to reside in the less sterically hindered anti conformation, with only minor differences in glycosidic torsion angle. The presence of either two independent conformers or different physical environments for each of the molecules in the asymmetric unit cell is evidenced by the narrow lines and crystallographic splittings that occur for two sugar ring and all base carbon resonances. Note that the C5 and C6 nuclei exhibit low intensity, as is the case for the cytidine monomer.

Due to the spectral similarities of the polycrystalline and lyophilized forms of uridine, two-dimensional data sets were collected for only the lyophilized material. The full RFDR spectrum (1 mixing cycle) and sequential carbon assignment for lyophilized uridine appears in Figure 6.8. The 1 and 3 cycle DRAWS experiments are shown in Figure 6.9 and Figure 6.10, respectively. Due to small sample size (7 mg of ^{13}C, ^{15}N labeled material), crosspeaks are weak in both RFDR and DRAWS data sets. The carbon skeleton for both conformations of the furanose moiety can be readily traced by inspection of the 1 cycle DRAWS data set. Correlations with directly coupled neighboring carbon atoms yield strong, negative cross-peaks: C1' (89.7 ppm) is correlated with C2' (73.0 ppm), C2' with C3' (66.6 ppm and 64.3 ppm), C3' with C4' (80.0 ppm), and C4' with C5' (59.5 and 56.5 ppm). The sugar ring assignment can be confirmed by inspection of the three cycle DRAWS spectrum. Positive crosspeaks (boxed connectivities) in this data set are due to indirect relay effects that arise at longer mixing times. The C3'-C5', C1'-C3', C1'-C5', and C2'-C4' sugar ring connectivities appear as weak positive cross-peaks. Additionally, a very weak negative connectivities between C1'-C4' is evidence of a longer range coupling.

The C2 chemical shifts (150.2 ppm and 149.3 ppm) may be identified by crosspeaks to C1' (89.7 ppm) from the one cycle RFDR data set and a strong, negative crosspeak in the three cycle DRAWS data set. Each of the C2 resonances is correlated with C4 (166.4 ppm and 164.0 ppm, respectively) and with C6 (140.8 ppm and 138.6 ppm, respectively). A weak positive correlation between C2-C2' is also visible in the 3 cycle DRAWS spectrum. C4 and C6 can be distinguished by comparison with the cytidine data. The remaining unidentified, upfield shifted resonance is assigned to C5 (92.0 ppm). The directly bonded C6 and C5 atoms do not show a crosspeak in either RFDR or DRAWS data sets due to low signal intensity.

6.3.3 Adenosine

2D-DRAWS, 2D-RFDR, and CP-MAS results for polycrystalline and lyophilized forms of the adenosine monomer are presented in this section. Examination of the lyophilized adenosine CP-MAS spectrum (Figure 6.11) clearly indicates the presence of at least two sugar ring conformers and more pronounced chemical shift dispersion than was observed in the spectra of either pyrimidine nucleoside. The sugar ring carbon nuclei can be readily assigned by inspection of the 1 cycle DRAWS data set (Figure 6.12). It is possible to trace out two distinct sequential assignment pathways for each conformer, with a slightly larger population for the upfield shifted species: C1' (90.2 ppm) is correlated with C2' (72.9 ppm), C2' with C3' (69.1 and 66.2 ppm), C3' with C4' (82.0 ppm), and C4' with C5' (62.7 and 56.7 ppm). Spectra for two and three cycles of DRAWS mixing (Figure 6.13 and 6.14, respectively) are useful for elucidating correlations with more weakly dipolar coupled ^{13}C nuclei in the sugar ring. Additional positive crosspeaks (boxed connectivities) between each of the 3' and 5' carbon atoms and between C1' and each of the C3' resonances are visible with two cycles of DRAWS mixing. A weak, negative crosspeak between C1'-C4' and a positive connectivity between C2'-C4' are also evident in this data set. With

three DRAWS cycles, an additional positive peak evolves for C1'-C5'. A weak, negative connectivity from C2' to one of the C5' carbons is evidence of a longer range dipolar coupling. From the 2 and 3 cycle DRAWS data sets, it is possible to correlate the C1' (90.2 ppm) to the C8 carbon (136.6 ppm) and C4 (145.2 ppm). These negative connectivities are quite intense in the 3 cycle DRAWS data set. Furthermore, the coupling between C8 and C4 yields a strong negative crosspeak in the 3 cycle DRAWS data set. C8 also produces a very weak positive crosspeak to C2' with three repetitions of the DRAWS mixing cycle. Inspection of the 1 cycle RFDR spectrum (Figure 6.15) suggests that the resonance at 119.7 ppm belongs to the C5 atom. The C5 assignment is confirmed by the presence of a negative crosspeak in the 2 cycle DRAWS spectrum to C4, which is in turn correlated with C8. The remaining most downfield shifted crosspeak to C5 belongs to C6 (152.9 ppm). C6 is also correlated with C4, by evidence of a weak positive crosspeak in the 3 cycle DRAWS spectrum. The C2 resonance (151.2 ppm) can be identified by a very weak negative correlation with C4 from the 3 cycle DRAWS data set.

The CP-MAS spectra for the polycrystalline form of adenosine appears in Figure 6.11. Inspection of the spectrum indicates that only one dominant molecular geometry is present, as evidenced by a lack of crystallographic splittings. This corroborates the complementary X-ray diffraction data (see Section 4.6) that indicates the presence of only one molecule per asymmetric unit cell [15]. The chemical shift assignment of crystalline adenosine can be established by inspection of the 1 cycle RFDR data set (Figure 6.16). C1' (90.0 ppm) is correlated with C2' (73.0 ppm), C2' with C3' (69.0 ppm), C3' with C4' (82.6 ppm), and C4' with C5' (60.7 ppm). The C8 carbon (135.6 ppm) may be identified by a weak crosspeak to C1'. Connectivities between the remaining unassigned carbon resonances of the aromatic heterocycle appear in Figure 6.16. The C5 resonance at 118.7 ppm is correlated to both C4 (146.0 ppm) and C6 (and/or C2) at 152.6 ppm. Our data for crystalline adenosine, which is known to possess a C3'-endo sugar ring pucker, exhibits a C3' chemical shift (69.0

ppm) that corresponds with the downfield shifted C3' resonance (69.1 ppm) of the lyophilized material. The C5' resonance for crystalline adenosine (60.7 ppm) is intermediate between each of the C5' resonances (62.7 and 56.7 ppm) for the lyophilized form. In order to confirm this preliminary assignment, a CP-MAS spectrum for polycrystalline adenosine-5'-phosphate monohydrate was collected (Figure 6.22). This monomer is known to crystallize with a C2'-endo sugar pucker and a syn base orientation [16]. The C3' and C5' nuclei for this compound resonate at 66.0 and 59.3 ppm, respectively. There are also significant perturbations in the C1' and C4' chemical shifts, which are probably the result of a 5'-phosphate group and the unusual syn base conformation. The C3' chemical shift corresponds with the upfield shifted C3' resonance for the lyophilized adenosine material. However, the C5' resonance falls intermediate between the C5' chemical shifts for the lyophilized compound. Based on these observations for the two different crystalline forms of adenosine, the downfield-shifted set of C3' and C5' resonances for the lyophilized material was tentatively assigned to the conformer with a C3'-endo sugar pucker. The second set of C3' and C5' chemical shifts are attributed to a conformer with a C2'-endo sugar ring conformation.

6.3.4 Guanosine

Our assignment of the guanosine monomer and discussion of its conformation in the solid state is based on a combination of 2D-RFDR and one-dimensional CP-MAS experiments for the lyophilized and polycrystalline material. The single crystal diffraction study of guanosine dihydrate (formed by hydration of guanosine crystals at 20% RH) reveals the presence of two crystallographically independent conformations per asymmetric unit cell. From the single crystal X-ray structure, the sugar ring is known to exist in two distinct conformations, C1'-exo and C2'-endo, and the purine heterocycle may be oriented in the anti position at either 123 or 42 degrees relative to the furanose moiety [17]. The CP-MAS spectrum of the lyophilized form of

guanosine is presented in Figure 6.17. Lyophilized guanosine, in contrast to lyophilized adenosine, does not appear to possess distinctly different puckering modes, however broadened resonances are evidence of substantial chemical shift dispersion. We attribute this additional line broadening to either static and/or dynamic disorder in the conformation of the furanose ring. The one cycle RFDR spectrum and carbon assignment for the lyophilized form of guanosine are shown in Figure 6.18. The sugar ring region of the one cycle RFDR spectrum contains only one set of crosspeaks for each pair of neighboring carbon atoms in the ribose ring. However, several features of this spectrum are particularly noteworthy. The C1' and C4' resonances are not nearly as well resolved as in the spectra of the other three ribonucleoside monomers. The C4' resonance is shifted downfield by 6 ppm relative to the pyrimidines and 4 ppm relative to adenosine. The C1' resonance, in comparison, is shifted slightly upfield (1-3 ppm) relative to the other ribonucleoside monomers. The C2' and C3' chemical shift resonances are also considerably less resolved than the corresponding resonances in either of the pyrimidines. However, the chemical shift difference between the C2' and C3' shifts is equivalent to that for the C2' and the more downfield shifted C3' of lyophilized adenosine. The chemical shifts of the C3' and C5' nuclei correspond with the downfield shifted C3' and C5' resonances of the lyophilized adenosine monomer. The aromatic region of the RFDR spectrum was assigned by comparison with the adenosine monomer. A crosspeak between the resonance at 138.1 ppm and C1' (87.4 ppm) is attributed to the C8 carbon atom in the purine moiety. The C4 (153.1 ppm) resonance is correlated both with the nearby C8 and the C5 nuclei (113.3 ppm). We were not able to confidently distinguish the remaining overlapped C2 and C4 resonances (153.1 ppm) from the two-dimensional data. By analogy with the assignment for the adenosine monomer, the remaining downfield shifted resonance that is correlated with C8 belongs to C6 (158.8 ppm).

When we attempted to repeat the analysis with the anhydrous polycrystalline material, sample heterogeneity was even more pronounced and resulted in extremely

broad line widths. Additional peak splittings for the C6, C8, C1', C4', C2', and C3' peaks are readily discernible in the CP-MAS spectrum for anhydrous, polycrystalline guanosine (Figure 6.17). Chemical shift multiplicity in the sugar ring carbon resonances of the anhydrous material are attributed to the presence of at least two different sugar ring conformations in the anhydrous crystalline form.

This particular monomer was also found to be highly disordered under anhydrous conditions in a related investigation by Sugawara et al., in which the transition of crystalline guanosine from an anhydrous (0% RH) to a hydrated (20%) form was explored using a combination of X-ray powder diffraction and CP-MAS [18]. The CP-MAS spectrum of anhydrous guanosine crystals from the Sugawara study exhibited both broad and/or multiply split resonances for both the sugar ring and base carbons, in agreement with our findings. These observations were shown by Sugawara and coworkers to be in accordance with the low crystallinity observed in their complementary X-ray powder diffraction study. Multiple C1' and C4' (86.5 and 85.1 ppm) and C2' and C3' signals (at 78.7, 75.9, and 72.3 ppm) were also noted by Sugawara and coworkers in their CP-MAS spectrum of guanosine dihydrate. These splittings were evidence of the two distinct conformational states for the ribose ring (C2'-endo and C1'-exo) in the dihydrate crystal.

Hydration of the anhydrous guanosine material to produce the dehydrate form resulted in drastic detuning of the probe and interfered with the cross-polarization match condition in our CP-MAS experiments. Attempts to collect ^{13}C data without CP on guanosine dihydrate were only marginally successful. However, the MAS spectrum for the dihydrate form (data not shown) does contain several distinct C2' and C3' resonances, which are listed in Table 6.1. Without the use of cross-polarization, two-dimensional data could not be collected for the dihydrate form of the guanosine monomer due to low signal intensity.

6.4 2'-Deoxynucleosides

One dimensional CP-MAS spectra were collected for the following deoxynucleosides: thymidine, 2'-deoxycytidine hydrochloride, 2'-deoxycytidine-5'-phosphate monohydrate, 2'-deoxyadenosine monohydrate, and 2'-deoxyguanosine. Two-dimensional RFDR data sets are also presented for 2'-deoxyguanosine and thymidine. Each monomer was crystallized in accordance with previously published literature procedures, with the exception of the 2'-deoxyguanosine monomer, which does not possess a published X-ray crystal structure [9, 19, 20]. The chemical shift assignments were made from either the two-dimensional shift correlation experiments or by comparison with solution-state measurements [21]. Table 6.2 contains a compilation of chemical shift values for each of the 2'-deoxynucleoside monomers studied in this dissertation. The ^{13}C solution-state chemical shift values are given in Table 6.4 for comparison.

6.4.1 Thymidine

Figure 6.19 shows the one-dimensional CP-MAS spectrum for polycrystalline thymidine. Inspection of the data indicates the presence of only one dominant conformer, in accordance with the previously published X-ray diffraction study by Young et al. [19]. The X-ray structure reveals that crystalline thymidine resides in a C3'-exo conformation with an anti orientation about the glycosidic bond. An extensive network of crosspeaks in the one cycle 2D-RFDR data set (Figure 6.20) can be used to identify each of the peaks in the CP-MAS spectrum. The most upfield-shifted resonance at 9.8 ppm belongs to the thymine methyl group. The methyl carbon is correlated with C5 (109.9 ppm), C4 (165.5 ppm), and C6 (136.0 ppm). The C2 resonance (149.2 ppm) is correlated with each of the carbon atoms in the pyrimidine ring and to C1' (86.1 ppm). C1' has an intense crosspeak to the directly bonded C2' (39.6 ppm).

C3' and C5' resonate at 71.3 ppm and 60.0 ppm, respectively. Although Santos et al. did not examine thymidine in their 2'-deoxynucleoside study, the C3' and C5' chemical shifts are reasonable for a pyrimidine deoxynucleoside with a C3'-exo conformation [8].

6.4.2 2'-Deoxyguanosine

The CP-MAS spectrum and chemical shift assignment for lyophilized 2'-deoxyguanosine is presented in Figure 6.19. Extensive splitting of the C3' and/or C5' resonances suggests the presence of more than one conformer in the sample, with the more downfield shifted species predominating. Despite very poor signal to noise due to a small sample size (7 mg $^{13}C,^{15}N$ labeled material), the sequential assignment for each of the independent conformers can be traced out by inspection of the 2 cycle RFDR data set (Figure 6.21). C1' (80.5 ppm) is correlated to C2' (37.8 ppm) and each of the C3' resonances (70.5 and 64.4 ppm). Each of the C3' resonances is correlated with C4' (83.6 ppm), and C4' is correlated with each of the C5' resonances (61.2 and 58.3 ppm). Weaker crosspeaks are also apparent for C2'-C4', C1'-C3', C1'-C5', and C3'-C5'. C1' is correlated to C8 (134.9 ppm) and C5 (114.1 ppm) in the purine ring. C5 has crosspeaks with C4 (148.3 ppm), C2 (151.4 ppm), and C6 (155.6 ppm). Additional correlations between the aromatic C2, C6, C4, and C8 nuclei are also evident in the 2D-RFDR spectrum.

6.4.3 2'-Deoxycytidine and 2'-Deoxyadenosine

The natural abundance ^{13}C CP-MAS spectra for two different crystalline forms of 2'-deoxycytidine appear in Figure 6.1. These spectra were discussed in Section 6.2 to illustrate the effect of sugar ring conformation on the ^{13}C chemical shift parameter. The aromatic resonances of the hydrochloride derivative could not be

identified due to extensive splitting by neighboring quadrupolar ^{14}N nuclei in the pyrimidine heterocycle. The natural abundance CP-MAS spectrum of polycrystalline 2'-deoxyadenosine monohydrate appears in Figure 6.22 and is indicative of a 2'-deoxynucleoside with a C3'-exo sugar ring conformation and an anti base orientation. The chemical shift assignments for the 2'-deoxycytidine and 2'-deoxyadenosine derivatives in the solid-state are based on the values reported by Santos and coworkers [8].

6.5 Nitrogen-15 Chemical Shifts

The solid-state proton-decoupled ^{15}N CP-MAS spectra for each of the ribonucleoside monomers are presented in Figure 6.23. Only a very tentative assignment can be suggested based on a comparison with natural abundance solution-state measurements (Table 6.3). The solution-state ^{15}N chemical shift values for each of the nucleoside monomers appear in Table 6.3 for comparison [22]. The more intense solid-state ^{15}N resonances belong to protonated (imino and amino) nitrogen nuclei that are more effectively cross-polarized during the CP-MAS experiment. Discrepancies in the ^{15}N chemical shifts for the solid- and solution-state (apart from differences in referencing) are largely the result of different protonation and/or hydrogen bonding states of the amino and imino nitrogen nuclei. However, this attribute could make the ^{15}N chemical shift a particularly sensitive probe of intermolecular interactions in the solid-state. A more confident assignment of ^{15}N chemical shifts in the solid-state would require the use of two-dimensional heteronuclear dipolar recoupling techniques that could correlate ^{13}C and ^{15}N resonances. The polycrystalline cytidine monomer possesses three nitrogen nuclei: 180.6 ppm, 146.8 ppm, and 96.0 ppm, which are assigned to N3, N1, and N6, respectively. Polycrystalline uridine has two ^{15}N nuclei in the pyrimidine ring (N3 and N1) which resonate at 158.2 and 123.4 ppm, respectively. The chemical shift assignment for the nitrogen nuclei of polycrystalline adenosine are

as follows: N7 (212.7 ppm), N3 (199.3 ppm), N1 (192.2 ppm), N9 (141.8 ppm), and N6 (70.6 ppm). The ^{15}N chemical shifts of the polycrystalline guanosine monomer are extensively split as was the case for the ^{13}C CP-MAS spectra presented above. We have assigned the three peaks at 218.4, 215.2, and 207.9 ppm to N7. The three peaks at 157.6, 154.9, and 151.7 ppm are assigned to N9. N3 resonates at 143.9 and 141.6 ppm. The N1 imino nitrogen resonates at 137.5 ppm. The two peaks at 84.9 and 81.2 ppm correspond to the amino nitrogen resonances.

6.6 Observations about Nucleoside Structure in the Solid-State

Examination of the 2D-DRAWS and 2D-RFDR spectra for crystalline and lyophilized nucleosides reveals valuable information about molecular conformation, in particular about the pucker of the furanose ring, and intermolecular interactions. High resolution ^{13}C spectra of amorphous solid samples often produce a multiplicity of chemical shifts due to the presence of different molecular geometries. Chemical shift dispersion is particularly significant in macromolecular systems which may adopt a multitude of conformations. The results indicate that two dimensional dipolar recoupling experiments can be successfully applied to systems that are highly heterogeneous and can yield adequate resolution for the assignment of chemical shifts even when multiple conformers are present.

The narrow resonances of the polycrystalline adenosine, thymidine, and cytidine monomer data indicate minimal chemical shift dispersion and the presence of only one dominant molecular species in accordance with the single crystal diffraction studies (see Section 4.6). Our 2D-DRAWS and 2D-RFDR results for polycrystalline adenosine complement those from a recent investigation by Fujiwara and coworkers [23]. These researchers applied a combination of homonuclear and heteronuclear chemical shift correlation experiments to complete the spectral assignment of adenosine. Inspection of their two-dimensional ^{13}C chemical shift correlation spectrum in-

dicates that only one molecular conformation is present, as evidenced by a lack of peak multiplicity, but with slightly different chemical shifts than were measured in this work. There is no mention in that report of the physical state of the sample, and it is possible that it was not prepared in an identical manner to the procedure used in this study. Differences in crystallization conditions could potentially result in alterations in either molecular conformation or physical environment of the sample.

Both the crystalline and lyophilized forms of uridine exhibit pronounced splittings in their C3', C5', C2, C4, and C6 resonances. The fact that lyophilized and crystalline material produce comparable spectra indicates that uridine exists in the same energetically favorable conformation in both forms. The uridine X-ray structure reveals that there are two independent molecules per asymmetric unit cell, each with a C3'-endo furanose ring pucker. The duplicity in C3' and C5' chemical shifts could be a consequence of there being two slightly different sugar ring conformers for each molecule in the unit cell. The presence of splittings in the base chemical shifts of uridine suggests that the base may be oriented about the glycosidic bond in one of two positions over the furanoside moiety. Although the C2-C1' distance remains fixed upon rotation about the glycosidic linkage, the local electronic environment of the ring carbons could be modulated by changes in this torsion angle. It is noteworthy that there would be such a difference in the carbon chemical shift resonances for the two species when the geometries of the two molecules are so similar in the crystal study. An alternative explanation is that the two chemically shifted conformers are the result of perturbations in the local electronic environment as a result of intermolecular forces (i.e., hydrogen bonding and/or crystal packing) and not in large discrepancies in their individual molecular conformations.

The furanose ring of the lyophilized adenosine monomer clearly exists in two entirely distinct conformations. The splitting of chemical shifts is most pronounced for the 5' and 3' sugar ring carbons. From a comparison with two different crystalline forms of adenosine, we have tentatively assigned the downfield set of C3' and C5'

resonances for the lyophilized material to the conformer with a C3'-endo sugar pucker. The upfield shifted set has been assigned to the conformer with a C2'-endo conformation. This result is in direct contrast to the findings from the complementary 2'-deoxynucleoside investigation by Santos and coworkers. Furthermore, the C5' resonance was not found to be particularly indicative of sugar ring pucker. Again, this contradicts the situation for 2'-deoxynucleosides. The chemical shift dispersion for sugar ring carbon atoms that is seen in the lyophilized adenosine, guanosine, and 2'-deoxyguanosine spectra suggests the possibility of a continuum of puckering states for the purine monomers. This may be a consequence of the greater conformational freedom that is afforded by the presence of a small, five-membered imidazole ring on the endo side of the ribose moiety.

6.7 Conclusion

The results show that 2D-DRAWS is a valuable homonuclear shift correlation experiment for the spectral assignment of complicated, multiply labeled spin systems. The sign alternation that accompanies this technique is particularly advantageous for distinguishing connectivities between neighboring and more distant atoms. Our investigation of crystalline and amorphous powders has also shown the degree of conformational variability that is accessible to nucleoside monomers in the solid state. A full assignment (based on ^{13}C atoms alone) may be best performed using a combination of both RFDR and DRAWS experiments. The measurement of connectivities to the aromatic ring carbons or between base and sugar ring atoms is most effectively accomplished using the RFDR experiment. This makes RFDR preferable for the assignment of systems which are sample limited. Both the RFDR and DRAWS experiments are susceptible to phase twisting and t_1 streaks. Phase twisting is the result of incomplete averaging of anisotropic interactions during the t_1 period. This artifact is most pronounced for nuclei with large chemical shift anisotropies. It should be

noted, that dipolar recoupling experiments which are used to correlate coherences between pairs of dipolar coupled ^{13}C atoms in such highly enriched systems are all prone to the effects of spin diffusion. An extensive discussion of the effects of spin diffusion in dipolar recoupling experiments on multiply labeled compounds is presented by Kiihne [24]. As demonstrated above, spectral assignment based on 2D-RFDR requires interpretation of crosspeak intensities to identify correlations with nearby and more distant nuclei. With even one or two RFDR mixing periods, the chemical shift assignment of a multiply labeled system can become ambiguous. However, because of the phase alternation of crosspeaks that accompanies the 2D-DRAWS experiment, direct and indirect connectivities can be identified confidently in the presence of spin diffusion. To further describe the structural details of the monomeric nucleoside subunit, chemical shift trends and the quantitative measurement of multiple interatomic distances and torsion angles need to be combined. Such measurements are most advantageously performed on selectively labeled compounds in the absence of spin diffusion. The measurement of endocyclic and glycosidic torsion angles and internuclear distances in selectively enriched nucleosides and DNA oligonucleotides is the focus of Chapters 5 and 7.

6.8 Notes to Chapter 6

[1] Haeberlen, U., *High Resolution NMR in Solids, Selective Averaging*. 1976, New York: Springer Verlag.

[2] Liu, F.L., Phung, C.G., Alderman, D.W., and Grant, D.M. (1996) *J. Am. Chem. Soc.*, **118**, p. 10629.

[3] Liu, F., Phung, C.G., Alderman, D.W., and Grant, D.M. (1995) *J. Am. Chem. Soc.*, **117**, p. 9323.

[4] McDowell, C.A., Naito, A., Sastry, D.L., and Takegoshi, K. (1988) *J. Magn. Reson.*, **78**, p. 498.

[5] Saito, H. (1986) *Magn. Reson. Chem.*, **24**, p. 835.

[6] Pfeffer, P.E. (1984) *J. Carbohyd. Chem.*, **3** (4), p. 613.

[7] Opella, S.J., Hexem, J.G., Frey, M.H., and Cross, T.A. (1981) *Phil. Trans. R. Soc. Lond.*, **A** (299), p. 665.

[8] Santos, R.A., Tang, P., and Harbison, G.S. (1989) *Biochemistry*, **28**, p. 9372.

[9] Subramanian, E. and Hunt, D.J. (1970) *Acta Cryst.*, **B26**, p. 303.

[10] Viswamitra, M.A., Reddy, B.S., Lin, G.H.Y., and Sundaralingam, M. (1971) *J. Am. Chem. Soc.*, **93**, p. 4565.

[11] Watson, D.G., Sutor, D.J., and Tollin, P. (1965) *Acta Cryst.*, **19**, p. 111.

[12] Furberg, S. (1950) *Acta Cryst.*, **3**, p. 325.

[13] Furberg, S., Petersen, C.S., and Rømming, C. (1965) *Acta Cryst.*, **18**, p. 313.

[14] Green, E.A., Rosenstein, R.D., Shiono, R., and Abraham, D.J. (1975) *Acta Cryst.*, **B31**, p. 102.

[15] Lai, T.F. and Marsh, R.E. (1972) *Acta Cryst.*, **B28**, p. 1982.

[16] Neidle, S., Kuehlbrandt, W., and Achari, A. (1976) *Acta Cryst.*, **B32**, p. 1850.

[17] Thewalt, U., Bugg, C.E., and Marsh, R. (1970) *Acta Cryst.*, **B26**, p. 1089.

[18] Sugawara, Y., Iimura, Y., Iwasaki, H., Urabe, H., and Saito, H. (1994) *J. Biomol. Struct. Dynam.*, **11** (4), p. 721.

[19] Young, D.W., Tollin, P., and Wilson, H.R. (1969) *Acta Cryst.*, **B25**, p. 1423.

[20] Young, D.W. and Wilson, H.R. (1975) *Acta Cryst.*, **B31**, p. 961.

[21] Jones, A.J., Winkley, M.W., Grant, D.M., and Robins, R.K. (1970) *Proc. Natl. Acad. Sci. (USA)*, **65** (1), p. 27.

[22] Hawkes, G.E., Randall, E.W., and Hull, W.E. (1977) *J. Chem. Soc.*, **Perkin II**, p. 1268.

[23] Fujiwara, T., Sugase, K., Kainosho, M., Ono, A., Ono, A.M., and Akutsu, H. (1995) *J. Am. Chem. Soc.*, **117**, p. 11351.

[24] Kiihne, S.R., *Ph.D. Dissertation*, 1998, University of Washington.

Table 6.1: Solid-State Ribonucleoside ^{13}C Chemical Shifts (ppm)

Compound	1'	4'	2'	3'	5'
rU[a]	89.7	80.0	73.0	66.6, 64.3	59.5, 56.5
rU[b]	89.7	80.0	73.0	66.6, 64.3	59.5, 56.5
rC[c]	88.8	80.1	71.9	62.8	56.3
rA[d]	90.2	82.0	72.9	69.1 , 66.2	62.7, 56.7
rA[e]	90.0	82.6	73.0	69.0	60.7
rAMP-H_2O[f]	86.7	76.5	73.8	66.0	59.3
rG[g]	87.4	86.5	72.0	69.3	62.3
rG[h]	87.5	82.7	75.4, 72.2	68.8	63.1
rG[i]	87.4	82.6	73.1	68.9	60.2

[a]lyophilized, [b]crystalline, [c]crystalline, [d]lyophilized, [e]crystalline, [f]crystalline, [g]lyophilized, [h]crystalline (anhydrous), [i]crystalline (dihydrate form).

Compound	6	2	4	8	5
rU	140.8, 138.6	150.2, 149.3	166.4, 164.0	—	100.3, 99.2
rU	138.3	150.2	166.4, 164.0	—	100.1
rC	138.9	154.3	164.0	—	92.0
rA	152.9	151.2	145.2	136.6	119.7
rA	152.6	152.6	146.0	135.6	118.7
rAMP-H_2O	*	*	*	*	*
rG	158.8	153.1	153.1	138.1	113.3
rG	158.4, 156.3	152.2	148.8	138.5, 133.9	116.3
rG	157.8	148.8	148.8	139.3	114.8

*Chemical shift not assigned.

Table 6.2: Solid-State Deoxynucleoside ^{13}C Chemical Shifts (ppm)

Compound	1' [a]	4'	3'	5'	2'	CH_3
dT	86.1	86.1	71.3	60.0	39.6	9.8
dG[b]	80.5	83.6	70.5, 64.4	61.3, 58.3	37.8	---
dA-H_2O	87.1	91.2	71.0	62.8	41.3	---
dCMP-H_2O	86.0	87.9	72.5	61.0	37.8	---
dC-HCl	93.6	86.4	65.9	58.7	37.9	---

[a]C1' and C4' resonances may be reversed. [b]lyophilized.

Table 6.2 (continued):

Compound	4	2	6	8	5
dT	165.5	149.2	136.0	---	109.9
dG	148.3	151.4	155.6	134.9	114.1
dA-H_2O	145.5	150.7	153.4	133.6	118.9
dCMP-H_2O	165.2	158.9	139.8	---	96.1
dC-HCl	*	*	*	*	*

*Chemical shift not assigned.

Table 6.3: Ribonucleoside ^{15}N Chemical Shifts (ppm)

Compound	7	3	1	9	NH_2
rU	—	158.2	146.7	—	—
rG	218.4, 215.2, 207.9	—	—	157.6, 154.9, 151.7	84.9, 81.2
rC	—	180.6	146.8	—	96.0
rA	212.7	199.3	192.2	147.7	70.6
rU*	—	137.3	123.4	—	—
rG*	226.8	146.1	127.1	149.8	52.8
rC*	—	189.1	132.7	—	74.0
rA*	220.9	216.2	203.3	147.7	60.8

*In DMSO, relative to $^{15}NH_4+$ in 5M $^{15}NH_4{}^{15}NO_3$ in 2N nitric acid. See text for details.

Table 6.4: Solution-State ^{13}C Chemical Shifts (ppm)

Compound	1'	4'	2'	3'	5'	CH_3
rU*	90.2	85.0	74.5	70.3	61.6	---
rA*	88.9	86.3	74.3	71.1	62.0	---
rC*	91.2	84.2	74.8	70.2	61.7	---
rG**	87.5	86.3	74.7	71.4	62.4	---
dT**	85.1	88.4	40.4	71.4	62.4	13.3
dG**	83.9	88.7	40.4	71.9	62.9	---
dA**	85.6	89.2	40.5	72.3	62.9	---
dC**	86.6	88.6	40.6	71.8	62.7	---

Table 6.4 (continued):

Compound	4	2	6	8	5
rU	166.9	152.4	142.6	---	103.1
rA	149.0	152.9	155.4	141.4	119.6
rC	166.9	158.2	142.4	---	96.9
rG	152.3	154.7	157.8	136.7	117.7
dT	164.8	151.5	137.3	---	110.5
dG	151.9	154.6	158.1	136.6	117.7
dA	150.0	153.6	157.1	140.9	120.5
dC	166.9	156.9	142.7	---	95.9

*in D_2O, **in DMSO-d_6.

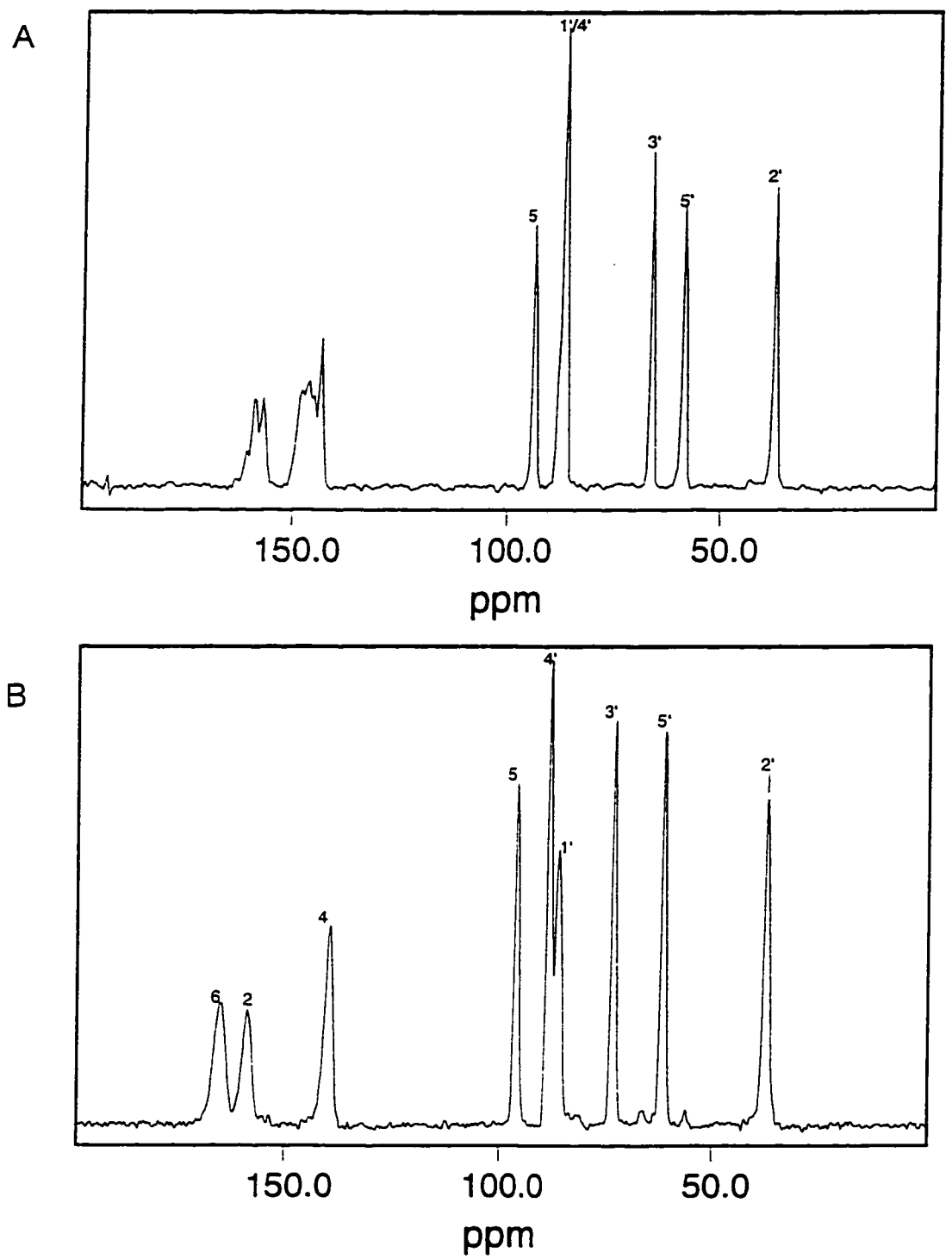

Figure 6.1: CP-MAS spectra for A) 2'-deoxycytidine hydrochloride (C3'-endo) and B) 2'-deoxycytidine-5'-phosphate monohydrate (C3'-exo). Note the upfield-shifted C3' and C5' chemical shifts for the hydrochloride derivative.

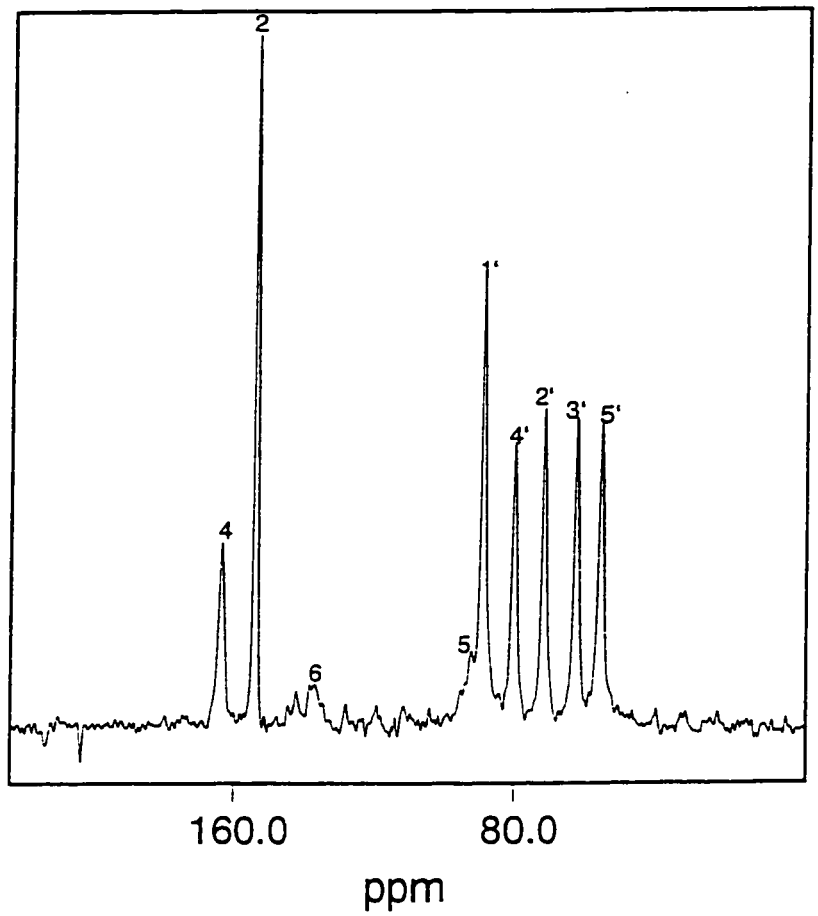

Figure 6.2: Carbon-13 CP-MAS spectrum for u-^{13}C, ^{15}N cytidine monomer.

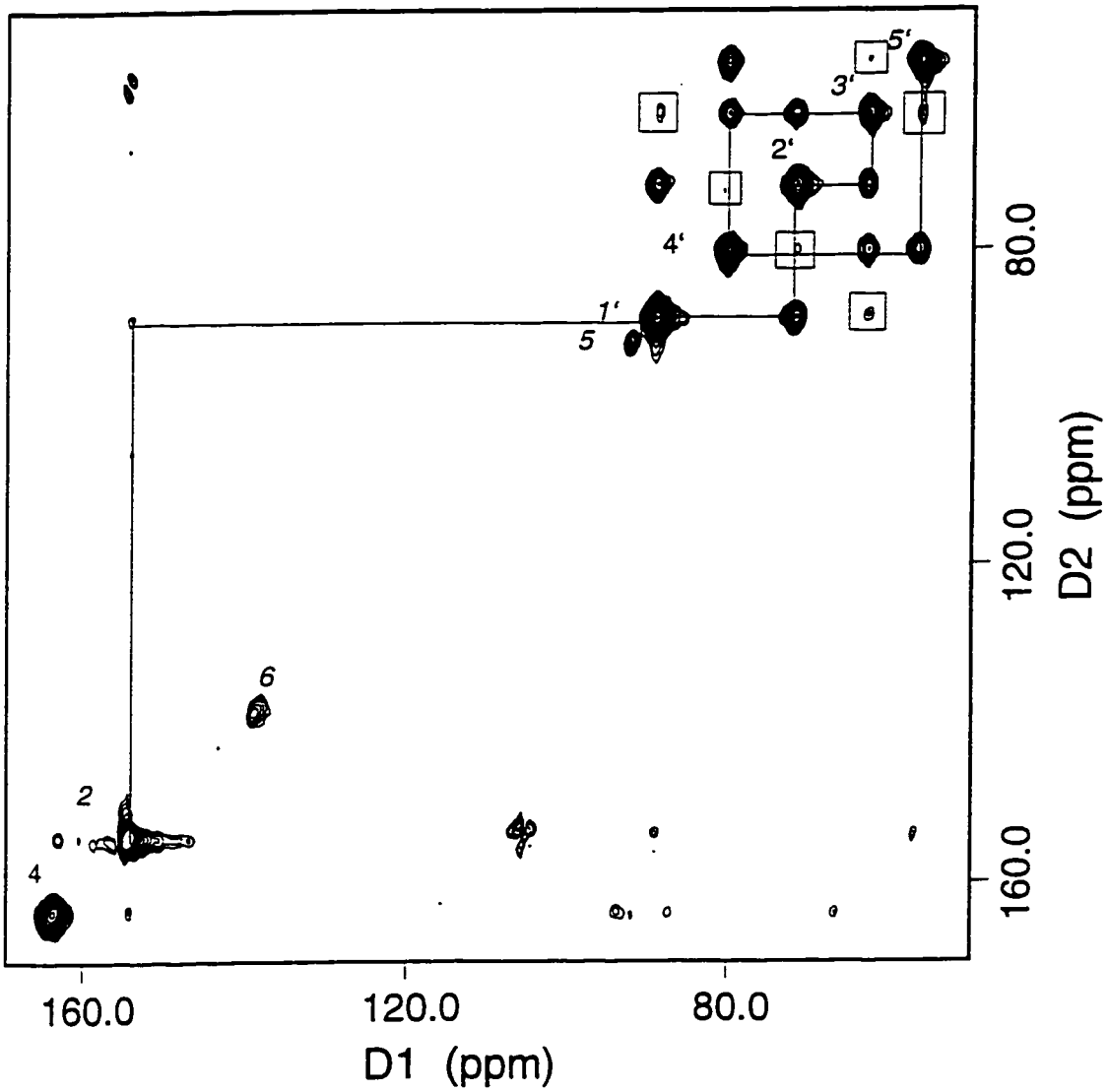

Figure 6.3: 1cycle DRAWS spectrum for polycrystalline cytidine.

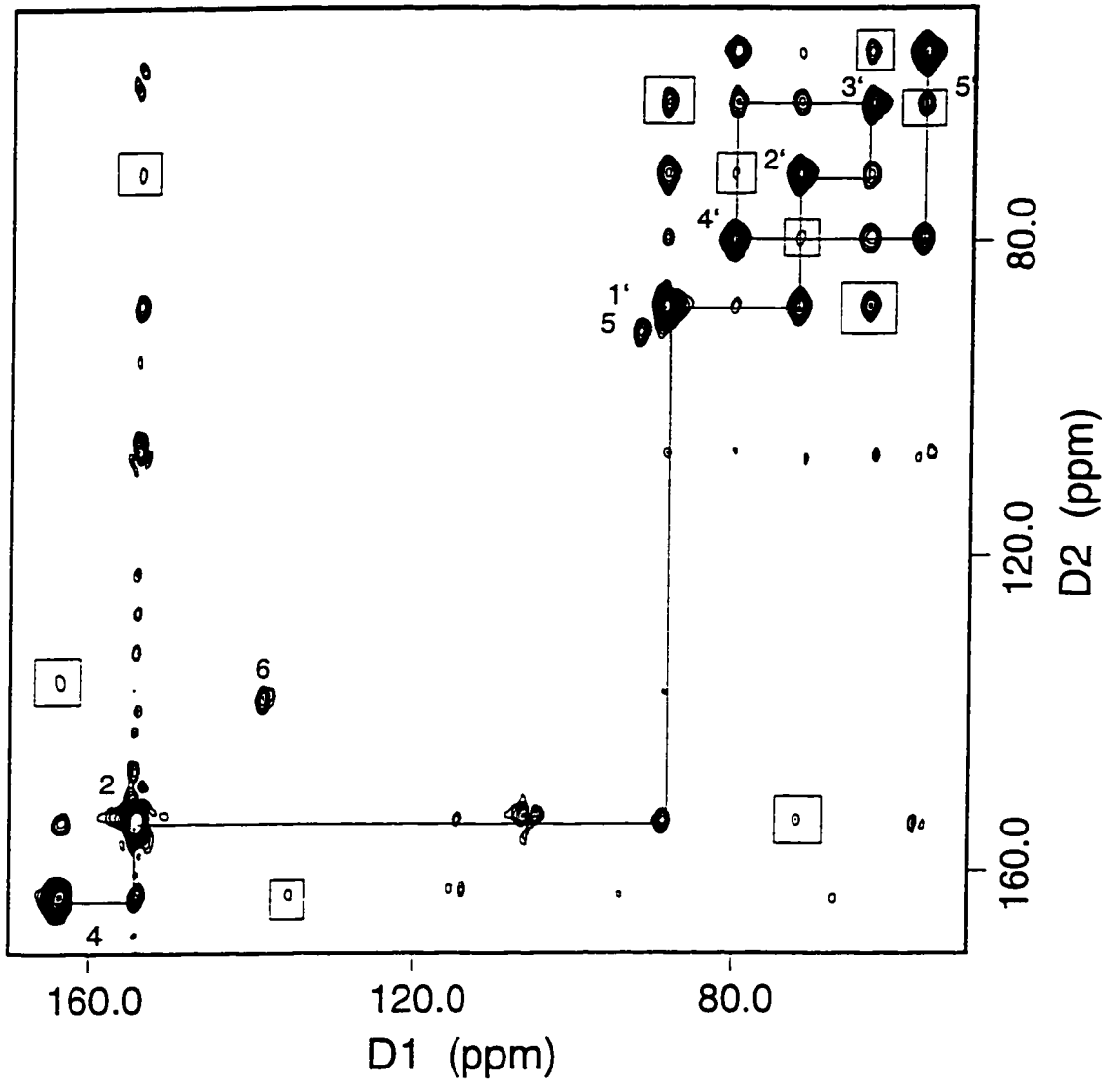

Figure 6.4: Two cycle DRAWS spectrum for polycrystalline cytidine.

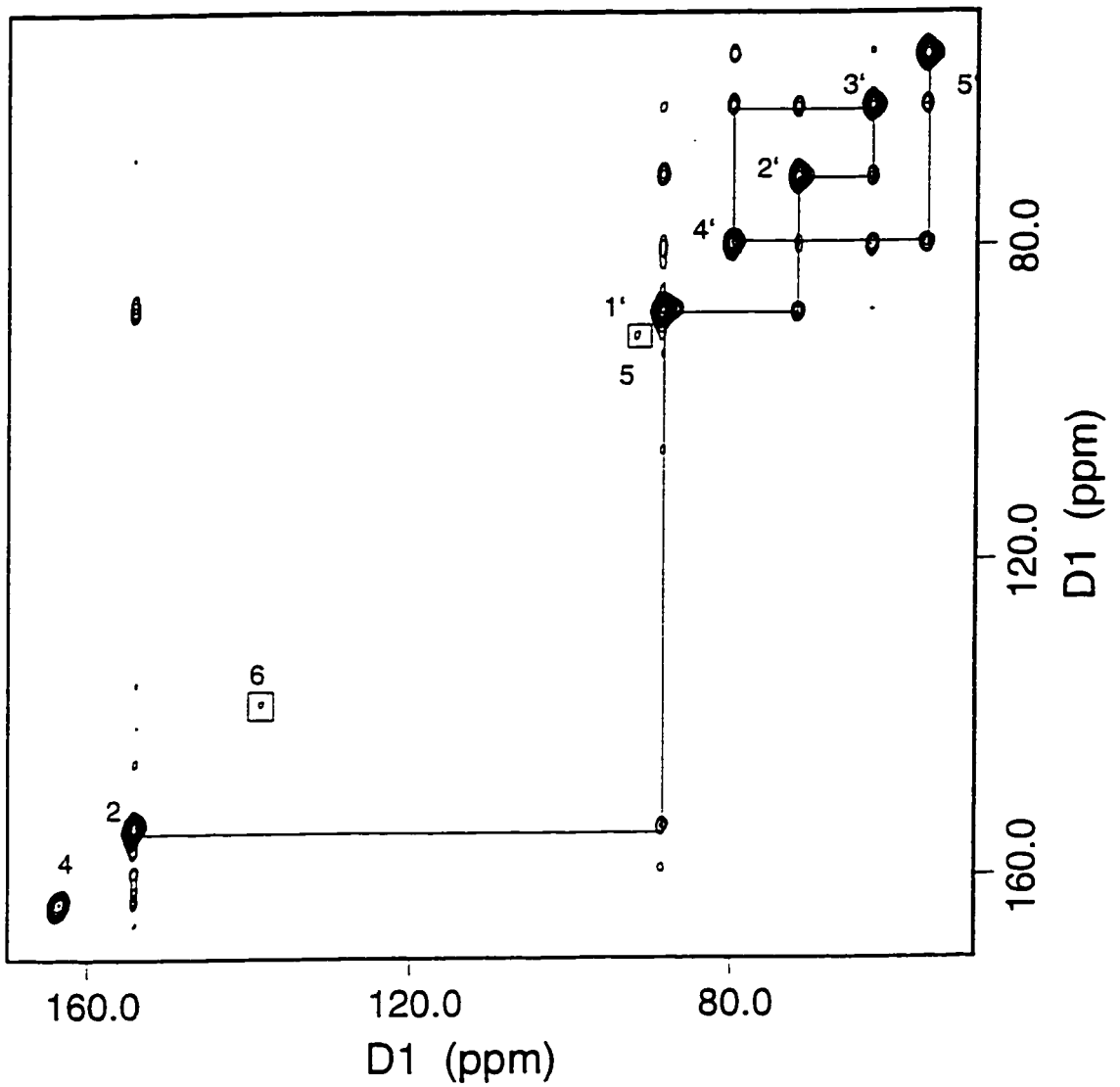

Figure 6.5: One cycle RFDR spectrum for polycrystalline cytidine.

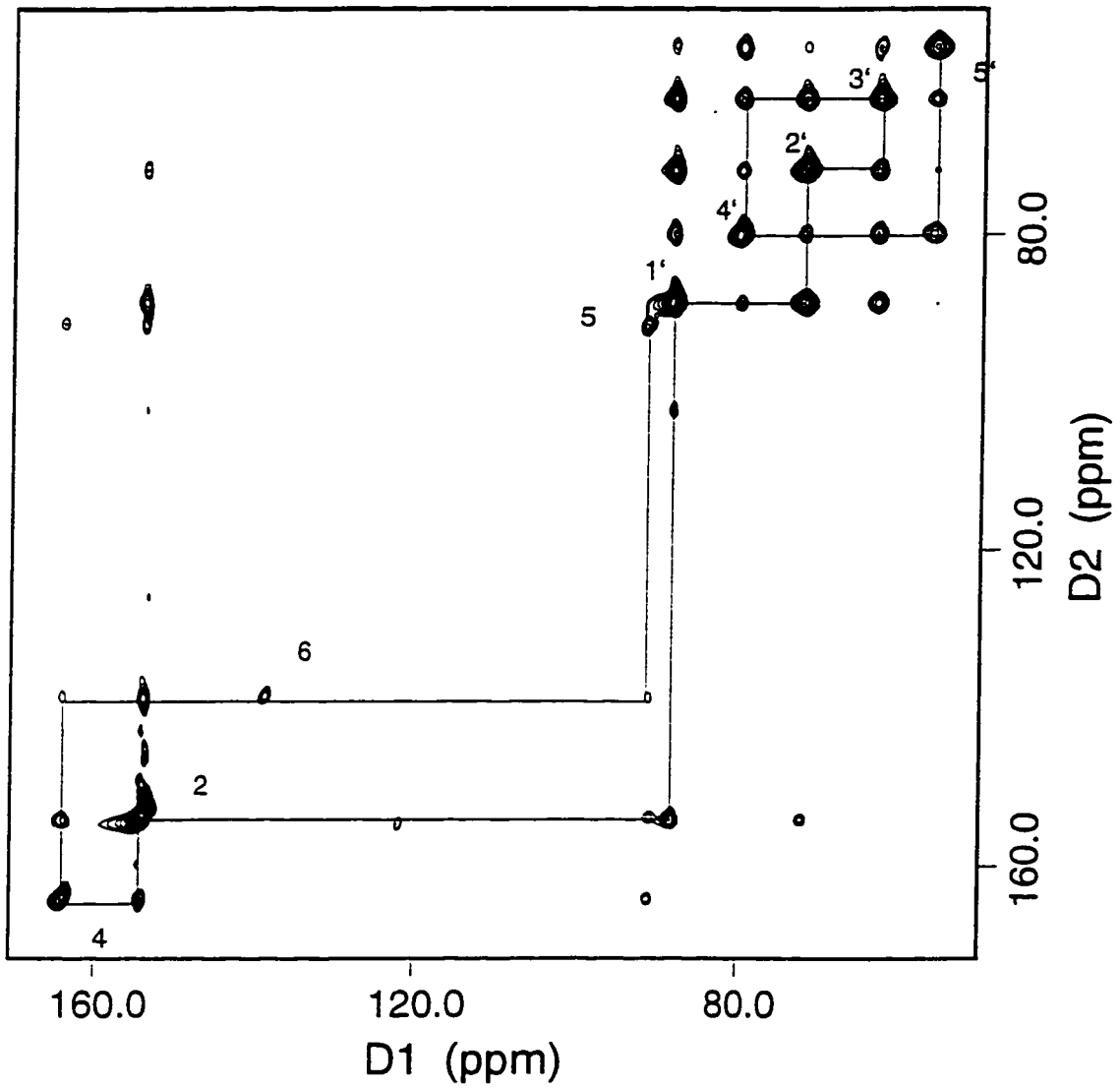

Figure 6.6: Two cycle RFDR spectrum for polycrystalline cytidine.

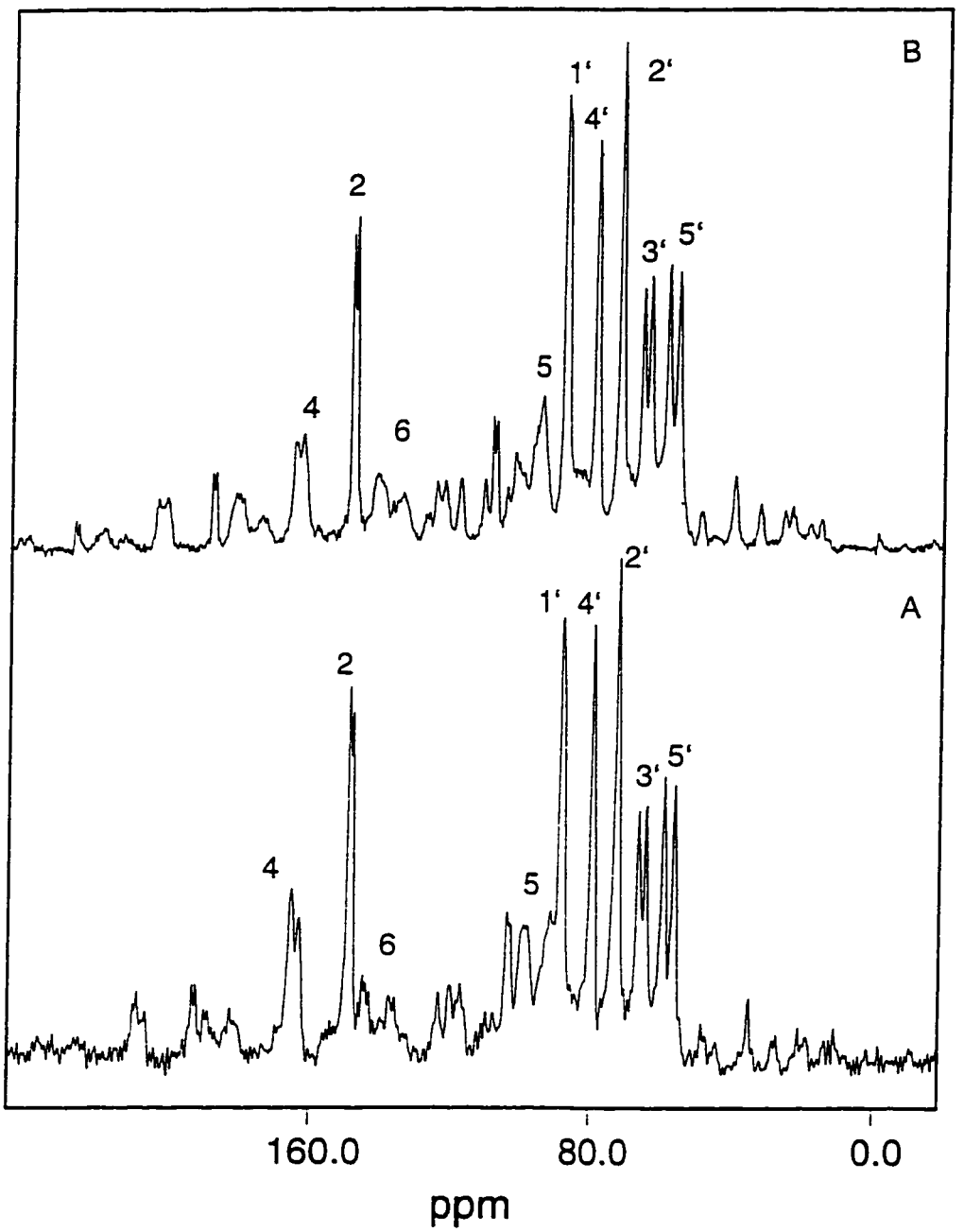

Figure 6.7: Carbon-13 CP-MAS spectra for lyophilized (A) and polycrystalline (B) uridine.

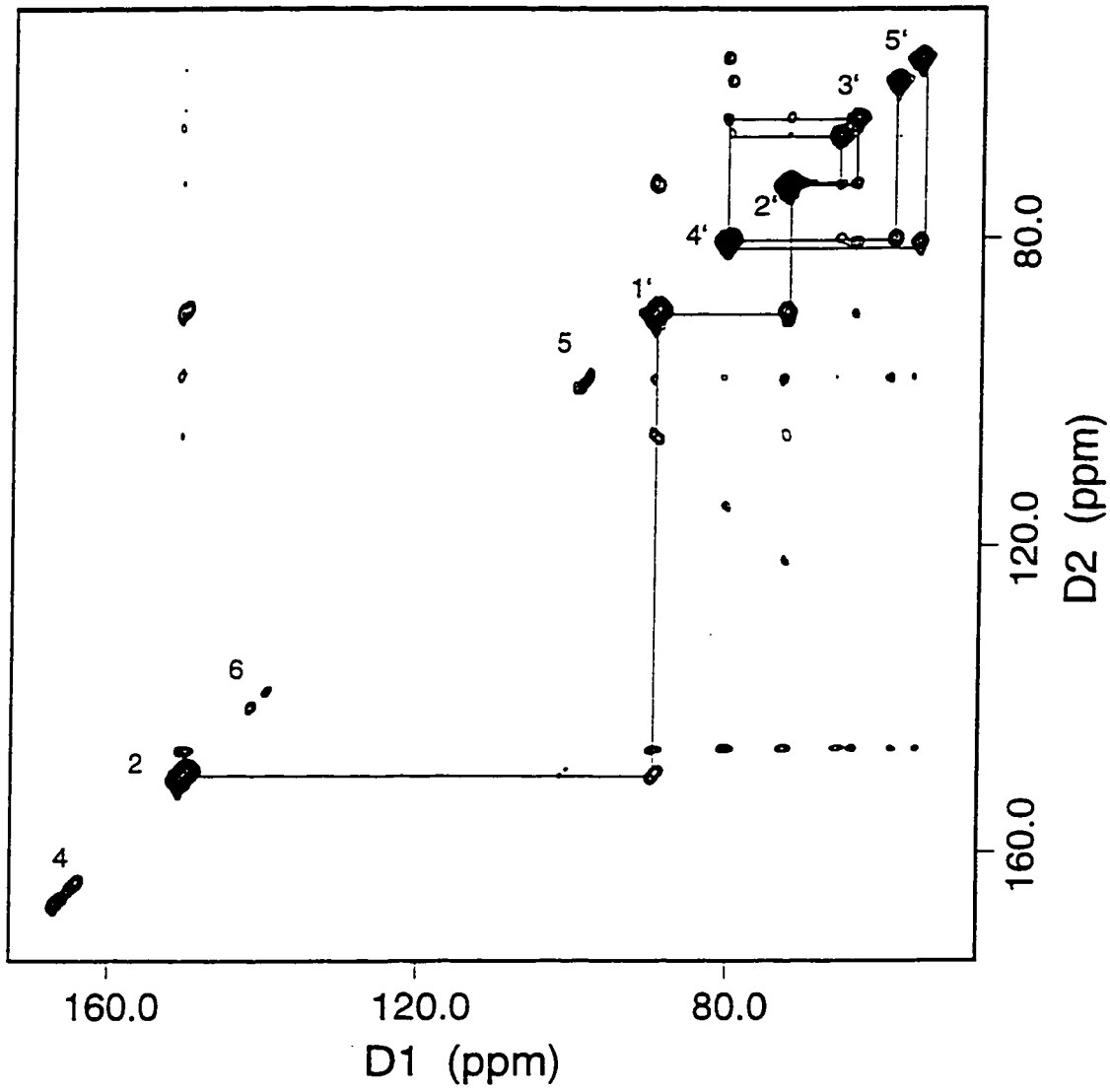

Figure 6.8: One cycle RFDR spectrum for lyophilized uridine.

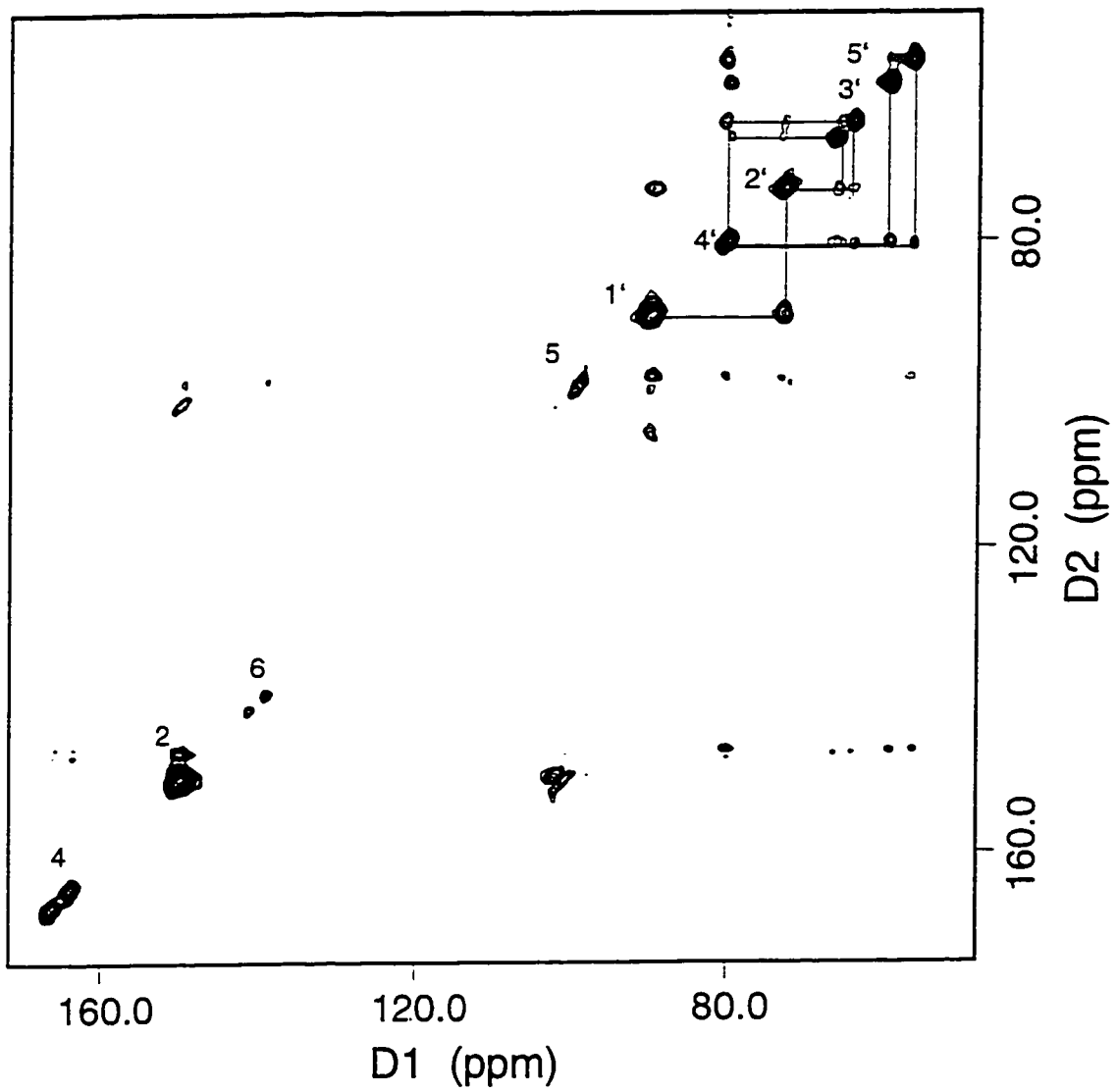

Figure 6.9: One cycle DRAWS spectrum for lyophilized uridine.

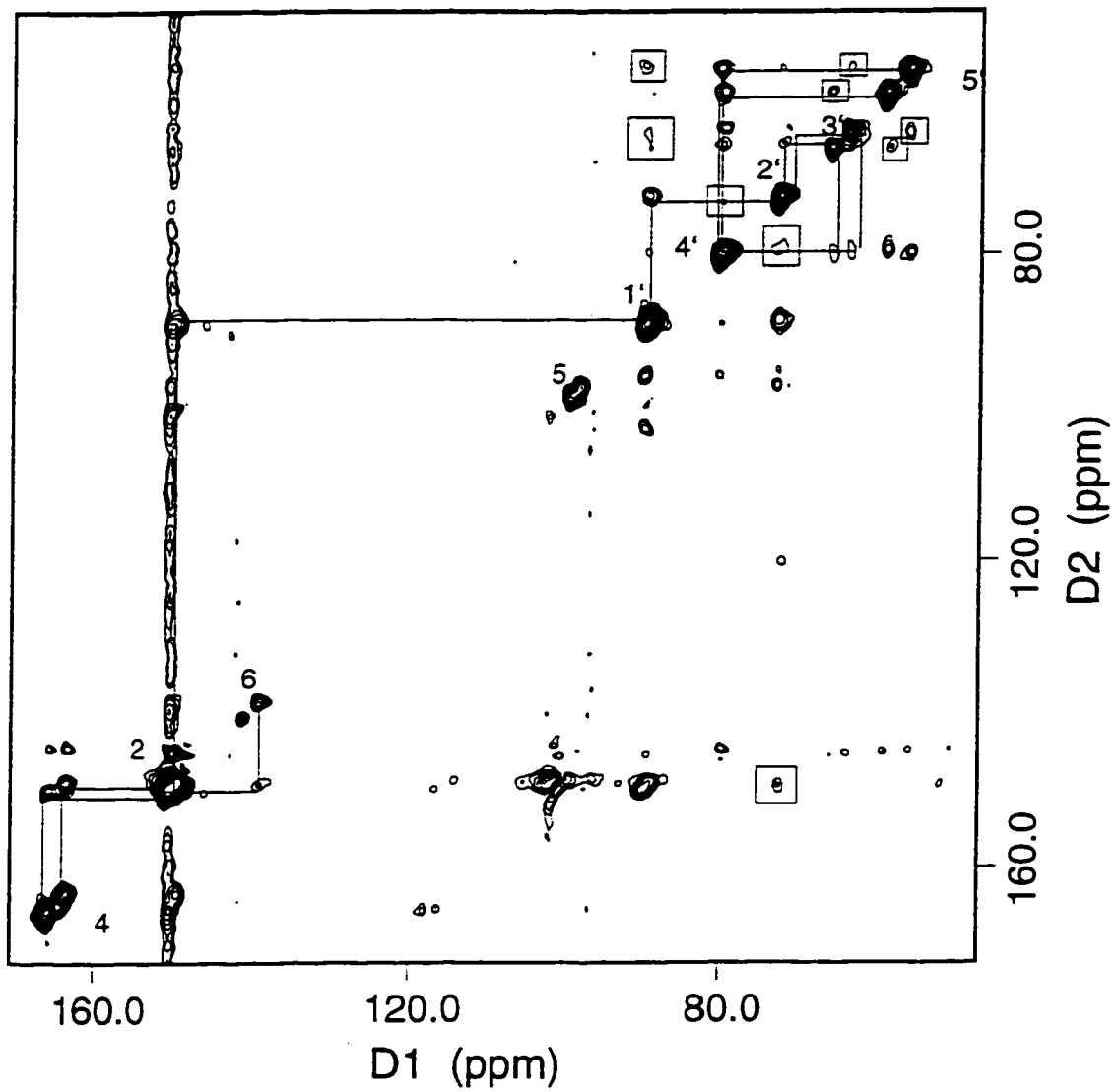

Figure 6.10: Three cycle DRAWS spectrum for lyophilized uridine.

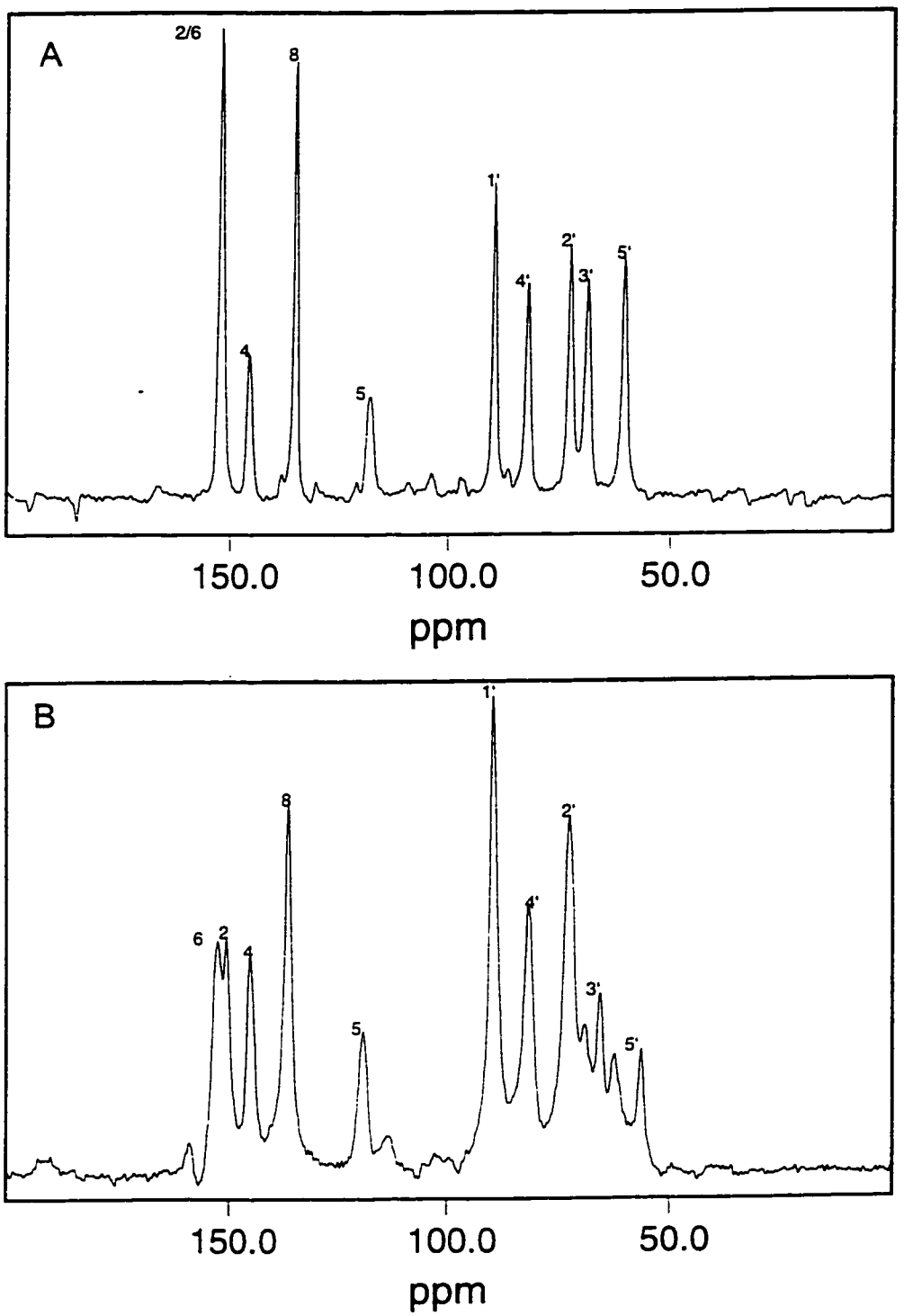

Figure 6.11: Carbon-13 CP-MAS spectra for polycrystalline (A) and lyophilized (B) adenosine, taken at 9.4 and 11.7 Tesla, respectively.

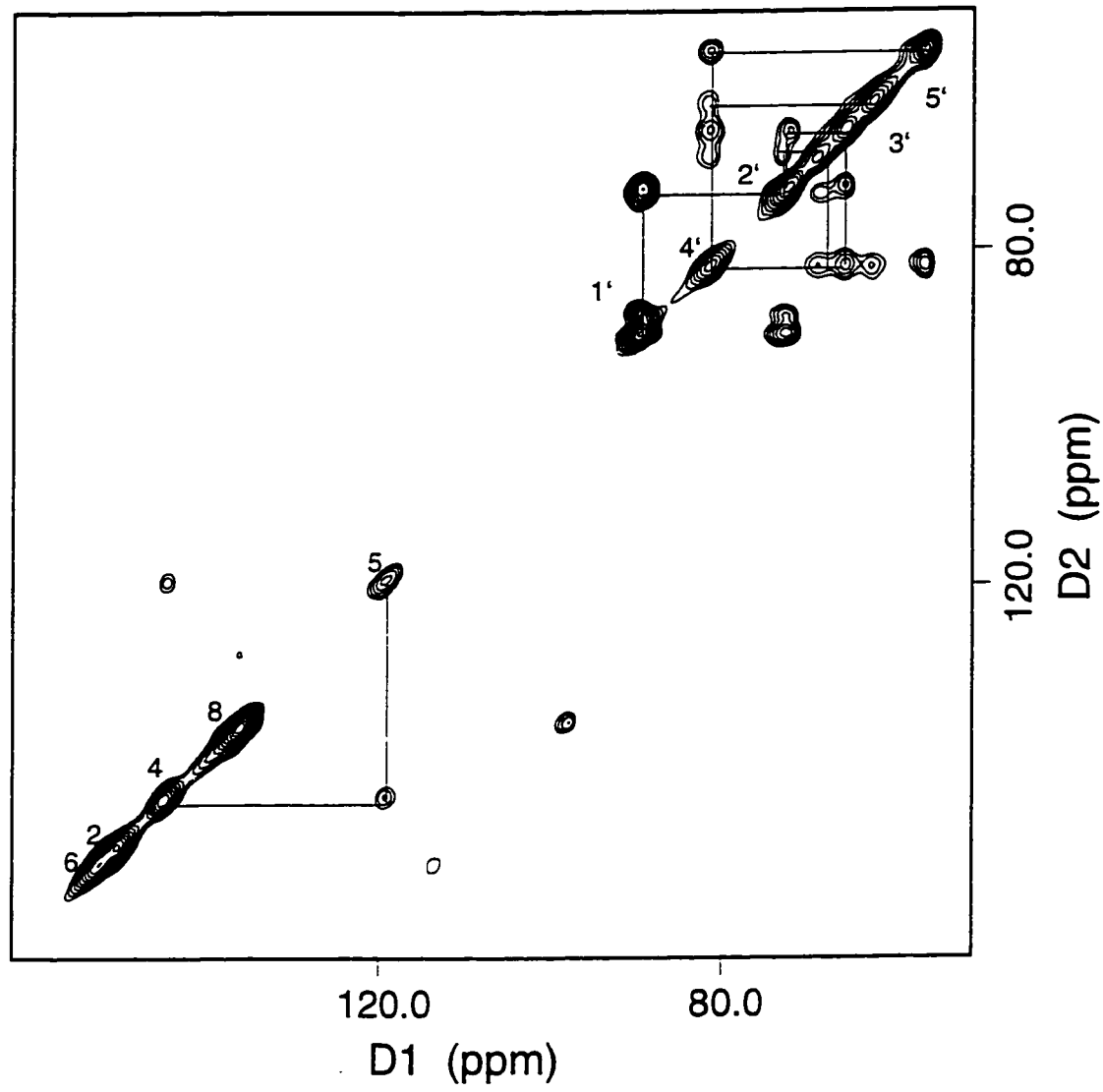

Figure 6.12: One cycle DRAWS spectrum for lyophilized adenosine, taken at 11.7 Tesla.

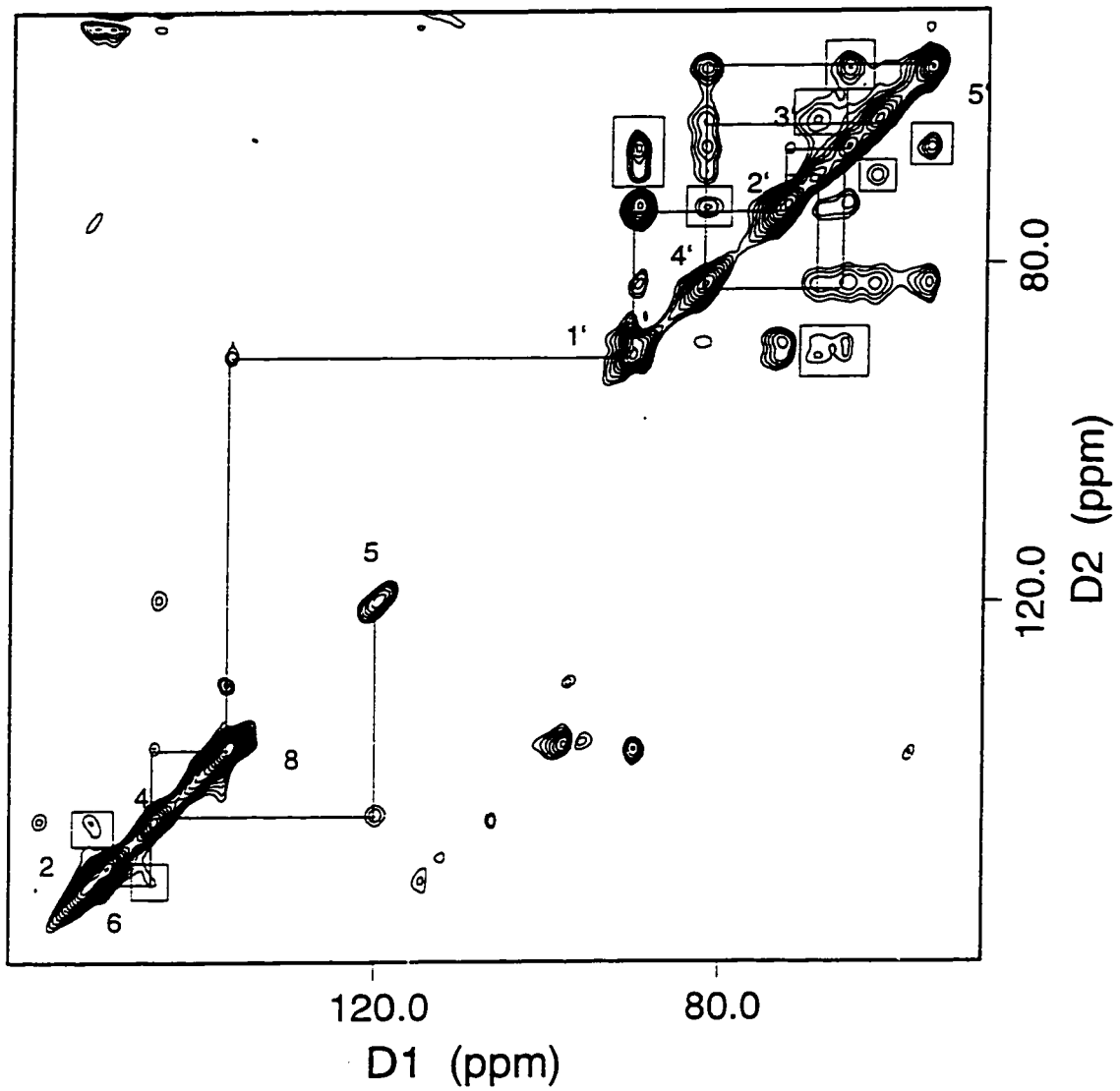

Figure 6.13: Two cycle DRAWS spectrum for lyophilized adenosine, taken at 11.7 Tesla.

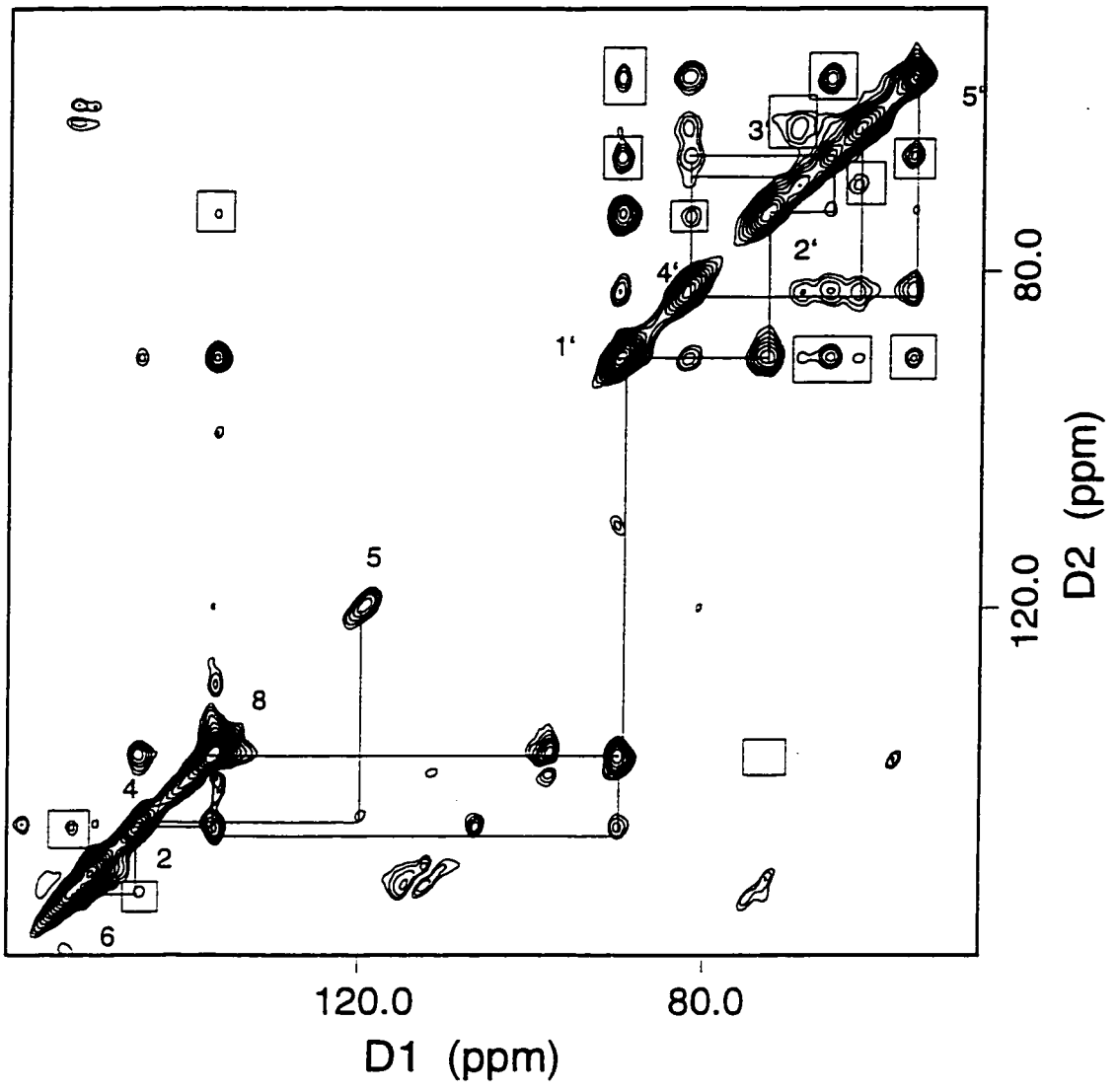

Figure 6.14: Three cycle DRAWS spectrum for lyophilized adenosine, taken at 11.7 Tesla.

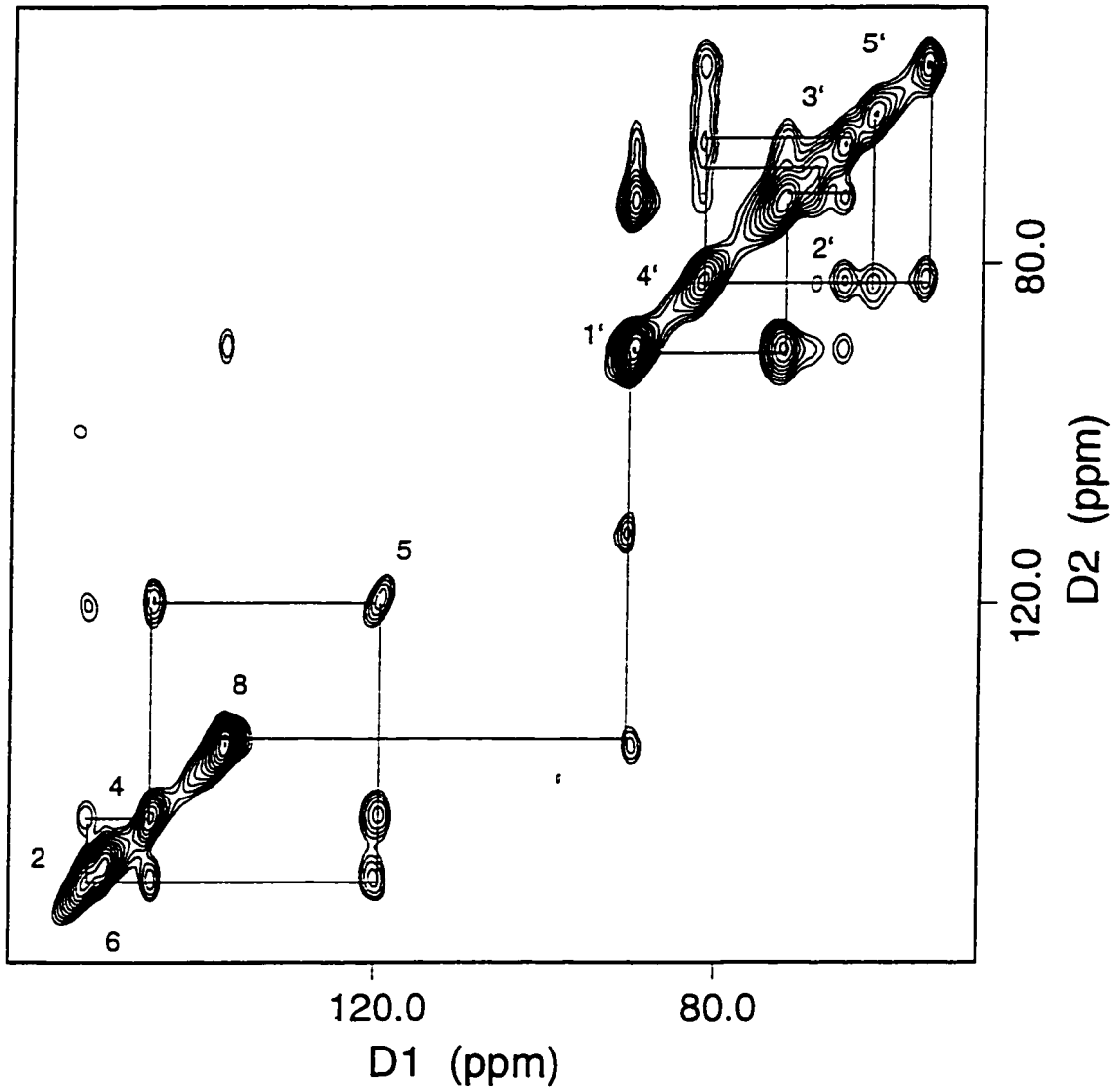

Figure 6.15: One cycle RFDR spectrum for lyophilized adenosine, taken at 11.7 Tesla.

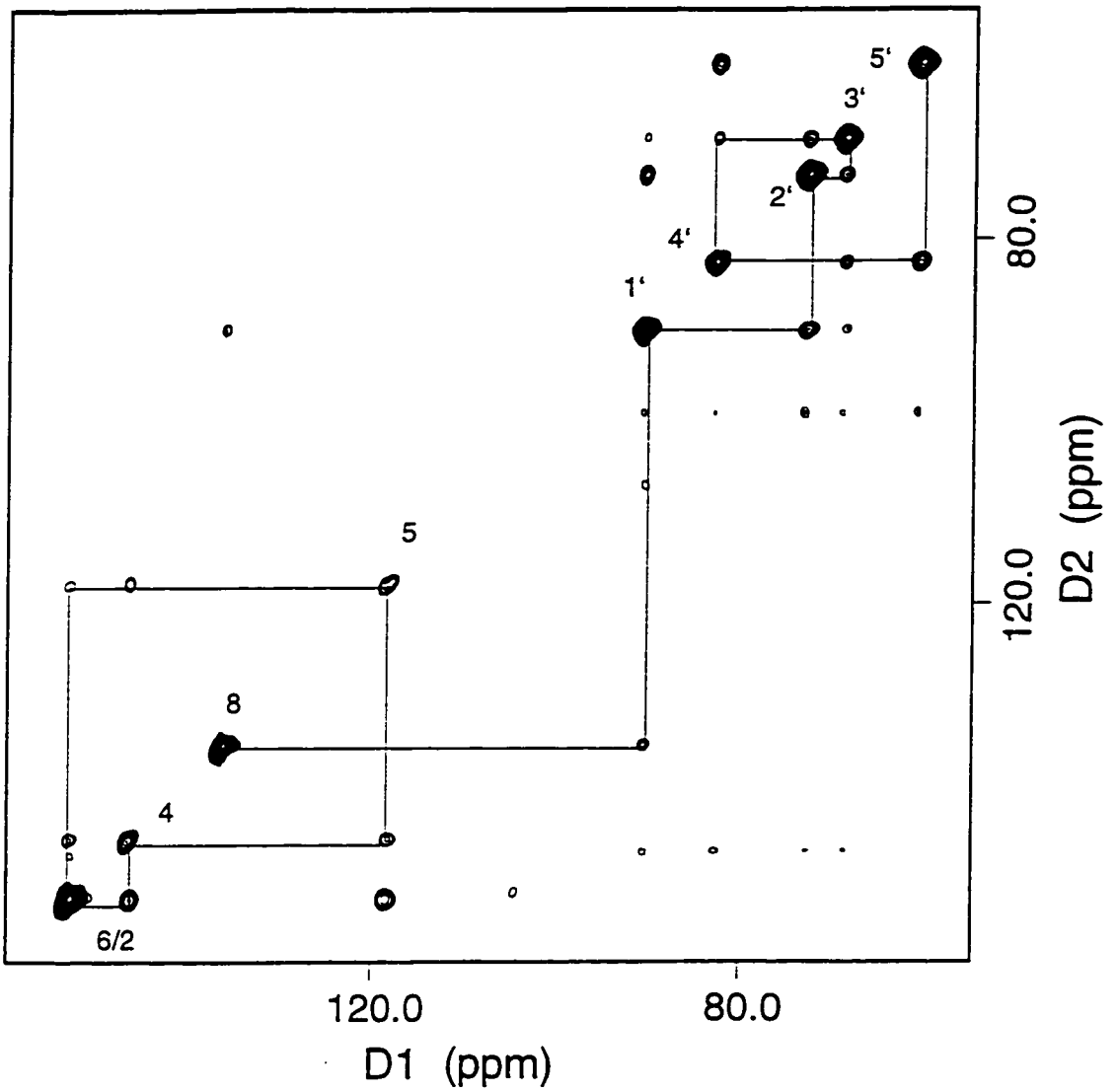

Figure 6.16: One cycle RFDR spectrum for polycrystalline adenosine, taken at 9.4 Tesla.

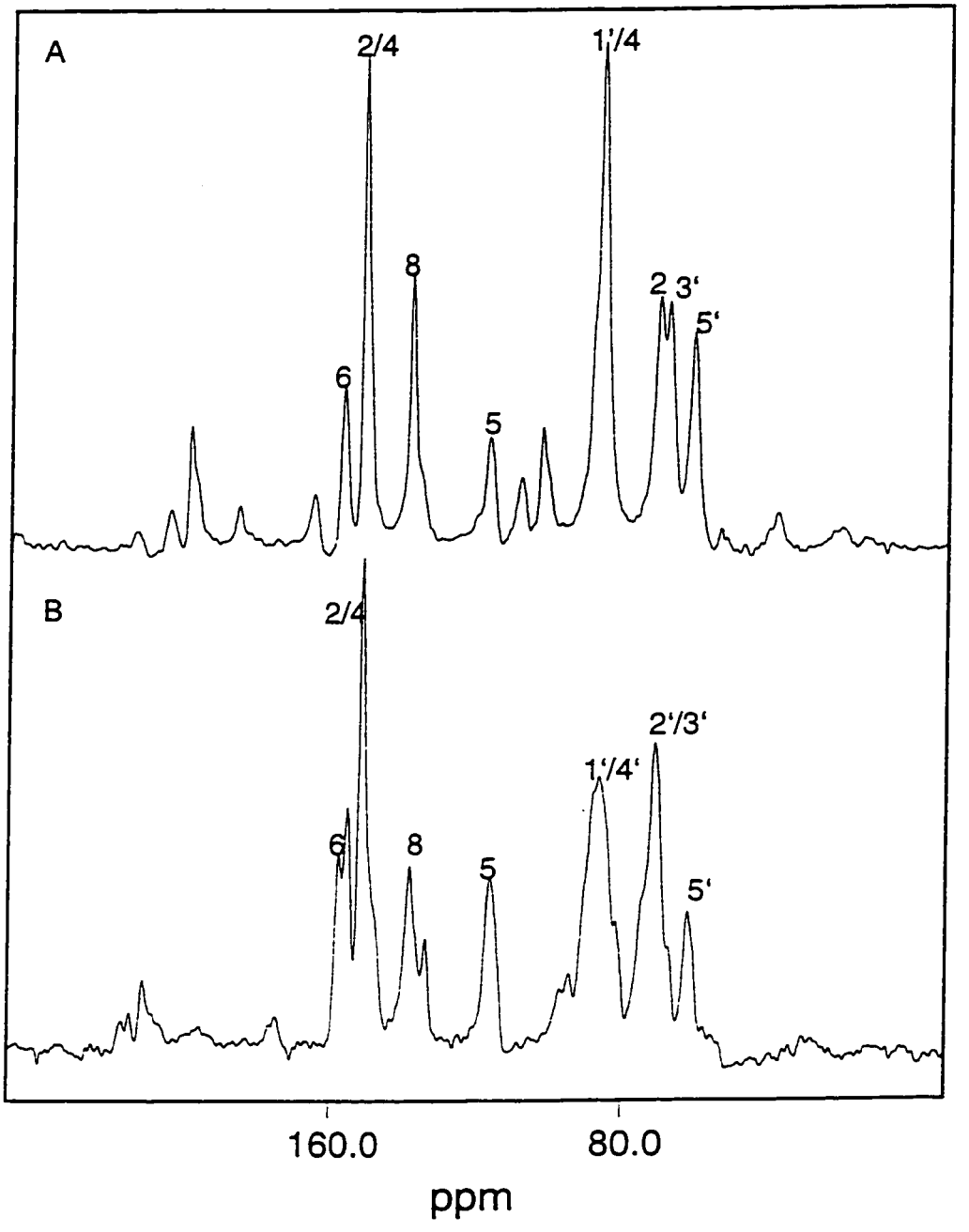

Figure 6.17: Carbon-13 CP-MAS spectra for lyophilized (A) and polycrystalline (B) guanosine, taken at 9.4 Tesla.

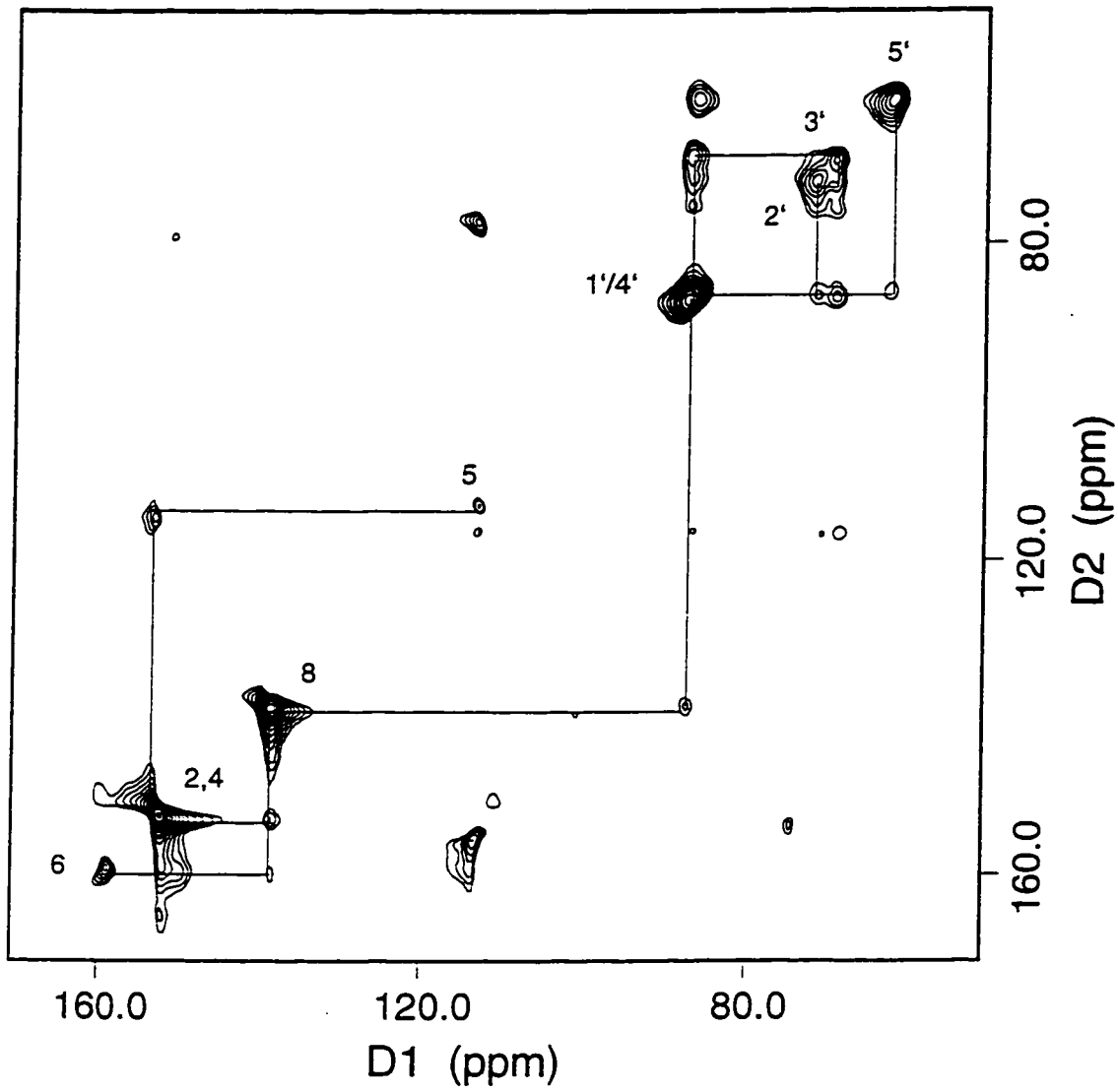

Figure 6.18: One cycle RFDR spectrum for lyophilized guanosine, taken at 11.7 Tesla.

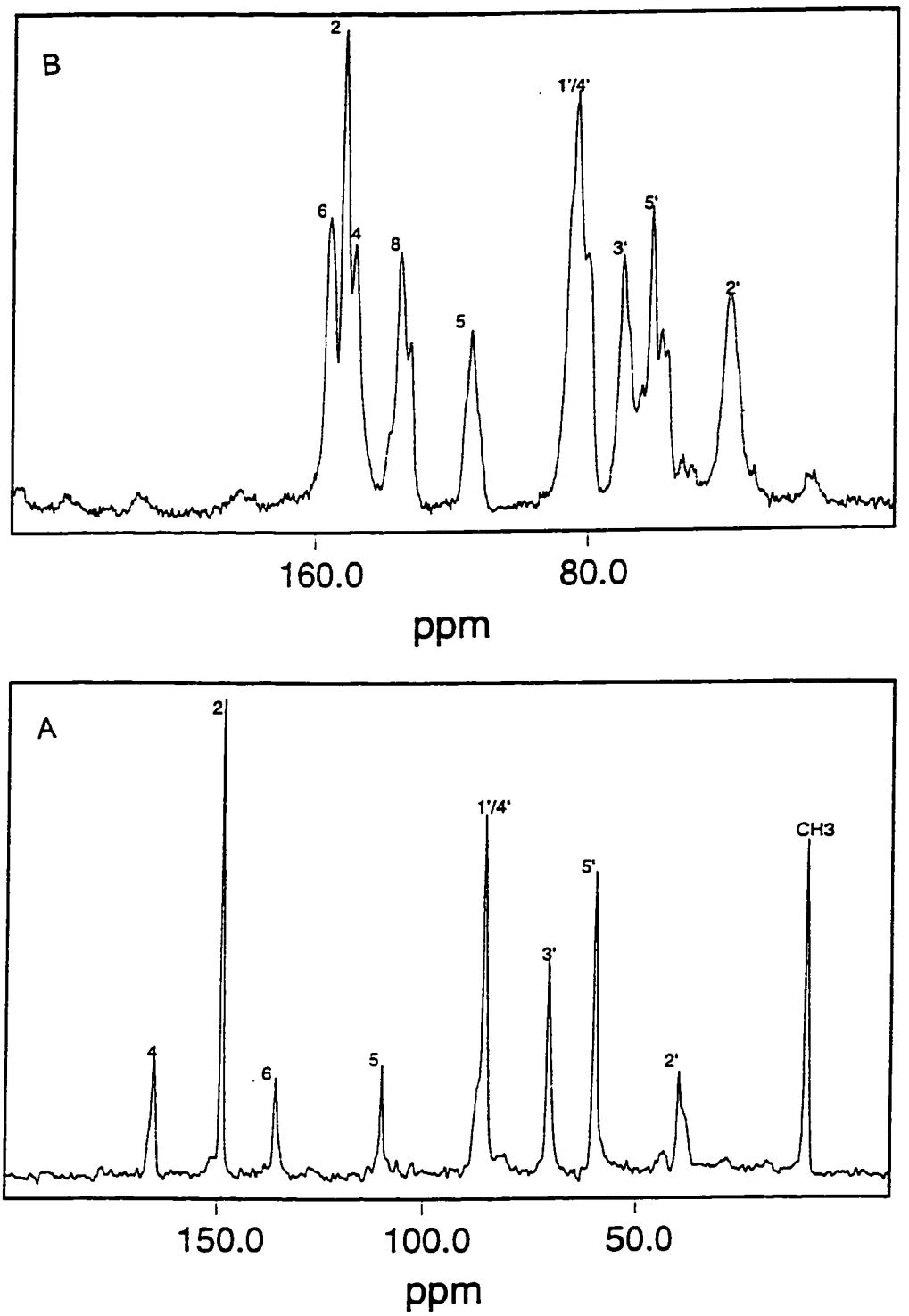

Figure 6.19: Carbon-13 CP-MAS spectra of polycrystalline thymidine (A) and lyophilized 2'-deoxyguanosine, taken at 9.4 and 11.7 Tesla, respectively.

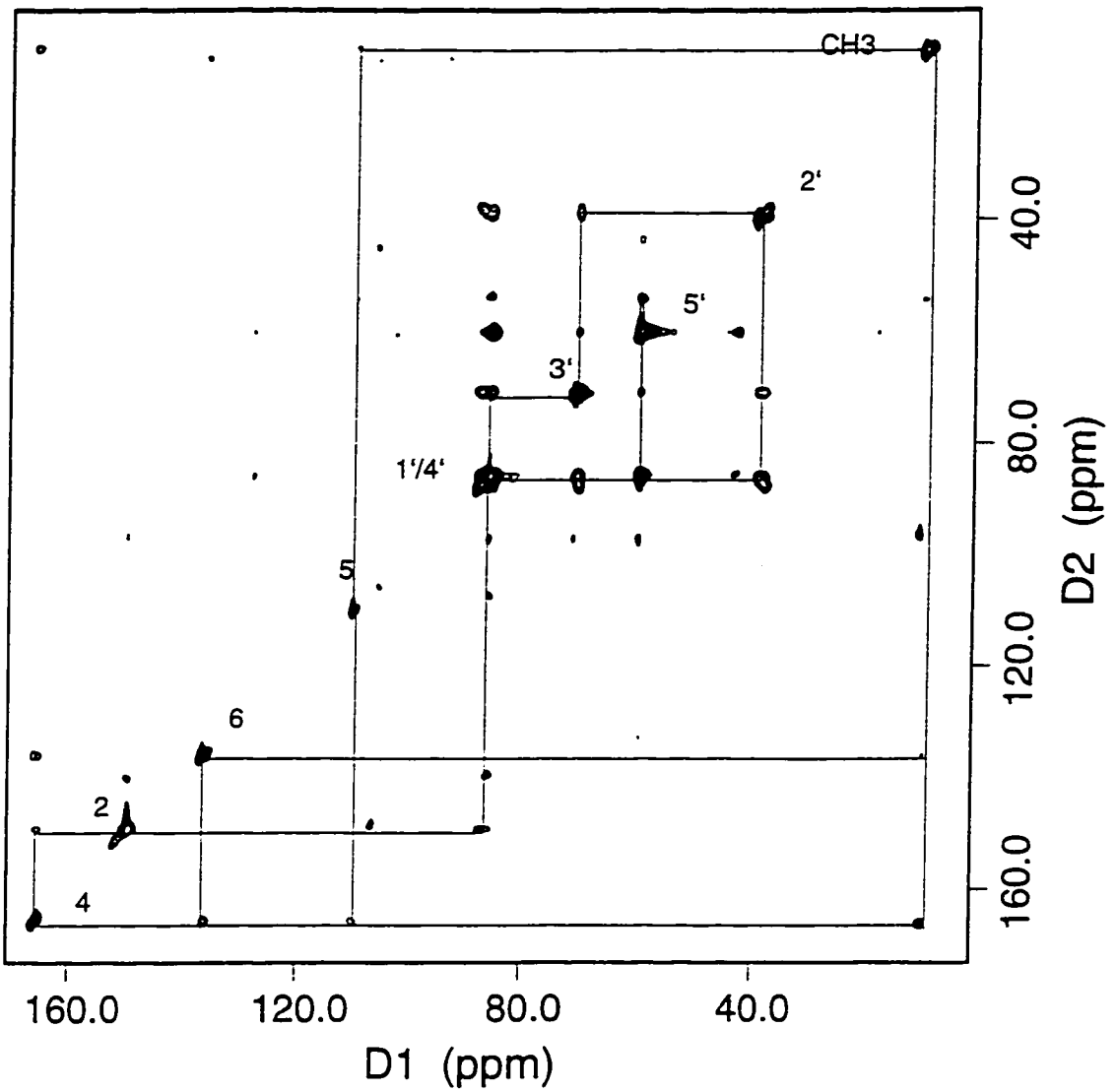

Figure 6.20: One cycle RFDR spectrum for polycrystalline thymidine, taken at 9.4 Tesla.

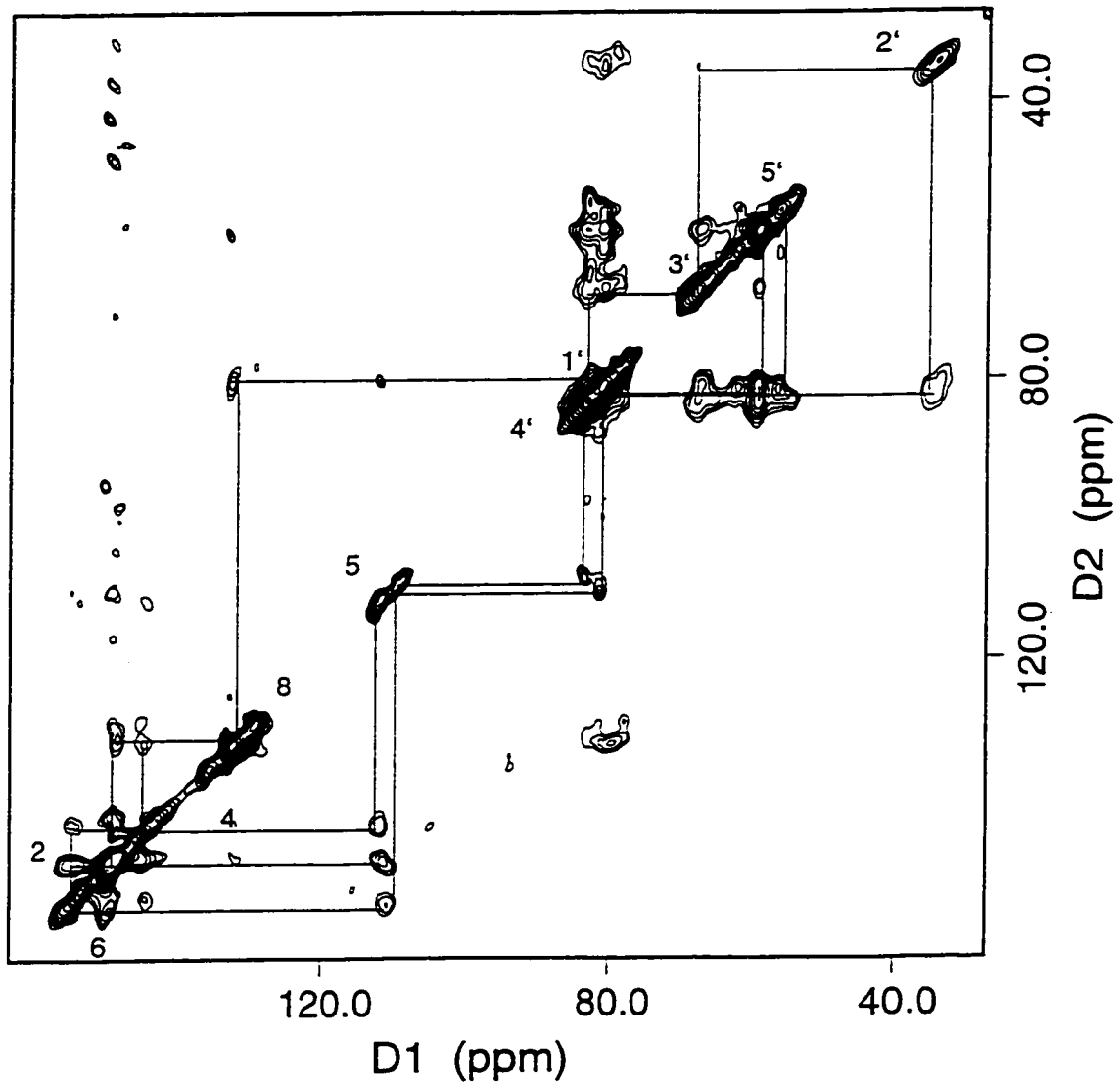

Figure 6.21: Two cycle RFDR spectrum for lyophilized 2'-deoxyguanosine, taken at 11.7 Tesla.

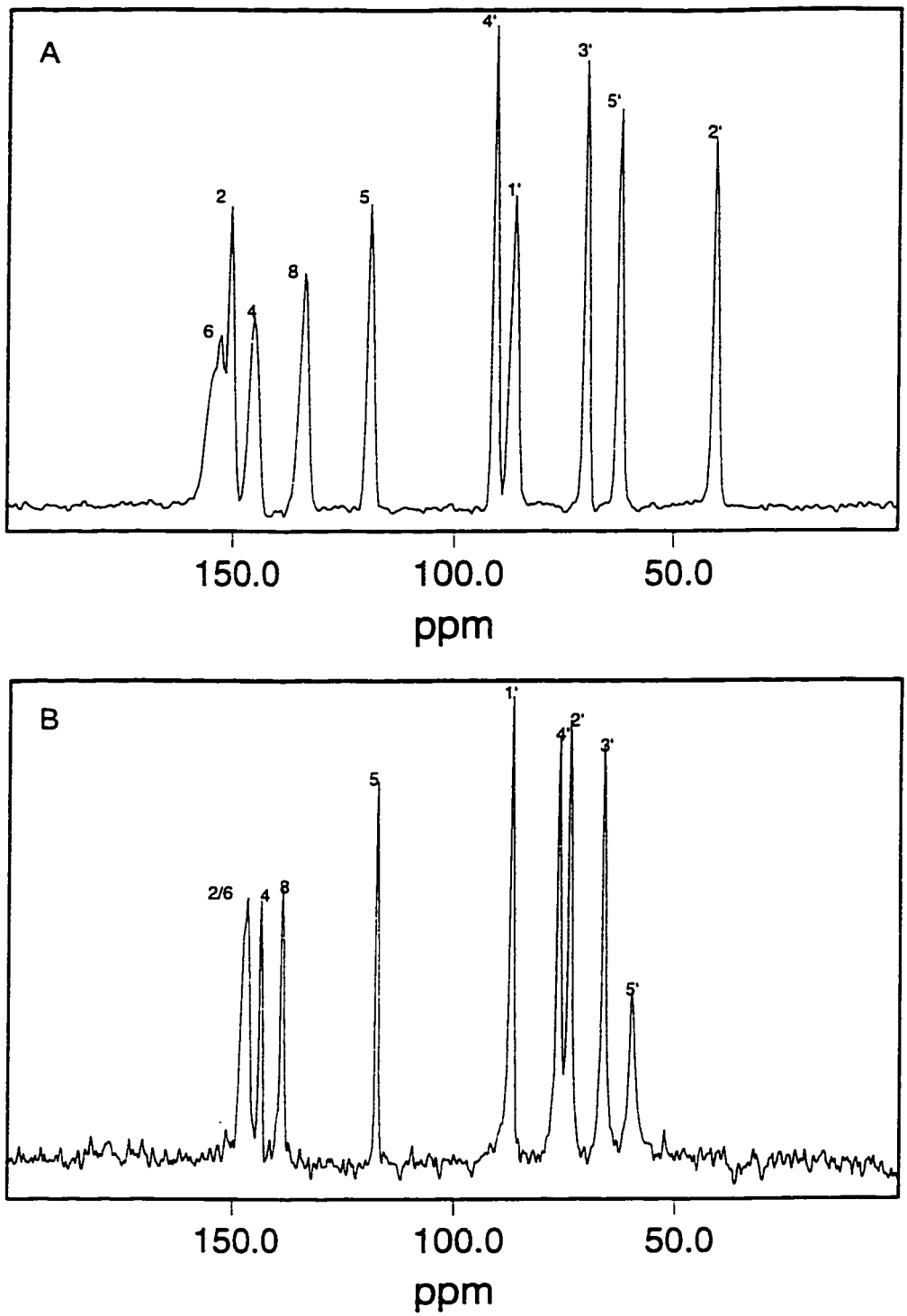

Figure 6.22: Carbon-13 CP-MAS spectra for polycrystalline 2'-deoxyadenosine monohydrate (A) and polycrystalline adenosine-5'-phosphate monohydrate (B), taken at 4.7 and 9.4 Tesla, respectively.

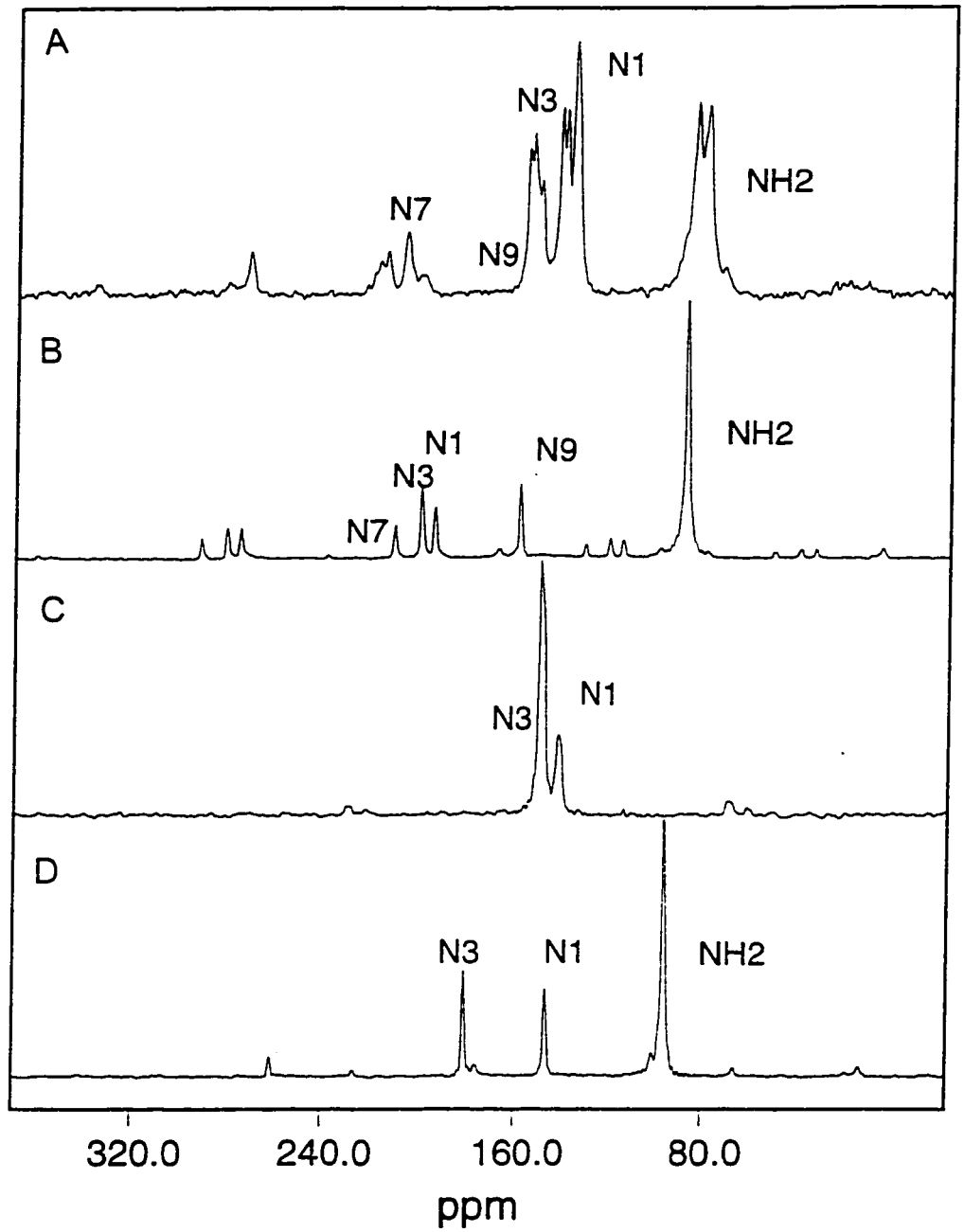

Figure 6.23: Nitrogen-15 CP-MAS spectra for polycrystalline guanosine (anhydrous form) (A), adenosine (B), uridine (C), and cytidine (D), taken at 9.4 Tesla using the TOSS pulse sequence.

Chapter 7
Double Quantum DRAWS Results

7.1 Introduction

This chapter presents double quantum (DQ) DRAWS results for several selectively and uniformly ^{13}C labeled nucleosides. The first section presents results for four different selectively ^{13}C labeled cytidine monomers. The second section presents DQ-DRAWS spectra for uniformly ^{13}C and ^{15}N enriched cytidine, adenosine, and thymidine. The creation and subsequent evolution of DQ coherence during the DRAWS experiment is sensitive not only to the dipolar coupling but also the mutual orientation of the chemical shift tensors (see also Chapter 3). Because the chemical shift tensor for each nucleus can be related to the molecular frame, it is possible to extract valuable information about the molecule's geometry from amplitudes of the DQ sideband intensities. The DQ spectrum is a complicated convolution of the DQ chemical shift spectrum, the duration of the preparation period, the magnitude and orientation of the single quantum tensors, the orientation of the dipole vector which connects the two nuclei, and the dipolar coupling strength. The following section illustrates the effect of several of these parameters on the appearance of the DQ-DRAWS spectrum for a series of doubly and triply ^{13}C-labeled, polycrystalline cytidine monomers. Additionally, an application of the DQ-filtered DRAWS experiment to a DNA dodecamer containing a uniformly ^{13}C, ^{15}N enriched nucleotide is presented in Section 7.4.

7.2 Selectively ^{13}C Labeled Cytidine DQ-DRAWS Results

This section presents DQ-DRAWS data from polycrystalline [2,2'-$^{13}C_2$], [2,1'-$^{13}C_2$], [2,2',5'-$^{13}C_3$], and [2,1',3'-$^{13}C_3$] cytidine monomers. Figure 7.1 presents the la-

beling schemes and relevant internuclear distances for each of the cytidine isotopomers. The full two-dimensional DQ-DRAWS data set for [2,2'-$^{13}C_2$] cytidine is given in Figure 7.2. The spectrum was collected at a spinning speed of 4525 Hz using a ^{13}C field of 38.36 kHz and three repetitions of the DRAWS mixing cycle. The CP-MAS (i.e. single-quantum) spectrum appears as a projection along the D1 dimension, while the DQ spectrum appears as a projection along the D2 axis. Selective column addition of the D1 vectors yields the one-dimensional DQ spectrum displayed in Figure 7.2. As discussed in Chapter 3, the isotropic DQ peak occurs at the sum of the two SQ chemical shift values. The isotropic peak (designated as the 0 peak) is surrounded by an envelope of DQ spinning sidebands (designated as ±1, ±2, etc.), which are spaced at an integral number of the spinning frequency. The experiment was repeated at a slower spinning speed (2525 Hz) with a 41.6 kHz ^{13}C field (as described in Section 4.8.3) to produce the spectra shown in Figure 7.3. Examination of the two data sets reveals the effect of decreased spinning speed on the appearance of the DQ spectrum. The most noticeable feature of these spectra is the difference in the intensity of the central isotropic DQ peak. At 4525 Hz, the isotropic peak is substantially smaller relative to the ±1 spinning sidebands than in the slower spinning spectrum. The DQ isotropic peaks are oftentimes absent or small for couplings to nuclei with small CSA's, such as the furanose ring carbons of nucleosides. This diminished centerband intensity has been predicted on theoretical grounds by Gregory and coworkers and has also been observed in DQ-DRAWS data for alanine [1]. Figure 7.4 presents the DQ-DRAWS data for [2,2',5'-$^{13}C_3$] cytidine collected at a spinning speed of 4901 Hz (41.7 kHz). The C5' resonance has an extremely low intensity in the SQ projection, despite the application of four repetitions of the DRAWS mixing cycle. This low intensity for C5' can be attributed to the presence of only weak long-range couplings between the C5'-C2 (5.54 Å) and C5'-C2' (3.75 Å) spin pairs. The DQ projection for this data set is almost identical to the 4525 Hz spectrum for [2,2'-$^{13}C_2$]

cytidine analogue, suggesting that the effect of the weakly coupled C5' nucleus on the appearance of the DQ spectrum is negligible.

An analogous experiment was performed on the [2,1'-$^{13}C_2$] cytidine monomer at 2525 Hz (shown in Figure 7.5) using two DRAWS cycles. Examination of the 2525 Hz spectra for the two different doubly labeled cytidine monomers clearly indicates how sensitive the DQ-DRAWS experiment is to differences in CSA tensor characteristics and dipolar coupling strength. The DQ-DRAWS experiment for [2,1',3'-$^{13}C_3$] cytidine at 4901 Hz using three DRAWS cycles is presented in Figure 7.6 for comparison. Crystallographic splitting is apparent for the C1' resonance in the triply labeled compound, which was not observed in the data set for the complementary [2,1'-$^{13}C_2$] cytidine monomer. The effect of third spin in the appearance of the DQ-DRAWS data is no longer negligible for this sample. Figure 7.7 compares the DQ slices for C2, C1', and C3' resonances. Each of the three slices contains very weak DQ isotropic peaks, surrounded by much higher intensity ±1 spinning sidebands. Due to rapid spinning frequency, few DQ sidebands are present in this data set. This is especially noticeable in the DQ slice for C3', which contains an isotropic DQ resonance due to the dipolar coupling with C1'. The C3' carbon is too weakly coupled to C2 (4.16 Å) to produce any substantial amount of DQ coherence even with three cycles of DRAWS. Similarly, the C2 slice contains only information due to couplings to the nearby C1' (2.46 Å). The C1' projection, in contrast, contains DQ sidebands for couplings with both C2 and C3'. Note the similarity in the appearance of the C1'-C3' manifold of DQ peaks in the C1' and C3' slices and the C2-C1' manifold in the C1' and C2 projections.

7.3 Uniformly ^{13}C, ^{15}N Labeled Nucleoside DQ-DRAWS Results

Figures 7.8 illustrates the effect of conducting the DQ-DRAWS experiment on a uniformly labeled cytidine monomer containing nine ^{13}C enriched nuclei. Figures

7.9 and 7.10 show the full DQ-DRAWS spectra for u-^{13}C, ^{15}N labeled adenosine and guanosine. Each data set was collected at a spin rate of 4901 Hz with one application of the DRAWS mixing cycle. Due to the high level of isotopic enrichment in these samples, there are significant contributions to the spectra from DQ, as well as higher order (multiple quantum), coherences with neighboring nuclei. This later effect evidences itself as phase-twisting in the DQ spectra of heavily ^{13}C enriched compounds. Crosspeaks occur for those atoms that are involved in double quantum coherences. For short mixing periods, coherences are only excited for atoms within 1.5-2.5 Å, allowing for the identification of nearby and more distant nuclei. In this capacity, the DQ DRAWS experiment can serve as a useful assignment tool for these complicated, multiply labeled spin systems. Only the DQ-DRAWS spectrum of uniformly ^{13}C,^{15}N labeled cytidine will be discussed here in detail. The DQ slices for the DQ-DRAWS spectrum of the uniformly ^{13}C,^{15}N labeled cytidine monomer (Figure 7.11) contain sideband manifolds that are due to the presence of more than one strongly coupled spin pair. The DQ slice for C2' contains one set of sidebands due to a coupling with C1' and another with C3'. Both DQ isotropic peaks are almost non-existent. The ±1 sidebands for the C2'-C1' and C2'-C3' are separated from the isotropic peak by 4901 Hz. Interestingly, the ±2 sidebands have zero intensity at this spinning speed and number of DRAWS cycles. The C1'-C2' manifold in the C1' slice shows a similar effect. The C2-C1' set is fairly weak in intensity, so only ±1 sidebands are visible in the C1' DQ projection. The C2 slice contains a DQ envelope due to a coupling with C1' (with ±1 and ±2 DQ sidebands at 4901 Hz and 9802 Hz about the DQ isotropic peak). The C2-C1' manifold in this slice is quite similar to the pattern in the C2 and C1' slices of the [2,1',3'-$^{13}C_3$] cytidine DQ-DRAWS spectrum. A second DQ sideband manifold is also evident in the C2 slice for u-^{13}C, ^{15}N labeled cytidine. This additional DQ spectrum is due to two-quantum coherence between the aromatic C2 with C6 nuclei.

7.4 DQ-Filtering in [u-^{13}C, ^{15}N]-dC9 DNA Dodecamer

The DQ-DRAWS experiment can also be implemented as a DQ-filtering technique by holding the t_1 increment constant at 1μs (see Section 3.7). Using DQ-filtering, it is possible to extract out only those signals that are due to DQ coherences between dipolar coupled nuclei in complicated samples containing labeled and unlabeled material. The DQ-filtered DRAWS experiment has been successfully implemented by Gregory et al. on a DNA dodecanucleotide, [d(CGCGAATTCGCG)]$_2$, containing singly ^{13}C labeled thymidine residues at positions dT7 and dT8 (underlined sites) [2]. The results of that work demonstrated that only the signal from the two labeled thymidine nucleotides in the sample would be observed as a result of the DQ-filtering experiment. Natural abundance background signal, which would be visible in a typical CP-MAS spectrum, was shown to be effectively eliminated in the DQ-filtered spectrum of the DNA. This technique has been applied to a DNA dodecamer with the following sequence, [d(CGCGAATTCGCG)]$_2$, containing a uniformly ^{13}C,^{15}N labeled 2'-deoxycytidine nucleotide at the dC9 position (underlined residue). The sample was constructed in order to observe the sugar ring resonances of the dC9 nucleotide under varying hydration levels independently from the natural abundance DNA background signal. This strategy expands on previous work done by Santos et al. (see Section 1.4). In this earlier study, natural abundance ^{13}C CP-MAS spectra were collected for high molecular weight calf-thymus DNA fibers to monitor the chemical shift changes for the furanose ring carbon nuclei under varying hydration levels and salt conditions [3]. A drawback to this approach was that chemical shifts for the particular nucleotide of interest could not be isolated from the natural abundance background signal. The DQ-filtering technique should theoretically reveal only those resonances belonging to the labeled dC9 nucleotide in the selectively enriched DNA dodecanucleotide. We attempted the DQ-DRAWS filtering experiment on 52.1 mg of u-^{13}C, ^{15}N dC9 DNA several times at both 66% and 75% RH, but were unsuc-

cessful at observing enough DQ signal to make any definite conclusions about the identity of the chemical shifts. The low intensity of the DQ-filtered signal was most likely due to a combination of factors. Most importantly, only 20% of the dC9 sites in the DNA dodecamer contained the uniformly labeled material (~ 0.5 mg total). A second problem for salted DNA samples is probe detuning, which is compounded by hydration of the sample. A final issue is poor DQ-filtering efficiency. Unfortunately, numerical simulations have shown that it is impossible to obtain DQ-filtering efficiencies greater than 50% in a powder sample [2]. More realistically, filtering efficiencies never surpass 25%, due to the effects of transverse relaxation, which attenuate antiphase and DQ coherences over the course of the experiment. Gregory and coworkers found that filtering efficiencies in the selectively ^{13}C labeled DNA dodecamer mentioned above were only between 3-5%. A future project may involve incorporating a nucleotide with a selectively ^{13}C labeled sugar ring (with a much higher level of isotopic enrichment) at the dC9 position of this DNA oligonucleotide. Possible labeling strategies could include those described in the previous section. Furthermore, by conducting the experiment at low temperatures (i.e. frozen) many of the motional processes that lead to lower DQ efficiencies can be attenuated. Lower temperatures improve sensitivity and minimize the effects of probe-detuning, both of which are important considerations for the successful implementation of the DQ-filtering experiment on hydrated biomacromolecules.

7.5 DQ-DRAWS Simulations

At the time of this writing, it has not been possible to simulate the DQ-DRAWS data presented in this chapter. Successful simulation of the data requires optimization of multiple adjustable parameters. The DQ sideband intensities are sensitive to the principal values of the chemical shift tensors, the internuclear distance, and five Euler angles: the three components of the solid Euler angle relating the PAS

frames of the two chemical shift tensors and the two angles orienting the internuclear vector in a reference frame common to the two chemical shift tensors. Knowledge of these tensor orientations is critical for successful simulation of DQ-DRAWS data. The C2 tensor orientations were presumed to be similar to those of the 2,4-$^{13}C_2$-deoxythymidine monomers. However, tensor orientations for the sugar ring C1', C2', C3', and C5' carbon atoms are not known with certainty, and can only be approximated from single-crystal data for related carbohydrate derivatives [4-6]. DQ-DRAWS simulations for the cytidine monomers have been further complicated by the presence of directly bonded quadrupolar ^{14}N atoms adjacent to the ^{13}C labeled positions. The dipolar coupling between ^{14}N and ^{13}C is not suppressed by MAS because the relatively large quadrupole interaction (on the order of 1-5 MHz) shifts the quantization axis of the ^{14}N spins away from the direction of the main applied magnetic field [7]. The resulting ^{13}C lineshapes are strongly influenced by the characteristics of the ^{14}N coupling tensor, resulting in broadened resonances and/or asymmetric splitting patterns [8]. The impact of ^{14}N on the ^{13}C lineshapes of pyrimidine ring carbons is quite apparent in the natural abundance CP-MAS spectrum of 2'-deoxycytidine hydrochloride (Figure 6.1) taken at 4.7 Tesla. Although ^{14}N effects are field-dependent, they are still significant at 9.4 Tesla. The presence of ^{14}N-^{13}C couplings on the outcome of the DQ-DRAWS experiment is to diminish and possibly alter the intensity of the DQ sidebands. Previous data for doubly labeled monomers and DNA oligonucleotides avoided this troublesome complication by incorporating ^{15}N labels at the N1 and N3 positions of the thymine base [1]. The present version of the DQ-DRAWS simulation code does not include the effects of quadrupolar coupling, so simulation of the experimental cytidine monomer data was not possible. Simulation of the DQ-DRAWS spectra for the multiply ^{13}C, ^{15}N enriched samples is also not computationally tractable at this time. Work is currently underway by other members of this laboratory to address the ^{14}N issue and to provide methods that could perform a "grid search" through the large parameter space that exists for DQ-DRAWS simulations.

7.6 Notes to Chapter 7

[1] Gregory, D.M., Mehta, M.A., Shiels, J.C., and Drobny, G.P. (1997) *J. Chem. Phys.*, **107** (1), p. 28.

[2] Gregory, D.M., Wolfe, G.M., Jarvie, T.P., Shiels, J.C., and Drobny, G.P. (1996) *Mol. Phys.*, **89** (6), p. 1835.

[3] Santos, R.A., Tang, P., and Harbison, G.S. (1989) *Biochemistry*, **28**, p. 9372.

[4] Liu, F., Phung, C.G., Alderman, D.W., and Grant, D.M. (1995) *J. Am. Chem. Soc.*, **117**, p. 9323.

[5] Liu, F.L., Phung, C.G., Alderman, D.W., and Grant, D.M. (1996) *J. Amer. Chem. Soc.*, **118**, p. 10629.

[6] Sastry, D.L., Takegoshi, K., and McDowell, C.A. (1987) *Carbohyd. Res.*, **165**, p. 161.

[7] Vanderhart, D.L., Gutowsky, H.S., and Farrar, T.C. (1967) *J. Am. Chem. Soc.*, **89**, p. 5056.

[8] Hexem, J.G., Frey, M.H., and Opella, S.J. (1982) *J. Chem. Phys.*, **77** (7), p. 3847.

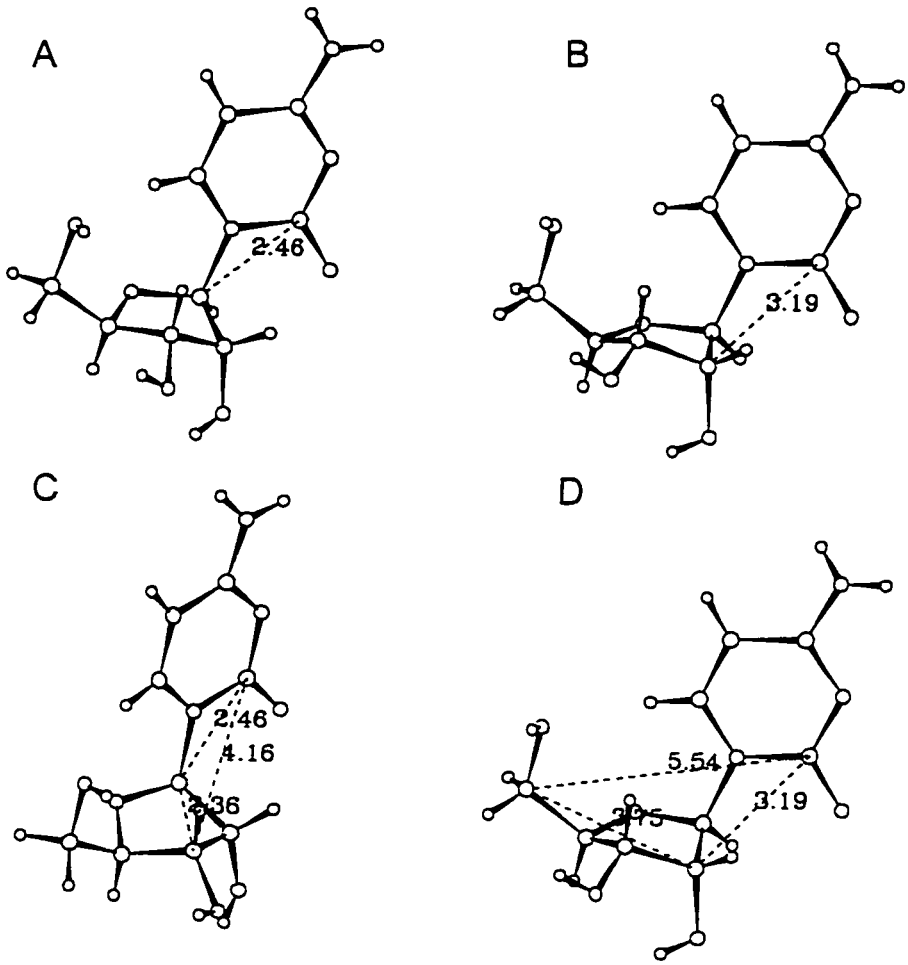

Figure 7.1: Representations of the four selectively labeled cytidine monomers: [2,1'-$^{13}C_2$]- (A), [2,2'-$^{13}C_2$]- (B), [2,1',3'-$^{13}C_3$]- (C), and [2,2',5'-$^{13}C_3$]-cytidine (D). The relevant internuclear ^{13}C-^{13}C distances (Å) for each sample appear as dashed lines. Atomic numbering appears in Figure 1.1.

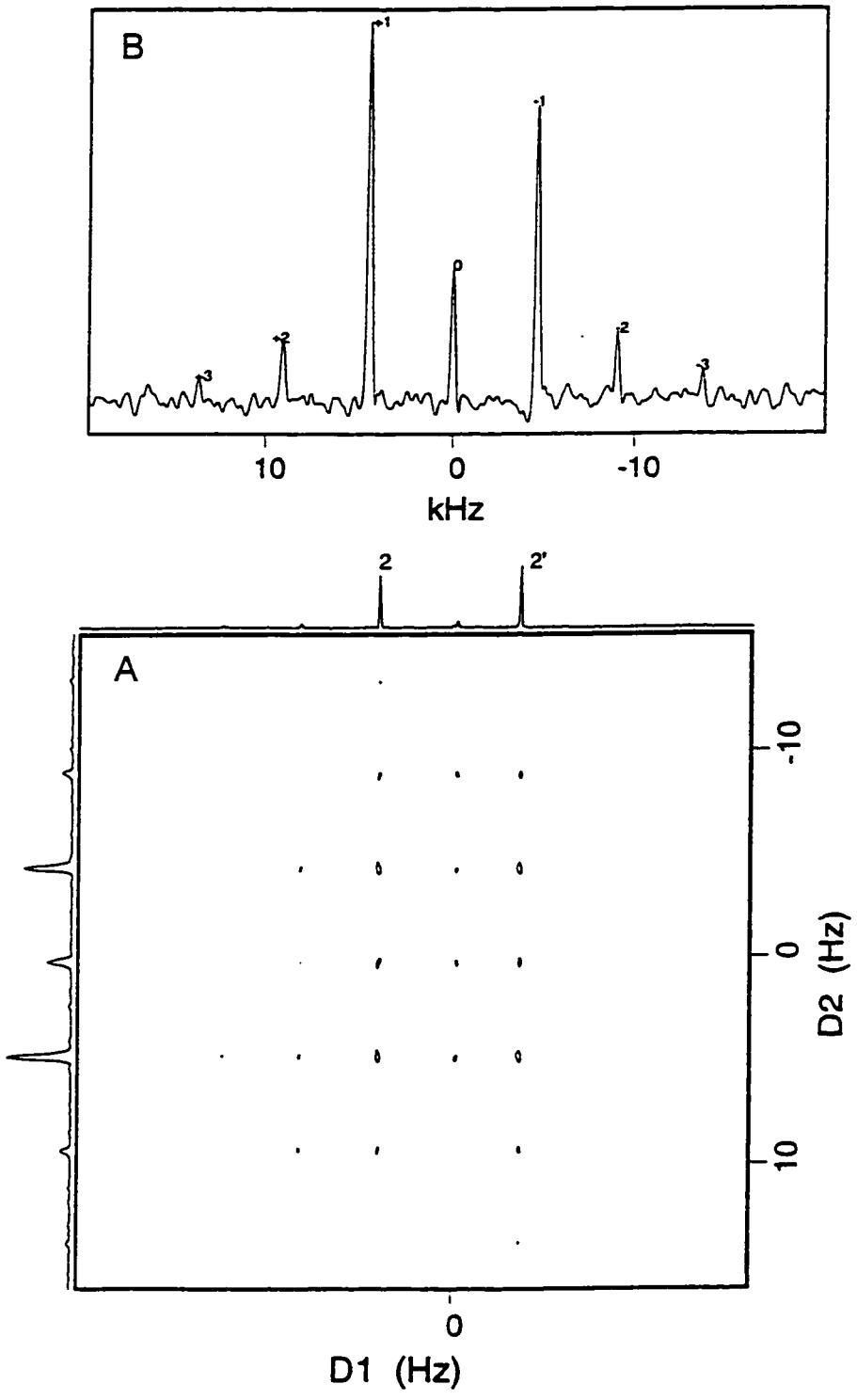

Figure 7.2: The full three cycle DQ-DRAWS spectrum for [2,2'-$^{13}C_2$]-cytidine taken at 4525 Hz (A). DQ spectrum obtained by selective column addition for the C2 and C2' resonances (B).

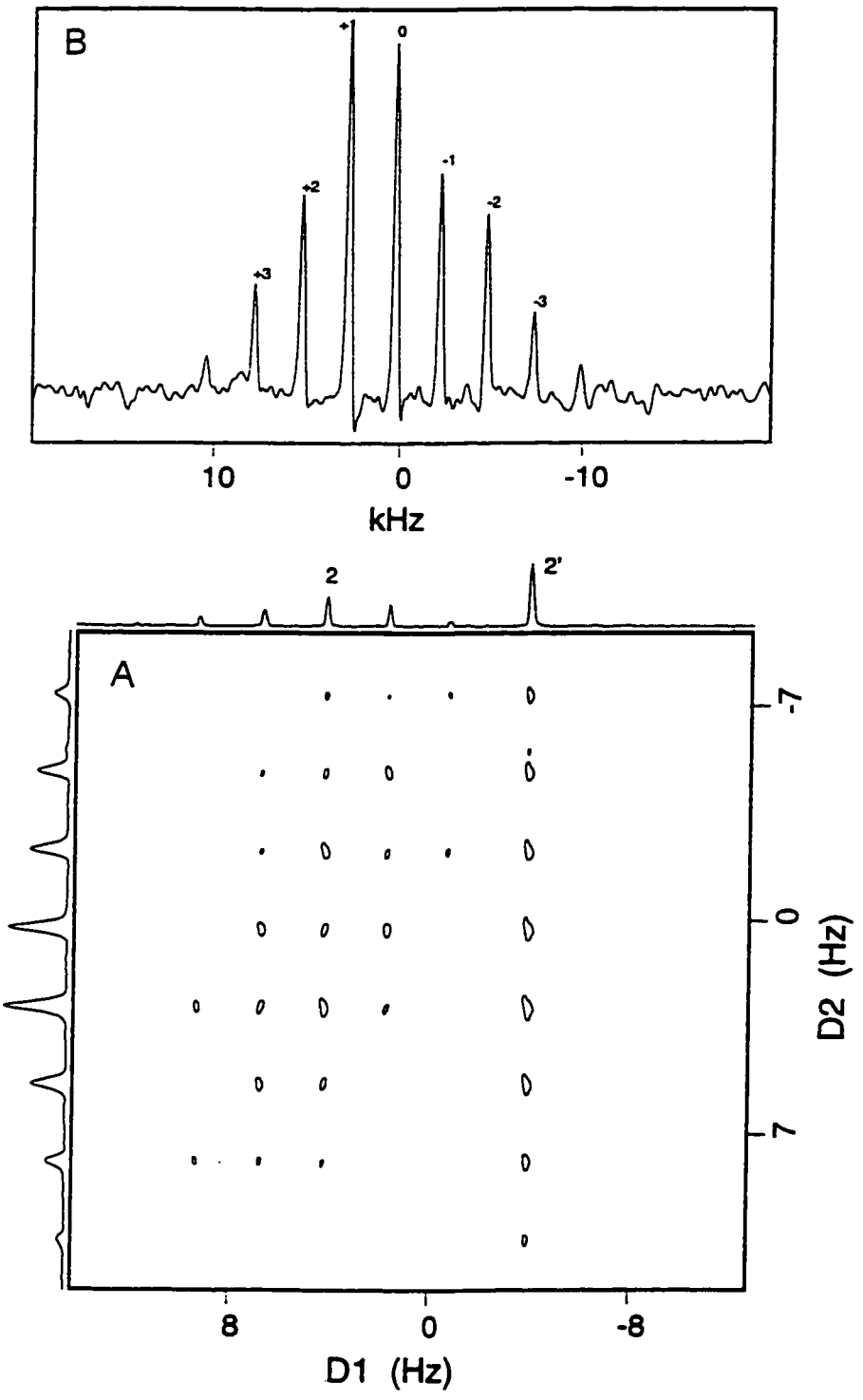

Figure 7.3: The full three cycle DQ-DRAWS spectrum for [2,2'-$^{13}C_2$]-cytidine taken at 2525 Hz (A). DQ spectrum obtained by selective column addition for the C2 and C2' isotropic peaks and sidebands (B).

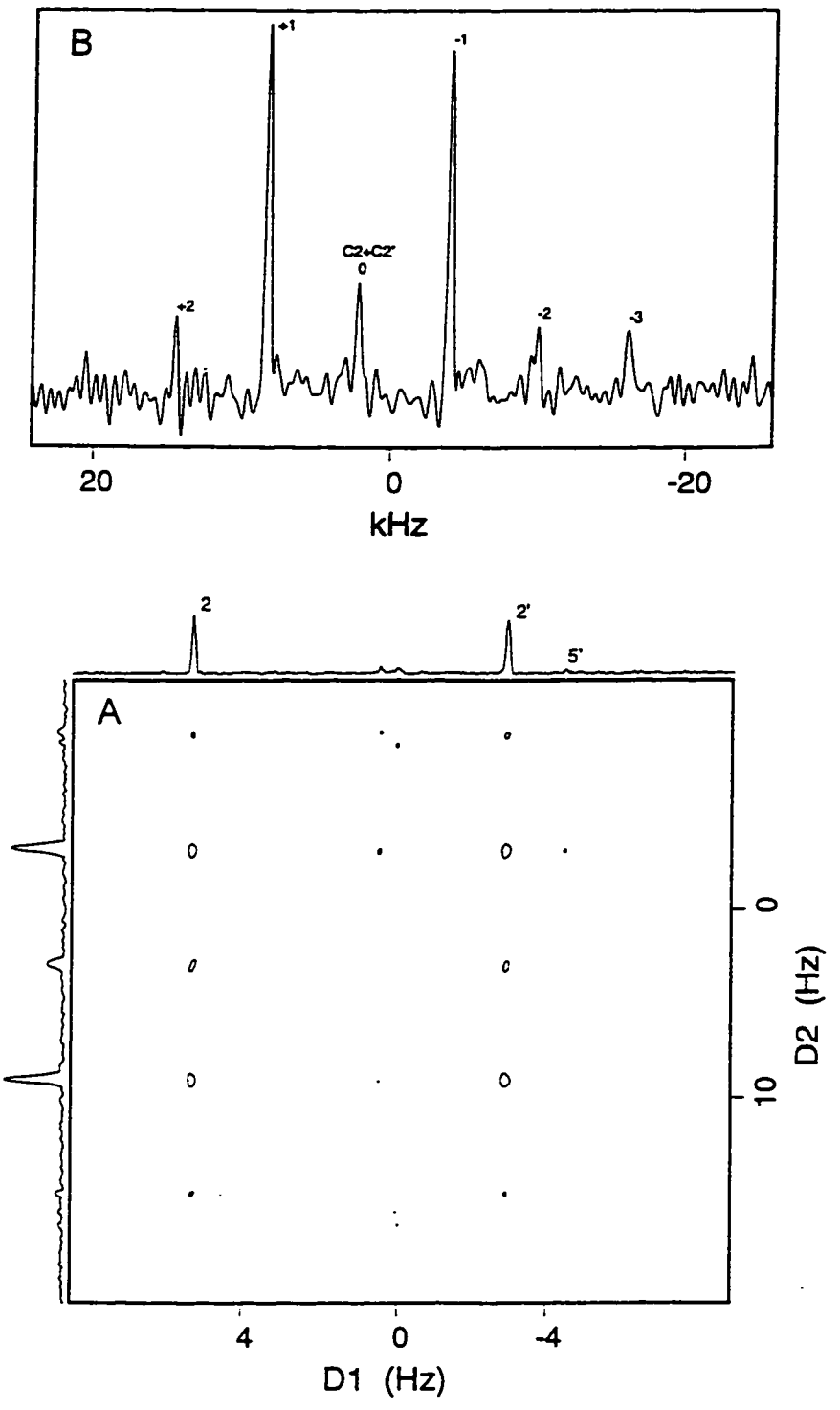

Figure 7.4: The full four cycle DQ-DRAWS spectrum for [2,2',5'-$^{13}C_3$]-cytidine taken at 4901 Hz (A). DQ spectrum obtained by selective column addition for the C2 and C2' peaks (B).

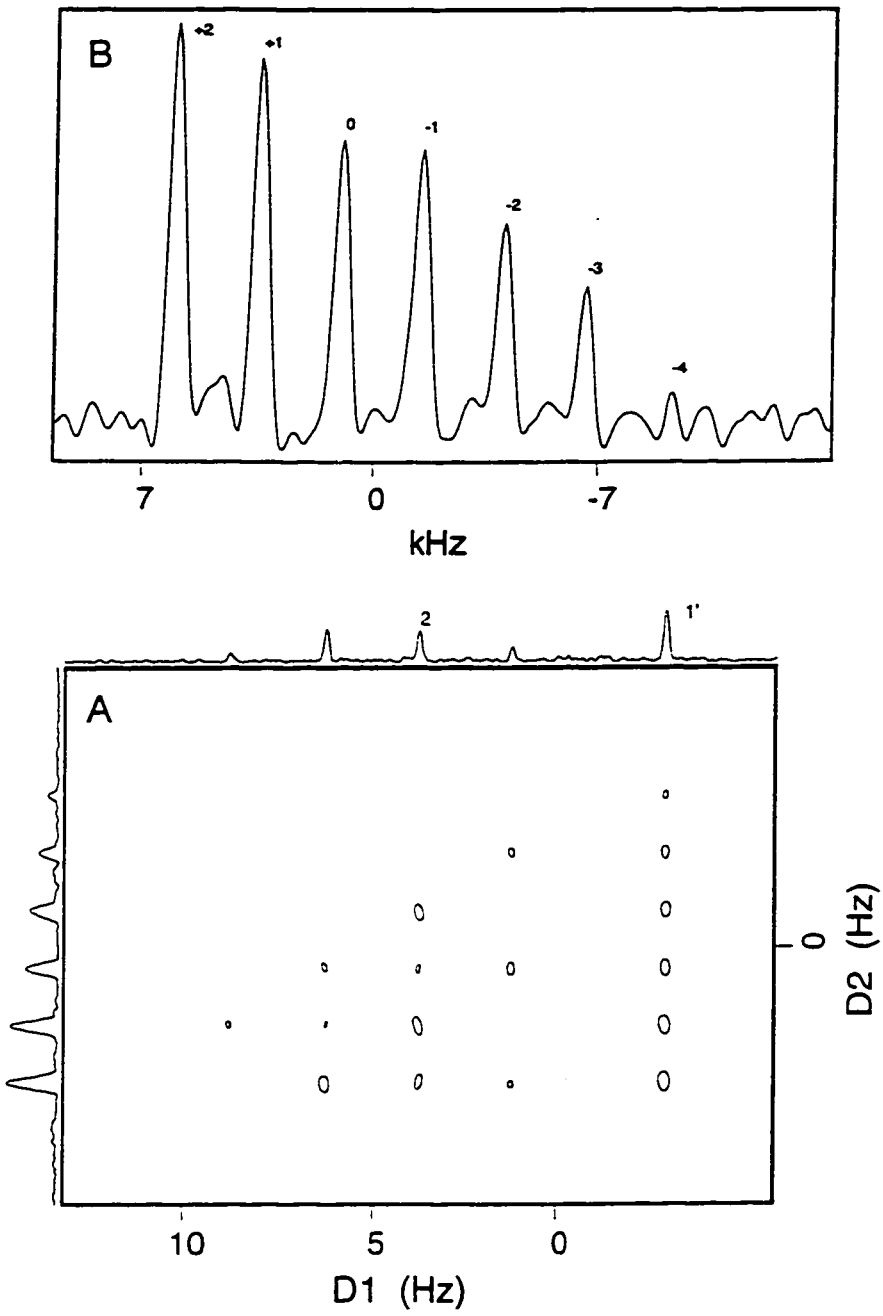

Figure 7.5: The full two cycle DQ-DRAWS spectrum for [2,1'-$^{13}C_2$]-cytidine taken at 2525 Hz (A). DQ spectrum obtained by selective column addition for the C2 and C1' isotropic peaks and spinning sidebands (B).

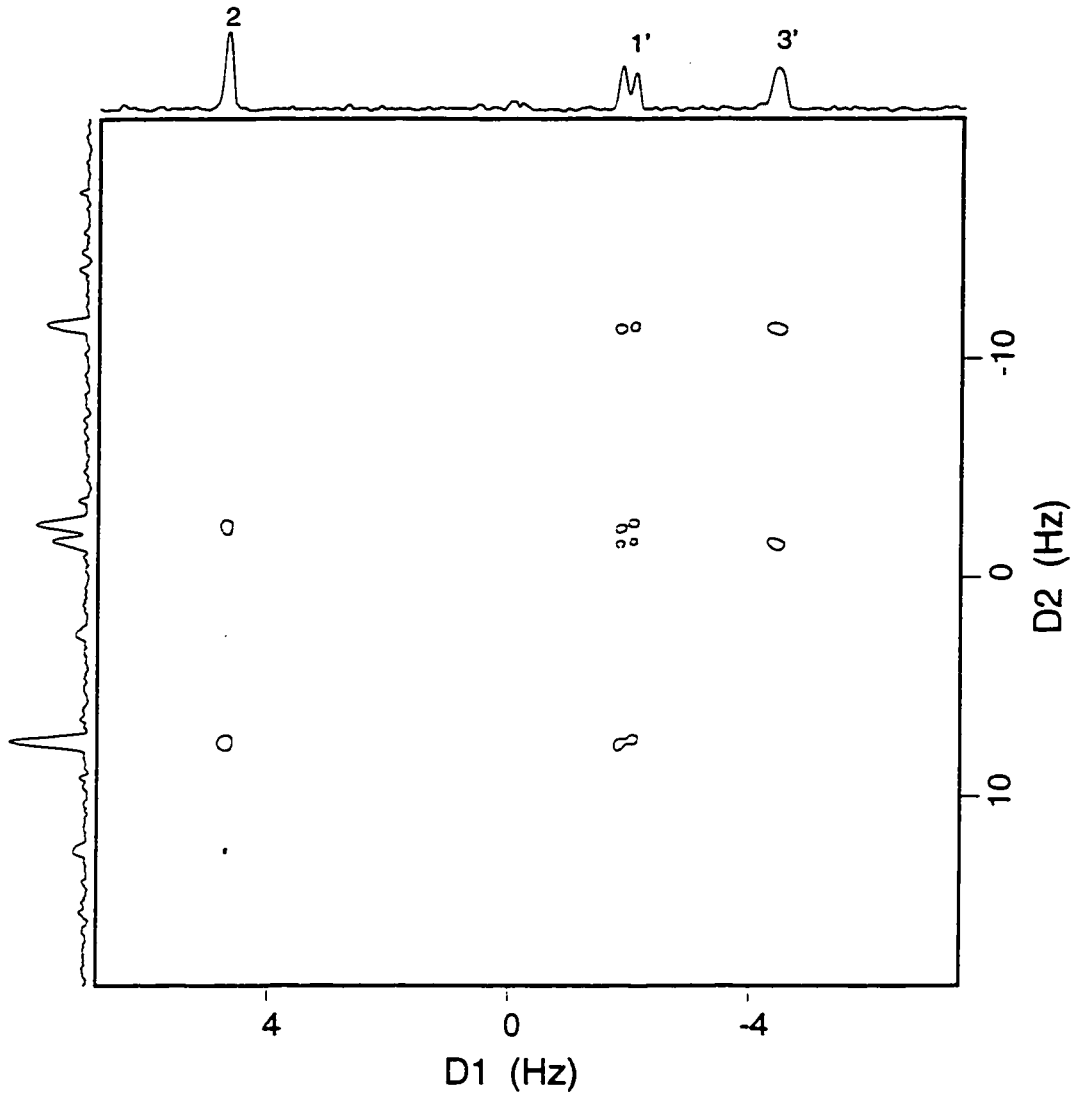

Figure 7.6: The full three cycle DQ-DRAWS spectrum for [2,1',3'-$^{13}C_3$]-cytidine taken at 4901 Hz.

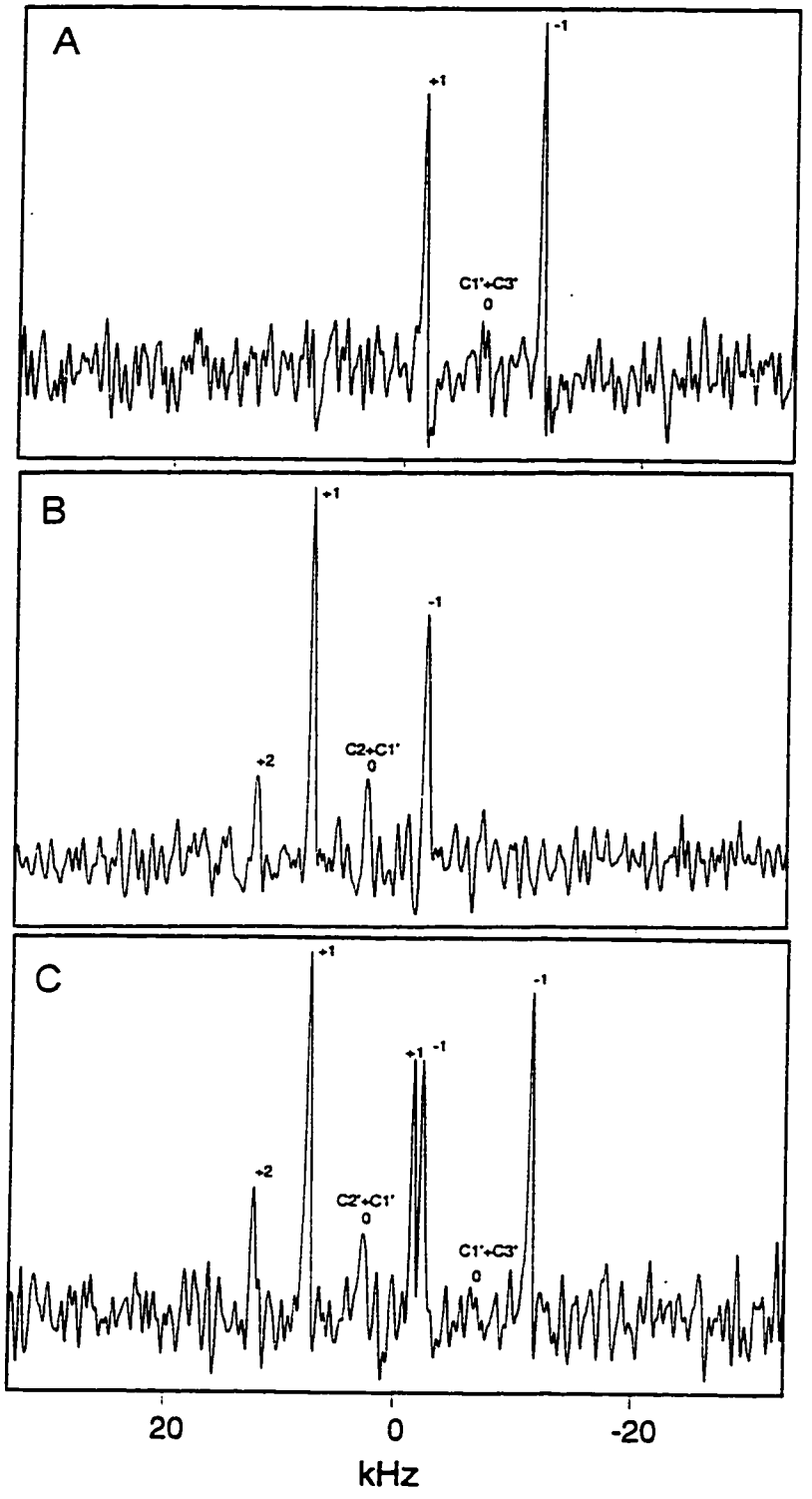

Figure 7.7: DQ spectra for C3' (A), C2 (B), and C1' (C) resonances of [2,1',3'-$^{13}C_3$]-cytidine.

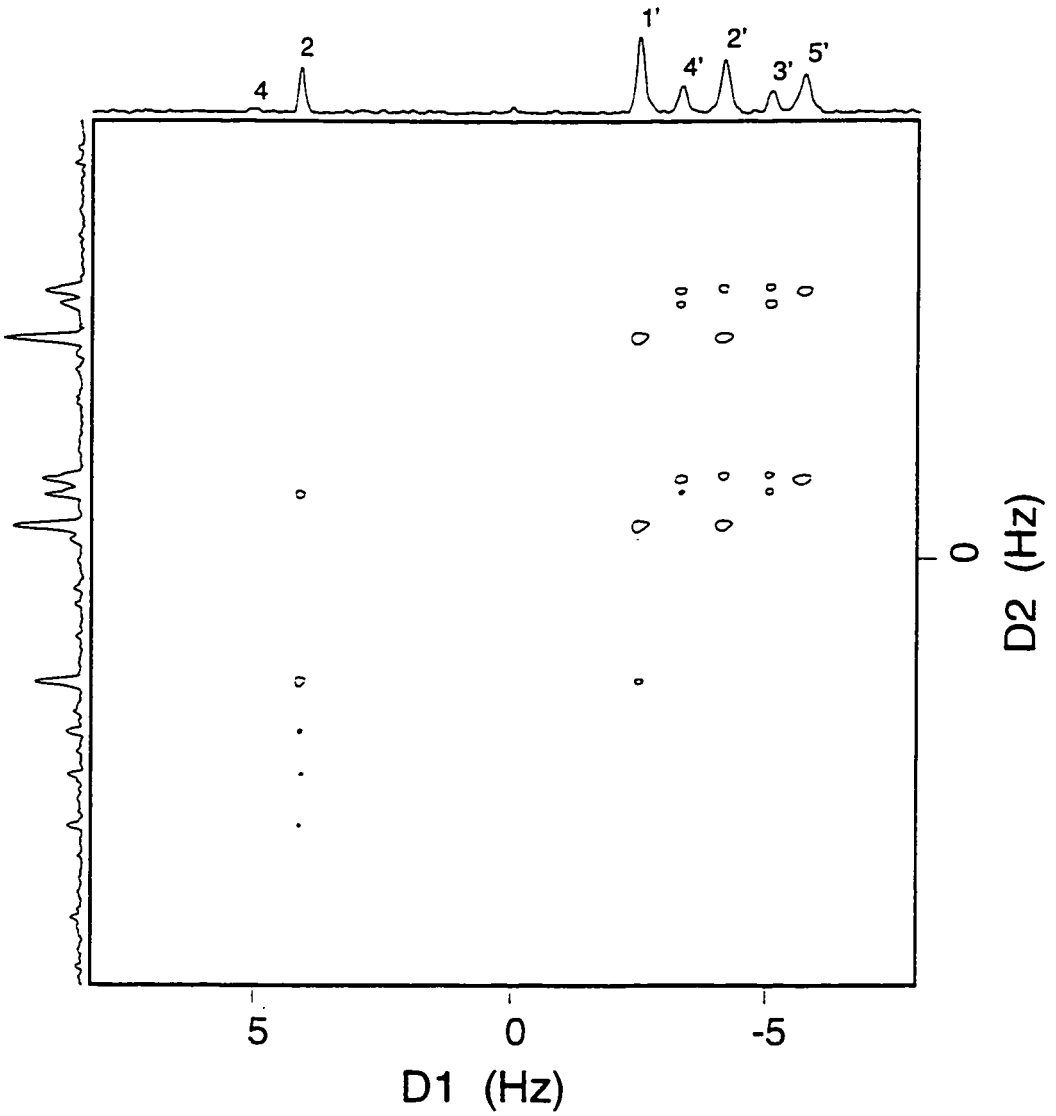

Figure 7.8: The full one cycle DQ-DRAWS spectrum for uniformly ^{13}C,^{15}N enriched cytidine taken at 4901 Hz.

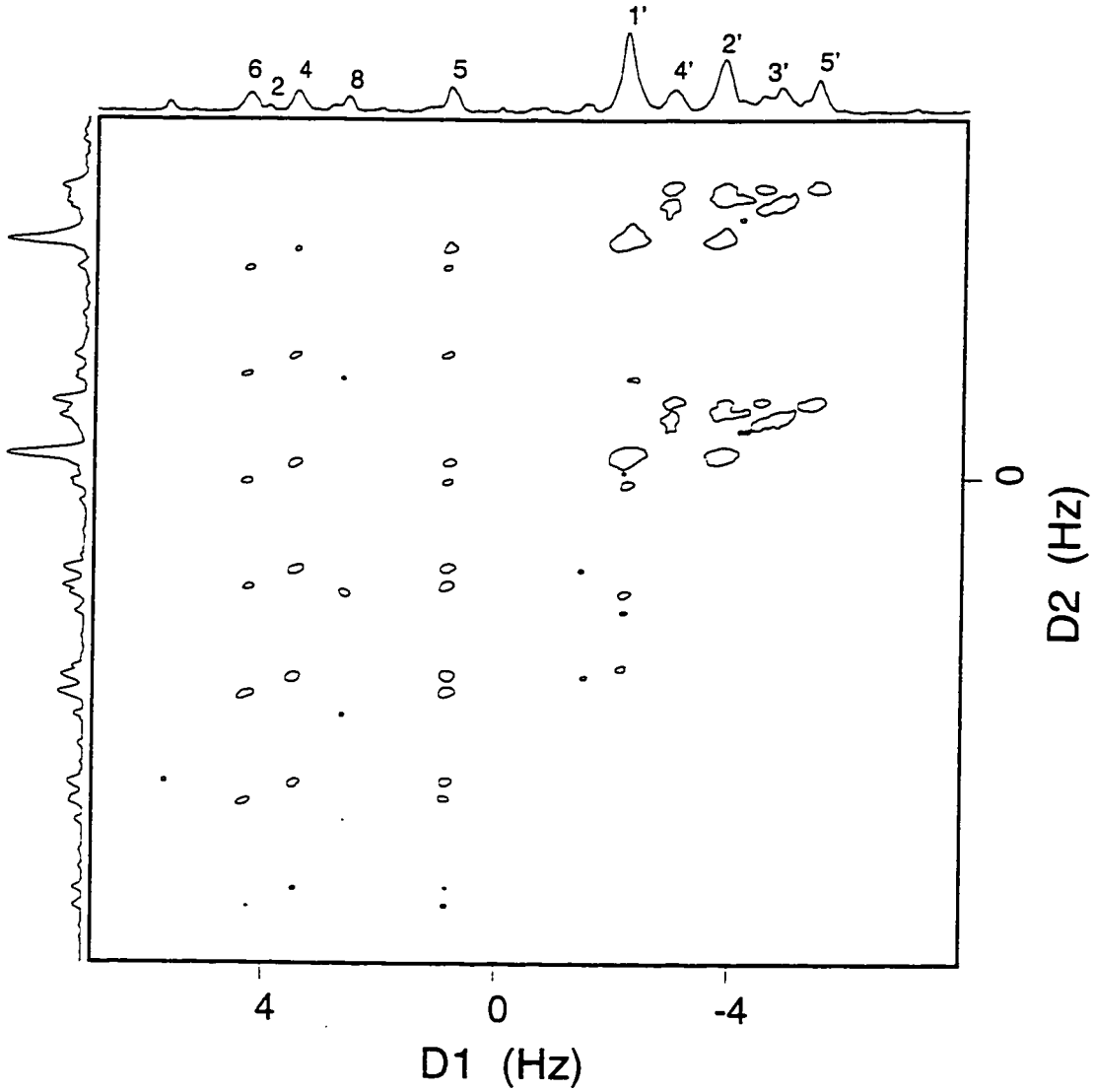

Figure 7.9: The full one cycle DQ-DRAWS spectrum for uniformly ^{13}C,^{15}N enriched adenosine taken at 4901 Hz.

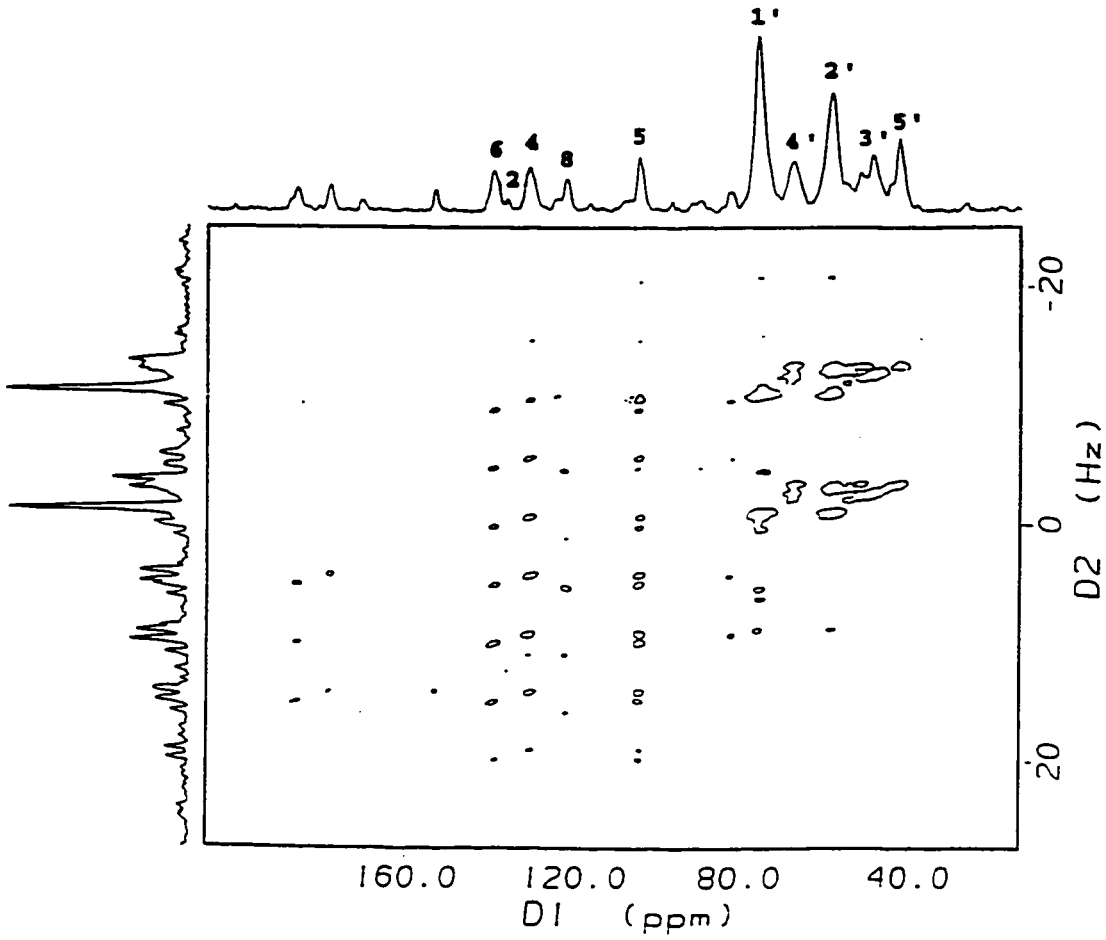

Figure 7.10: The full one cycle DQ-DRAWS spectrum for uniformly $^{13}C,^{15}N$ enriched guanosine taken at 4901 Hz.

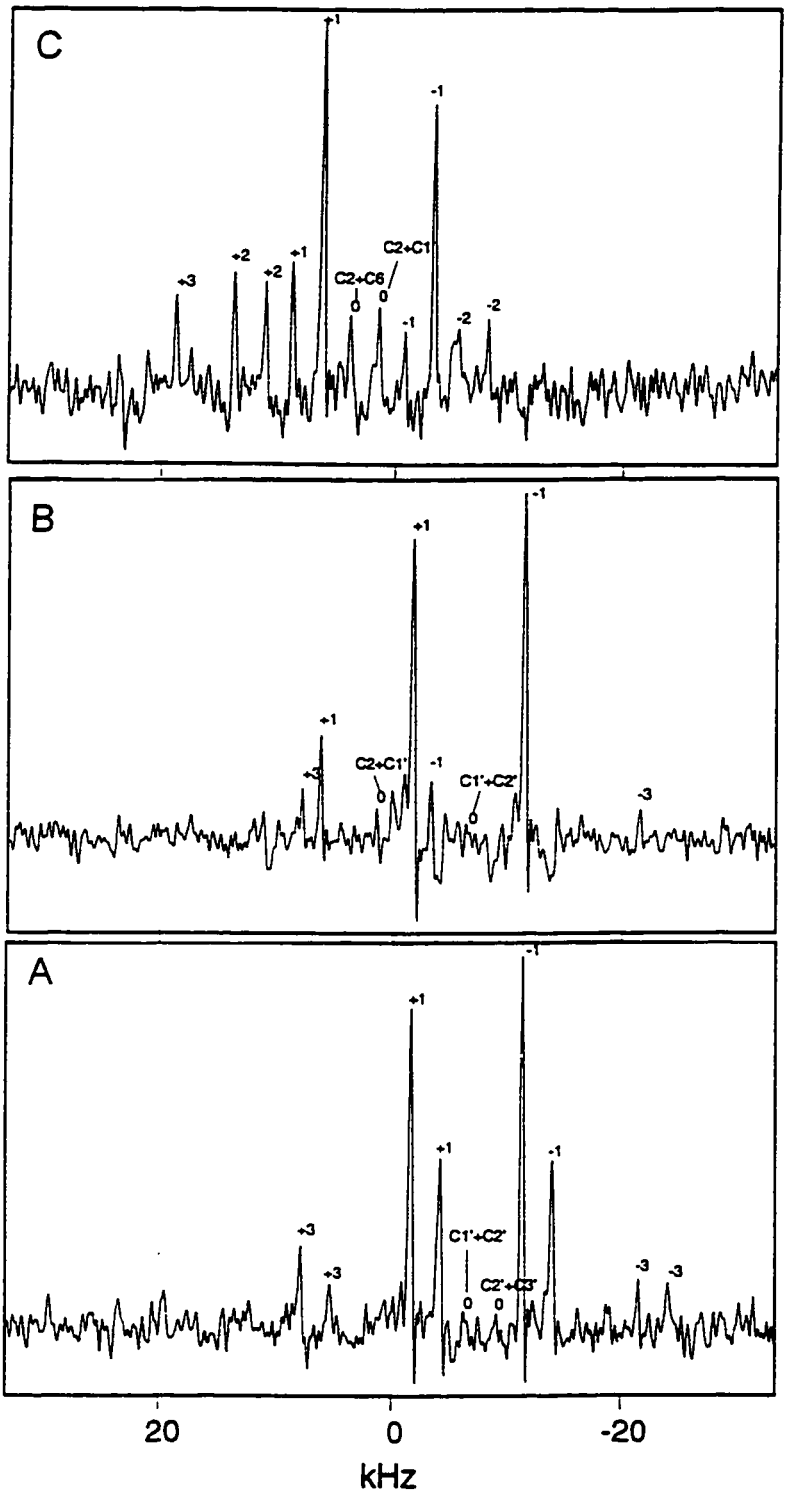

Figure 7.11: DQ slices for C2' (A), C1' (B), and C2 (C) resonances in the full DQ-DRAWS data set for u-^{13}C,^{15}N cytidine at 4901 Hz.

Chapter 8
Deuterium Dynamics Results

8.1 Introduction

This chapter presents solid-state ^{2}H NMR quadrupolar echo lineshape and spin-lattice relaxation data for a DNA dodecanucleotide, d(CGCGAATT^{5Me}CGCG)]$_2$, which contains 5-methyl-2'-deoxycytidine at the C9 position (underlined residue). Solid-state ^{2}H NMR spectroscopy has been used to characterize the effect of cytosine methylation on the internal dynamics of the backbone, sugar ring, and base heterocycle moieties of the C9 residue as a function of hydration level. This work complements the structural investigations of the T8pC9pG10 segment in this same DNA dodecamer presented in Chapter 5. The results of this chapter demonstrate that replacement of the C9 residue with its methylated analogue radically perturbs the large-amplitude dynamics of the exocyclic methylene group but only marginally alters the mobility of the furanose ring that were noted in a previous study by Hatcher and coworkers [1]. Reduced flexibility of the ^{5Me}C9 site may be directly correlated with inhibition of hydrolysis by the EcoRI restriction enzyme (see also Section 1.6). The solid-state ^{2}H NMR findings presented in the following sections indicate that there may be a dynamic component in the sequence-specific EcoRI protein-DNA recognition mechanism that is hindered by methylation of the C9 residue.

Although this work is focused on a methylated CpG step in a bacterial system, this same DNA sequence can serve as a model for understanding the structural and dynamical implications of methylation at CpG steps in eukaryotes (see also Section 1.6). In particular, CpG methylation has important implications for gene transcription. Many transcription factors whose DNA binding site contains one or more CpG

dinucleotides are no longer able to efficiently bind DNA when the site is methylated (e.g. CREB, USF, Sp1, and E2F) [2, 3]. Other studies indicate that methylation inhibits gene function through the formation of nuclease-resistant, transcriptionally inactive chromatin structures [4]. Gene silencing in eukaryotes is thought to result either directly, by interfering with the interaction of the transcription factor with its recognition site, or indirectly, by attracting proteins that have a high affinity for methylated DNA. The biological consequences of cytosine methylation may arise from alterations in local DNA conformation (and/or flexibility), in addition to direct protein-DNA interactions [5]. Recently, methylation-induced structural and/or dynamical changes within a triplet of CpG dinucleotides have been shown to directly contribute to the translational positioning of nucleosomes [6]. Methylation at CpG sites also influences DNA-DNA recognition by promoting DNA self-fitting and stabilization of major groove-backbone interactions, suggesting that CpG methylation acts on DNA super-structures rather than on local DNA structure [7]. Despite the evidence supporting the biological importance of methylation at CpG steps (in eukaryotes and prokaryotes), few reports exist on the influence of methylation on DNA structure/dynamics at the atomic level (see also Section 1.9). Consequently, the mechanisms by which DNA methylation exerts its influence on biological activity still remain ambiguous.

Prior to a discussion of the data for the methylated C9 analogue, it is useful to summarize some of the previously published solid-state ^2H NMR results for various nucleotides in the unmethylated DNA dodecamer, $[d(CGCGAATTCGCG)]_2$, since they will be referred to repeatedly in the following sections of this chapter.

8.2 Dynamics in the EcoRI Restriction Enzyme Binding Site

Solid-state deuterium NMR has been used extensively in this laboratory to probe the internal dynamics in the DNA dodecamer, $[d(CGCGAATTCGCG)]_2$, in an

effort to understand the details of site-specific recognition between the DNA and the EcoRI enzyme. These studies have probed the localized dynamics as a function of relative humidity (RH) for selectively base-, furanose ring-, and backbone-deuterated nucleotides, which have been incorporated into the dodecamer at the C3, G4, A5, A6, T7, T8, and C9 positions.

Localized motions of the furanose rings were first studied by Huang et al. [8] In this early study, [2"-^{2}H]-2"-deoxyadenosine was incorporated at the A5 and A6 positions of the Dickerson dodecamer. The data indicated that the sugar rings were undergoing rapid, small-amplitude librations ($\tau_c \leq 1$ ns, 6°-10°) that persisted throughout the hydration series (dry-92% RH). The presence of a slower ($\tau_c \leq$ 10-100 μs) component of the motion at hydration levels characteristic of the B-form structure (≥75% RH) were shown to correspond with collective helix motion. Similar results were obtained for furanose ring deuterons incorporated into the dodecamer at either the T7, T8, or G4 positions [9]. Solid-state ^{2}H NMR investigations of uniformly labeled purine and selectively T7, T8, and C9 base labeled dodecamers also indicated rapid, small-amplitude librations, with the onset of slow collective helix motions at higher hydration levels (≥ 75% RH) [1, 10-12].

In a recent solid-state ^{2}H NMR study by Hatcher and coworkers, unusual large amplitude (half angle of ±38°) dynamics on the 0.1 μs time scale were measured for both the furanose ring and helix backbone moieties of the C9 residue at hydration levels ≥75%. Similar dynamics have also been observed for the sugar ring of the C3 residue, which lies directly adjacent to the enzyme binding site [9]. The large amplitude motions of the C9 and C3 furanose deuterons have been attributed to an interconversion between conformational states of the furanose ring (C3'-endo ↔ C2'-endo). The lineshape for [5'/5"-^{2}H]-C9 DNA sample at 75% RH resembles the C3 and C9 furanose labeled dodecamer lineshapes at 93% RH, as evidenced by a dramatic reduction in QCC_{eff} (≈60 kHz). The C9 backbone lineshape differs dramatically from data for a doubly backbone-labeled T7/T8 dodecamer, which revealed only

a 12 kHz decrease in QCC_{eff} from dry to 75% RH [13]. This difference in QCC_{eff} with increasing water content confirms that the C9 backbone must also be a highly mobile moiety. The solid-state ^2H data suggests that the internal motion of the sugar ring (76-84° libration of the 2' methylene group) requires conformational mobility in the helix backbone, because sugar pucker and the δ torsion angle are interdependent [14]. A consequence of the change in δ at C9 is a fast, large amplitude rocking of the C5' methylene group. The ^2H NMR results indicate that the differential mobility of base, sugar, and backbone entities cannot be entirely the result of a collective libration of the C9 nucleotide. This hypothesis is in marked contrast to the conclusions drawn from "segmented rigid body analysis" of the X-ray diffraction data for this dodecamer by Holbrook and Kim [15].

The extensive ^2H lineshape and relaxation data indicates that the furanose rings and backbone at CpG steps are much more mobile than any other moieties in the EcoRI enzyme binding site. It is noteworthy that both C3 and C9 nucleotides exhibit large amplitude dynamics and are at CpG steps in the vicinity of the enzyme cleavage site. The C9 nucleotide is also involved in many of the structural anomalies observed in earlier X-ray and solution-state studies (see Sections 1.7 and 1.8). These regions of unusual flexibility are also the points in the binding site that must undergo further structural modification (type II neokinks) upon protein-DNA binding. Further evidence from a ^{31}P solution-state NMR study by Ott and Eckstein supports the possibility of increased localized mobility of the phosphodiester backbone. In that report, the C3 and C9 phosphate resonances occurred at a lower field than expected, which was attributed to a "break in conformation" [16]. Hatcher et al. have suggested that these ^{31}P findings may be the result of motions of the phosphate groups which accompany changes in the δ torsion angles [1]. The flexibility of the helix backbone and furanose ring at C9 and C3 may enable the extension of the phosphorus-phosphorus distance (7.3-7.4 Å) and the helix bending (20-40°) which ultimately occurs in the EcoRI-DNA complex [17]. It was concluded by Hatcher et al. that the presence of large am-

plitude dynamics (and the concomitant structural modulations) at the C3 and C9 positions may be crucial for specific EcoRI enzyme binding and cleavage. The solid-state ^2H NMR findings presented in the following sections reveal that the unusual mobility of the C9 nucleotide is altered by methylation of the 5-position of the cytosine heterocycle.

8.3 ^{5Me}C9 Base Dynamics

Quadrupolar echo lineshapes and spin-lattice relaxation data were obtained for [α_3,6-$^2H_4$]-5-methyl-2'-deoxycytidine, incorporated at the C9 position of the DNA dodecanucleotide, [d(CGCGAATTCGCG)]$_2$, at 75% RH (W=7.9) and 84% RH (W=12.1). The data is compared to previously published solid-state ^2H NMR results for the unmethylated, base-deuterated T7, T8, and C9 dodecamers [1, 11]. The results of these investigations are given in Table 8.1. The quadrupolar echo spectrum for 85.3 mg of [α_3,6-$^2H_4$]-^{5Me}C9-DNA (Figure 8.1) at W = 7.9 resembles a typical Pake doublet quadrupolar powder pattern. This presence of both methyl and H6 deuterated moieties in this sample is evidenced as two resolved powder patterns in Figure 8.1. A wider, low intensity component belongs to the heterocylic H6 deuteron. The narrower component belongs to the methyl deuterons and is dominated by the fast reorientation of the methyl group about the C_3 symmetry axis. If molecular motion is rapid on the time scale of ω_Q^{-1} (such as is the case here), experimental lineshapes can be parameterized by an effective quadrupolar coupling constant, QCC_{eff}, and an effective asymmetry parameter, η_{eff} (see Section 2.10). QCC_{eff} for the methyl group (QCC_{eff}=50±0.5 kHz; η_{eff}=0.05) was determined by simulation of the experimental powder pattern, assuming no motional model. Simulation of deuterium lineshapes using the MXQET program has been described in detail elsewhere [9, 18]. An effective value for QCC for the H6 deuteron was approximated directly from the splitting between the perpendicular edges of the powder pattern ($QCC_{eff}\approx$ 170 kHz) [19]. The

observed lineshape at W=12.1 (Figure 8.1) is almost identical in appearance to the W=7.9 lineshape except for a slight decrease in intensity at the center of the spectrum. Losses of signal intensity with increasing W are indicative of slow motion that occurs on a time scale comparable to the time scale required for formation of the quadrupolar echo (τ_c=10^{-6}-10^{-4} s) [1, 20]. Comparable values for QCC_{eff} were reported by Alam et al. for the methyl deuterons of T7 and T8 in a dodecamer of the same sequence at 75% and 80% RH (QCC_{eff} =51.0 ± 0.5 and 50.0 ± 0.5 kHz at W=10.4 and 11.6, respectively) [13]. In this previous study, experimental lineshapes at W=10.4 and 11.6 were simulated by using a rapid 3-fold jump for the methyl rotation (10-50 ps), a fast four-site libration of the base plane ($\tau < 10^{-6}$ s), and a slower six-site helix motion (k=1 kHz). For the unmethylated [5,6-^{2}H]-C9 derivative, QCC_{eff} was found to be 168±2 kHz at 10.1 and 16.2 waters per nucleotide [1], which is comparable to the value obtained from the outer powder pattern in this study. The deuterium lineshape for [5,6-^{2}H]-2'-deoxycytidine incorporated at the C9 position has been simulated as a rapid (10^6 Hz) two-site libration (±6°) of the base. The dynamical model included a second motion about the helix axis at a rate of 10^4 Hz. The fact that the overall spectral width is not substantially narrowed with increasing W suggests that there is no large amplitude motion of the base on a time scale fast compared to the time scale of the quadrupolar interaction ($\tau_c < 10^{-7}$ s) in either that T7/T8, C9 or ^{5Me}C9 DNA dodecamers.

The inversion recovery data for the [α_3,6-$^2H_4$]-^{5Me}C9 dodecamer sample at W=7.9 was fit with a single exponential giving a $\langle T_{1Z} \rangle$ of 128 ms (Figure 8.2A). This $\langle T_{1Z} \rangle$ value reflects contributions to the relaxation from both the methyl and base deuterons. The partially recovered spectra as a function of pulse delay are given in Figure 8.3. Previous measurements for the unmethylated DNA (W=10.1) yielded a Zeeman relaxation time of 100±15 ms for the base deuterons of C9 [1]. Alam et al. reported $\langle T_{1Z} \rangle$ values for the methyl deuterated T7/T8 dodecamer of 213±10 ms and 173±12 ms at W=11.6 and W=16.3, respectively, which are slightly longer than the

$<T_{1Z}>$ reported in this study. The combined lineshape and Zeeman relaxation results for the T7/T8, C9, and ^{5Me}C9 base-labeled samples indicate that the aromatic heterocycle is undergoing small amplitude librations (< 10°) about a single equilibrium conformation in the fast rate limit ($\tau_c < 10^{-7}$ s) [13]. The data for the [α_3,6-$^2H_4$]-^{5Me}C9 dodecamer reveals that methylation of the C9 nucleotide has little effect of the dynamics of the cytosine base relative to the unmethylated C9 species.

8.4 ^{5Me}C9 Backbone Dynamics

Quadrupolar echo lineshapes and spin-lattice relaxation data for 85.0 mg [5'/5"-^{2}H]-5-methyl-2'-deoxycytidine incorporated at the C9 position in the DNA dodecamer, [d(CGCGAATT^{5Me}CGCG)]$_2$, were collected as a function of relative humidity ranging from 66% RH (W=5.7) to 84% RH (W=16.5). The quadrupolar echo spectra at the four different hydration levels are shown in Figure 8.4. The results of this investigation are compared to previously published data for the unmethylated C9 and T7/T8 backbone labeled dodecamers and are compiled in Table 8.2 [1, 13]. An effective quadrupolar coupling constant and asymmetry parameter for the [5'/5"-^{2}H]-^{5Me}C9 DNA sample (W=5.7) was determined by simulation of the powder pattern assuming no motional model (QCC_{eff}=155±2 kHz; η_{eff}=0.06). A similar calculation for the DNA sample at 75% RH (W=13.1) yielded a QCC_{eff} =148±2 kHz and an η_{eff}= 0.06. Assuming $QCC_{static} \approx$ 175 kHz, the 5'/5" deuteron lineshape for ^{5Me}C9 yields a reduction factor, $\Lambda = QCC_{eff}/QCC_{static} \approx 0.85$ at W=13.1. Increasing the water content to 79% (W=15.2) and 84% RH (W=16.5) resulted in a dramatic decrease in signal intensity, indicating the onset of additional slower motions, as described above [13]. Despite the loss of signal intensity with increased water content, the powder patterns do not exhibit characteristics of extreme motional narrowing.

A comparable reduction in QCC_{eff} as a function of W was reported by Alam et al. for the 5'/5" deuterons of T7 and T8 in a dodecamer of the same sequence. In that

study, QCC_{eff} was determined to be 150 kHz (Λ=0.86) and 143 kHz (Λ=0.82) at W=11.9 and 16.3, respectively [13]. Figure 8.5 compares the backbone data for the T7/T8 dodecamer 75% RH with the lineshape obtained at 75% RH for the methylated analogue. The moderate reduction in QCC_{eff} for the T7/T8 and ^{5Me}C9 samples suggests that isomerization of the methylene group about the C4'-C5' bond is minimal in this hydration range. The T7/T8 backbone data was modeled using a four-site jump model for the fast internal motions, with a root mean square amplitude that was 2-6° larger than that observed for the base or sugar labeled dodecamers at this site. Interestingly, the observed T7/T8 5'/5" lineshape could not be simulated with a rapid three-site trans-gauche isomerization. The slower motions were simulated using a six-site jump about the helix axis, as described above. In comparison, the backbone data for the unmethylated [5'/5"-^{2}H]-C9-DNA at W=10.5 (also shown in Figure 8.5 for comparison) reveals that QCC_{eff} does not exceed 60 kHz, indicating that the backbone methylene group is extremely mobile [1]. This dramatic reduction in QCC_{eff} for the C9 sample was attributed to rapid interconversion of the methylene group between all three rotational conformers.

The inversion recovery spectra for the [5'/5"-^{2}H]-^{5Me}C9 dodecamer sample at W=5.7 and W=13.1 as a function of pulse delay appear in Figure 8.6 and 8.7, respectively. The data at each hydration level were defined by a single exponential and resulted in a $\langle T_{1Z} \rangle$ of 87 ms and 55ms, respectively. The Zeeman relaxation time at W=16.5 (84% RH) was 44 ms. The inversion recovery curves for the backbone deuterated ^{5Me}C9 sample at 75% RH and 84% RH are presented in Figure 8.8. Our $\langle T_{1Z} \rangle$ results closely resemble the values reported by Alam et al. for the methylene deuterated T7/T8 dodecamer (59 ms, 41 ms, and 40 ms at W = 10.5, 11.9, and 16.3, respectively) [13]. In comparison, previous measurements for the unmethylated DNA (W=10.5) yielded a Zeeman relaxation time of 30±10 ms for the backbone deuterons of C9 [1]. The deuterium lineshape and relaxation data indicate that the dynamics of the C9 backbone vary considerably from the dynamics of the T7/T8 DNA. However,

the similar lineshape and relaxation trends for the T7/T8 and ^{5Me}C9 backbone deuterons suggest that the motions of these samples are comparable. The solid-state ^{2}H NMR results for the [5'/5"-^{2}H]-^{5Me}C9 analogue over a hydration range of W=5.7-16.5 show that methylation of the C9 nucleotide effectively reduces the unusual flexibility of the 5' methylene group that was observed for the unmethylated sample.

8.5 ^{5Me}C9 Furanose Ring Dynamics

To monitor furanose ring dynamics for the methylated C9 dodecamer, quadrupolar echo lineshapes and spin-lattice relaxation data were obtained for 53.6 mg of [2"-^{2}H]-^{5Me}C9 labeled DNA at two hydration levels: 75% (W=9.5) and 79% RH (W=13.0). The results of these experiments are compared to previously published data for [2"-^{2}H]-2'-deoxycytidine incorporated at the C9 position of [d(CGCGAATTCGCG)]$_2$. Table 8.3 contains the lineshape parameters and relaxation times for these samples. Figure 8.9 presents the powder lineshapes for the [2"-^{2}H]-^{5Me}C9- and [2"-^{2}H]-C9-DNA samples at W=9.5 and W=10-11, respectively. The spectrum at 75% RH for the unmethylated [2"-^{2}H]-C9-DNA dodecamer has been shown to result from large amplitude (half amplitudes = 38°) intermediate motional averaging ($\tau_c \approx 10^{-6}$-10^{-7} s) of the C2'-D2" vector [1]. Qualitative inspection of the lineshape for the [2"-^{2}H]-^{5Me}C9 analogue reveals that the 2" deuteron is still relatively mobile, with spectral distortions characteristic of a C-D bond that is undergoing large amplitude motions ($\geq$ 15°) in the intermediate rate regime. We attribute the altered appearance of the spectrum to a slight reduction in the amplitude of sugar ring puckering for the ^{5Me}C9 nucleotide relative to the unmethylated derivative. The quadrupole echo lineshape was repeated on the [2"-^{2}H]-^{5Me}C9-DNA at W=13.0. The quadrupole echo lineshapes for the [2"-^{2}H]-^{5Me}C9- and [2"-^{2}H]-C9-DNA samples at 79% RH and 84% (shown in Figure 8.10) indicate that the furanose rings in both dodecamers are still undergoing intermediate motional averaging.

Figures 8.11 and 8.12 show the partially recovered lineshapes for the methylated and non-methylated C9 dodecanucleotides at 75% and 80% RH, respectively. Both samples produced inversion recovery curves with substantial non-single exponential behavior. The inversion recovery experiment for the [2"-^{2}H]-^{5Me}C9 dodecanucleotide sample at W=9.5 was defined by an equally weighted biexponential with a slow time constant of 147 ms and a fast time constant of 17±2 ms (see Figure 8.2B). Attempts to fit this data with a single exponential resulted in a $<T_{1Z}>$=17±2 ms. In comparison, $<T_{1Z}>$ for the [2"-^{2}H]-C9-DNA dodecamer at W=12.3 was 20±10 ms (determined using a single exponential fit). A fast $<T_{1Z}>$ for the ^{5Me}C9-DNA suggests that motions of the furanose ring are still quite efficient at inducing spin-lattice relaxation of the 2" deuteron, despite the presence of an additional methyl group on the cytosine heterocycle.

8.6 Conclusions

It is evident from a comparison of the [2"-^{2}H]-, [α_3,6-$^{2}H_4$]-, and [5'/5"-^{2}H]-^{5Me}C9 lineshape and relaxation data, that methylation of the cytosine heterocycle perturbs the localized mobility (amplitude and/or rate) of methylene and furanose moieties differently. Methylation has frozen out the rapid, large amplitude fluctuations of the phosphodiester backbone that produced the extremely short $<T_{1Z}>$ values and the motionally averaged lineshapes in the unmethylated backbone C9-DNA investigations. The impact of cytosine methylation on localized base and furanose ring dynamics at C9 seems less pronounced. This reduction in flexibility may result from structural modifications in the DNA that arise from substitution of an additional methyl group on the cytosine heterocycle. Furthermore, there could be a close correlation between reduced mobility of the phosphodiester backbone and inhibition of hydrolysis by the EcoRI endonuclease.

We propose that the reduction in backbone mobility is most likely the result of steric interactions between the base and the backbone of the ^{5Me}C9 residue. The phosphodiester linkage is known to be in close proximity to H6 of cytosine (within approximately 3Å) when the heterocycle is oriented in the favored anti position. A minor rearrangement in base stacking may be incurred in order to alleviate steric interactions resulting from the presence of an additional methyl group in the major groove. Such a structural change (achieved through rotations about the glycosidic bond) could potentially alter the orientation between the base and backbone subunits. Inspection of the X-ray coordinates for the B-DNA dodecamer, $[d(CGCGAATT^{5Me}CGCG)]_2$, indicates that both the C6-P and C6-O5' distances for the ^{5Me}C9 residue increase by approximately 0.5 Å relative to the native dodecanucleotide [21]. It is conceivable that such subtle changes in the structure of the ^{5Me}C9 nucleotide could impact localized backbone motion. It has also been proposed that the orientation about the χ angle is strongly correlated with the δ torsion angle (see Figure 1.3), which in turn defines the pucker of the furanose ring [22]. The DRAWS distance measurements described in Chapter 5 have demonstrated that changes in the stacking between T8 and ^{5Me}C9 are rather negligible (i.e. little change in the χ angle of ^{5Me}C9). Due to the strong χ-δ correlation, this small change in χ would yield only small changes in δ (i.e. no effect on sugar ring conformation). Consequently, the sugar ring is only marginally influenced by methylation of the base and remains a highly mobile entity. Furthermore, because χ and γ are thought to be only very weakly correlated in nucleic acids, a change in the orientation about the glycosidic bond would have little effect on the orientation of the exocyclic methylene group about the C4'-C5' bond. Rather, the effect of methylation must be a consequence of direct steric interactions between the phosphodiester backbone and the aromatic heterocyle. This model serves to reconcile the differential mobilities of the sugar ring and backbone moieties of the ^{5Me}C9 nucleotide. Future work in this laboratory will be directed towards testing this model using a variety of dipolar recoupling techniques.

8.6 Notes to Chapter 8

[1] Hatcher, M.E., Mattiello, D.L., Orban, J., and Drobny, G.P. (1997) *J. Am. Chem. Soc.*, accepted.

[2] Radtke, F., Hug, M., Georgiev, O., Matsuo, K., and Schaffner, W. (1996) *Biol. Chemistry Hoppe-Seyler*, **377**, p. 47.

[3] Clark, S.J., Harrison, J., and Molloy, P.L. (1997) *Gene*, **195**, p. 67.

[4] Cedar, H. (1988) *Cell*, **53**, p. 3.

[5] Brennan, C.A., Van Cleve, M.D., and Gumport, R.I. (1986) *J. Biol. Chem.*, **261** (16), p. 7270.

[6] Davey, C., Pennings, S., and Allan, J. (1997) *J. Mol. Biol.*, **267**, p. 276.

[7] Mayer-Jung, C., Moras, D., and Timsit, Y. (1997) *J. Mol. Biol.*, **270**, p. 328.

[8] Huang, W.C., Orban, J., Kintanar, A., Reid, B.R., and Drobny, G.P. (1990) *J. Am. Chem. Soc.*, **112**, p. 9059.

[9] Hatcher, M.E., *Ph.D. Dissertation*, 1996, University of Washington.

[10] Alam, T.A. and Drobny, G.P. (1991) *Chem. Rev.*, **91**, p. 1545.

[11] Alam, T.M. and Drobny, G.P. (1990) *Biochemistry*, **29**, p. 3421.

[12] Kintanar, A., Alam, T.M., Huang, W., Schindele, D.C., Wemmer, D.E., and Drobny, G.P. (1988) *J. Am. Chem. Soc.*, **110**, p. 6367.

[13] Alam, T.M., Orban, J., and Drobny, G.P. (1991) *Biochemistry*, **30**, p. 9229.

[14] Saenger, W., *Principles of Nucleic Acid Structure*, ed. C.R. Cantor. 1984, New York: Springer-Verlag New York, Inc.

[15] Holbrook, S.R. and Kim, S.H. (1984) *J. Mol. Biol.*, **173**, p. 361.

[16] Ott, J. and Eckstein, F. (1985) *Biochemistry*, **24**, p. 2530.

[17] McClarin, J.A., Frederick, C.A., Wang, B., Greene, P., Boyer, H.W., Grable, J., and Rosenberg, J.M. (1986) *Science*, **234**, p. 1526.

[18] Greenfield, M.S., Ronemus, A.D., Vold, R.L., and Vold, R.R. (1987) *J. Magn. Reson.*, **72**, p. 89.

[19] Brandes, R. and Kearns, D.R. (1986) *Biochemistry*, **25**, p. 5890.

[20] Spiess, H.W. and Sillescu, H. (1981) *J. Magn. Reson.*, **42**, p. 381.

[21] Partridge, B.L. and Salisbury, S.A., *Structural Studies on Nucleic Acids, Ph.D. Dissertation*, 1996, Cambridge University.

[22] Dickerson, R.E., *DNA Structures*. Methods in Enzymology: Part A Synthesis and Physical Analysis of DNA, ed. D.M.J. Lilley and J.E. Dahlberg. Vol. 211. 1992, Harcourt Brace Jovanovich Publishers: San Diego. p. 67.

Table 8.1: Lineshape Parameters and Relaxation Rates for Base Labeled [d(CGCGAATTCGCG)]$_2$

Compound	W	%RH	QCC_{eff}(kHz)	η_{eff}	$\langle T_{1Z} \rangle$ (ms)
[α_3,6-$^2H_4$]-^{5Me}C9	7.9	75	50.0±0.5	0.05	128±10
	12.1	84	50.0±0.5	0.00	*
[5,6-$^2H_2$]-C9	10.1	75	168±2	0.06±0.01	100±15
	16.2	88	168±2	0.06±0.01	60±10
[α_3-$^2H_3$]-T7/T8	10.4	75	51.0±0.5	0.05	204±10
	11.6	80	50.5±0.5	0.05	213±11
	16.3	88	45.5±0.5	0.05	173±2

*Quantity not measured.

Table 8.2: Lineshape Parameters and Relaxation Rates for Backbone Labeled [d(CGCGAATTCGCG)]2

Compound	W	%RH	QCC_{eff}(kHz)	η_{eff}	$\langle T_{1Z} \rangle$ (ms)
[5'/5"-^2H]-^{5Me}C9	5.7	66	155±2	0.06	87±5
	13.1	75	148±2	0.06	55±5
	15.2	79	*	*	*
	16.5	84	*	*	44±5
[5'/5"-^2H]-C9	10.5	75	≤ 60	< 0.10	30±10
[5'/5"-^2H]-T7/T8	4.8	66	164±1	0.06	206±21
	10.5	75	152±2	0.06	59±10
	11.9	80	150±2	0.06	41±10
	16.3	88	143±2	0.00	40±10

*Quantity not measured.

Table 8.3: Lineshape Parameters and Relaxation Rates for Furanose Ring Labeled $[d(CGCGAATT\underline{C}GCG)]_2$

Compound	W	%RH	QCC_{eff}(kHz)	η_{eff}	$<T_{1Z}>$ (ms)
[2"-^{2}H]-^{5Me}C9	9.5	75	*	*	17±2;147±10
	13.0	79	*	*	*
[2"-^{2}H]-C9	5.5	66	166±2	0.04±0.01	180±50
	13.6	80	*	*	20±10
	12.3	75	*	*	20±10
	16.8	88	78±2	0.04±0.01	20±10

*Quantity not measured.

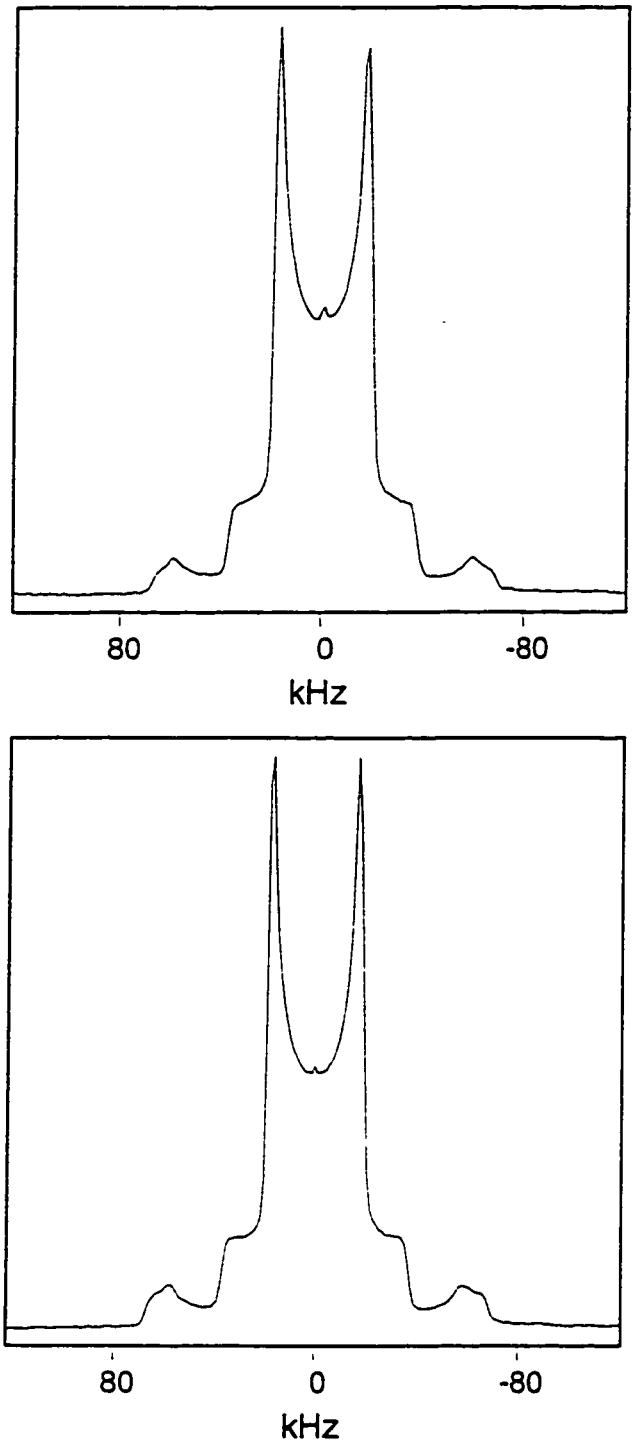

Figure 8.1: Comparison of experimental lineshapes for $[\alpha_3,6\text{-}^2H_4]\text{-}^{5Me}C9\text{-}[d(CGCGAATTCGCG)]_2$ at 75% RH (W=7.9) (top) and at 84 % RH (W=12.1) (bottom).

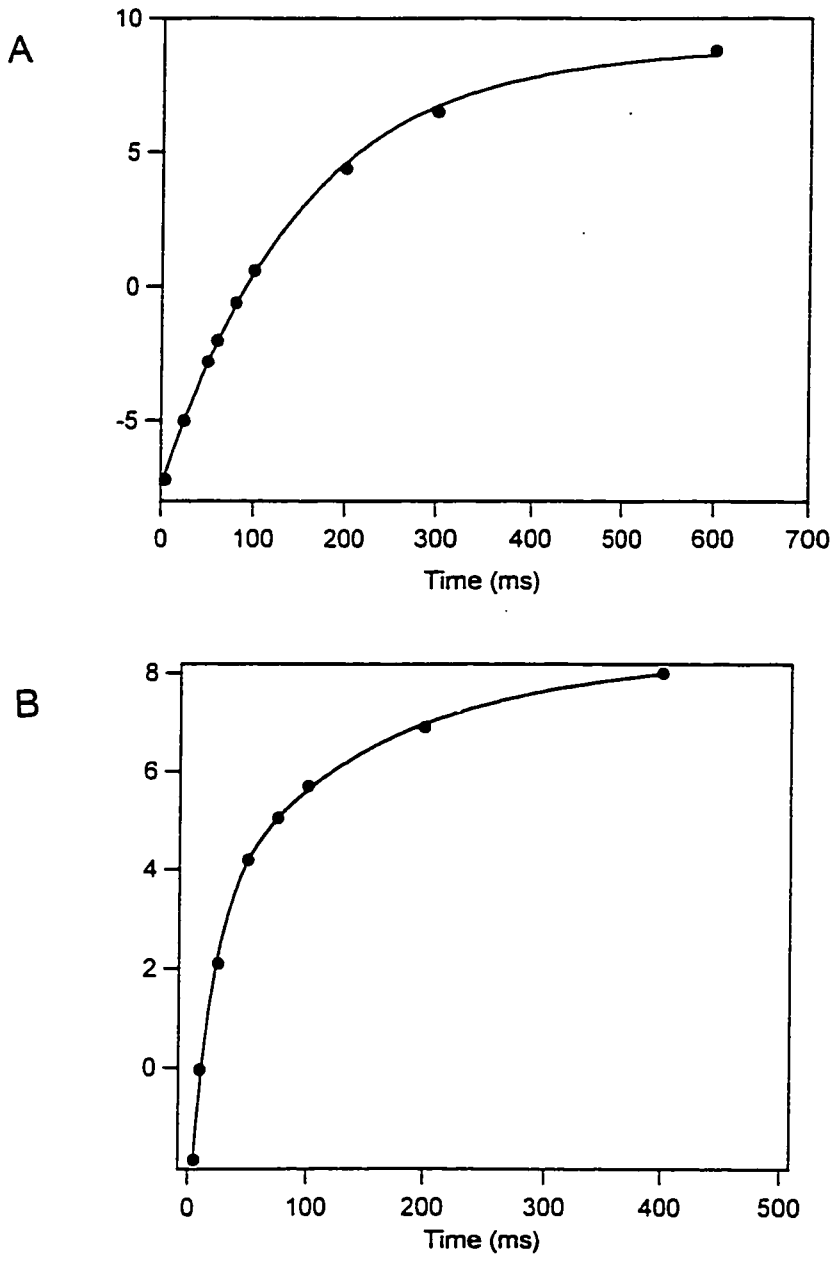

Figure 8.2: (A) T_{1Z} inversion recovery curve for [α_3,6-$^2H_4$]-^{5Me}C9-dodecamer (W=7.9). Least squares fit of data gives $<T_{1Z}>$=128 ms. (B) T_{1Z} inversion recovery curve for [2"-^{2}H]-^{5Me}C9-dodecamer (W=9.5). Data was fit with an equally weighted biexponential with a slow time constant of 147 ms and a fast time constant of 17.6 ms.

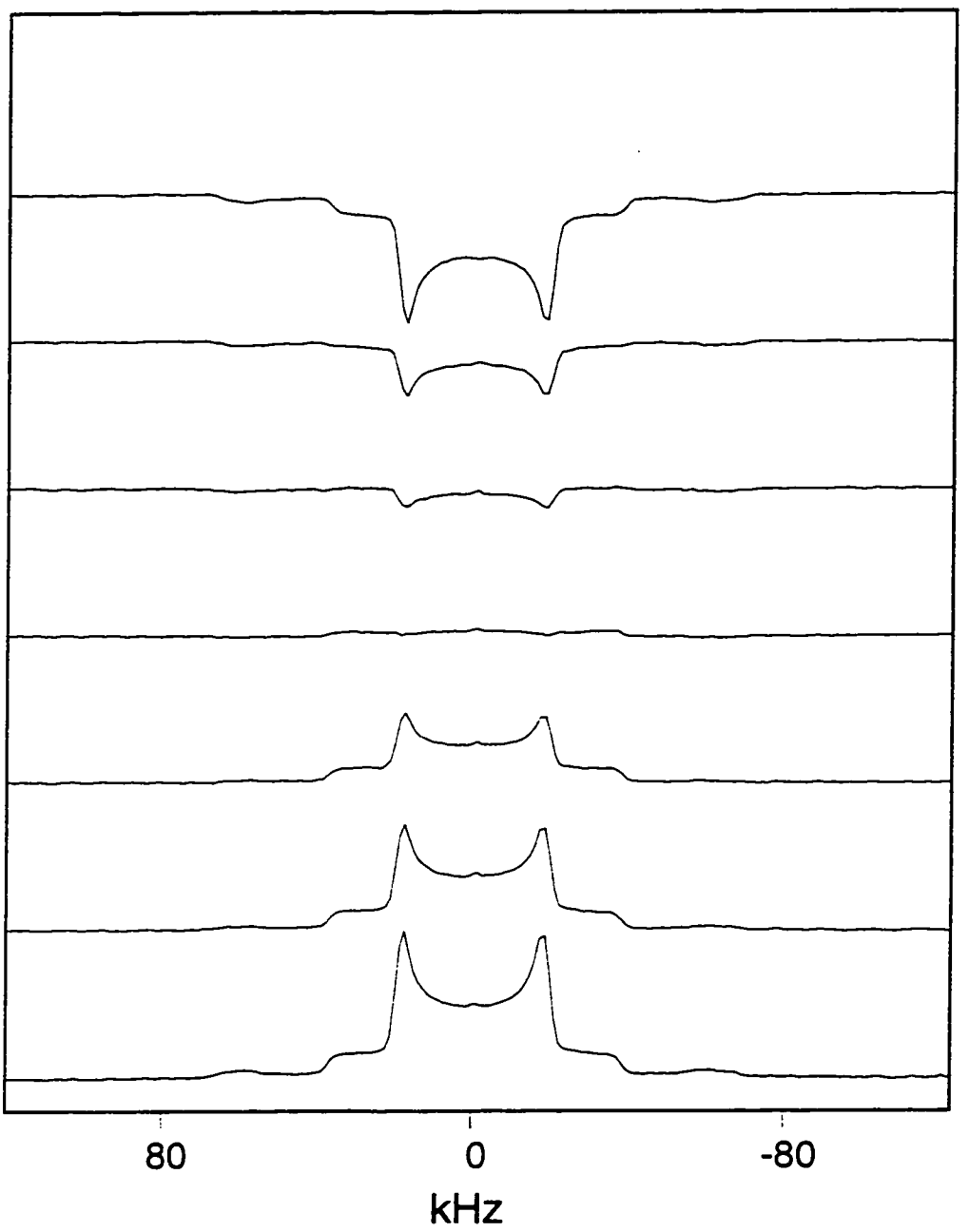

Figure 8.3: Partially recovered lineshapes for [α_3,6-$^2H_4$]-^{5Me}C9-dodecamer at 75% RH (W=7.9): vtau= 5ms, 50ms, 80ms, 100ms, 200ms, 300ms, 600ms (top to bottom).

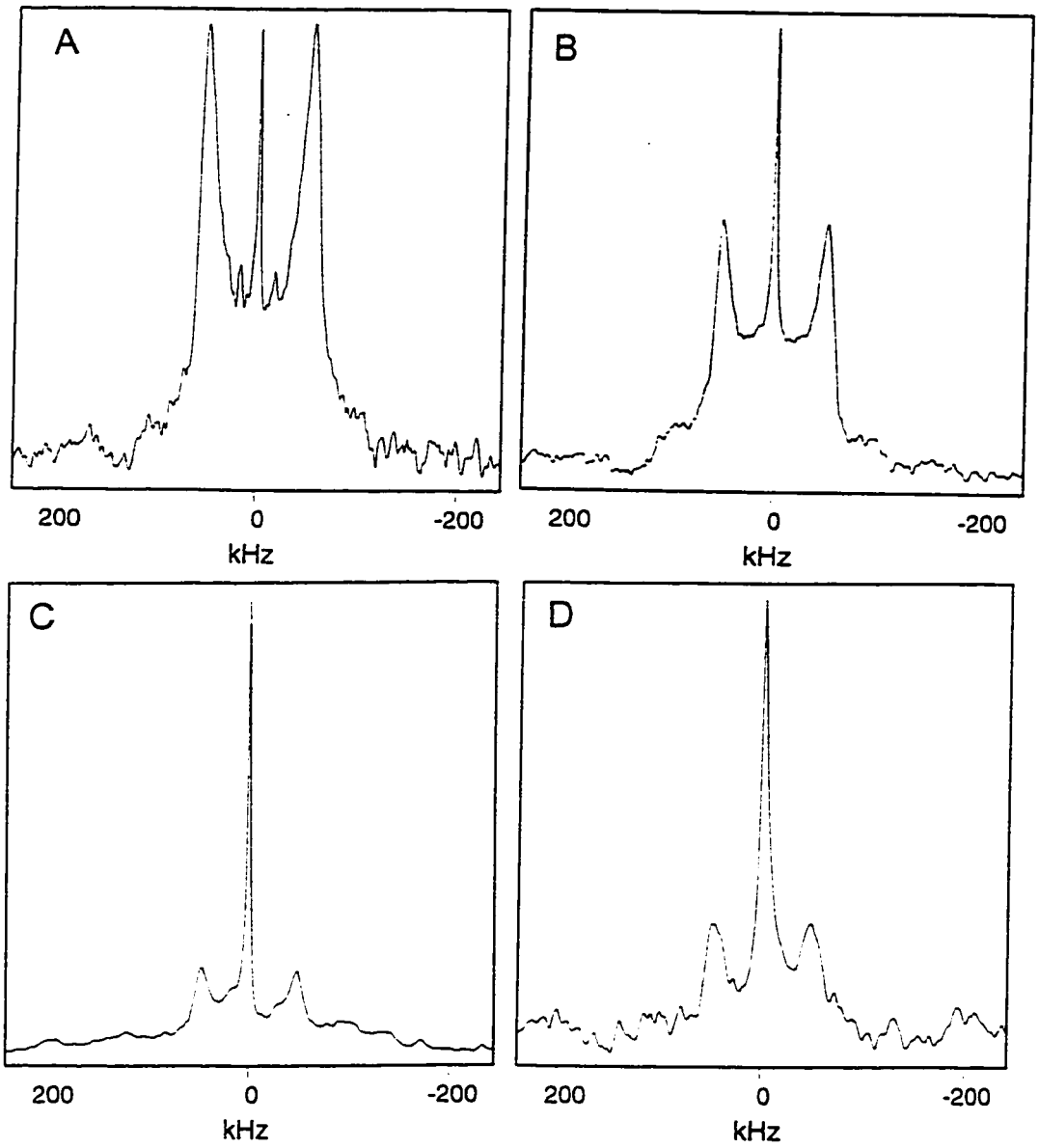

Figure 8.4: Comparison of experimental lineshapes at various hydration levels for DNA dodecamer. $[d(CGCGAATT\underline{C}GCG)]_2$, labeled with [5'/5"-^{2}H]-5-methyl cytidine at the C9 position. (A) 66% RH (W=5.7), (B) 75% RH (W=13.1), (C) 79% RH (W=15.2), and (D) 84% RH (W=16.5). The central isotropic component is due to residual HDO at higher hydration levels.

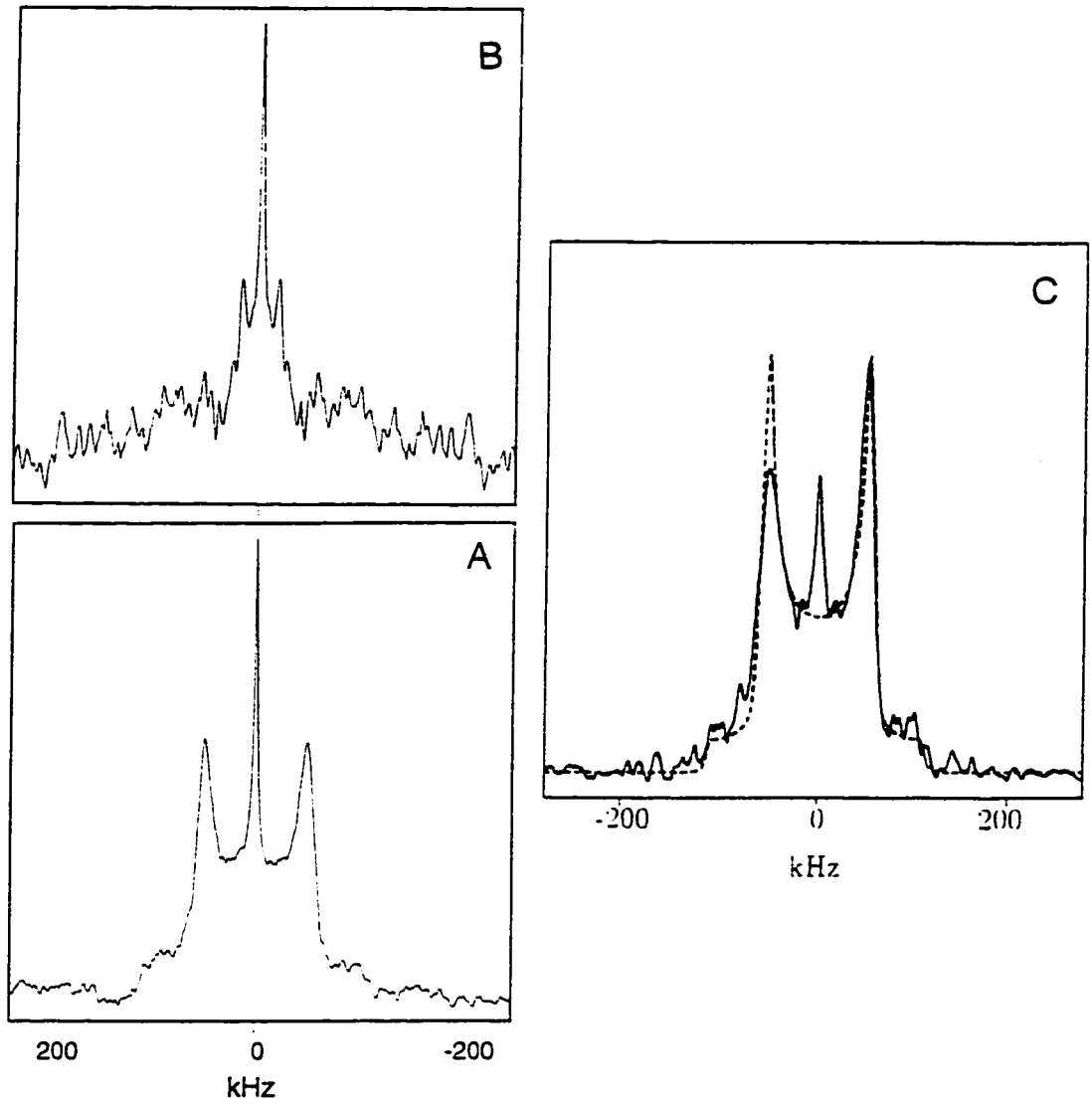

Figure 8.5: Comparison of experimental lineshapes at 75% RH for DNA dodecamer, $[d(CGCGAATTCGCG)]_2$, labeled with (A) [5'/5"-^{2}H]-5-methyl cytidine at the C9 position (W=13.1), (B) [5'/5"-^{2}H]-cytidine at the C9 position (W=10.5), and (C) [5'/5"-^{2}H]-thymidine at the T7 and T8 position (W=10.5). Simulation parameters T7/T8 DNA are described in the text.

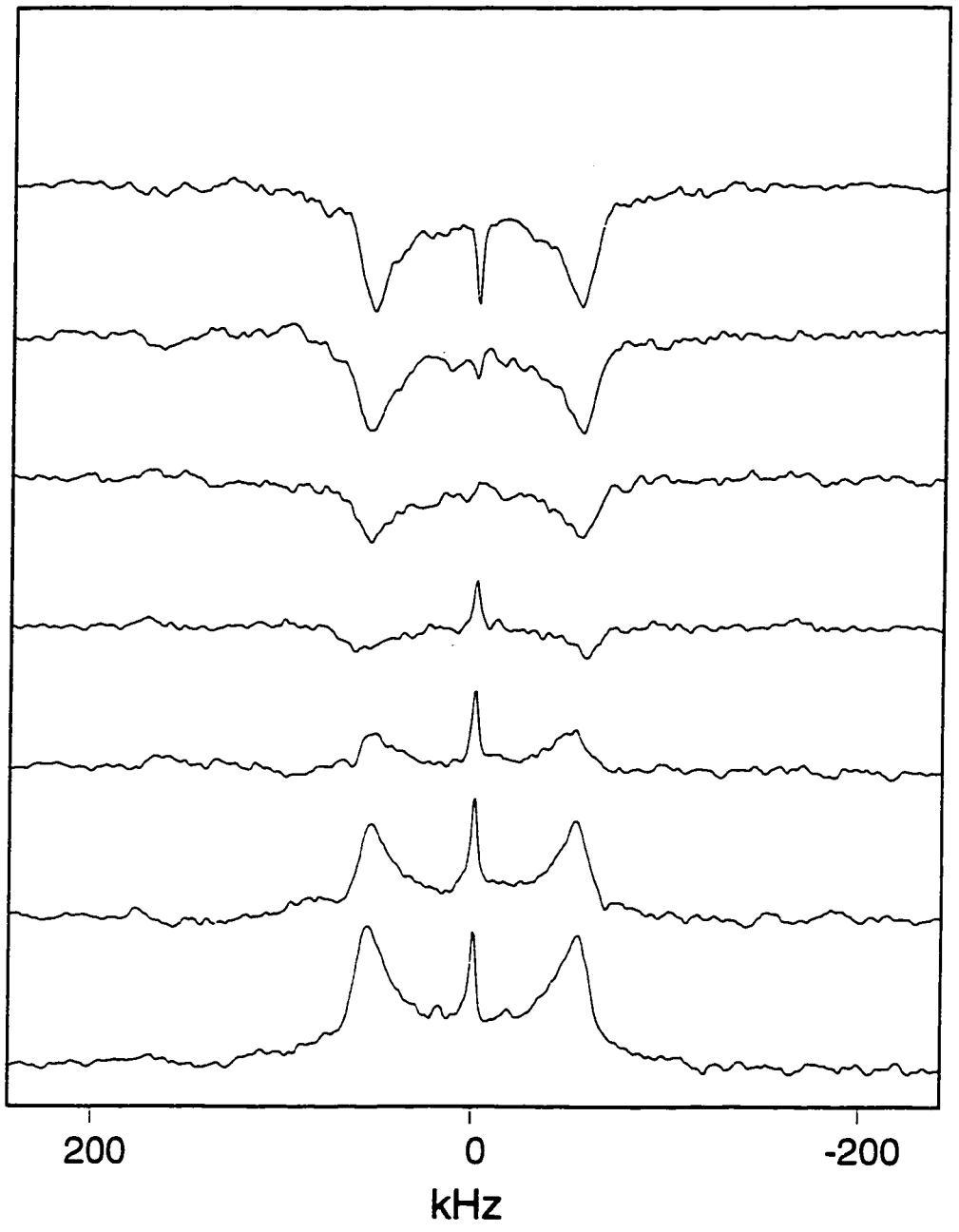

Figure 8.6: Partially recovered lineshapes for [5'/5"-^{2}H]-^{5Me}C9-dodecamer at 66% RH (W=5.7): vtau= 500μs, 10ms, 25ms, 50ms, 100ms, 20ms, 500ms (top to bottom).

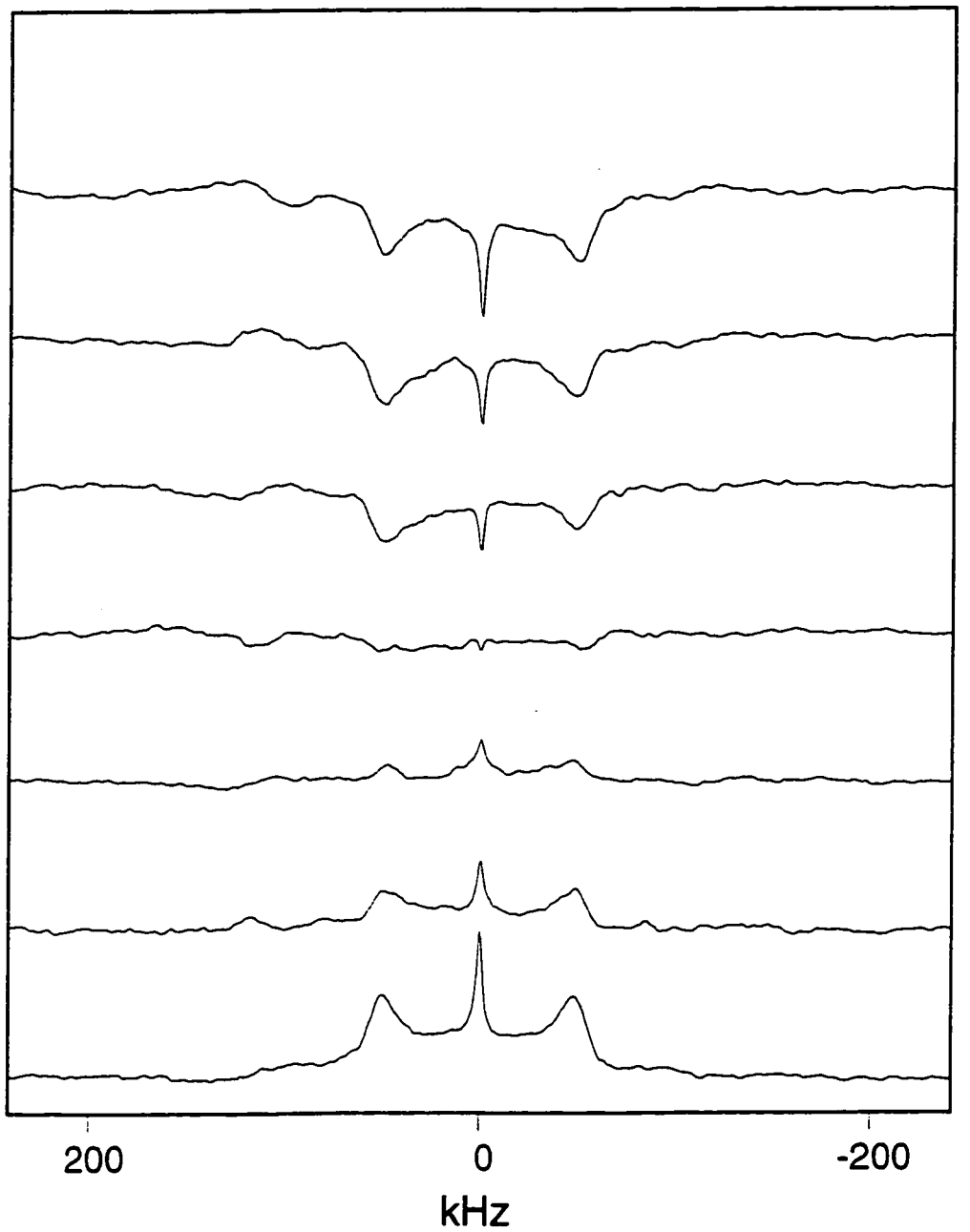

Figure 8.7: Partially recovered lineshapes for [5'/5"-^{2}H]-^{5Me}C9-dodecamer at 75% RH (W=13.1): vtau= 1ms, 5ms, 10ms, 25ms, 50ms, 75ms, 500ms (top to bottom).

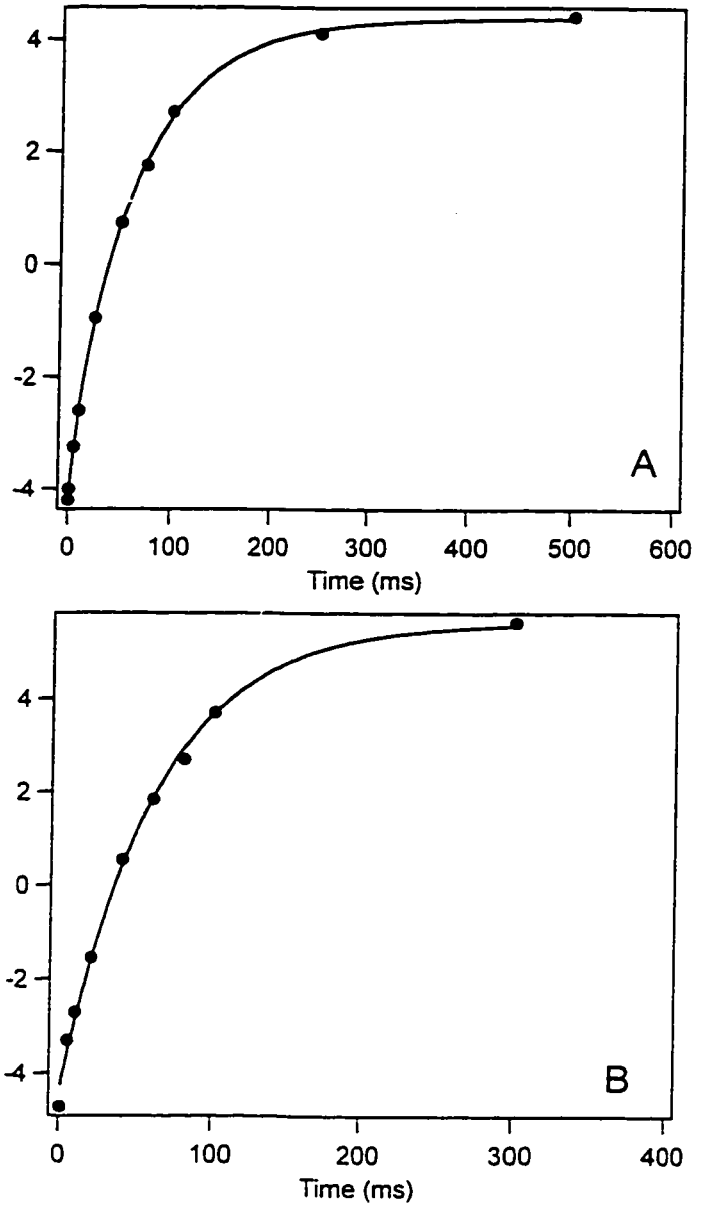

Figure 8.8: T_{1Z} inversion recovery curves for DNA dodecamer, $[d(CGCGAATTCGCG)]_2$, labeled with [5'/5"-^{2}H]-5-methyl cytidine at the C9 residue at (A) 75% RH (W=13.1) and (B) 84% RH (W=16.5). Both data sets were fit with a single exponential, giving $\langle T_{1Z} \rangle$=55 ms and 44 ms, for 75% RH and 84% RH data, respectively.

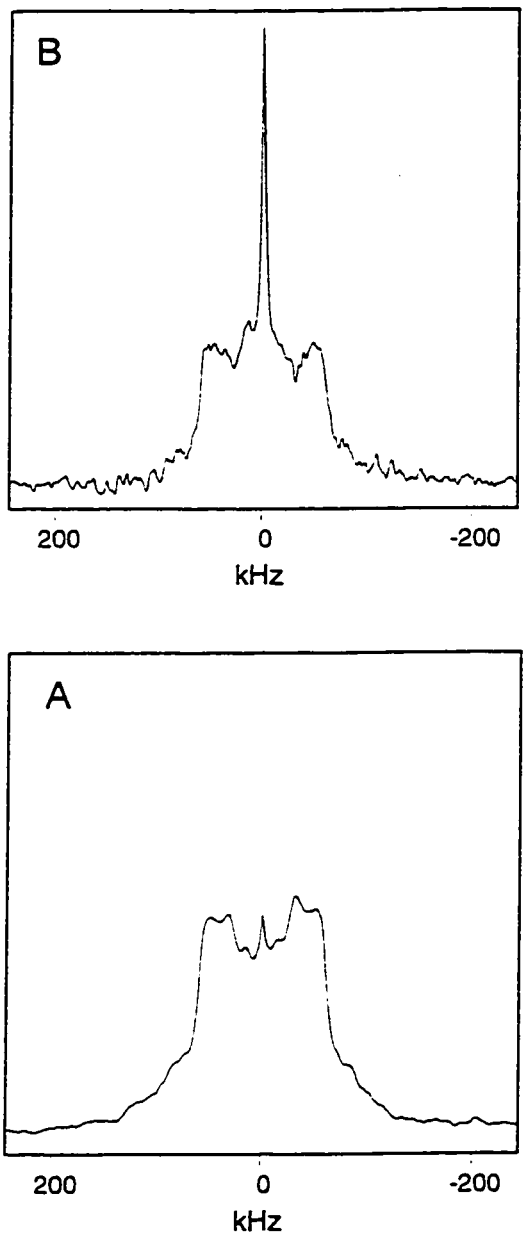

Figure 8.9: Comparison of experimental lineshapes at 75% RH for DNA dodecamer, $[d(CGCGAATTCGCG)]_2$, labeled with (A) [2"-^{2}H]-5-methyl-cytidine at the C9 position (W=9.5) and (B) [2"-^{2}H]-cytidine at the C9 position (W=10-11).

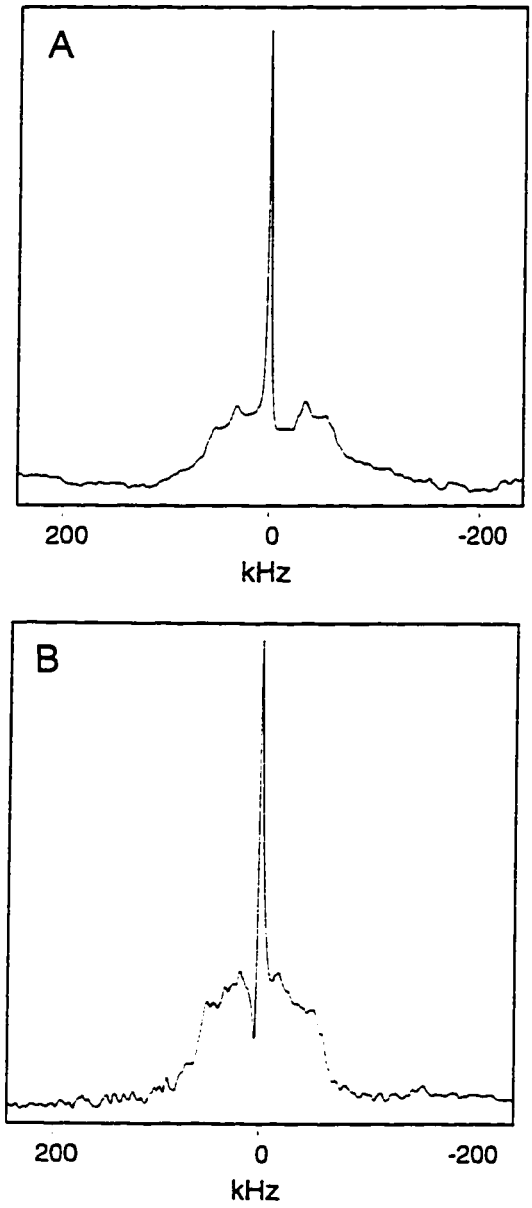

Figure 8.10: Comparison of experimental lineshapes for DNA dodecamer, $[d(CGCGAATTCGCG)]_2$, labeled with (A) [2"-^{2}H]-5-methyl cytidine at the C9 residue at 79% RH (W=13.0) and (B) [2"-^{2}H]-cytidine at the C9 residue at 84% RH (W=15.2).

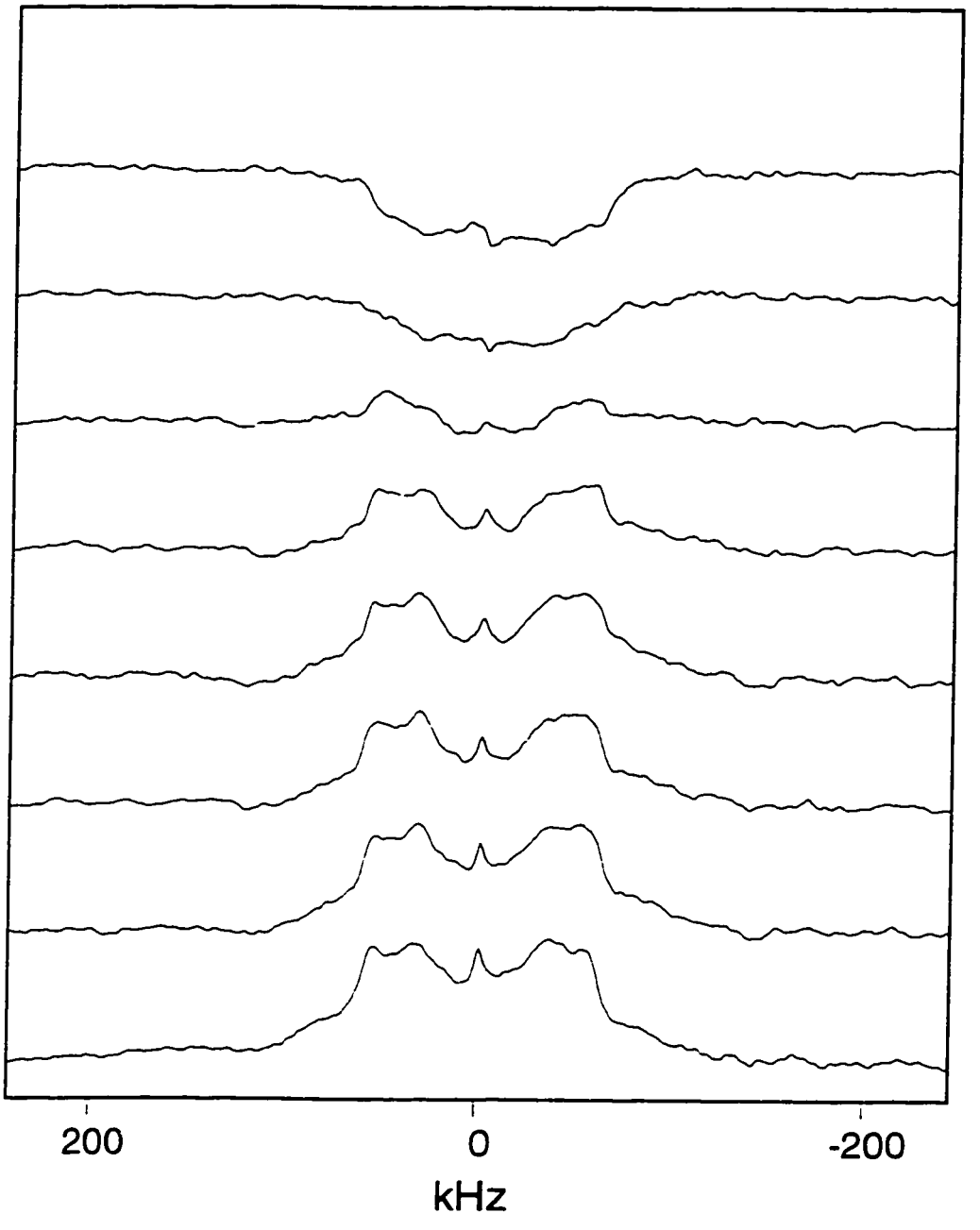

Figure 8.11: T_{1Z} inversion recovery spectra for [2"-^{2}H]-^{5Me}C9-dodecamer at 75% RH (W=9.5): vtau= 5ms, 10ms, 25ms, 50ms, 75ms, 100ms, 200ms, 400ms (top to bottom).

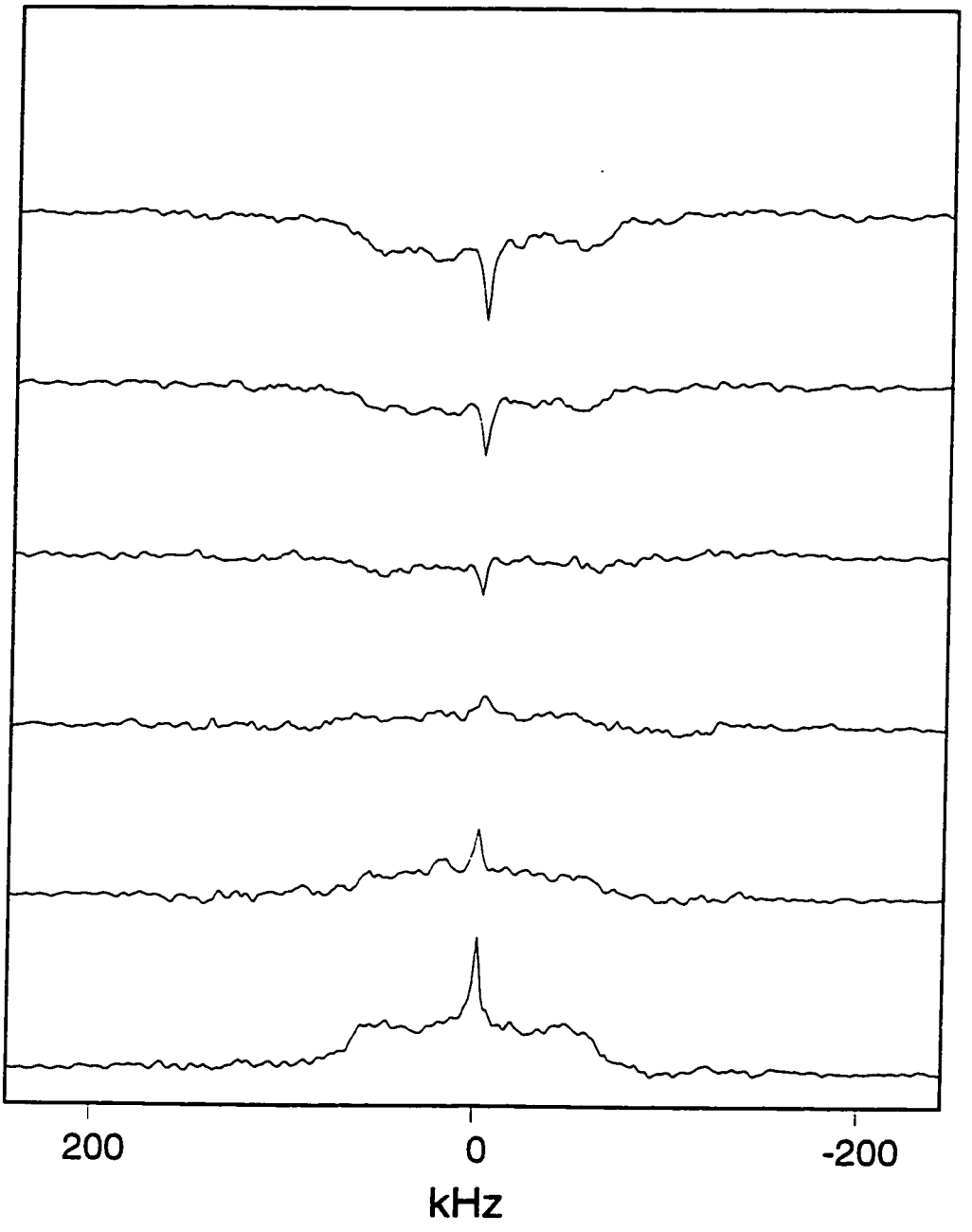

Figure 8.12: T_{1Z} inversion recovery spectra for [2"-^{2}H]-C9-dodecamer at 80% RH (W=10-11): vtau= 1ms, 5ms, 10ms, 25ms, 50ms, 200ms (top to bottom).

Bibliography

[1] Abragam, A., *Principles of Nuclear Magnetism*. 1961, New York: Oxford University Press.

[2] Adams, R.L. (1990) *Biochem. J.*, **265**, p. 309.

[3] Ahmad, I. and Rao, D. (1996) *Critical Reviews in Biochemistry and Molecular Biology*, **31** (5-6), p. 361.

[4] Alam, T.M. and Drobny, G.P. (1990) *Biochemistry*, **29**, p. 3421.

[5] Alam, T.M., Orban, J., and Drobny, G.P. (1991) *Biochemistry*, **30**, p. 9229.

[6] Alam, T.A. and Drobny, G.P. (1991) *Chem. Rev.*, **91**, p. 1545.

[7] Allison, S.A. and Schurr, J.M. (1979) *Chem. Phys.*, **41**, p. 35.

[8] Altona, C. and Sundaralingam, M. (1972) *J. Am. Chem. Soc.*, **94** (23), p. 8205.

[9] Altona, C. and Sundaralingam, M. (1973) *J. Am. Chem. Soc.*, **94**, p. 8205.

[10] Altona, C., *High resolution NMR studies of nucleic acids*, in *Methods in Structural Molecular Biology*, D.B. Davies, W. Saenger, and S.S. Danyluk, Eds. 1981, Plenum Press: London. p. 161.

[11] Andrew, E.R., Bradbury, A., and Eades, R.G. (1958) *Nature*, **182**, p. 1659.

[12] Arnott, S., Hukins, D.W., and Dover, S.D. (1972) *Biochem. Biophys. Res. Commun.*, **48**, p. 1392.

[13] Barbara, T.M., Greenfield, M.S., Vold, R.L., and Vold, R.R. (1986) *J. Magn. Reson.*, **69**, p. 311.

[14] Barker, R. and Fletcher Jr., H.G. (1961) *J. Org. Chem*, **26**, p. 4605.

[15] Batey, R.T., Inada, M., Kujawinski, E., Puglisi, J.D., and Williamson, J.R. (1992) *Nuc. Acids Res.*, **20** (17), p. 4515.

[16] Bax, A. and Lerner, L. (1988) *J. Magn. Reson.*, **79**, p. 429.

[17] Behe, M. and Felsenfeld, G. (1981) *Proc. Natl. Acad. Sci. (U.S.A.)*, **78**, p. 1619.

[18] Bennett, A.E., Ok, J.H., Vega, S., and Griffin, R.U. (1992) *J. Chem. Phys.*, **96**, p. 8634.

[19] Bhat, C.C. (1968) *Synthetic Procedures in Nucleic Acid Chemistry*, **1**, p. 521.

[20] Bird, A.P. (1996) *Cancer Surveys*, **28**, p. 87.

[21] Bloomfield, V.A., Crothers, D., and Tinoco, I., *Physical Chemistry of Nucleic Acids*. 1974, New York: Harper & Row.

[22] Brandes, R. and Kearns, D.R. (1986) *Biochemistry*, **25**, p. 5890.

[23] Brennan, C.A., Van Cleve, M.D., and Gumport, R.I. (1986) *J. Biol. Chem.*, **261** (16), p. 7270.

[24] Brennan, C.A., Van Cleve, M.D., and Gumport, R.I. (1986) *J. Biol. Chem.*, **261** (16), p. 7279.

[25] Burum, D.P., Linder, M., and Ernst, R.R. (1981) *J. Magn. Reson.*, **43**, p. 463.

[26] Cedar, H. (1988) *Cell*, **53**, p. 3.

[27] Clark, S.J., Harrison, J., and Molloy, P.L. (1997) *Gene*, **195**, p. 67.

[28] Codington, F. and Fox, J.J. (1963) *Meth. Carbohyd. Res.*, **2**, p. 113.

[29] Coll, M., Saal, D., Frederick, C.A., Rich, A., and Wang, A. (1989) *Nucleic Acids Res.*, **17**, p. 911.

[30] Collins, M. and Myers, R.M. (1987) *J. Mol. Biol.*, **198**, p. 737.

[31] Cowart, M., Gibson, K.J., Allen, D.J., and Benkovic, S.J. (1989) *Biochemistry*, **28**, p. 1975.

[32] Davey, C., Pennings, S., and Allan, J. (1997) *J. Mol. Biol.*, **267**, p. 276.

[33] Davies, D.B. and Danyluk, S.S. (1974) *Biochemistry*, **13** (21), p. 4417.

[34] Davies, D.B. (1978) *NMR Spectrosc.*, **12**, p. 135.

[35] de Leeuw, F.A. and Altona, C. (1983) *J. Comp. Chem.*, **4** (3), p. 428.

[36] DeFontaine, D.L., Ross, D.L., and Ternai, B. (1975) *J. Magn. Reson.*, **18**, p. 276.

[37] Dekker, C.A. (1965) *J. Am. Chem. Soc.*, **87**, p. 4027.

[38] Diaz, R. (1998), personal communication.

[39] Dickerson, R.E. and Drew, H.R. (1981) *Proc. Natl. Acad. Sci. (USA)*, **78**, p. 7318.

[40] Dickerson, R.E. and Drew., H.R. (1981) *J. Mol. Biol.*, **149**, p. 761.

[41] Dickerson, R.E., *DNA Structures*. Methods in Enzymology: Part A Synthesis and Physical Analysis of DNA, ed. D.M.J. Lilley and J.E. Dahlberg. Vol. 211. 1992, Harcourt Brace Jovanovich Publishers: San Diego. p. 67.

[42] Dixon, W.T. (1982) J. Chem. Phys., **77** (4), p. 1800.

[43] Drew, H.R., Wing, R.M., Takano, T., Broka, C., Tanaka, S., Itakura, K., and Dickerson, R.E. (1981) *Proc. Natl. Acad. Sci. (USA)*, **78** (4), p. 2179.

[44] Dyson, F.J. (1949) *Phys. Rev.*, **75**, p. 486.

[45] Fratini, A.V., Kopka, M.L., Drew, H.R., and Dickerson, R.E. (1982) *J. Biol. Chem.*, **257** (24), p. 14686.

[46] Fujiwara, T., Sugase, K., Kainosho, M., Ono, A., Ono, A.M., and Akutsu, H. (1995) *J. Am. Chem. Soc.*, **117**, p. 11351.

[47] Furberg, S. (1950) *Acta Cryst.*, **3**, p. 325.

[48] Furberg, S., Petersen, C.S., and Rømming, C. (1965) *Acta Cryst.*, **18**, p. 313.

[49] Gait, M.J., ed. *Oligonucleotide Synthesis: A Practical Approach*. 1984, IRL Press Limited: Oxford, England.

[50] Geen, H., Levitt, M.H., and Bodenhausen, G. (1992) *Chem. Phys.Lett.*, **200**, p. 350.

[51] Geen, H. and Bodenhausen, G. (1992) *J. Chem. Phys.*, **97** (5), p. 1.

[52] Green, E.A., Rosenstein, R.D., Shiono, R., and Abraham, D.J. (1975) *Acta Cryst.*, **B31**, p. 102.

[53] Greenfield, M.S., Ronemus, A.D., Vold, R.L., and Vold, R.R. (1987) *J. Magn. Reson.*, **72**, p. 89.

[54] Gregory, D.M., Mitchell, D.J., Stringer, J.A., Kiihne, S., Shiels, J.C., Callahan, J., Mehta, M.A., and Drobny, G.P. (1995) *Chem. Phys. Lett.*, **246**, p. 654.

[55] Gregory, D.M., Wolfe, G.M., Jarvie, T.P., Shiels, J.C., and Drobny, G.P. (1996) *Mol. Phys.*, **89** (6), p. 1835.

[56] Gregory, D.M., *Ph.D. Dissertation*, 1996, University of Washinton.

[57] Gregory, D.M., Mehta, M.A., Shiels, J.C., and Drobny, G.P. (1997) *J. Chem. Phys.*, **107** (1), p. 28.

[58] Griffin, R.G. (1981) *Methods Enzymol.*, **72**, p. 108.

[59] Griffiths, J.M. and Griffin, R.G. (1993) *Anal. Chim. Acta*, **283**, p. 1081.

[60] Gullion, T. and Conradi, M. (1990) *J. Magn. Reson.*, **89** (3), p. 479.

[61] Gullion, T. and Vega, S. (1992) *Chem. Phys. Lett.*, **194** (4,5,6), p. 423.

[62] Haasnoot, C.A., De Leeuw, F.A., and Altona, C. (1980) *Tetrahedron*, **36**, p. 2783.

[63] Habener, J.F., Vo, C.D., Le, D.B., Gryan, G.P., and Ercolani, L. (1988) *Proc. Natl. Acad. Sci. (USA)*, **85**, p. 1735.

[64] Haeberlen, U., *High Resolution NMR in Solids. Selective Averaging*. 1976, New York: Springer Verlag.

[65] Harbison, G.S. and Spiess, H.W. (1986) *Chem. Phys. Lett.*, **124**, p. 128.

[66] Harbison, G.S., Vogt, V.D., and Spiess, H.W. (1987) *J. Chem. Phys.*, **86**, p. 1206.

[67] Harbison, G.S. (1993) *J. Am. Chem. Soc.*, **115**, p. 3026.

[68] Hartmann, S.R. and Hahn, E.L. (1962) *Phys. Rev.*, **133**, p. 2042.

[69] Hatcher, M.E., *Ph.D. Dissertation*, 1996, University of Washington.

[70] Hatcher, M.E., Mattiello, D.L., Orban, J., and Drobny, G.P. (1997) *J. Am. Chem. Soc.*, accepted.

[71] Hawkes, G.E., Randall, E.W., and Hull, W.E. (1977) *J. Chem. Soc.*, **Perkin II**, p. 1268.

[72] Heinemann, U. and Alings, C. (1991) *EMBO J.*, **10** (1), p. 35.

[73] Herzfeld, J. and Berger, A. (1980) *J. Chem. Phys.*, **73**, p. 6021.

[74] Hexem, J.G., Frey, M.H., and Opella, S.J. (1982) *J. Chem. Phys.*, **77** (7), p. 3847.

[75] Hodges-Garcia, Y. and Hagerman, P.J. (1992) *Biochemistry*, **31**, p. 7595.

[76] Holbrook, S.R. and Kim, S.H. (1984) *J. Mol. Biol.*, **173**, p. 361.

[77] Hruska, F.E., Wood, D.J., Mynott, R.J., and Sarma, R.H. (1973) *FEBS Lett.*, **31**, p. 153.

[78] Huang, W.C., Orban, J., Kintanar, A., Reid, B.R., and Drobny, G.P. (1990) *J. Amer. Chem. Soc.*, **112**, p. 9059.

[79] Hubbard, A.J., Jones, A.S., and Walker, R.T. (1984) *Nuc. Acids Res.*, **12**, p. 6827.

[80] Jack, W.E., Rubin, R.A., Newman, A., and Modrich, P., eds. *Gene Amplification and Analysis*. Vol. 1. 1981, Elsevier/North-Holland: New York. p. 165.

[81] Jeener, J., Meier, B.H., Bachmann, P., and Ernst, R.R. (1979) *J. Chem. Phys.*, **71**, p. 4546.

[82] Jones, A.J., Winkley, M.W., Grant, D.M., and Robins, R.K. (1970) *Proc. Natl. Acad. Sci. (USA)*, **65** (1), p. 27.

[83] Juang, C., Tang, P., and Harbison, G.S., eds. *Solid-State NMR of DNA*. Methods in Enzymology. Vol. 261. 1995, Academic Press.

[84] Karplus, M. (1959) *J. Chem. Phys.*, **30** (1), p. 11.

[85] Kiihne, S.R., Mehta, M.A., Stringer, J.A., Gregory, D.M., Shiels, J.C., and Drobny, G.P. (1997) *J. Phys. Chem.*, in press.

[86] Kiihne, S.R., *Ph.D. Dissertation*, 1998, University of Washington.

[87] Kilpatrick, J.E., Pitzer, K.S., and Spitzer, R. (1947) *J. Am. Chem. Soc.*, **69**, p. 2483.

[88] Kintanar, A., Alam, T.M., Huang, W., Schindele, D.C., Wemmer, D.E., and Drobny, G.P. (1988) *J. Am. Chem. Soc.*, **110**, p. 6367.

[89] Kline, P.C. and Serianni, A.S. (1989) *J. Am. Chem. Soc.*, **112**, p. 7373.

[90] Kopka, M.L., Fratini, A.V., Drew, H.R., and Dickerson, R.E. (1983) *J. Mol. Biol.*, **163**, p. 129.

[91] Krenitsky, T.A., Rideout, J.L., Chao, E.Y., Koszaika, G.W., Gurney, F., Crouch, R.C., Cohn, N.K., Wolberg, G., *et al.* (1986) *J. Med. Chem.*, **29**, p. 138.

[92] Lai, T.F. and Marsh, R.E. (1972) *Acta Cryst.*, **B28**, p. 1982.

[93] Langowski, J., Fujimoto, B.S., Wemmer, D.E., Benight, A.S., Drobny, G.P., Shibata, J.H., and Schurr, J.M. (1985) *Biopolymers*, **24**, p. 1023.

[94] Lee, Y.K., Kurur, N.D., Helmle, M., Johannessen, O.G., Nielsen, N.C., and Levitt, M.H. (1995) *Chem. Phys. Lett.*, **242**, p. 304.

[95] Lefebvre, A., Mauffret, O., El Antri, S., Lescot, E., and Fermandjian, S. (1995) *Eur. J. Biochem.*, **299**, p. 445.

[96] Lesser, D.R., Kurpiewski, M.R., and Jen-Jacobson, L. (1990) *Science*, **250**, p. 776.

[97] Lesser, D.R., Kurpiewski, M.R., Waters, T., Connolly, B.A., and Jen-Jacobson, L. (1993) *Proc. Natl. Acad. Sci. (USA)*, **90**, p. 7548.

[98] Liu, F., Phung, C.G., Alderman, D.W., and Grant, D.M. (1995) *J. Am. Chem. Soc.*, **117**, p. 9323.

[99] Liu, F.L., Phung, C.G., Alderman, D.W., and Grant, D.M. (1996) *J. Am. Chem. Soc.*, **118**, p. 10629.

[100] Lomonosoff, G.P., Butler, P.J.G., and Klug, A. (1981) *J. Mol. Biol.*, **149**, p. 745.

[101] Long, J. and Kiihne, S.R. (1998), unpublished results.

[102] Ludemann, H.D. and Westhof, E., *Solution Conformations of purine (β) nucleosides and analogs*, in *Nuclear Magnetic Resonance Spectroscopy in Molecular Biology*, B. Pullman, Editor. 1978, D. Reidel Publishing Company: Dordrecht, Holland. p. 41.

[103] Magnus, W. (1954) *Commun. Pure and Appl. Math.*, **7**, p. 649.

[104] Maricq, M.M. and Waugh, J.S. (1979) *J. Chem. Phys.*, **70**, p. 3300.

[105] Mayer-Jung, C., Moras, D., and Timsit, Y. (1997) *J. Mol. Biol.*, **270**, p. 328.

[106] McClarin, J.A., Frederick, C.A., Wang, B., Greene, P., Boyer, H.W., Grable, J., and Rosenberg, J.M. (1986) *Science*, **234**, p. 1526.

[107] McDowell, C.A., Naito, A., Sastry, D.L., and Takegoshi, K. (1988) *J. Magn. Reson.*, **78**, p. 498.

[108] Mehring, M., *Principles of High Resolution NMR in Solids*. 1983, New York: Springer Verlag.

[109] Mehta, M.A., Gregory, D.M., Kiihne, S., Mitchell, D.J., Hatcher, M.E., Shiels, J.C., and Drobny, G.P. (1996) *Solid State Nucl. Magn. Reson.*, **7**, p. 211.

[110] Merritt, M.M. (1998), unpublished results.

[111] Mitchell, D.J., *Ph.D. Dissertation*, 1996, University of Washington.

[112] Munowitz, M., *Coherence and NMR*. 1988, New York: John Wiley & Sons, Inc.

[113] Neidle, S., Kuehlbrandt, W., and Achari, A. (1976) *Acta Cryst.*, **B32**, p. 1850.

[114] Nerdal, W., Hare, D.R., and Reid, B.R. (1989) *Biochemistry*, **28** (1008),.

[115] Ollila, J., Lappalainen, I., and Vihinen, M. (196) *FEBS Lett.*, **396**, p. 119.

[116] Ollis, D.L. (1987) *Chem. Rev.*, **87**, p. 981.

[117] Opella, S.J., Hexem, J.G., Frey, M.H., and Cross, T.A. (1981) *Phil. Trans. R. Soc. Lond.*, **A** (299), p. 665.

[118] Opella, S.J. and Morden, K.M., *Dynamic Properties of Biomolecular Assemblies*, S.E. Harding and A.J. Rowe, Eds. 1989, The Royal Society of Chemistry: Cambridge. p. 196.

[119] Ott, J. and Eckstein, F. (1985) *Biochemistry*, **24**, p. 2530.

[120] Partridge, B.L. and Salisbury, S.A., *Structural Studies on Nucleic Acids, Ph.D. Dissertation*, 1996, Cambridge University.

[121] Pfeffer, P.E. (1984) *J. Carbohyd. Chem.*, **3** (4), p. 613.

[122] Radtke, F., Hug, M., Georgiev, O., Matsuo, K., and Schaffner, W. (1996) *Biol. Chemistry Hoppe-Seyler*, **377**, p. 47.

[123] Ramsahoye, B.H., Davies, C.S., and Mills, K.I. (1996) *Blood Reviews*, **10**, p. 249.

[124] Recondo, E.F. and Rinderknecht, G.L. (1959) *Chim. Acta.*, **42**, p. 1171.

[125] Redwine, C.M. and Whaley, T.W. (1979) *J. Label. Comp. Radiopharm.*, **16**, p. 1529.

[126] Robins, M.J., Wilson, J.S., and Hansske, F. (1983) *J. Am. Chem. Soc.*, **105** (12), p. 4059.

[127] Robinson, B.H. and Drobny, G.P. (1995) *Annu. Rev. Biophys. Biomol. Struct.*, **24**, p. 523.

[128] Saenger, W., *Principles of Nucleic Acid Structure*, ed. C.R. Cantor. 1984, New York: Springer-Verlag New York, Inc.

[129] Saito, H. (1986) *Magn. Reson. Chem.*, **24**, p. 835.

[130] Sambrook, J., Fritsch, E.F., and Maniatis, T., eds. *Molecular Cloning: A Laboratory Manual*. 1989, Cold Spring Harbor Press: Cold Spring Harbor, New York.

[131] Santos, R.A., Tang, P., and Harbison, G.S. (1989) *Biochemistry*, **28**, p. 9372.

[132] Sastry, D.L., Takegoshi, K., and McDowell, C.A. (1987) *Carbohyd. Res.*, **165**, p. 161.

[133] Schurr, J.M., Fujimoto, B.S., P., W., and Song, L., *Fluorescence Studies of Nucleic Acids: Dynamics, Rigidities, and Structures*, in *Biochemical Applications*, J.R. Lakowicz, Ed. 1992, Plenum Press: New York. p. 137.

[134] Slichter, C.P., *Principles of Magnetic Resonance*. 3rd ed. 1990, New York: Springer Verlag.

[135] Spiess, H.W., *NMR Basic Principles and Progress*. Vol. 15. 1978, Berlin/Heidelberg/New York: Springer-Verlag.

[136] Spiess, H.W. and Sillescu, H. (1981) *J. Magn. Reson.*, **42**, p. 381.

[137] States, D.J., Haberkorn, R.A., and Ruben, D.J. (1982) *J. Magn. Reson.*, **48**, p. 286.

[138] Stejskal, E.O., Schaefer, J., and McKay, R.A. (1977) *J. Magn. Reson.*, **25**, p. 569.

[139] Stolarski, R., Egan, W., and James, T. (1992) *Biochemistry*, **31**, p. 7027.

[140] Stringer, J.A. and Drobny, G.P. (1998) *Rev. Sci. Instr.*, accepted.

[141] Stringer, J.A., unpublished results.

[142] Subramanian, E. and Hunt, D.J. (1970) *Acta Cryst.*, **B26**, p. 303.

[143] Sugawara, Y., Iimura, Y., Iwasaki, H., Urabe, H., and Saito, H. (1994) *J. Biomol. Struct. Dynam.*, **11** (4), p. 721.

[144] Sun, B.Q., Costa, P.R., Kociski, D., Lansbury, P.T., and Griffin, R.G. (1995) *J. Chem. Phys.*, **102** (2), p. 702.

[145] Sundaralingam, M. (1969) *Biopolymers*, **7**, p. 821.

[146] Thewalt, U., Bugg, C.E., and Marsh, R. (1970) *Acta Cryst.*, **B26**, p. 1089.

[147] Torchia, D.A. and Szabo, A. (1982) *J. Magn. Reson.*, **49**, p. 107.

[148] Tycko, R. (1983) *Phys. Rev. Lett.*, **51**, p. 775.

[149] Tycko, R. and Dabbagh, G. (1990) *Chem. Phys. Lett.*, **173** (5-6), p. 461.

[150] Vanderhart, D.L., Gutowsky, H.S., and Farrar, T.C. (1967) *J. Am. Chem. Soc.*, **89**, p. 5056.

[151] Viswamitra, M.A., Reddy, B.S., Lin, G.H.Y., and Sundaralingam, M. (1971) *J. Am. Chem. Soc.*, **93**, p. 4565.

[152] Vold, R.L. and Vold, R.R., in *Adv. Magn. and Opt. Reson.* 1991, Academic Press: San Diego.

[153] Vorbrüggen, H., Krolikiewicz, K., and Bennua, B. (1981) *Chem. Ber.*, **114**, p. 1234.

[154] Watson, D.G., Sutor, D.J., and Tollin, P. (1965) *Acta Cryst.*, **19**, p. 111.

[155] Weast, R.C., ed. *Handbook of Chemistry and Physics*. 60th ed. 1979, CRC: Boca Raton, FL.

[156] Weintraub, O. and Vega, S. (1993) *J. Magn. Reson. A*, **105**, p. 245.

[157] Williamson, J.R. and Boxer, S.J. (1988) *Nuc. Acids Chem.*, **16**, p. 1529.

[158] Wittebort, R.J. and Szabo, A. (1978) *J. Chem. Phys.*, **69**, p. 1722.

[159] Wittebort, R.J., Olejniczak, E.T., and Griffin, R.G. (1987) *J. Chem. Phys.*, **86** (10), p. 5411.

[160] Wüthrich, K., *NMR of Proteins and Nucleic Acids*, New York: John Wiley & Sons, Inc.

[161] Young, D.W., Tollin, P., and Wilson, H.R. (1969) *Acta Cryst.*, **B25**, p. 1423.

[162] Young, D.W. and Wilson, H.R. (1975) *Acta Cryst.*, **B31**, p. 961.

[163] Zhu, L., *Ph.D. Dissertation*, 1994, University of Washington.

[164] Zhu, L., Reid, B.R., Kennedy, M., and Drobny, G.P. (1994) *J. Magn. Reson. Series A*, **111**, p. 195.

[165] Zimmer, D.P. and Crothers, D.M. (1995) *Proc. Natl. Acad. Sci. (USA)*, **92**, p. 3091.

KAREN B. GEAHIGAN

Education

Ph.D. in Physical/Biophysical Chemistry (March 1998)
University of Washington, Seattle, WA
Dissertation Title:
"A Solid-State NMR Investigation of Structure and Dynamics in Nucleosides and Methylated DNA Oligonucleotides"
Research Supervisor: Professor Gary P. Drobny

B.S. in Chemistry, summa cum laude (1990)
State University of New York, College at Purchase, Purchase, NY
Senior Thesis Title:
"Test for the Existence of an Iodyl Intermediate in Displacement Reactions at Iodine"
Research Supervisor: Professor Thomas Nalli

B.A. in History and German (1987)
Cornell University, Ithaca, NY

Employment History

Research Assistant (1993-1998)
University of Washington, Department of Chemistry
Teaching Assistant (1992-1993)
University of Washington, Department of Chemistry
Research Chemist (1990-1992)
Ensign-Bickford Coatings Company, Simsbury, CT

Awards and Affiliations

NIH Molecular Biophysics Pre-Doctoral Training Grant (1994, 1995, 1996)
W.W. Stout Fellowship (1995)
American Chemical Society, member (1994-present)
SUNY Division of Natural Sciences, Outstanding Undergraduate Research Award (1990)
Ciba-Geigy Undergraduate Research Grant, SUNY College at Purchase (1990)

Publications

"Chemical Shift Study of Uniformly ^{13}C, ^{15}N Labeled Ribonucleosides Using Two-Dimensional Dipolar Recoupling Solid State NMR," K.B.Geahigan, S.R.Kiihne, J.M.Miller, G.P.Drobny, J. Am. Chem. Soc. (1998), submitted.

"Modification of Localized Dynamics upon Methylation of C_9pG_{10} Junction in the DNA Dodecamer, $d(CGCGAATTCGCG)_2$," K.B. Geahigan, M.E. Hatcher, G.A.J. Meints, G.P. Drobny, Science (1998), in preparation.

"Distance Measurements in Multiply-Labeled Crystalline Cytidines," S.R. Kiihne, K.B. Geahigan, M.A. Mehta, H. Zebroski, G.P. Drobny, J. Phys. Chem. (1998), submitted.

"Electron Transfer from Cyclic Diaryliodine Species to Arenediazonium Salts. On the Intermediacy of 9-I-2 Structures in Iodine Atom Transfer Reactions," K.B. Geahigan, R.J. Taintor, B.M. George, D.A. Meagher, T.W. Nalli, J. Org. Chem. (1997), in press.

Presentations

"Solid-State NMR Investigation of ^{13}C,^{15}N, ^{19}F Labeled Nucleosides and Nucleic Acids Using DRAWS," K.B. Geahigan, S.R. Kiihne, J.M. Miller, G.P. Drobny, 39th Rocky Mountain Analytical Chemistry Conference, Denver, CO (July 1997).

"Solid-State NMR Investigation of ^{13}C,^{15}N Labeled Nucleosides Using DRAWS and Applications to Oligonucleotides," K.B. Geahigan, S.R. Kiihne, M.A. Mehta, J.M. Miller, H. Zebroski, G.P. Drobny, Gordon Research Conference on Magnetic Resonance in Biology and Medicine, Ventura, CA (January 1997).

"Solid-State ^{13}C NMR Investigation of Sugar Ring Conformations in the Dickerson Sequence, $[d(CGCGAATTCGCG)]_2$." K.B. Geahigan, J.A. Stringer, J.M. Miller, G.P. Drobny, 38th Rocky Mountain Analytical Chemistry Conference, Denver, CO (July 1996).

"Solution-State NMR Structure Determination of Reductively Activated FR66979 Cross-Linked to $[d(CATACGTATG)]_2$," K.B. Geahigan, H. Huang, L. Zhu, P.B. Hopkins, and G.P. Drobny, Gordon Research Conference on Magnetic Resonance, Wolfeboro, NH (June 1995).

"Test for the Existence of an Iodyl Intermediate in Displacement Reactions at Iodine," oral presentations at SUNY Natural Science Student Symposium and American Chemical Society Student Association Symposium, Purchase, NY (May 1990).

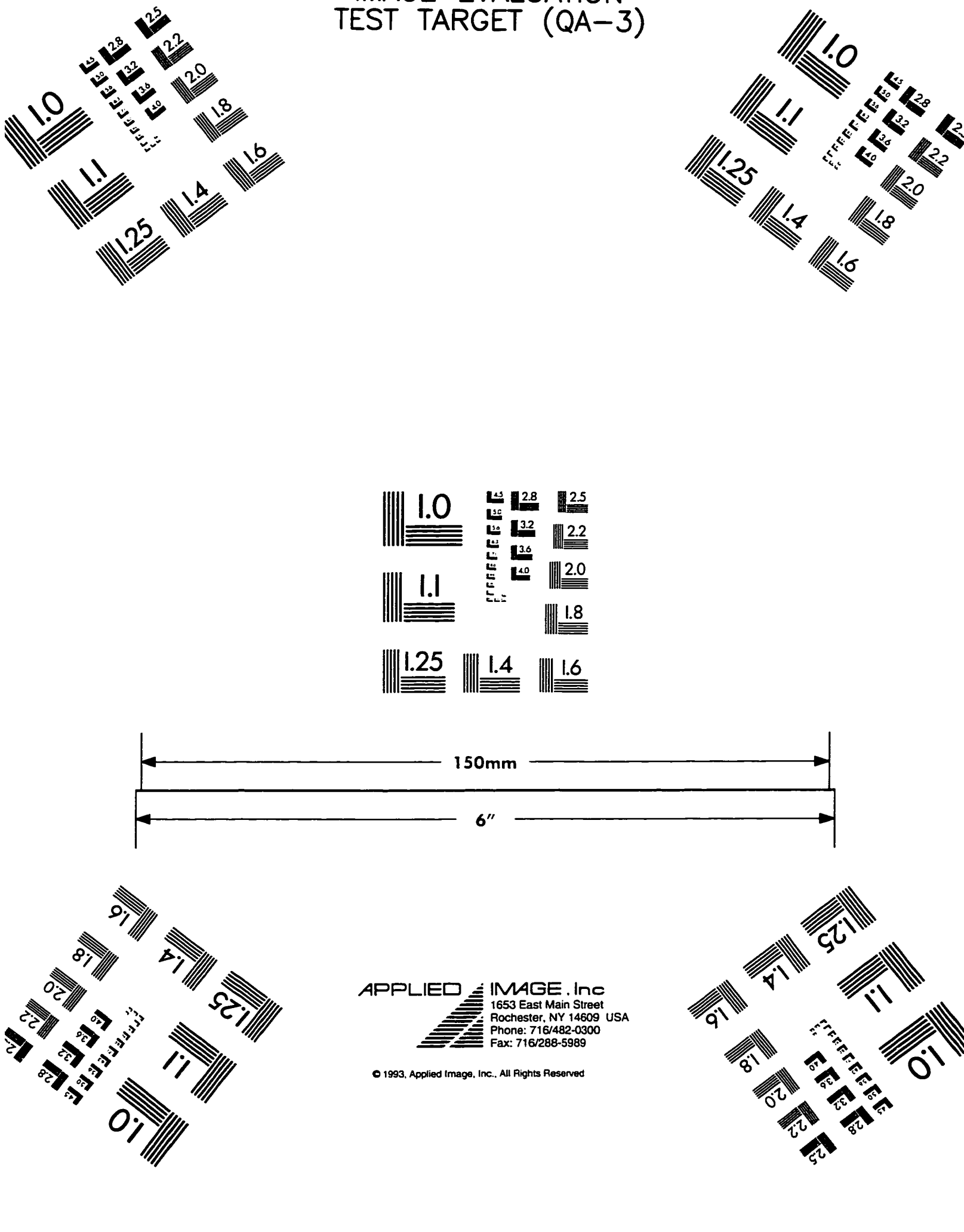
IMAGE EVALUATION
TEST TARGET (QA-3)
1.0
1.1
1.25
1.4
1.6
1.8
2.0
2.2
2.5
2.8
3.2
3.6
4.0
150mm
6"
APPLIED IMAGE, Inc
1653 East Main Street
Rochester, NY 14609 USA
Phone: 716/482-0300
Fax: 716/288-5989
© 1993, Applied Image, Inc., All Rights Reserved